Department of Physics and Astronomy
UCL

Growth and characterisation of uranium nanostructures

James Chivall

Submitted in partial fulfilment of the requirements
for the degree of Doctor of Philosophy
at University College London

May 2012

"I, *James Chivall*, confirm that the work presented in this thesis is my own. Where information has been derived from other sources, I confirm that this has been indicated in the thesis."

Abstract

Uranium is the only element in the periodic table to exhibit a charge-density wave and superconductivity at ambient pressure. The competition between these effects in technologically important high-temperature superconducting systems has come under increasing scrutiny, and uranium offers a model system in which to study the CDW. However, the element is difficult to grow in single-crystals in the bulk. We describe the growth by magnetron sputtering and characterisation of single-crystal epitaxial thin-films of alpha-uranium in the (110) orientation on the Nb(110)/A-plane sapphire buffer layer/substrate system. We use X-ray scattering methods to determine the influence of the thickness of the component layers of the samples on the microstructure, and find that there is a non-trivial dependence of the microstructural state of the uranium layers on both the thickness of the uranium layers themselves and the thickness of the niobium buffer layers upon which they are grown. In particular, the widths of the uranium peaks decrease when the uranium layer thickness is increased, but increase when the buffer layer thickness is increased.

An extensive review of the methods for characterisation of thin-film microstructures using X-ray diffraction is given, and several widely used models and interpretations are critically discussed, in particular those given in the many instances in which two-component lineshapes are seen in transverse scans from thin-films.

We also use X-ray diffraction from high-intensity synchrotron sources to characterise the charge-density wave state in these samples, and discuss the effect of uranium-layer thickness on its characteristics as a function of temperature. Important differences between the CDW seen in bulk uranium and in thin-films are seen and discussed in terms of the microstructure of the films. In particular, no incommensurate–commensurate transition is seen in the films, and a large intensity asymmetry is seen between the $2^{+}2^{+}1^{\pm}$ and $2^{+}2^{-}1^{\pm}$ CDW satellites. Furthermore, the correlation-length of the CDW is limited in the plane of the film, and dependent on the thickness of the uranium layers.

For Rhiannon

Thank you for your support and patience

4

Acknowledgements

Thanks to everyone in the CMMP who has helped with the work included in this thesis and offered advice along the way. Particular thanks go to Andrew Walters, Chris Howard, Patrick Cullen, David Buckley, Helen Walker and Richard D'Arcy, along with Professor Neil Skipper and Dr. Mark Ellerby.

A great deal of advice has been given to me by members of the uranium nanostructures collaboration, in particular, Ross Springell and Gerry Lander, Roger Ward and Sean Langridge. Thanks also go to the staff at XMaS: Peter Normile, Simon Brown, Laurence Bouchenoire and Paul Thompson.

I would also like to thank my examiners, Professors Goff and Hesjedal, for their robust and constructive criticism, from which the quality of this thesis has gained immensely.

Finally, many thanks indeed to my supervisor, Stan Zochowski.

5

Contents

List of Figures

List of Tables

Chapter 1

Introduction

1.1 Uranium — a singular element

Uranium is a fascinating element for many reasons. Famous (and perhaps infamous) for its extensive nuclear applications it is of great interest to the condensed-matter physicist for the wealth of physical phenomena that it exhibits. A comprehensive review is provided by Lander et al.[1]. Of principle interest is the almost unique ability of uranium amongst the elements to form a charge-density wave (CDW) ground state, in which the electron density forms a structure that is distinct from the ionic lattice. Like other important low-temperature grounds states such as ferromagnetism, antiferromagnetism and superconductivity, a large amount of scientific endeavour is devoted to understanding the CDW state. It has profound effects on many physical properties, including the elastic constants and heat capacity, and occurs in a wide variety of materials, including the high-T_C superconducting cuprates[2].

Uranium is the heaviest naturally-occuring element by atomic weight, and correspondingly has the largest number of electrons of any element found on earth. The behaviour of this large number of electrons drives interest in the metal. We may describe the arrangement

of the electrons in U as $[Rn]7s^26d^15f^3$; due to relativistic effects arising from the high velocities of electrons in the 5f and 6d electron shells, the 7s shells are lower in energy, and are therefore fill preferentially. In Figure 1.1 we see the effect of the progressive filling of the 5f electron shell as atomic number increases across the actinide series, from Ac to Es. For the light actinides, from Ac to Pu, the trend in the atomic volume mirrors that of the 3d transition metals, whereas for heavier metals the atomic volumes tend towards those of the 4f metals. The change in behaviour across the series is associated with a change in the strength of the electronic interactions between neighbouring metallic ions from strong correlations in the light actinides, to weak correlations in the heavy actinides. For this reason, 5f electrons in the light actinides have more *itinerant* character, whereas those in the heavy actinides are *localised* in atomic-like energy levels. We notice that U is positioned close to the turning-point of the curve. Uranium is non-magnetic, but uranium compounds such as uranium pnictides and uranium chalcogenides are.

Uranium adopts an open orthorhombic structure at low temperatures that is of low symmetry and unique amongst the elements. The unit cell is shown in Figure 1.2, and the lattice parameters are a=2.8537 Å, b=5.8695 Å, and c=4.9548 Å under ambient conditions. The metal has a density of $19.05\,\mathrm{g\,cm^{-1}}$ under standard conditions. On cooling from the melt, the metal is of bcc structure (γ-U). At 1049 K it undergoes a phase transition to the tetragonal β phase, which is stable above 961 K. Below this temperature the α phase is stable.

1.1.1 The charge-density wave ground-state in uranium

Experiments aiming to deduce the behaviour of the physical properties of uranium at low temperature in the 1950s and 60s found that an unusual phase transition occurs at around 43 K. Anomalies were seen in the thermal expansion coefficients[3] , Hall coefficient[4] and thermal conductivity[5], but no evidence for a crystallographic phase transition. Most notably, a lambda-type anomaly is seen in the elastic constants, especially on c_{11}, which

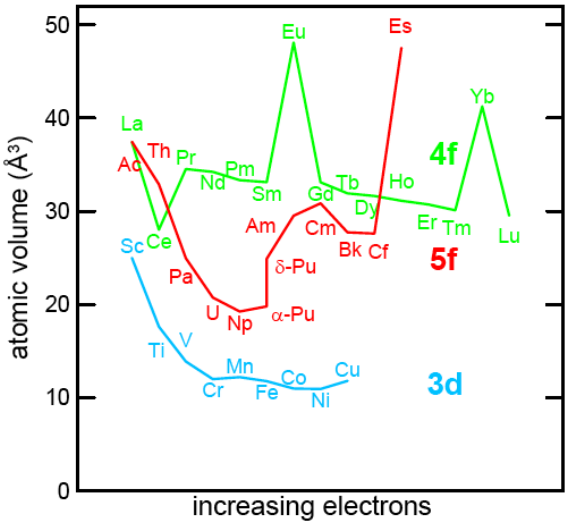

Figure 1.1: The atomic volumes of elements from the actinide series of metals, with progressive filling of the 5f electron shell from left to right (red line). Also shown are the atomic volumes of elements from the 3d transition metals (blue line) and elements from the lanthanide series of metals (green line), with progressive filling of the 3d and 4f electron shells, respectively, from left to right . We see that for the *light actinides*, which include the elements Ac to Pu, the behaviour of the 3d metals is mirrored, whereas the behaviour of heavier metals more closely follows that of the 4f metals.

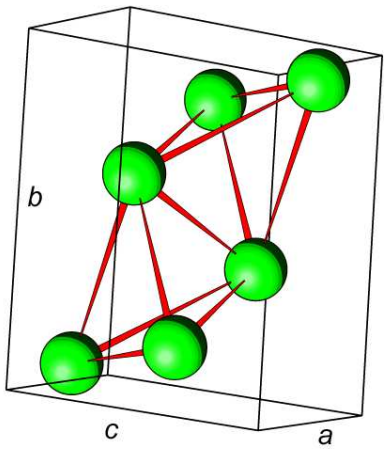

Figure 1.2: The unit cell of the low-temperature alpha phase of uranium metal. The lattice parameters are a=2.8537 Å, b=5.8695 Å, and c=4.9548 Å under ambient conditions.

relates extensional strain to extensional stress along the [100] crystal direction[6]. X-ray diffraction measurements of the lattice constants showed that the coefficient of thermal expansion becomes *negative* between 46 and 18 K[7]. X-ray scattering data showing the temperature-dependence of the uranium lattice parameters in this temperature-range is reproduced in Figure 1.3. Heat-capacity measurements[8] found anomalies at 37 K and 22 K, corresponding to a first-order transition, along with that at 43 K, which corresponds to a second-order transition (although recent evidence[9] suggests this transition to be first-order). With no evidence for a crystallographic phase transition, it was unclear what was responsible for the above transitions until the early 1980s. The various efforts to explain these phenomena are related in the review of Lander et al.[1].

An important discovery leading to an explanation of the phenomena was the discovery, using inelastic neutron scattering, of a softening of a phonon near $\mathbf{q} = [\frac{1}{2}, 0, 0]$, propagating along the [100]-direction, as temperature is decreased. Essentially, the phonon condenses below around 40 K, and the displacements of the atoms associated with the phonon are 'frozen-in'. This leads to a doubling of the unit cell in this direction and the appearance of satellite peaks in the diffraction pattern around the half-integer positions in H[10]. The deformation was then quickly ascribed to the formation of a *charge-density wave* where coupling between electron and phonon dynamics allows the outer $5f$ electrons of the metal to lower their energy by a transition that opens up a gap at the Fermi energy.

The charge-density wave (CDW) state is usually associated with low-dimensional materials, with 1D electron chains shown to be unstable with respect to such a transition by Peierls[11] and the most commonly-studied CDW materials being layered structures such as the transition metal di-chalcogenides[12,13], and more recently the superconducting cuprates[14,15] and pnictides[16,17]. Good theoretical introductions may be found in Grüner, 1988[18] or Grüner, 1994[19].

In low-dimensional materials the high-symmetry of the Fermi-surface increases the likelihood of there being areas of many occupied states separated from many unoccupied states

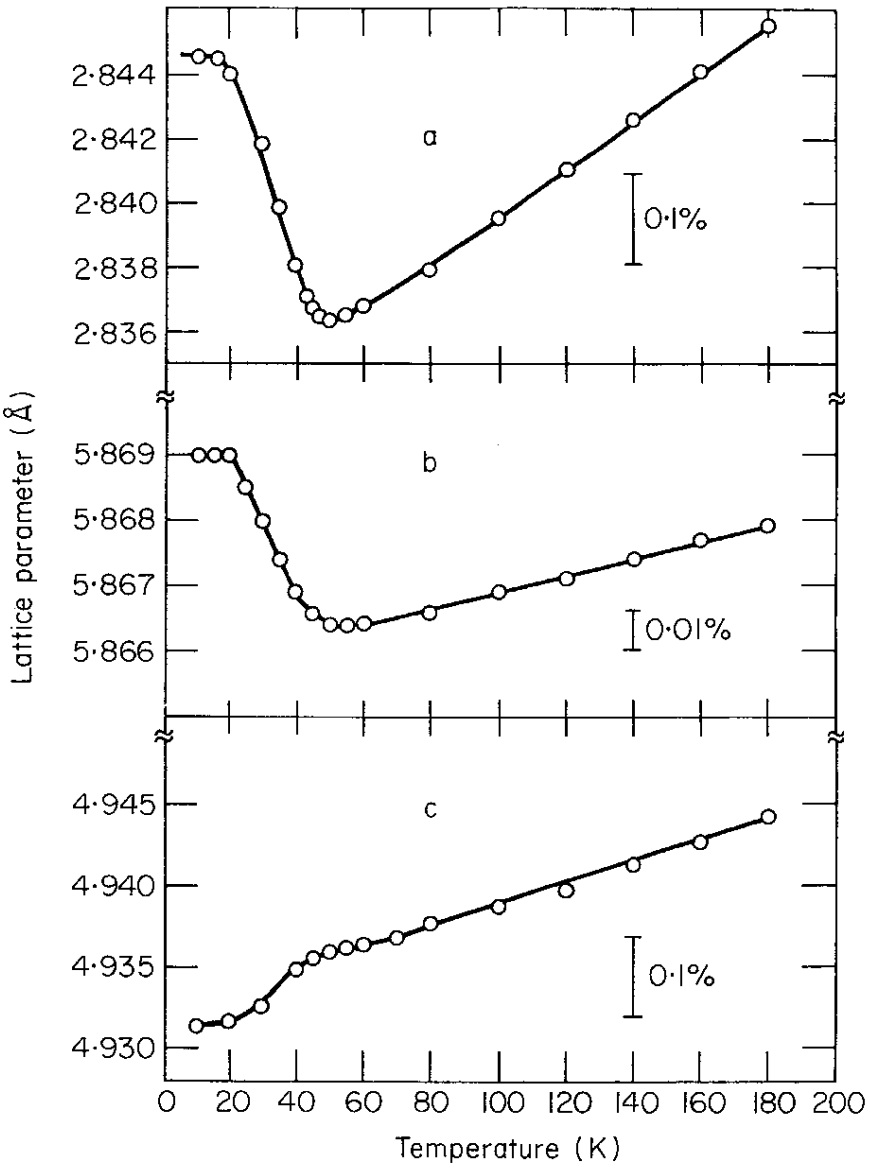

Figure 1.3: The temperature-dependence of the uranium lattice parameters in the temperature range 0–200 K. As deduced from: The U(400)-reflection (top panel), the U(080)-reflection (middle panel) the U(006)-reflection (bottom panel). Reproduced from Lander et al.[1], with original data from Barrett et al.[7]

by a single wavevector, q, that allow the coupling (often described as *nesting*) of states across the Fermi surface and the opening of a gap in the electron density-of-states, thereby lowering the electronic energy[11,20].

These conditions are rarely met in elemental crystals, and uranium and chromium are the only elements that display the charge-density wave ground state. In chromium the CDW is present as a result of a spin-density wave (SDW) state, which forms due to similar pairings across the Fermi-surface of electrons and holes of opposite spin (see Dubiel and Cieślak[21], Hill et al.[22], Jacques et al.[23], Fry et al.[24], Laurent et al.[25], Fawcett[26] and references therein), whereas uranium is the sole element in which a CDW forms independently, despite some researchers positing their existence in the alkali metals[27–29]. Uranium is unique among the elements in adopting an unusual rhombohedral crystal structure in its α phase, which has low symmetry, and with the narrow f-band of electrons and a large density of states at the Fermi level there is a enhanced energy gain from forming a gap at the Fermi level, with a small cost from breaking the symmetry of the lattice[30]. The role of the f-electrons in the formation of the CDW state suggests that neighbouring actinides might display the CDW state, but there is no evidence for this[31].

In the prevailing scientific climate, where grants for superconductivity research make up 1/40 of the UK Engineering and Physical Science Research Council budget[32], and with over 100,000 papers published on the subject since Beidnorz and Mülcer unveiled the first high-T_C superconductor[33], there is a motivation to study the CDW in real materials due to its persistent links with superconductivity[2,16,34,35]. The two phenomena are generally considered to compete, since the same electrons in states near the Fermi level are involved in electron-hole pairing in the CDW state and electron-electron (Cooper) pairing in the superconducting (SC) state[36]. There is a large amount of evidence that suggests that suppression of the CDW by doping[16,37–39], pressure[34,40,41] or other means[35] allows an increase in the superconducting transition temperature, (T_C). However, there is also evidence for the ability of the two states to co-exist[42,43].

Superconductivity has been reported in α-uranium at ambient pressure[1,44,45], although was not seen in recent experiments on very high purity, strain-free samples[46]. A large increase in the superconducting T_C from $< 0.1\,\mathrm{K}$ to $2.1\,\mathrm{K}$ is seen in polycrystalline α-U as the pressure is increased to $22\,\mathrm{kbar}$[47,48], and a smaller increase seen in a single crystal sample[49]. This corresponds with evidence for the suppression of the CDW transitions with increasing pressure[48].

The CDW state and the superconducting (SC) state coexist in several systems including the transition metal dichalcogenides[50] and the high-T_C cuprate superconductors, and the competition between the CDW and the SC states is becoming a topic under increasing scrutiny[2,16,35,51]. In sulfur, the CDW state is also thought to compete with the formation of the superconducting state;[34] its suppression at high-pressure resulting in an increase in the superconducting transition temperature. In uranium a 20-fold increase in the superconducting transition temperature is evident as pressure is increased from 1 atmosphere to $2.1\,\mathrm{kbar}$[47]. The ability of uranium to form a charge-density wave *and* to superconduct is unique amongst the elements. In the bulk, low-temperature alpha-phase of uranium, the CDW state forms below $43\,\mathrm{K}$, and the metal becomes superconducting below $1\,\mathrm{K}$, although the exact superconducting transition temperature is very sensitive to impurities and sample fabrication methods, and has not been confirmed experimentally.

1.1.2 Charge-density wave or strain-wave?

The vast majority of the literature concerning the low-temperature ground-state of uranium described above is written in terms of the charge-density wave, yet much of the movement in charge is due to a strain-wave; a displacement of the metallic ions.

A similar situation is seen in chromium films[52], although chromium also exhibits a spin-density wave (SDW), which drives the formation of CDW and SW, as described above. In a study of bulk chromium the asymmetry of intensity of satellite reflections across Bragg peaks is shown to be due to the charge density wave by Mori and Tsunoda[53]; a pure strain

wave would lead to symmetrical satellite intensities.

Abbamonte[54] describes a general method using resonant X-ray scattering to distinguish between the charge (valence) modulation and the strain wave associated with a charge density wave. In this method the strain amplitude, u_0, and the charge-modulation amplitude, ν_0, may be objectively determined, along with their relative phase. The ratio of the two, $W = \frac{\nu_0}{u_0}$, could then be used to determine whether the CDW is driven mainly by electron-phonon interactions, when $W \sim 1\,\text{Å}$, or by many-body effects, for large W.

1.2 Thin-films

Thin-film devices are the basis of much modern technology, from CMOS transistors to high-density computer memory. Built up by the condensation of individual atomic, ionic or molecular species onto a solid substrate, there are three major reasons why the thin-film state is so important to modern physics. Firstly, the very slow layer-by-layer fabrication of thin-films by techniques such as magnetron sputtering, chemical vapour deposition or pulsed laser ablation allow fine control of the crystal structure, microstructure and size of the layers, often far from what would be an equilibrium state in the bulk. Secondly, severely limiting size in one or more dimensions leads to the emergence of physical phenomena not normally seen. Finally, for thin layers, the behaviour at the interfaces becomes significant, and so by stacking a number of thin-layers into a *multilayer* interfacial behaviour may be magnified. Thin-films are the nanostructures that are the subject of this thesis.

1.2.1 Microstructural features of epitaxial films

The microstructure of materials in the present context refers to the microscopic arrangements of the atoms that depart from the perfection of the crystal lattice. Most materials are not perfect crystals but contain defects that are a product of their manufacture[55]. The functional behaviour of any material is closely related to its structure, and for this

reason it is crucial to deduce the 'real structure'[56].

It is often expected that for many technological applications, crystalline perfection is desired, and this is true in many cases. In light-emitting diodes, the efficiency of the transfer of electrical energy to light is heavily dependent on the crystalline perfection of the semiconductors involved[57–59]. However, in some applications functionality may be enhanced by the deliberate inclusion of defects or strain, such as in CMOS electronics[60], functional multiferroic oxides[61] and high-temperature superconducting wire[62].

The importance of detailed study of the microstructure of commonly used systems such as Nb/sapphire[63] is indisputable. However, in the literature there is little in the way of systematic study of the how microstructural changes due to variables such as film thickness and growth temperature on the basis system affect the structure of the overlayers deposited upon them.

Epitaxial thin-films of many kinds exhibit similar microstructural features, which result from both the size and shape of the structures and the methods of their fabrication.

1.2.1.1 Epitaxial strain

Firstly, if there is any difference in the lattice-parameters of the layer of interest and the substrate upon which it is grown there will be an *epitaxial strain* in the layer. In many cases the substrate is assumed to be rigid, but for metallic substrates, or samples with several layers of similar thickness both components may be strained. A comprehensive introduction to the origins and consequences of stress and strain in thin-films is given in Freund[64].

The misfit in the lattice parameters between the niobium (110) crystal face and the sapphire $(11\bar{2}0)$ is significant, as shown in Table 1.1.

Interface	Lattice directions	Misfit
Al_2O_3–Nb	$[0001]_{Al_2O_3} \parallel [1\bar{1}1]_{Nb}$	1.9 %
	$[\bar{1}100]_{Al_2O_3} \parallel [\bar{1}1\bar{2}]_{Nb}$	12 %
Nb–U	$[001]_{Nb} \parallel [\bar{1}10]_{U}$	-1.1 %
	$[\bar{1}10]_{Nb} \parallel [001]_{U}$	6.2 %

Table 1.1: The misfits in the lattice parameters along parallel crystal directions at the Al_2O_3–Nb and Nb–U interfaces in the current samples. The Al_2O_3–Nb data was taken from Grier et al.[65] and the Nb–U data from Springell et al.[66].

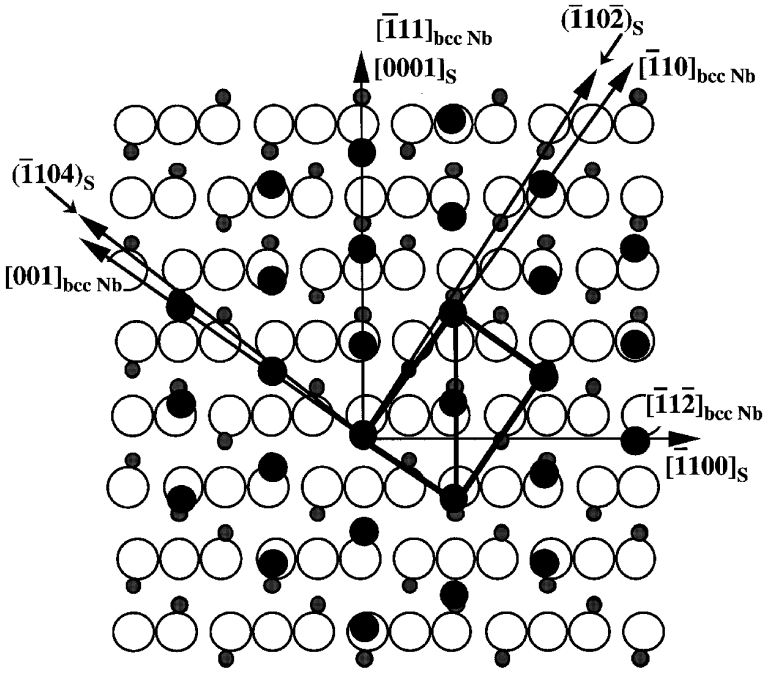

Figure 1.4: The epitaxial arrangement of niobium grown on the $(11\bar{2}0)$ crystal surface of Al_2O_3. Taken from Oderno et al.[67]. White circles correspond to oxygen, black circles to niobium and the smallest circles, in grey, correspond to the aluminium positions. The Nb atoms are expected[68] to continue the Al sub-lattice of the sapphire, and hence have specific adsorption sites on the $(11\bar{2}0)$ surface.

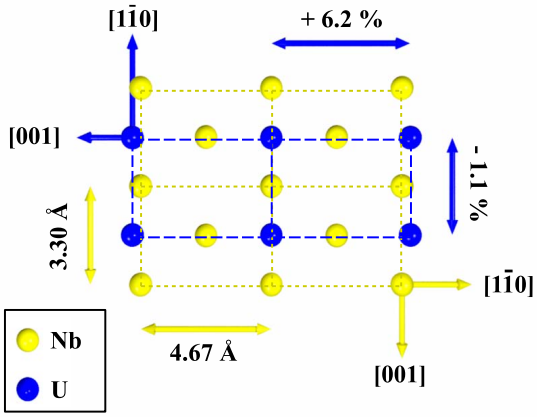

Figure 1.5: The epitaxial arrangement of uranium grown on the (110) crystal surface of Nb. The bulk U [001] lattice vector is 4.9548 Å in length and [1$\bar{1}$0] vector $(2 \times 3.2637 = 6.5265)$ Å in length. Taken from Springell et al.[66].

1.2.1.2 Dislocations

In an epitaxial system the strain that results from mismatch in the lattice parameters of the film and the substrate provides an energetic driving force for the formation of defects that relieve stress. The primary defects associated with strain relief are *dislocations*[69]. Here we shall give a brief discussion of the form and properties of dislocations. An *edge dislocation* may be thought of as the introduction of an extra half-plane of atoms into the lattice. The *line-vector* of the dislocation lies along the edge of the half-plane, and the lattice is disrupted with cylindrical symmetry around this line, which is referred to as the *core* of the dislocation. The *Burgers vector* of the dislocation is found by tracing a loop around the dislocation core by moving from lattice-site to lattice-site. For example, if the line vector of the dislocation is along [001], a loop might be traced by moving 3 atomic-spacings along [010], 3 along [001], then 3 along [0$\bar{1}$0] and finally 3 atomic-steps along [00$\bar{1}$]. Prior to the introduction of the dislocation the loop is closed, but if the loop encloses the dislocation-line there is a gap between the start- and end-points. The vector joining these points is the Burgers vector, **b**. If **b** lies purely in the (001) plane, it is a pure edge dislocation, but if **b** has a component *along* [001], it has some "screw" character. A *screw dislocation* has Burgers vector parallel to the line vector, and a *mixed dislocation* has

both edge and screw components. These points, along with a discussion of the equilibrium stress field due to a dislocation, are treated in Freund [64].

Due to energy considerations there are preferred line and Burgers vectors in each crystal. Usually the *glide plane*, that plane which contains the line and Burgers vector, of a dislocation is the closest-packed plane of the crystal, and the Burgers vector is often the smallest lattice vector. The glide plane and line vector of a dislocation describe the *slip system* on which it operates, and by symmetry operations in the crystal similar crystal planes and directions are part of the same slip system. For example, in body-centred cubic crystals such as niobium the predominant glide planes are the equivalent $\{112\}$ planes, and the Burgers vectors are along the equivalent $\langle 111 \rangle$ crystal directions, such that the slip system is described as $\{112\}\langle 111 \rangle$ [70]. In uranium the dominant slip system is $\{010\}[100]$ [71].

The stress field implies that there is an energetic cost associated with the formation of a dislocation, which for a dislocation to spontaneously form in a crystal, must be accounted for by the reduction in strain energy in the volume of the crystal relieved by the presence of the dislocation. In a thin-film the misfit-strain causes dislocations to move towards the film-substrate interface, such that misfit dislocations are generally found close to the interface. Hence, the volume of the film relieved by the presence of a dislocation of the interface is dependent on the film thickness, and there exists a critical thickness, h_c, below which the strain energy relieved by the presence of the dislocation is exceeded by the work done in forming the dislocation, and the formation of a dislocation is energetically unfavourable. An expression relating h_c to the Burgers vector, often known as the Matthews-Blakeslee condition [64,72], is

$$h_c = \frac{b}{2\pi f} \frac{1 - \nu \cos^2 \alpha}{1 + \nu \cos \lambda} \left(\ln \frac{h_c}{b} + 1 \right), \tag{1.1}$$

where ν is the Poisson ratio for the film, λ is the angle between the slip direction and that direction in the film plane which is perpendicular to the line of intersection of the slip plane and the interface and α is the angle between the dislocation line and its Burgers vector.

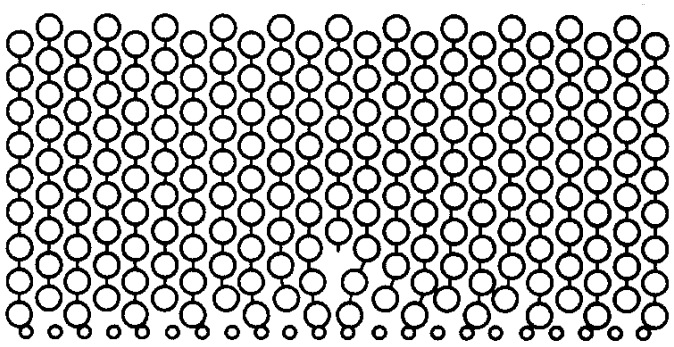

Figure 1.6: A model for the interface between niobium (large circles) and sapphire (small circles), showing a misfit dislocation located between the 3rd and 4th atomic layers. Only the top layer of the sapphire substrate is shown.

The misfit dislocations in niobium films grown on A-plane $(11\bar{2}0)$ sapphire have been studied using electron microscopy for MBE-grown[65] and sputter-deposited[73] films. Since the Nb layer is strained biaxially, at least two systems of dislocations are needed to relieve the strain in the lattice, and these are identified by Grier et al.[65] to have Burgers vectors $\mathbf{b}=\frac{1}{2}[1\bar{1}1]$ and $\mathbf{b}=\frac{1}{2}[\bar{1}11]$, which agrees with investigations on other orientations of the system by Gutekunst[74–76].

The critical thickness for spontaneous dislocation formation is shown by Grier et al.[65] to be 72 Å. The distance between misfit dislocations, d_{MD}, may be found from the component of the burgers vector parallel to the interface, and the misfit in that direction,

$$d_{\mathrm{MD}} = \frac{|\mathbf{b}_{\mathrm{MD}}|}{\delta}, \tag{1.2}$$

where the misfit, $\delta = \frac{a_{\mathrm{Nb}} - a_{\mathrm{S}}}{a_{\mathrm{S}}}$. Grier et al.[65] estimate $d_{\mathrm{MD}} = (2.1 \pm 0.2)\,\mathrm{nm}$.

1.2.1.3 Other features

The substrates used in this study are prepared to an "epitaxial finish" and are of the same provenance as those used in a number of other studies[65,66,77,78]. The surface normal corresponds to the $[11\bar{2}0]$ direction of the sapphire crystal to within $\pm 0.5^{\circ}$. Any deviation

of the surface normal from the crystal results in the formation of *vicinal steps* separated by atomically-flat terraces. The growth of niobium on sapphire is generally agreed[63] to follow a step-flow model[79], in which niobium adatoms diffuse to step edges and nucleate coherent patches which spread across the terraces. The initial structure is anomalously hexagonal[77], but after a few monolayers regular oscillations are seen in the intensity of RHEED patterns, corresponding to a "Frank-van der Merwe" layer-by-layer growth[80]. The substrate miscut is also cited as leading to atomic-height oscillations that persist throughout the film[81].

1.2.1.4 The mosaic crystal model

The growing patches are unlikely to share the same orientation in the plane of the film, so when separately nucleated patches coalesce there will be a disruption of the translational symmetry of the growing crystal. When the disruption in the crystal is large the separate patches are referred to as grains, separated by grain boundaries. For small misorientations the disruption of the crystal is accommodated by arrays of dislocations[82] and the *mosaic crystal* model is appropriate[83,84].

1.2.2 The motivation for thin-film uranium

Thin-film uranium provides an excellent system in which to study the formation of the CDW state[85]. There is a motivation to study factors that influence its formation, such as film thickness and epitaxial strains due to the orientation of the crystal with respect to the substrate, and its suppression in these samples might lead to an increase in the superconducting T_C at ambient pressure, which would be a major achievement.

1.3 Thin-film growth methods

1.3.1 Chemical vapour deposition

In chemical vapour deposition (CVD) methods[86], the desired film constituents are condensed as the solid products of a chemical reaction, from precursors in the vapour phase. A wide variety of materials may be deposited using CVD methods, and the techniques lead to high uniformity films, even over complex shapes and large areas. However, since the reactions proceed over narrow ranges of deposition conditions, it is difficult to investigate the relationship between processing conditions and structure. For example, the temperature of the substrates may not independently be controlled. These factors make it difficult to predict growth mechanisms and optimum deposition parameters.

1.3.2 Physical vapour deposition

In physical vapour deposition (PVD) methods a vapour consisting of the species required for the thin-film layer is directed towards a substrate, where the material condenses, without any chemical reaction taking place. This can allow more control over the deposition conditions, allowing an easier route to optimisation of the growth parameters. Here we shall briefly outline three of the most commonly-used techniques. A good introduction to PVD processes may be found in Mattox[87].

1.3.2.1 Molecular-beam epitaxy

Molecular-beam epitaxy (MBE) is an evaporation method, such that thermal energy beams of the desired molecular or ionic components of the films are directed at the substrate at elevated temperature. The layer constituent is heated in a cavity with a small orifice, with frequent calibration and precise temperature control needed to maintain the desired flux of material. MBE methods allow very slow deposition rates ($< 1\,\text{monolayer}\,\text{s}^{-1}$), and

at high substrate temperatures such that surface diffusion may lead to high crystalline perfection and extremely flat layers. However, the process is complex, slow and expensive. Due to concerns over contamination, access to MBE growth systems is extremely limited for actinide science.

1.3.2.2 Pulsed-laser deposition

In pulsed-laser deposition (PLD) methods, very short (30 ns), intense pulses of laser energy directed at a target cause explosive evaporation and ejection of small clusters of atoms of the target material, which may settle on a nearby substrate. These methods are suitable for a wide range of materials and growth environments, and in particular allow deposition of complex compounds such as superconducting oxides. However, the equipment is very expensive, limiting access.

1.3.2.3 Magnetron sputtering

The most adaptable and convenient PVD method is magnetron sputtering, which may be used for a wide variety of materials. The technique is relatively cheap and allows wide variation of deposition temperatures and conditions, allowing rapid prototyping and growth optimisation. It is ideal for the current project, and access to a dedicated system for the sputtering of uranium-based samples has been possible.

For deposition to take place, a plasma of an inert gas, usually Ar, is formed in a vacuum chamber and the gaseous ions accelerated in an electric field towards a target of the desired film material. The collision of the energetic species with the target causes a chain of collisions that result in the ejection of the target atoms into the vapour.

The method has several limitations. In order to maintain the plasma discharge, a relatively large pressure (around 1 Pa) of gas is required, such that secondary electrons ejected from the target collide with gas atoms in sufficient quantity. This means that the sputtered

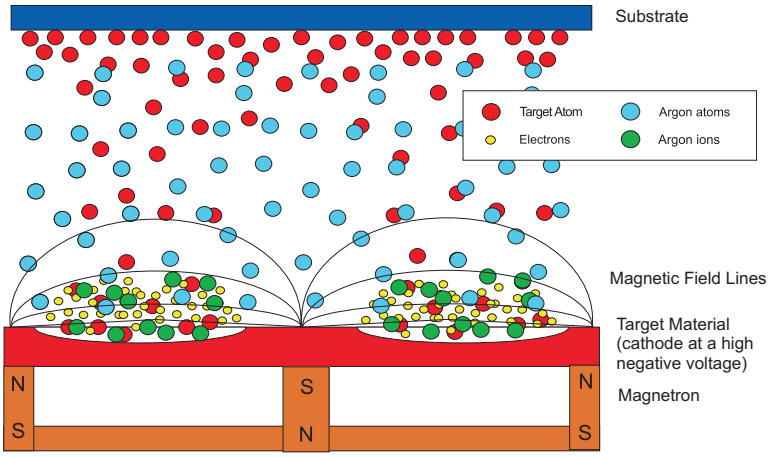

Figure 1.7: A schematic diagram of the magnetron sputtering process. The magnetic field around the magnetrons combines electrons close to the target material, and allows a plasma to be maintained at lower gas pressures. Argon ions are accelerated towards the target material, and the bombardment causes ejection of target atoms towards the substrate where the target atoms condense. Note that sputtering rates vary across the surface of the target.

species must pass through the gas in order to reach the substrate and efficiency is low. In addition, the species are of high energy (several tens of eV) so have a large velocity as they reach the substrate, which can lead to structural disorder in the growing phase.

A way of improving the performance of the gas sputtering system is trap electrons near the surface of the target using a the magnetic field from a *magnetron* shown in Figure 1.7. As the path of the electrons is confined close to the target there is an increased probability of collision with the gas, and so the plasma discharge at the target can be maintained over a much wider range of gas pressures. Lower gas pressures allow for higher deposition rates as fewer sputtered atoms are scattered by the gas. The geometry of the magnetrons used for the fabrication of the current samples is shown in the left panel of Figure 2.2.

1.4 The charge-density wave in thin U films

Previously published data[85] compares the CDW state in a 5000 Å-thick uranium film to that in the bulk. We shall review these findings before presenting the results from X-ray scattering experiments on a series of epitaxial uranium films of varying thickness.

1.4.0.4 Temperature-dependence of the CDW-wavevector

In Figure 1.8 we see that the temperature-dependence of the CDW wavevector is qualitatively different from that of the bulk. In these films, which are oriented with the U[110] lattice direction normal to the surface, the q_z-component lies in the plane of the film, and we see that it is almost temperature-independent. This suggests that the displacements in the [001] direction due to the CDW (as shown in Figure 2.12) are constrained by the presence of the substrate.

1.4.0.5 Satellite Intensities

One of the most striking features of the scattering from the CDW in thin films as opposed to in the bulk is an asymmetry in the intensities of the satellites. Figure 1.9 shows the CDW satellites around the U(221) reflection in the 5000 Å sample. A large intensity asymmetry (IA, to borrow terminology from Ravy, 2006[89]) is seen between the satellites, with those with scattering vector $\mathbf{G}_{221} + q_x\mathbf{a}^* + q_y\mathbf{b}^* \pm q_z\mathbf{c}^*$ around an order of magnitude greater in intensity than those with $\mathbf{G}_{221} + q_x\mathbf{a}^* - q_y\mathbf{b}^* \pm q_z\mathbf{c}^*$. A similar IA is seen between satellites with $\mathbf{G}_{221} + q_x\mathbf{a}^* \pm q_y\mathbf{b}^* + q_z\mathbf{c}^*$ and $\mathbf{G}_{221} + q_x\mathbf{a}^* \pm q_y\mathbf{b}^* - q_z\mathbf{c}^*$. Here we shall introduce notation that distinguishes between the satellites, such that for the satellites around the $\mathbf{G}_{221}$ reciprocal-space position, the satellite with $\mathbf{Q} = \mathbf{G}_{221} + \mathbf{q}_{\mathrm{CDW}}$ and that with $\mathbf{Q} = \mathbf{G}_{221} - \mathbf{q}_{\mathrm{CDW}}$ are referred to as the $2^+2^+1^+$ and $2^-2^-1^-$ satellites respectively, if $\mathbf{q}_{\mathrm{CDW}} = (+q_x, +q_y, +q_z)$.

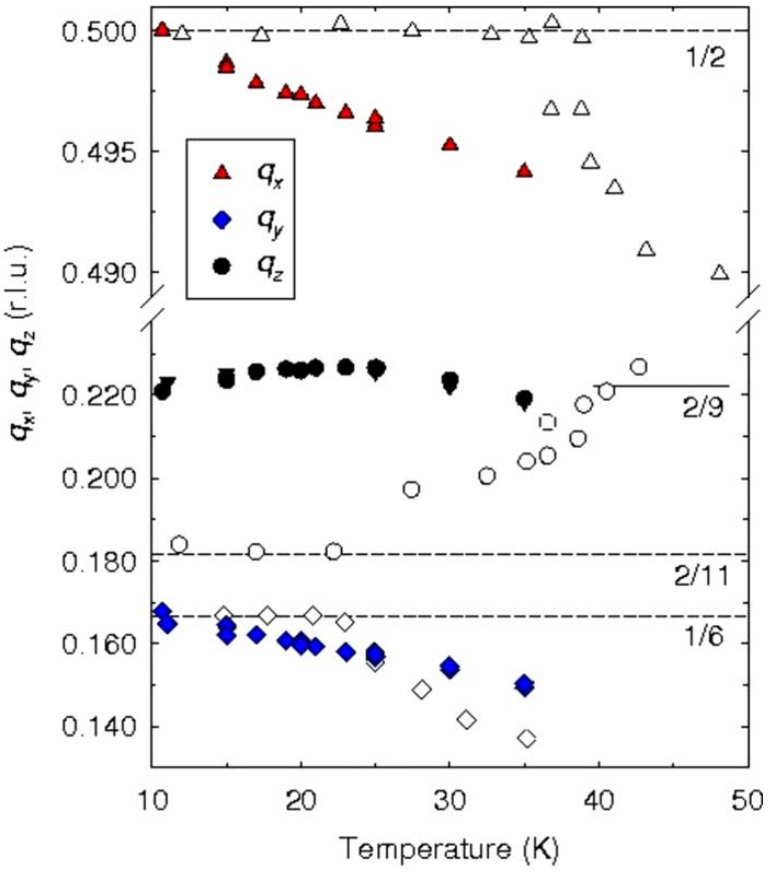

Figure 1.8: Components of the CDW wave vector $\mathbf{q}$ in the 5000 Å film of α-U (solid points) as a function of temperature, taken from Springell et al.[85]. The bulk values are indicated by open points and are taken from Grübel et al.[88], as in Figure 2.11. CDW phase transitions occur at 22 K and 37 K in the bulk.

The other satellites arise since a number of different $\mathbf{q}_{\mathrm{CDW}}$-vectors exist in the crystal, taken from the following possibilities:

$$\mathbf{q}_1 = (+q_x, +q_y, +q_z)$$
$$\mathbf{q}_2 = (+q_x, -q_y, +q_z)$$
$$\mathbf{q}_3 = (+q_x, +q_y, -q_z)$$
$$\mathbf{q}_4 = (+q_x, -q_y, -q_z),$$

along with a further four that arise by reversing all the signs, equivalent to the action of the time-reversal operator. (These further domains may be ignored as no information is

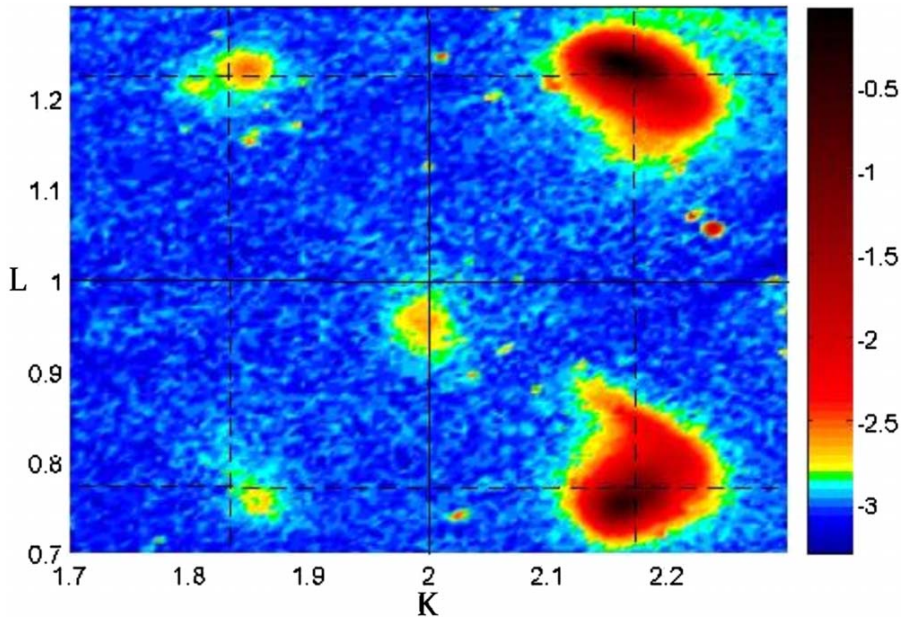

Figure 1.9: The intensity of scattering at 10 K in the $(2.5, K, L)$-plane of reciprocal space for a 5000 Å film of uranium, shown using a logarithmic colour scale. The satellites due to the PLD are visible at $(2 + \frac{1}{2}, 2 \pm q_y, 1 \pm q_z)$, with $q_y = \frac{1}{6}$ and $q_z = \frac{2}{9}$. Taken from Springell et al.[85]

added by including them.) It has been shown that in fact the CDW exists with only two $\mathbf{q}_{\mathrm{CDW}}$-vectors are present together (a 2-$\mathbf{q}$ state), and in the following combinations $\mathbf{q}_1 \pm \mathbf{q}_4$ and $\mathbf{q}_2 \pm \mathbf{q}_3$. A discussion of this is given in Lander, 1994, pp.77–79[1]. As satellites arising from both combinations are seen together, we can say that multiple CDW-domains exist within the crystal, each with different $\mathbf{q}_{\mathrm{CDW}}$.

We may hence label the four satellites in Figure 1.9, moving clockwise from the $(2.5, 2\frac{1}{6}, 1\frac{2}{9})$ position, as follows: $2^+2^+1^+$, $2^+2^+1^-$, $2^+2^-1^-$, and $2^+2^-1^+$.

1.4.0.6 Smith-satellite

Historically, the first satellite-peaks seen in α-U were those at approximately $((h+\frac{1}{2}), k, l)$[10]. These "Smith-satellites" arise from the boundaries between CDW domains (see Yamada, 1993[90]). There was no sign of the Smith-satellites at the (2.5,0,0) position in the 5000 Å film. (The intensity near this position in Figure 1.9 is temperature-independent and hence

spurious.)

1.4.0.7 Temperature-dependence of the lattice parameters

The strong electron-phonon coupling responsible for the formation of the CDW is evidenced by a minimum in the lattice d_{110} lattice spacing at the transition temperature, as shown by Barrett et al.[7]. In a 5000 Å U the minimum was smaller and more rounded than in the bulk, which is shown in Figure 1.3.

1.4.1 The influence of the thin-film geometry in other systems

The effects of the thin-film state have been investigated in similar systems involving modulated ground states. In the elemental spin-density wave antiferromagnet chromium, mentioned above, a theoretical study[91] predicted the quantisation of the SDW wavevector in thin Cr films. In this system the CDW/strain-wave that accompanies the SDW has wavevector parallel to, but half the length of the SDW-wavevector. In addition, two spin-density waves of different wavelengths were predicted to co-exist for certain thicknesses of around 45 monolayers. These predictions have been borne-out by experiment[92] in films between of thickness between 175 and 506 Å. In bcc chromium the SDW wavevectors lie along one of the ⟨100⟩ lattice directions in each domain with equal probability, but in the thin films[92] , domains with $\mathbf{q}_{\mathrm{CDW}}$ in the plane of the film occupied only 8 % of the film volume. Furthermore, only two CDWs, with wavelengths leading to consecutive numbers of periods within the film thickness, were shown to coexist. In a thicker film (∼3500 Å) the effects of wavevector quantisation are not seen and the behaviour is governed by the growth of the SDW-domains at low temperature.

In a separate series of experiments[52], the period of the CDW in thin films was shown to increase with decreasing film thickness, and increase with temperature more quickly in thinner films. The dependence of the intensity of the satellites on temperature deviated

from the bulk behaviour, with intensity persisting above the bulk transition temperature.

Holmium, which has an hcp crystal structure, orders antiferromagnetically below $T_N \approx 131\,K$, with the atomic spins aligned ferromagnetically within atomic planes perpendicular to the c direction, but rotated between planes by a phase angle $\phi = \tau\pi$, where τ is the wavevector of the modulation, forming a spiral structure. Close to T_N, $\tau \approx 0.28$, and it decreases with temperature. In the bulk τ locks-in to a value of $\frac{1}{6}$ at around 17 K, which marks the onset of a transition to a conical structure, with a component of the magnetic moment forming along the c-axis. In thin-films[93] and superlattices[94] the lock-in to $\frac{1}{6}$ does not occur, and there is some evidence of the co-existence of two phases with slightly different wavevector[94]. Interestingly, a discrepancy exists between the wavevectors found using X-rays and neutrons, as in uranium, mentioned above.

1.5 Other work

Necessarily this thesis documents a coherent body of work that has been followed to a satisfactory conclusion. However, this does not, of course, reflect the reality of scientific research, and is indeed representative of only a proportion of the total amount of work done during the course of this project, some more of which will be discussed, briefly, here.

1.5.1 Uranium/rare-earth multilayers

Alongside the extension of the uranium thin-films project into the area of single-crystal epitaxial layers, efforts have been made to extend the multilayers project into new areas, specifically the growth and characterisation of U/Ho and U/Tb multilayers. The inclusion of these metals aimed to investigate the influence of the uranium on the special magnetic properties of each. Multilayers of good crystallinity and low roughness have been grown in several compositional series and characterised using SQUID magnetometry. Terbium has the largest magnetic moment of all elements, and is strongly associated with perpendicular

magnetic anisotropy in multilayer systems[95,96]. Hysteresis loops from our samples below the Néel temperature of Tb show two sets of moments with different coercive fields. Ho exhibits a spiral magnetic structure and the influence of uranium spacer layer in multilayer samples is to be investigated using polarised neutron reflectivity at ISIS. Ho exhibits a spin-slip spiral magnetic structure across the non-magnetic spacer layers in Ho/Y multilayers[97].

1.5.2 Epitaxial uranium thin-films in other orientations

The influence of the orientation of uranium epitaxial layers on the CDW was also investigated with a series of samples grown on W, such that the [001]-direction is normal to the plane of the film, in contrast with the [110]-oriented samples grown on Nb. The attraction of this orientation is that the direction of the largest component of the CDW, along H, lies in the plane of the film, and will therefore be constrained by the substrate. Synchrotron diffraction experiments performed at the ESRF have been undertaken to characterise the CDW in these samples, including scattering experiments on the undulator beam line ID20, and the use of inelastic scattering on beam line ID31, which has a very high energy resolution, to study the lattice dynamics around the Σ_4 branch of the phonon dispersion curves. Low temperature X-ray scattering experiments aiming to validate these experiments are ongoing, and for this reason the results unfortunately could not be included in this thesis.

1.6 Plan of thesis

This thesis describes the efforts towards three major objectives. The first consists of the growth and characterisation of high-quality thin-films of uranium by magnetron sputtering. Secondly, we wish to make a systematic study of the effect of changing the thickness of the the component layers of the samples on the microstructure of the uranium. Finally, we aim to observe and characterise the charge-density wave ground state in thin-film uranium, and to begin to describe the effect of changing uranium-layer thickness in terms of the

changes in film microstructure.

In Chapter 3 we describe the growth process by magnetron sputtering, a simple and convenient method of growing high-quality thin-films in novel configurations. We describe the results of initial *ex situ* characterisation by X-ray reflectometry and high-angle X-ray diffraction, which show that the films of high crystalline quality. Chapter 4 describes an extensive analysis of X-ray diffraction data from two series of samples in which either the uranium layer thickness has been kept constant and the niobium buffer-layer thickness has been varied, or vice versa. We find that there is a non-trivial dependence of the microstructure on the thickness of each layer, and in addition a narrow composition range for the growth of samples of optimal quality.

Chapter 5 presents the results of our work, primarily conducted at the ESRF, characterising the charge-density wave in uranium thin-films of varying configurations. Scattering measurements from high-brilliance sources are an excellent method for studying the charge-density wave in thin-films.

The following chapter introduces the experimental and analytical techniques that have been employed for the current study.

Chapter 2

Experimental techniques

Here we shall introduce the experimental techniques used in the growth and characterisation of the samples in this study.

2.1 Growth techniques

The controls placed around the use of uranium are a major constraint for the experimentalist wishing to investigate and exploit its properties. It is likely that the increased control possible using MBE growth methods would allow excellent films to be grown.

Magnetron sputtering was chosen for the growth of the current films as its simplicity and versatility mean that it is an inexpensive way to develop the growth of thin uranium films. The small investment needed to set-up the sputtering equipment mean that a single system may be solely devoted to uranium nanostructures.

The sputtering equipment used for the current study is located in the Clarendon Laboratory in the University of Oxford and is shown in Figure 2.1. The equipment was maintained by Professor Roger Ward at Oxford, but has recently moved to the University of Bristol under the maintenance of Dr. Ross Springell.

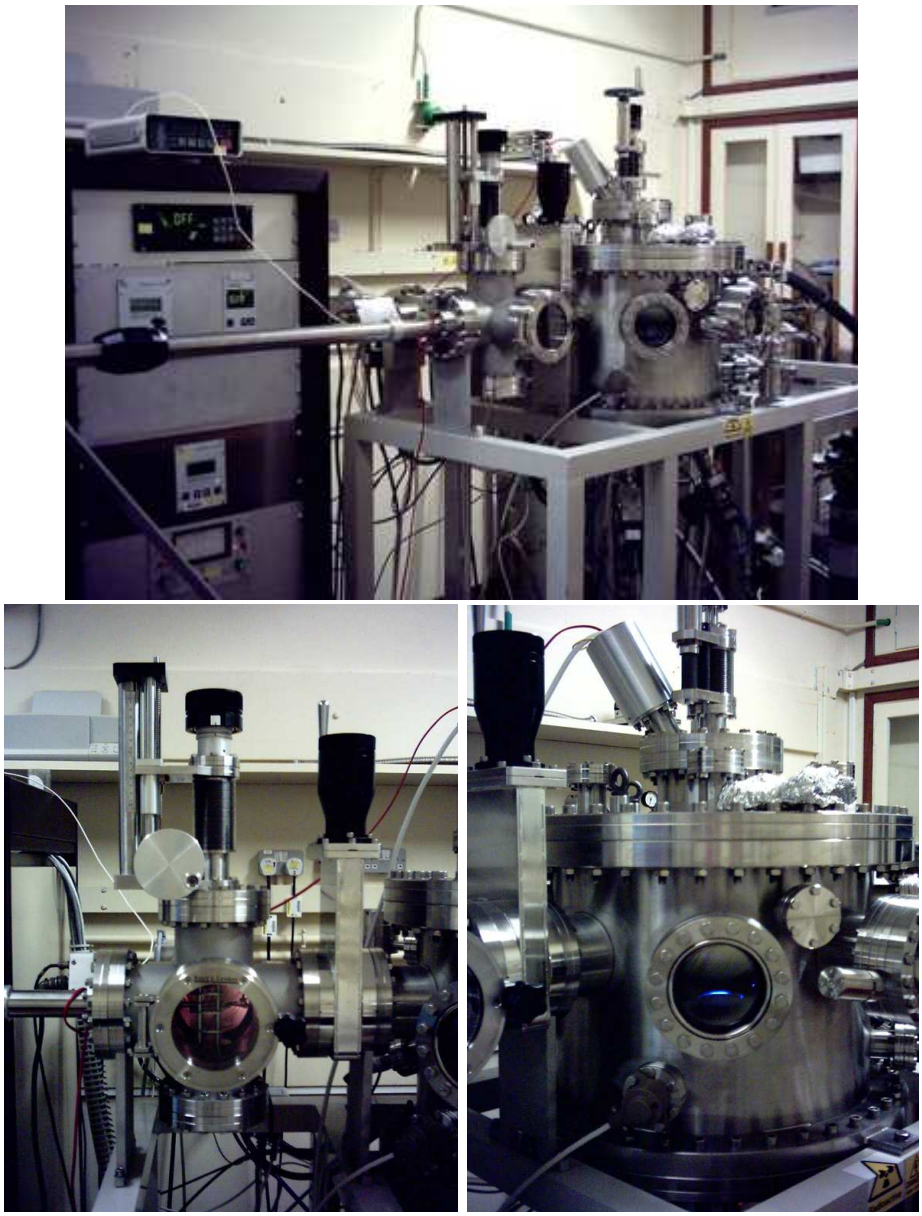

Figure 2.1: Panel 1, top: The sputtering equipment used for the fabrication of the current samples. The manipulator arm is seen extending towards the left of the picture. Panel 2, bottom left: The loading chamber. Panel 3, bottom right: The main sputtering chamber. Pictures courtesy of Dr. Ross Springell.

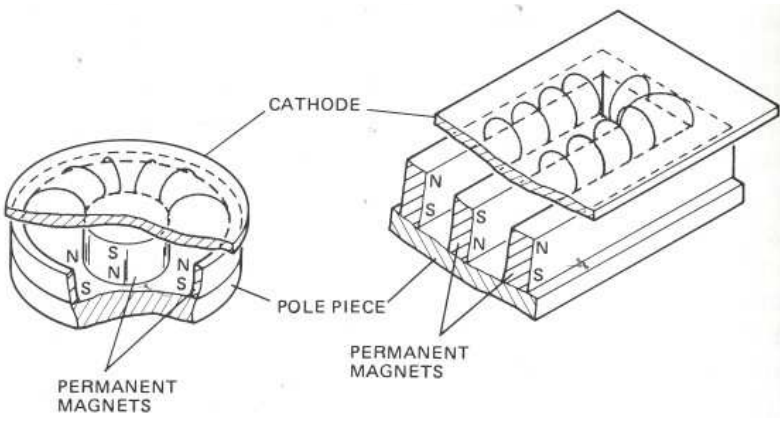

Figure 2.2: The geometry of planar magnetrons. Circular magnetrons, as shown in the left panel, were used in the current study. The higher sputtering rates in the regions between the magnetic poles causes the development of *"race-tracks"* of eroded regions. Since the target must be replaced when it has sputtered through at any point, the uneven sputtering rate across the surface of the target leads to wastage of target material. The rectangular geometry shown in the right panel is commonly used and allows improved economy the of target material.

Along with the pressure of the sputtering gas, the power supplied to the magnetrons determines the sputtering rate. The argon pressure of 5×10^{-3} mbar and sputtering power of 50 W used in the present system gave a growth rate of 0.5–1 Å s^{-1} for U and Nb. A Ta wire heating, selected for its low outgassing properties, mounted close behind the sample stage provides temperature control. A thermocouple in thermal equilibrium with the sample stage provides some measure of the substrate temperature, but in order to avoid systematic errors the power supplied to the heater for each required temperature was kept constant between samples.

2.1.1 Ultra-high vacuum

In general, the quality of the films deposited increases as the base pressure in the chamber, i.e. the pressure measured before the introduction of the sputtering gas, is decreased. *Ultra-high vacuum* (UHV) methods, used in the fabrication of the present samples allow base pressures approaching 10^{-10} Pa, leading to negligible contamination of the films.

Various techniques exist for optimising the vacuum in the chamber. The chamber is evacuated using a system of turbomolecular pumps, which spin at very high speeds on magnetic bearings, *backed* by roughing pumps. After sealing the system using copper gaskets and knife-edge seals, the chamber is *baked-out* for several hours at 180° C.

The vacuum improves over several days of pumping, so in order to avoid venting the main chamber during normal use a secondary chamber of smaller volume is used for loading samples. When this *loading chamber* is vented, a gate valve seals the main chamber, and a positive pressure of pure nitrogen in the loading chamber prevents inflow of contaminating gases. Substrates are transferred to the main chamber once the loading chamber is evacuated.

2.1.2 Substrates and buffer layers

In order to grow highly crystalline thin-films the use of *epitaxy* is employed, whereby the material is deposited onto the surface of a perfect crystal substrate that has a lattice spacing and symmetry which closely matches the required structure. If a rigid perfect crystal with the required structure is not available, or there is a chemical incompatibility between a suitable substrate and the desired material, which might include a high intersolubility or reactivity, a *buffer layer* with a better match of structure or chemistry may be deposited onto the substrate before the film is grown.

A detailed exposition of the growth process of the samples used for the present study is given in Chapter 3.

2.2 Brief introduction to X-ray techniques

In the following chapters, we shall use two commonly-deployed techniques that analyse the elastic scattering of monochromatic X-rays from our samples. The first, X-ray reflectivity

(XRR), probes length scales of tens to thousands of ångströms, and is particularly useful for determining the thicknesses of the individual layers that comprise our samples, along with a measure of the roughness at the interfaces between the layer.

The second technique, high-angle X-ray diffraction (HAXRD), probes length scales of the order of the atomic separations within materials, and hence gives detailed information on the lattice spacings of the crystals. Also, as we shall see in Chapter 4, the technique gives an idea of the microstructure of the films, showing the presence of defects such as dislocations and other deviations from crystal perfection.

Firstly we shall give an overview of the interaction of X-rays with crystalline materials, and then go on to describe each technique, and the data that we have obtained from each, in turn.

2.2.1 X-ray sources

In this thesis we make use of two sources of X-rays for diffraction. One is the common, laboratory-based X-ray tube source, and the second is the high intensity synchrotron source. We shall discuss these sources and their principle characteristics below.

2.2.1.1 X-ray tubes

Electromagnetic radiation is generated when charged particles are accelerated. In a laboratory X-ray tube, invented by Coolidge, electrons drawn off a wire in a vacuum are accelerated by a high voltage towards a water-cooled anode. As the high-velocity electrons are decelerated by the anode material, radiation of various energies is released, called *bremsstrahlung*. An incident electron may collide with an inner-shell electron of one of the atoms of the anode and eject it, leaving behind a vacant energy level. Radiation of characteristic energy is released when an electron in a higher-energy level relaxes to fill the gap, and it is this radiation, called the Kα radiation, that is used for diffraction, as it is

several orders of magnitude more intense than the bremsstrahlung.

There are several limitations of the laboratory X-ray tube. Firstly, the emitted power is limited by the rate of cooling of the anode. Secondly, the radiation is emitted isotropically, so in order to produce a focussed, collimated beam only a fraction of the emitted photons may be utilised. Finally, the wavelength of the radiation is limited to the characteristic emission energies of the element used for the anode, so it is not possible to probe the dynamics of materials by scanning in energy, or to take advantage of resonance effects.

Two laboratory-based X-ray sources have been used to investigate the structure of the current samples. The first is a Philips X'Pert MPD system with a Cu X-ray tube, primarily used for high-angle scattering, and is based in UCL. The characteristic wavelengths emitted by the Cu tube are designated Kα and Kβ. A Ni filter is used to reduce the intensity of the Kβ radiation, which has a wavelength of 1.3926 Å. The Kα emission is used for diffraction. The Kα line has two components, called Kα_1 and Kα_2, with wavelengths 1.540562 Å and 1.544390 Å[98], which may be resolved in longitudinal scans from high-quality crystals. The system optics consist of programmable divergence, anti-scatter, and receiving slits, incident and diffracted beam soller slits, a curved graphite diffracted beam monochromator, and a proportional counter detector, in the Bragg-Brentano geometry. A schematic of the optics is shown in Figure 2.3. The system optics were tuned to give an optimum trade-off between resolution and X-ray counts. Samples were mounted on glass slides using vacuum grease. By using spacers of substrate off-cuts it was possible to ensure that the sample surface was at the centre of the diffraction circle. The supply to the X-ray tube was fixed at 50 mA and 40 kV. An image of the diffractometer set-up is shown in Figure 2.4.

X-ray reflectometry measurements were primarily made using a less sophisticated Philips diffractometer based at the Clarendon laboratory in the University of Oxford. No optics were present beyond a Ge monochromator in the incident beam, the Ni filter and fixed slits. The diffractometer was optimised for low-angle diffraction measurements. The samples

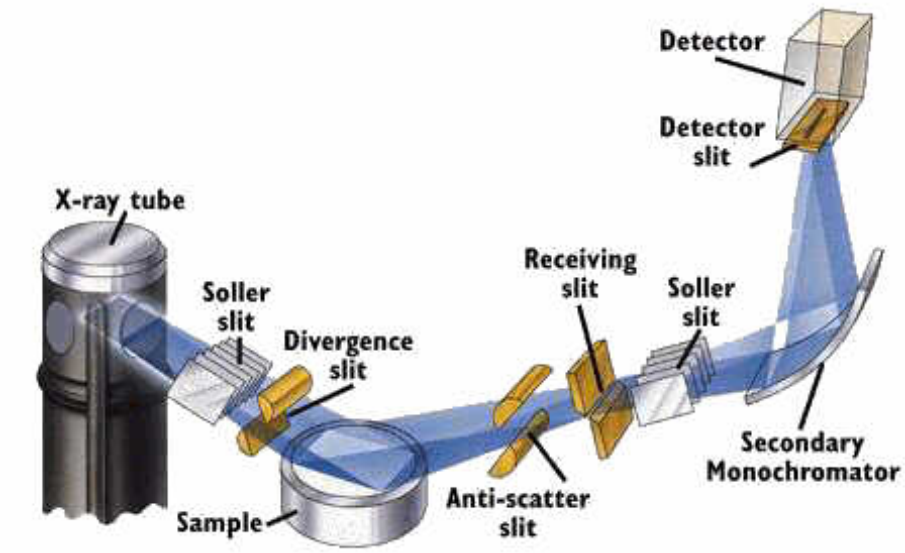

Figure 2.3: A schematic diagram showing the optics of the Philips X'Pert MPD X-ray diffractometer based at UCL used for this thesis. In the *Bragg-Brentano geometry* the X-ray source is fixed, and the sample stage and detector arm, which supports all the diffracted-beam (i.e. *post-sample*) optics, may move around a circle centred at the sample surface.

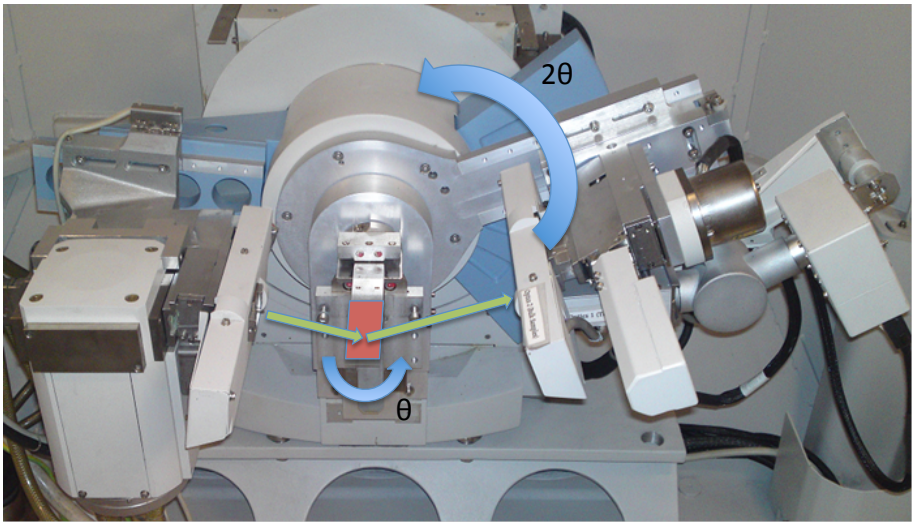

Figure 2.4: An annotated image of the Philips X'Pert MPD X-ray diffractometer based at UCL used for this thesis, showing the path of the X-rays (green arrows) from the X-ray tube to the sample (red), and the path of the diffracted beam from the sample to the detector. The approximate motions of the θ and 2θ circles are indicated (blue arrows).

were mounted on brass stubs with sticking tape, and the height of the stub adjusted so that the sample surface was in the centre of rotation using a rigid rod as a guide. The supply to the X-ray tube was fixed at 40 mA and 30 kV.

2.2.1.2 Synchrotron radiation

It is not possible to observe the scattering from the charge-density wave in thin-film samples using a laboratory X-ray source as the intensity of X-rays is insufficient. A more intense source of X-rays is needed.

The second type of X-ray source utilised in this thesis is that emitted by electrons moving at relativistic speeds in a storage ring. A *synchrotron* is a type of particle accelerator that keeps electrons moving at constant energy, and the radial accelerations used to cause the electrons to follow a circular path lead to the tangential emission of radiation of very high intensity. Synchrotron X-ray sources suffer from none of the limitations mentioned above for X-ray tubes, and emit highly collimated, tuneable radiation of a brilliance[a], up to ten orders of magnitude greater than a laboratory source. This allows the study of subtle phenomena such as lattice dynamics and magnetic X-ray scattering, along with a great decrease in the time needed for a conventional diffraction experiment. It is therefore ideal for the study of the CDW in thin-film samples. Good introductions to synchrotron radiation science may be found in Baruchel et al.[99] and Als Nielsen and McMorrow[100].

So-called *first-generation* synchrotron light sources were simply accelerators for particle-physics research at which the resulting synchrotron radiation was used parasitically for spectroscopic or scattering experiments. The development of storage rings enabled particles to circulate for longer periods of time, with corresponding benefits to the users of the synchrotron radiation. The first storage ring solely used for the purpose of generating

[a] A figure of merit that includes the intensity and divergence of a source, defined as

$$\text{Brilliance} \equiv \frac{\text{Photons/second}}{(\text{mrad})^2(\text{mm}^2\,\text{source area})(0.1\%\text{bandwidth})} \tag{2.1}$$

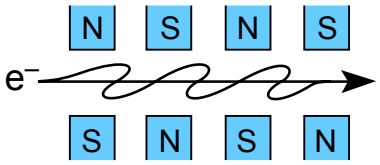

Figure 2.5: An insertion device uses alternately-oriented pairs of permanent magnets to cause the electrons in the synchrotron storage-ring to traverse an oscillating path. In the electron frame of reference the acceleration of the electron causes it to radiate as a dipole. Since the electrons are moving at relativistic speeds in the synchrotron frame of reference, the wavelength is Lorentz-contracted and Doppler-shifted to X-ray wavelengths. In addition it is concentrated in a bright central cone along the length of the device. (Diagram credit: D. Attwood, University of California at Berkeley)

useful synchrotron light (a *second-generation* source) was built at Daresbury Laboratory in the UK, and began operating in 1981. Storage rings consist of straight sections between regions where a magnetic field is applied to bend the electron paths into a circle. In these sections *insertion devices* may be added for further light generation. Insertion devices, either *undulators* or *wigglers*, cause electrons to follow an oscillatory path as shown in Figure 2.5, and emit high brilliance radiation. A comparison between the various sources is shown in Figure 2.6. *Third-generation* sources include insertion devices as the primary means of generating radiation. The European Synchrotron Radiation Facility (ESRF) in Grenoble was the first third-generation synchrotron light source to be built and opened to users in 1994. Partly-funded by eighteen european countries, access to the beam lines for experimental time (*beamtime*) is available to researchers from the member countries upon submission of an experimental proposal. Research committees for each beamline review submitted proposals and allocate beamtime for the most promising experiments. Experiments at the ESRF usually last six days.

The range of applications of synchrotron radiation is large and expanding. Branching off tangentially from the storage ring at a synchrotron are a large number (~ 60 at the ESRF) of *beamlines*, which consist of optical components to modify and direct the radiation toward a sample and then measure the effect of the sample in a particular way. Each beamline is built and optimised for a specialised application of X-ray radiation, and may therefore be

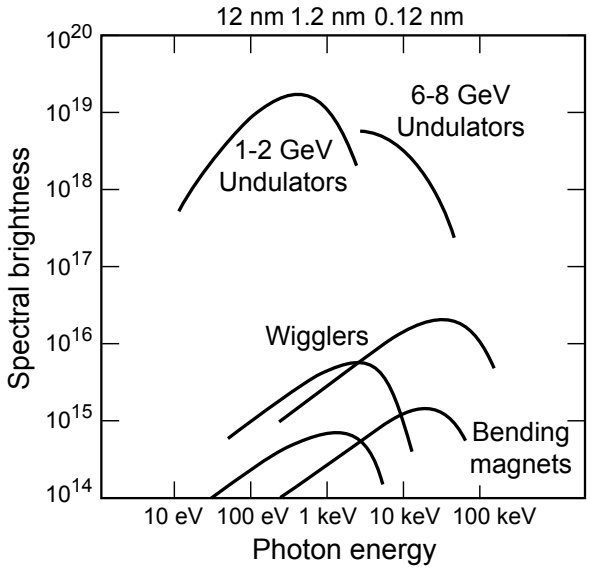

Figure 2.6: A comparison between the various light sources at a typical synchrotron. Undulators and wigglers are insertion devices. Undulators have shorter periods than wigglers and have enhanced brightness and beam coherence. Wigglers produce higher photon energies and photon flux. The electrons circulating in the storage ring at the ESRF have an energy of 6 GeV. (Diagram credit: D. Attwood, University of California at Berkeley)

more or less suited to a particular technique.

Synchrotron experiments described in this thesis are confined to scattering experiments performed on beamline BM28 at the ESRF. BM28 utilises the radiation from one of the 0.4 T *bending magnets* that provide centripetal acceleration to the electrons in the storage rings. The beamline is funded and run by a collaboration based in the UK, and is built to investigate X-ray magnetic scattering, from which it derives the acronym *XMaS*. The beamline is particularly suited to the investigation of the scattering from the CDW, which is described in Chapter 5, as it is of a similar intensity to magnetic scattering. A total of 18 days beamtime was allocated for the study of the present samples at XMaS, in three experimental sessions between 2008 and 2010.

The ESRF storage ring has a circumference of 850 m and circulates electrons at an energy of 6 GeV and a current of 200 mA. The storage ring is fed with electrons from a 6 GeV

booster synchrotron (with circumference 300 m) functioning at 10 MHz, which is in turn fed from a LINAC pre-injector.

The XMaS beamline comprises a unique combination of instrumentation for high-resolution and magnetic single-crystal diffraction, in particular at the soft (low) X-ray energies needed for studies of magnetic actinide compounds. The beamline combines the capability for high-quality structural and magnetic diffraction studies of single crystals with that for investigation of thin-films and multilayers through grazing-incidence diffraction and reflectometry[101]. The beamline is ideal for the present work, despite the lower incident photon flux compared with an insertion device beamline.

For the purposes of this study only a brief description of the beamline optics is necessary, since the beamline is used in perhaps it's most straightforward capacity for the study of elastic scattering, with no applied magnetic field. The first optical component that the white beam arising from the bending magnet meets is the *monochromator*, which uses two diffracting Si(111) crystals of extreme perfection to select a particular X-ray wavelength with an energy resolution better than 0.0003%. Fine mechanical control of the crystals' positions allows different energies to be selected, and even allows scans in energy to be performed. The monochromator is water-cooled to avoid any change in the crystal lattice-spacings through thermal expansion; the incident beam can cause significant heating. A rhodium-coated Si single-crystal *focussing mirror* of length 1200 mm×200 mm width is bent pneumatically to a toroidal form in order to focus the beam at the sample position to ~ 0.8 mm vertical size and ~ 0.3 mm horizontal size. Rhodium-coated pyrex mirrors reject harmonic contamination of the beam from the monochromator, and further optical components allow selection of linearly- or circularly-polarised light for magnetic studies, but these were not used in the present work. A set of Al and Mo sheets of varying thickness act as *attenuators*, which allow control of the X-ray intensity at the sample position as they may be moved in and out of the beam independently. The majority of the beamline is kept under vacuum, such that the X-ray beam may traverse a minimum of a few cm of air and < 1 mm of Be before reaching the detector.

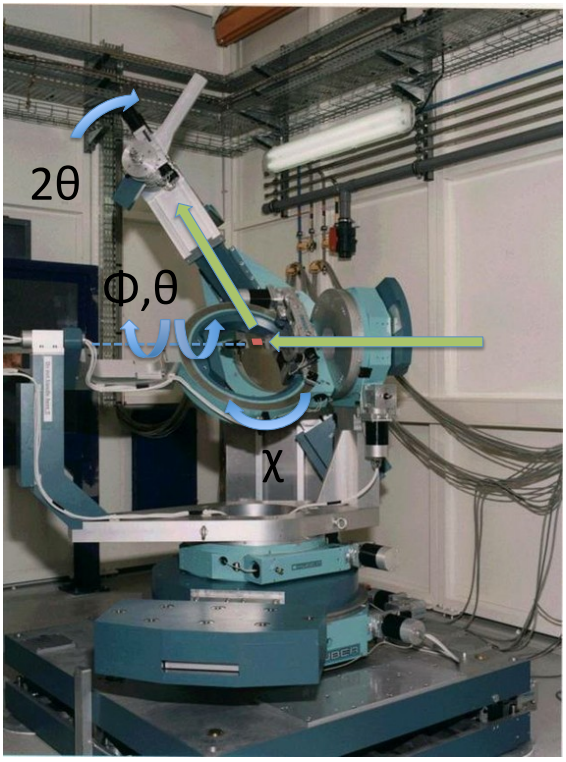

Figure 2.7: An annotated image of the X-ray diffractometer on the XMaS beamline used for this thesis, showing the path of the X-rays (green arrows) from the incident X-ray optics to the sample (red), and the path of the diffracted beam from the sample to the detector arm, upon which the detector is mounted. The approximate motions of the θ, 2θ, ϕ and χ circles are indicated (blue arrows). For the position of χ shown, the θ and ϕ motions are the same. For different positions of χ, the θ axis remains the same, but the ϕ axis moves with χ. ϕ is best thought of as the sample azimuthal angle.

The sample is affixed to a Cu stub mounted on a Huber 11-circle diffractometer, which with the use of SPEC software (from Certified Scientific Software), allows access to a large proportion of reciprocal-space in both horizontal and vertical scattering geometries. For the present study the diffractometer was used in four-circle $(\theta, 2\theta, \chi, \phi)$ mode in the vertical scattering plane. An ARS *displex cryostat* mounted on the diffractometer circle allows temperature control between 8 K and ambient temperature. Two X-ray detectors were used at different points in the study: The first, a *Bicron* NaI scintillator has very good sensitivity at low X-ray count rates, but the response becomes non-linear above

$\sim 30,000$ counts. The second, an *avalanche photodiode*, is less sensitive but has a linear response over seven orders of magnitude of count rates.

2.2.2 The interaction of X-rays with matter

2.2.2.1 X-ray scattering from one electron

Following the arguments in Als Nielsen and McMorrow [100] and Warren [102], we start by finding at a distance R the electric field radiated by an electron that is accelerated by the electric field of an incident X-ray. The energy density must decay as R^{-2}, and it is proportional to $|E_{\mathrm{rad}}|^2$. The field is proportional to the charge on the electron, -e, and to the acceleration of the electron seen by the observer. The acceleration must be that evaluated at a time t', R/c earlier than the time of observation, t. The correct SI units are obtained by multiplying by $1/4\pi\epsilon_0 rc^2$. This gives

$$\mathrm{E}_{\mathrm{rad}}(R,t) = -\frac{-e}{4\pi\epsilon_0 c^2 R} a_X(t'). \tag{2.2}$$

The minus sign emerges from a rigorous treatment. We may find the acceleration of the electron by using Newton's third law and considering the force on the electron due to the incident electron field, $\mathrm{E}_{\mathrm{in}} = \mathrm{E}_{x0}\mathrm{e}^{i\omega t}$:

$$a_X(t') = \frac{-e}{m}\mathrm{E}_{x0}\mathrm{e}^{-i\omega t'}\cos\psi = \frac{e}{m}\mathrm{E}_{\mathrm{in}}\mathrm{e}^{i\omega\left(\frac{R}{c}\right)}\cos\psi. \tag{2.3}$$

Hence,

$$\frac{E_{\mathrm{rad}(R,t)}}{E_{\mathrm{in}}} = -\left(\frac{\mathrm{e}^2}{4\pi\epsilon_0 mc^2}\right)\frac{\mathrm{e}^{i\mathbf{k}R}}{R}\cos\psi \tag{2.4}$$

$$= -r_0\frac{\mathrm{e}^{i\mathbf{k}R}}{R}\cos\psi. \tag{2.5}$$

Here r_0 is called the Thomson scattering length, and has a value of 2.82×10^{-5} Å.

Now, the measured intensity of X-rays may be thought of as

$$I_{\rm sc} = \frac{\text{Power flowing through area of detector}}{\text{energy per photon}}, \tag{2.6}$$

$$\Longrightarrow \frac{I_{\rm sc}}{I_0} = \frac{|E_{\rm rad}|^2 R^2 \Delta\Omega}{|E_{\rm in}|^2 A_0}. \tag{2.7}$$

If we then normalise this expression by the incident flux $\left(\frac{I_0}{A_0}\right)$ and by the solid angle of the detector, $\Delta\Omega$, we have an expression for the *differential cross-section*,

$$\left(\frac{{\rm d}\sigma}{{\rm d}\Omega}\right) = \frac{\text{No. of X-rays per sec into } \Delta\Omega}{(\text{Incident flux})(\Delta\Omega)}. \tag{2.8}$$

From the above equations we can find the differential cross-section for Thomson scattering from an electron

$$\left(\frac{{\rm d}\sigma}{{\rm d}\Omega}\right)_{\text{Thomson Scattering}} = \frac{I_{\rm sc}}{\left(\frac{I_0}{A_0}\right)\Delta\Omega} = \frac{|E_{\rm rad}|^2 R^2}{|E_{\rm in}|^2} = r_0 \cos^2\psi. \tag{2.9}$$

Integrating this over all scattering angles gives of course the total Thomson scattering-length for an electron

$$\sigma_{\rm T} = \left(\frac{8\pi}{3}\right) r_0^2 = 0.665 \times 10^{-24}\,{\rm cm}^2 = 0.665\,\text{barn}. \tag{2.10}$$

The differential cross-section may also be generalised to include different X-ray sources by introducing the polarisation factor, P, such that

$$\left(\frac{{\rm d}\sigma}{{\rm d}\Omega}\right) = r_0^2 P \tag{2.11}$$

with

$$P = \begin{cases} 1 & \text{vertical scattering plane (synchrotron light)} \\ \cos^2\psi & \text{horizontal scattering plane (synchrotron light)} \\ \frac{1}{2}(1+\cos^2\psi) & \text{unpolarized source} \end{cases} \tag{2.12}$$

2.2.2.2 Scattering from an atom

An atom has a number density of electrons, $\rho(\mathbf{r})$. When considering the scattering from an atom we need to take into account the phase of the incident wave as it interacts with the volume element at the origin and when it interacts with that at $\mathbf{r}$. The resulting phase difference between the incident and scattered waves, $\mathbf{k}$ and $\mathbf{k}'$, at $\mathbf{r}$ is

$$\Delta\phi(\mathbf{r}) = (\mathbf{k} - \mathbf{k}') \cdot \mathbf{r} = \mathbf{Q} \cdot \mathbf{r}. \tag{2.13}$$

Here, $\mathbf{Q}$ is the *momentum transfer*, which is a convenient wavelength-independent representation of the scattering probe. Since $|\mathbf{k}| = |\mathbf{k}'|$ for elastic scattering,

$$|\mathbf{Q}| = 2|\mathbf{k}|\sin\theta = \frac{4\pi}{\lambda}\sin\theta. \tag{2.14}$$

Now, a volume element $\mathrm{d}\mathbf{r}$ at $\mathbf{r}$ will contribute an amount $-r_0\rho(\mathbf{r})\mathrm{d}\mathbf{r}$ to the scattered field with a phase factor $\mathrm{e}^{i\mathbf{Q}\cdot\mathbf{r}}$.

The total scattering length of the atom is

$$-r_0 f^0(\mathbf{Q}) = -r_0 \int \rho(\mathbf{r})\mathrm{e}^{i\mathbf{Q}\cdot\mathbf{r}}\mathrm{d}\mathbf{r}, \tag{2.15}$$

where $f^0(\mathbf{Q})$ is the *atomic form factor*.

By way of verification

$$f^0(\mathbf{Q}) = \begin{cases} Z & |\mathbf{Q}| = 0 \\ 0 & |\mathbf{Q}| \to \infty \end{cases} . \tag{2.16}$$

.

The atomic form factor also depends on

1. Resonance effects due to the quantum nature of atomic electrons (f')
2. Damping effects, since the scattering electron is a forced harmonic oscillator (f''),

so we have

$$f(\mathbf{Q}, \hbar\omega) = f^0(\mathbf{Q}) + f'(\hbar\omega) + if''(\hbar\omega). \tag{2.17}$$

f' and f'' are the *dispersion corrections*.

2.2.2.3 Scattering from a crystal

A crystal may be defined as a three-dimensional lattice of unit cells located at positions $\mathbf{R}_n$, which are composed of atoms located at positions $\mathbf{r}_j$. The structure factor for a crystal therefore is the product of the sums of the structure factors of the unit cells over the entire lattice:

$$F^{\text{crystal}}(\mathbf{Q}) = -r_0 \sum_{\mathbf{r}_j} f_j(\mathbf{Q}) \mathrm{e}^{i\mathbf{Q}\cdot\mathbf{r}} \sum_{\mathbf{R}_n} \mathrm{e}^{i\mathbf{Q}\cdot\mathbf{R}}. \tag{2.18}$$

If $\mathbf{Q} \cdot \mathbf{R}_n = 2\pi \times$ integer, the terms in the lattice sum are no longer randomly positioned on the unit circle on the Argand diagram (with sum of order 1), but all have value 1, so their sum becomes of order N (the number of unit cells).

Now,

$$\mathbf{R}_n = n_1\mathbf{a}_1 + n_2\mathbf{a}_2 + n_3\mathbf{a}_3, \tag{2.19}$$

with $(\mathbf{a}_1, \mathbf{a}_2, \mathbf{a}_3)$ the basis vectors of the lattice. It is useful here to introduce the *reciprocal lattice*, with basis vectors $(\mathbf{a}_1^*, \mathbf{a}_2^*, \mathbf{a}_3^*)$, such that

$$\mathbf{a}_1^* = 2\pi\frac{\mathbf{a}_2 \wedge \mathbf{a}_3}{\mathbf{a}_1 \cdot \mathbf{a}_2 \wedge \mathbf{a}_3}, \mathbf{a}_2^* = 2\pi\frac{\mathbf{a}_3 \wedge \mathbf{a}_1}{\mathbf{a}_1 \cdot \mathbf{a}_2 \wedge \mathbf{a}_3}, \mathbf{a}_3^* = 2\pi\frac{\mathbf{a}_1 \wedge \mathbf{a}_2}{\mathbf{a}_1 \cdot \mathbf{a}_2 \wedge \mathbf{a}_3}. \tag{2.20}$$

We might give each site in the reciprocal lattice a *reciprocal lattice vector*

$$\mathbf{G} = h\mathbf{a}_1^* + k\mathbf{a}_2^* + l\mathbf{a}_3^*, \tag{2.21}$$

so that

$$\mathbf{G} \cdot \mathbf{R}_n = 2\pi(hn_1 + kn_2 + ln_3) = 2\pi \times \text{integer} \tag{2.22}$$

and therefore

$$\mathbf{Q} = \mathbf{G} \tag{2.23}$$

for our condition for scattering. This is the *Laue condition.*

2.3 X-ray reflectivity

2.3.1 Theory

Practically, the detailed analysis of XRR datasets from real thin-film samples that contain multiple components is possible only using computer-based modelling. Despite this, it remains instructive to see how we might extend an intuitive understanding of refraction

and reflection of light at an interface into a quantitative description of reflection and refraction of X-rays at multiple interfaces.

2.3.1.1 Refraction of light

The refractive index, n, is the materials parameter that determines the change of the direction of light as it crosses the interface between dissimilar materials. This change of direction is called *refraction*. The directions of the light before and after the interface are related by *Snell's law*:

$$n_1 \sin\theta_1 = n_2 \sin\theta_2, \tag{2.24}$$

where n_1 and n_2 are the refractive indices of materials before and after the interface, respectively, and θ_1 and θ_2 are the angles the light ray makes with the normal to the interface before and after the interface, respectively. For most transparent materials the refractive index for visible light is greater than that of the vacuum, $n_{\text{vacuum}} = 1$, such that n ranges typically from 1.2 to about 2. However, we see a familiar splitting of white light into its component colours after passing through a prism since the refractive index is dependent on the wavelength of the light. Generally the refractive index increases as the photon energy, $\hbar\omega$, approaches that corresponding to an electronic transition within the atoms or molecules comprising the material. In the X-ray region the energy of the radiation is above most electronic transitions, excluding perhaps those of inner shell electrons, and so the refractive index decreases with increasing energy, such that $n < 1$ for X-rays. We can see from Equation 2.24, therefore, that, for an X-ray passing over the interface between a vacuum and a material, $\frac{n_1}{n_2} > 1$ and hence there exists an angle, θ_c, above which the refracted angle $\theta_2 > 90^\circ$ and the light is *totally externally reflected*.

Generally, we may express the refractive index for X-rays as

$$n \equiv 1 - \delta + i\beta, \tag{2.25}$$

with δ arising from the the Thomson scattering of X-rays by the electrons in the material, and β accounting for absorption processes. Considering that the wavevector of the radiation changes from $\mathbf{k}$ in the vacuum to $n\mathbf{k}$ in the material, we see that at a distance, z, from the interface,

$$\mathrm{e}^{in\mathbf{k}z} = \mathrm{e}^{[i(1-\delta)\mathbf{k}z]}\mathrm{e}^{-\beta\mathbf{k}z}. \tag{2.26}$$

The attenuation length, μ, of a material corresponds to $\mu = 2\beta\mathbf{k}$.

Finally, we can describe refraction as a scattering process taking into account the dispersion corrections from Section 2.2.2.2. δ depends on the atomic form-factor, f^0, and the local electron density, ρ_a, and is expressed as $\delta = \dfrac{2\pi\rho_a f_0(0) r_0}{\mathrm{k}^2}$, so writing the atomic scattering length as $f(\mathbf{Q}) = f^0(\mathbf{Q}) + f'' + if''$ from Equation 2.17 we have

$$n \equiv 1 - \frac{2\pi\rho_a r_0}{\mathrm{k}^2}(f^0(0) + f' + if''). \tag{2.27}$$

2.3.1.2 Snell's and Fresnel's equations for X-rays

Now, even at incident angles below θ_c a portion of the energy of the incident wave is externally reflected. Since the angle of reflection, θ_r, must equal the angle of incidence, θ_i, the proportions of the wave transmitted and reflected are dependent only on the refractive indices of the materials before and after the interface and θ_i, and may be calculated by ensuring that the amplitude of the wave and its derivative are continuous across the interface. This treatment leads to the *Fresnel equations*. In the following we shall use the following nomenclature to denote the characteristics of the waves, as in Ref[100]: The incident, reflected and transmitted amplitudes are a_I, a_R and a_T, respectively, and their corresponding wavevectors are $\mathbf{k}_\mathrm{I}$, $\mathbf{k}_\mathrm{R}$, and $\mathbf{k}_\mathrm{T}$. The boundary conditions require that

$$a_\mathrm{I} + a_\mathrm{R} = a_\mathrm{T}, \tag{2.28}$$

and,

$$a_{\mathrm{I}}\mathbf{k}_{\mathrm{I}} + a_{\mathrm{R}}\mathbf{k}_{\mathrm{R}} = a_{\mathrm{T}}\mathbf{k}_{\mathrm{T}}. \tag{2.29}$$

We continue by taking components of $\mathbf{k}$ parallel and perpendicular to the interface, and, for clarity, we shall consider these in terms of the incident grazing angle, $\alpha = 90^\circ - \theta_i$ and the angle the transmitted ray makes with the interface, α', for a ray moving from the vacuum into a material with refractive index n. The wavenumbers of the rays before and after the interface are $|\mathbf{k}_{\mathrm{I}}| = |\mathbf{k}_{\mathrm{R}}| =$k, and $|\mathbf{k}_{\mathrm{T}}| = n$k, giving

$$a_{\mathrm{I}}\mathrm{k}\cos\alpha + a_{\mathrm{R}}\mathrm{k}\cos\alpha = a_{\mathrm{T}}n\mathrm{k}\cos\alpha' \tag{2.30}$$

along the interface and

$$-(a_{\mathrm{I}} - a_{\mathrm{R}})\mathrm{k}\sin\alpha = -a_{\mathrm{T}}(n\mathrm{k})\sin\alpha' \tag{2.31}$$

normal to the interface. Snell's law results from considering Equations 2.28 and 2.30 together, yielding

$$\cos\alpha = n\cos\alpha'. \tag{2.32}$$

If we consider Equation 2.28 with Equation 2.31 it follows that

$$\frac{a_{\mathrm{I}} - a_{\mathrm{R}}}{a_{\mathrm{I}} + a_{\mathrm{R}}} = n\frac{\sin\alpha'}{\sin\alpha} \simeq \frac{\alpha'}{\alpha}. \tag{2.33}$$

Now we define the amplitude reflectivity, r, and the amplitude transmittivity, t, as the ratio of the reflected and transmitted amplitudes to the incident amplitude respectively and from Equation 2.33 derive the Fresnel equations:

$$\begin{aligned} r &\equiv \frac{a_{\mathrm{R}}}{a_{\mathrm{I}}} = \frac{\alpha - \alpha'}{\alpha + \alpha'} \\ t &\equiv \frac{a_{\mathrm{T}}}{a_{\mathrm{I}}} = \frac{2\alpha}{\alpha + \alpha'}. \end{aligned} \tag{2.34}$$

We may re-write Equation 2.34 in more convenient variables for diffraction phenomena by considering the wavevector transfers of the waves in question, and normalising them to that of a wave at the critical angle, α_c. The wavevector transfer is defined as

$$Q \equiv 2\mathrm{k}\sin\alpha \simeq 2\mathrm{k}\alpha, \tag{2.35}$$

so we may use the dimensionless counterparts to α and α',

$$q \equiv \frac{Q}{Q_c} \simeq \left(\frac{2\mathrm{k}}{Q_c}\right)\alpha, \text{and } q' \equiv \frac{Q'}{Q_c} \simeq \left(\frac{2\mathrm{k}}{Q_c}\right)\alpha'. \tag{2.36}$$

Fresnel's equations become:

$$r(q) = \frac{q - q'}{q + q'} \; ; \quad t(q) = \frac{2q}{q + q'}. \tag{2.37}$$

2.3.1.3 Reflectivity of a single layer on an infinitely-thick substrate

We are now in a position to consider the total reflectivity from a single transparent layer on a substrate in vacuum. Some of the incident light is reflected as it meets the vacuum-layer interface, and some of the remainder is reflected at meets the layer-substrate interface and so may then be transmitted back into the vacuum. However, as there is a portion of the wave reflected back into the substrate, we must hence consider an infinite number of reflections and re-reflections. The total reflectivity is the sum of all the portions of these re-reflections that are transmitted at the layer-vacuum interface. We assume the substrate to be so thick that we may ignore waves transmitted into it.

If we denote the amplitude reflectivity or transmittivity at the interface between media i and j to be r_{ij} and t_{ij} respectively, and the the vacuum, layer and substrate as 0, 1 and 2, we can see that the total reflectivity,

$$r = r_{01} + t_{01}t_{10}r_{12}p^2 \sum_{N=0}^{\infty} (r_{10}r_{12}p^2)^N. \tag{2.38}$$

$p = \mathrm{e}^{iQ\Delta}$ is a phase factor, and Δ is the layer thickness. The sum to infinity may be evaluated as $\sum_{N=0}^{\infty} x^N = \dfrac{1}{1-x}$, so Equation 2.38 becomes

$$r = r_{01} + \frac{t_{01}t_{10}r_{12}p^2}{1 - r_{10}r_{12}p^2}, \tag{2.39}$$

which we may further simplify by noticing that from Equation 2.37

$$r_{01} = \frac{q_0 - q_1}{q_0 + q_1} = -\frac{q_1 - q_0}{q_0 + q_1} = -r_{10}, \text{ and,} \tag{2.40}$$

$$\begin{aligned} r_{01}^2 + t_{01}t_{10} &= \frac{q_0^2 - 2q_0q_1 + q_1^2}{(q_0 + q_1)^2} + \frac{4q_0q_1}{(q_0 + q_1)^2} \\ &= 1, \end{aligned} \tag{2.41}$$

so we have

$$r = \frac{r_{01} + r_{12}p^2}{1 + r_{10}r_{12}p^2} \tag{2.42}$$

2.3.1.4 Reflectivity of a multiple-layer sample

By far the most common method of evaluating the reflectivity from a multiple-layer sample uses a recursive formula of Parrat[103]. Starting at the N^{th} layer, closest to the substrate, the reflectivity at the interface between the $a = N - j^{\text{th}}$ layer and the $b = N - (j-1)^{\text{th}}$ layer is calculated using a formula similar to Equation 2.42:

$$r_{a,b} = \frac{r'_{a,b} + r_{b,c}p_b^2}{1 + r'_{b,a}r_{b,c}p_b^2}, \tag{2.43}$$

where the b^{th} layer lies above the $c = N - (j-2)^{\text{th}}$ layer. Importantly, we must see that here r' does not include multiple reflections, and depends on the refractive indices of the three relevant layers, which may be considered to be $n_m = 1 - \delta_m + i\beta_m$ for the m^{th} layer. Care must hence be taken in calculating r' using Equation 2.37. The wavevector transfer

in the m^{th} layer becomes $\mathbf{Q}_m = 2\mathbf{k}_m \sin\theta_m = 2\mathrm{k}_{z,m}$, where

$$\mathrm{k}_{z,m} = (n_m \mathrm{k})^2 - k_x^2. \tag{2.44}$$

The wavevector component in the plane of the layers, k_x, does not change throughout the multilayer. This allows us to calculate

$$r'_{a,b} = \frac{\mathbf{Q}_a - \mathbf{Q}_b}{\mathbf{Q}_a + \mathbf{Q}_b} \qquad \text{using} \tag{2.45}$$

$$\mathbf{Q}_m = \sqrt{\mathbf{Q}^2 - 8\mathbf{k}^2\delta_m + 8i\mathbf{k}^2\beta_m} \tag{2.46}$$

for $m = a, b$.

2.3.1.5 Accounting for non-ideal interfaces

The above discussion has assumed ideally flat, sharp interfaces between the layers. This is unrealistic, as interdiffusion of species, along with roughness introduced during the growth process, are present in most systems, including the present. An extension of the Parratt formulism, most notably by Névot and Croce[104] allows for a gradual change in the density, and hence the refractive index, across the interface. It should be made clear that the following approach is only valid in the kinematical limit, $Q > Q_c$, and breaks down close to the critical angle.

The reflectivity, δr, is calculated for an infinitesimally thin slab, at depth z, with the density profile of the interface varying with the function $f(z)$, which is defined such that $f(z) \to 1$ as $z \to \infty$. The superposition of the reflectivities from the individual layers

proceeds as follows:

$$\delta r = -i\left(\frac{Q_c^2}{4Q}\right) f(z)\mathrm{d}z, \quad \text{so} \tag{2.47}$$

$$\begin{aligned} r(Q) &= -i\left(\frac{Q_c^2}{4Q}\right)\int_0^\infty f(z)\mathrm{e}^{iQz}\mathrm{d}z \\ &= i\frac{1}{iQ}\left(\frac{Q_c^2}{4Q}\right)\int_0^\infty f'(z)\mathrm{e}^{iQz}\mathrm{d}z \\ &= r_\mathrm{F}(Q)\phi(Q), \end{aligned} \tag{2.48}$$

where $r_\mathrm{F}(Q)$ is the Fresnel reflectivity, and $\phi(Q)$ is defined by

$$\phi(Q) = \int_0^\infty f'(z)\mathrm{e}^{iQz}\mathrm{d}z \tag{2.49}$$

from Equation 2.37 with $q >> 1$.

The measured intensity, $R(Q) = r^2(Q)$ is related to the ideal Fresnel reflectivity by the *master formula* for a graded interface:

$$\frac{R(Q)}{R_\mathrm{F}(Q)} = \left|\int_0^\infty \left(\frac{\mathrm{d}f}{\mathrm{d}z}\right)\mathrm{e}^{iQz}\mathrm{d}z\right|^2. \tag{2.50}$$

We see that the integral is the Fourier transform of the gradient of the density distribution. A convenient form of the density distribution is the error function, since its derivative is a Gaussian function, and the Fourier transform of a Gaussian is also a Gaussian. We then find the reflectivity simply attenuated by a factor that depends on the width of the graded region, σ:

$$R(Q) = R_\mathrm{F}(Q)\mathrm{e}^{-Q^2\sigma^2} \tag{2.51}$$

An extension of this argument can be made for rough interfaces, with a similar result, but for which σ gives the root-mean square roughness of the interface, assuming uncorrelated roughness. We see that it is therefore difficult to separate the effects of interdiffusion and roughness using this model. Correlated roughnesses lead to what is called *diffuse*

scattering, as any correlation in the deviations in height of the interface in the plane of the film will lead to constructive interference at a corresponding value of the wavevector transfer in the plane of the film. A similar discussion of diffuse scattering in HAXRD will be made below.

2.4 High-angle x-ray diffraction

2.4.1 Theoretical development

In Section 2.2.2.3 we saw that the Laue condition for scattering scattering from a perfect crystal is satisfied when the scattering vector coincides with that of a reciprocal lattice point. Reciprocal lattice vectors, $\mathbf{G}$, correspond to crystal planes, and we shall here introduce a commonly used formulation of the scattering law, Bragg's equation, which relates the lattice spacing for a particular set of planes, d_{hkl}, to the scattering angle, θ.

$$\lambda = 2d_{hkl}\sin\theta. \tag{2.52}$$

If we recognise from the definition of the reciprocal lattice that for each reciprocal lattice vector, $G_{hkl} = \dfrac{2\pi}{d_{hkl}}$, and remember the definition of the momentum transfer,

$$\begin{aligned} Q &= \mathbf{k}' - \mathbf{k} \\ &= 2|\mathbf{k}|\sin\theta \\ &= \frac{4\pi\sin\theta}{\lambda}, \end{aligned} \tag{2.53}$$

we see that

$$\begin{aligned} &G_{hkl} = Q, && \text{gives} \\ &\frac{2\pi}{d_{hkl}} = \frac{4\pi \sin\theta}{\lambda}, \\ &\Rightarrow \lambda = 2d_{hkl} \sin\theta, \end{aligned}$$

and the Laue and Bragg formulations are equivalent. Furthermore we can also see the relationship between the momentum transfer, Q, and the length-scale probed by the scattering, in that,

$$Q = \frac{2\pi}{d_{hkl}} \tag{2.54}$$

.

From equation 2.20 we see that the lattice spacings, d_{hkl}, are related to the lattice constants by

$$\frac{1}{d_{hkl}^2} = \frac{h^2 + k^2 + l^2}{a^2}, \tag{2.55}$$

for cubic crystals such as Nb, and

$$\frac{1}{d_{hkl}^2} = \frac{h^2}{a^2} + \frac{k^2}{b^2} + \frac{l^2}{c^2} \tag{2.56}$$

for an orthorhombic crystal such as U.

For an infinite, perfect crystal, diffracted intensity is only found for scattering vectors, Q, satisfying the Laue condition, but in many cases we see intensity away from reciprocal lattice points. First of all, we see that when one or more dimensions of the crystal are reduced, Intensity is found between the reciprocal lattice positions, such that the points of reciprocal space become lengthened in one or more directions, and are referred to as *crystal truncation rods*[105].

2.4.2 X-ray microstructural analysis techniques

2.4.2.1 Microstructure analysis by X-ray diffraction

X-ray diffraction patterns are very sensitive to changes in the periodicity of the electron density and in principle any disruption of the lattice on scales of below 1 μm will contribute to the diffraction pattern. In addition, X-ray diffraction analysis of microstructure has great advantages over complementary techniques such as electron microscopy since in most cases no special sample preparation is necessary. The technique is non-destructive, whilst probing large proportions of the sample volume.

2.4.2.2 Peak broadening

It was very shortly after the discovery of the diffraction of X-rays by crystals by Friedrich, Kipping and von Laue in 1912 that Scherrer, in 1918 [106], reported a relationship between the broadening of X-ray diffraction lines and the dimensions of the diffracting particles. The *Scherrer equation* forms the basis of many researchers' ideas about the deduction of microstructure from X-ray scattering, with the original form

$$h = 2\sqrt{\frac{\ln 2}{\pi}}\frac{\lambda}{\Lambda \cos\theta} \tag{2.57}$$

relating the full-width of the peak at half-maximum intensity (FWHM), h, to a measure of crystallite size Λ, at diffraction angle θ and wavelength λ. The initial factor is usually replaced with the *Scherrer constant*, K, which depends on the shape of the diffracting crystallites, and which converts Λ into a measure of 'true' size, defined as the cube root of the crystallite volume.

By way of illustration we shall show how a treatment of the Bragg equation , $\lambda = 2d\sin\theta$, leads to a relationship between size and broadening. We first multiply the Bragg equation

by the number of diffracting planes, N, and see the effect of a variation in N, as follows:

$$\begin{aligned} N\lambda &= 2Nd\sin\theta \\ (N+1)\lambda &= 2D\sin(\theta+\delta\theta) \\ &= 2D(\sin\theta\cos\delta\theta + \cos\theta\sin\delta\theta) \\ &= 2D(\sin\theta + \cos\theta\delta\theta) \quad \text{for small } \delta\theta. \end{aligned}$$

Here, $\delta\theta$ is a measure of the angular distance from the maximum in intensity to zero. If we now subtract $N\lambda = 2D\sin\theta$,

$$\begin{aligned} \lambda &= 2D\cos\theta\delta\theta \\ &= 2D\delta(\sin\theta) \\ \implies \frac{1}{D} &= \frac{2}{\lambda}\delta(\sin\theta) = \delta\left(\frac{2\sin\theta}{\lambda}\right), \end{aligned}$$

and we see that the broadening, measured in terms of $2\sin\theta/\lambda$, is simply related to the reciprocal of the crystal size, D, parallel to the diffraction vector.

Limited size is not, however, the only reason that Bragg peaks are broadened. Here we see the effect of a small change in the interplanar spacing, d, which could be due to localised

strain, for example:

$$\begin{aligned} d &= \frac{\lambda}{2\sin\theta} \\ \delta d &= \frac{\lambda}{2}\delta\left(\frac{1}{\sin\theta}\right) \\ &= \frac{\lambda}{2}\left(-\frac{\cos\theta}{\sin^2\theta}\right)\delta\theta \\ &= d\left(-\frac{\cos\theta}{\sin\theta}\right)\delta\theta \\ \implies \frac{2\sin\theta}{\lambda}\frac{\delta d}{d} &= \frac{2\sin\theta}{\lambda}\left(-\frac{\cos\theta}{\sin\theta}\right)\delta\theta \\ &= -\frac{2\cos\theta}{\lambda}\delta\theta \\ \implies -\delta\left(\frac{2\sin\theta}{\lambda}\right) &= \frac{2\sin\theta}{\lambda}\frac{\delta d}{d}. \end{aligned}$$

We see that the peak broadening due to strain-effects is dependent on the diffraction angle, but the broadening due to finite size is independent of scattering angle. This is a point we shall return to below.

2.4.2.3 Measures of broadening

There are two generally-used measures of the broadening of a diffraction peak-profile. The *full-width at half-maximum intensity* (FWHM) is generally favoured by experimentalists as it is straightforward to measure. Often more convenient for rigorous analysis, however, is the integral breadth (β), which is defined as the width of a rectangle with the same area and height as the peak in question. Measurement of the integral breadth requires the determination of the extent of the tails of the peak at low intensity, and can therefore be hard to determine if there are multiple overlapping peaks in close proximity.

Dislocations cause a distortion of the lattice around their core, as mentioned above, and this results in a broadening of the diffraction peaks in reciprocal space.

2.4.2.4 Transverse scans

For thin-film samples the truncation of the crystal in the out-of-plane direction, as seen in the longitudinal scans in Section 2.4 is significant and means that broadening due to other features is hard to see. This is often avoided by taking scans across Bragg positions in reciprocal-space that vary the length of the scattering vector that lies in the plane of the film, so-called *transverse scans*. The geometry of such a scan for a symmetrical Bragg position is compared to that of a longitudinal scan in Figure 2.8. For such scans the size of the crystal is large on the scale of the probe and as such the broadening due to the truncation of the crystal is negligible. This allows broadening from other effects to be seen more easily. Practically, true transverse scans such as that shown in Figure 2.8 require sophisticated software control of the diffractometer as the length of the scattering vector must be gradually varied so that the out-of-plane component is kept constant. For many laboratory-based diffraction experiments an approximation to a transverse scan is achieved by keeping the position of the detector constant, so maintaining the diffraction angle and the length of the scattering vector constant, and varying the angle of incidence of the X-rays on the sample. Such a scan is referred to as an *ω-rocking-curve*, indicating the diffractometer circle that is being varied, and, in reciprocal space describes the arc of a circle, centred at the origin.

We may describe the diffraction vector in terms of its out-of-plane and in-plane components, denoted q_z and q_x respectively. In terms of the diffractometer angles, θ, and ω, they are given as follows[108]:

$$q_x = K\left[\cos(\theta-\omega)-\cos(\theta+\omega)\right], \text{ and} \tag{2.58}$$

$$q_z = K\left[\sin(\theta-\omega)-\sin(\theta+\omega)\right], \tag{2.59}$$

where $K = \frac{2\pi}{\omega}$ is the magnitude of the X-ray wave-vector.

In many reports[66,78,109–114 and others] the breadth in degrees of the ω-rocking-curve is

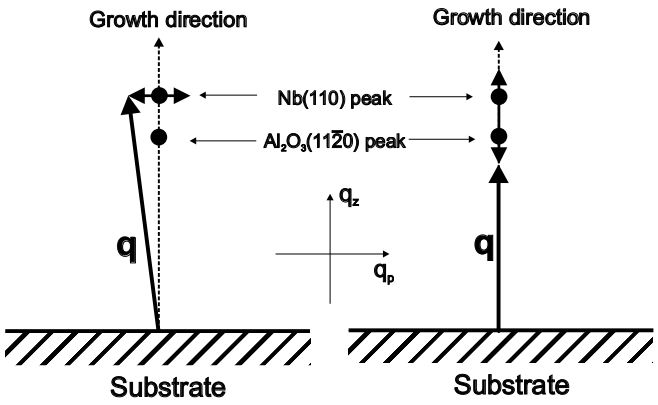

Figure 2.8: (left panel) The geometry of a transverse scan across a symmetrical Bragg peak, showing the change in the diffraction vector within the plane of the film. (right) The geometry of a longitudinal scan across a symmetrical Bragg peak, showing the change in the diffraction vector out-of-the-plane of the film. Figure taken from Wölfing et al. [107]

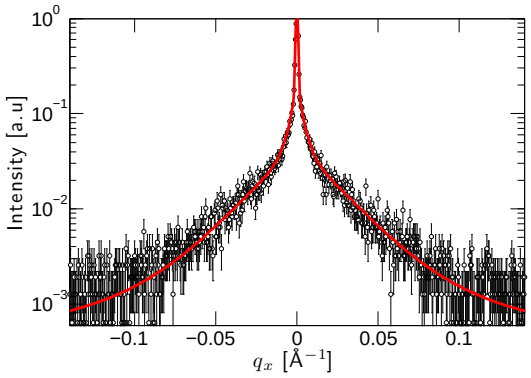

Figure 2.9: Transverse scan across the Nb(110) peak for a 61 Å Nb, 150 Å U thin-film (SN330, in Table 4.1). A very narrow component is superimposed on a component of 1/100th of the peak intensity of the narrow component and full-width at half-maximum intensity (FWHM) about 0.05 Å^{-1}. There also a component of intermediate intensity with FWHM approximately 0.01 Å^{-1}. The red line is a least-squares fit to a model as described in the text. The scan was performed at UCL.

quoted as a measure of crystalline quality, and referred to as the "mosaic-spread".

2.4.2.5 Two-component peak profiles

In thin-films, however, there is a near-ubiquitous two-component shape to the rocking curve, with a narrow, often resolution-limited peak component superimposed upon a broad-component, similar to that seen in the current samples, an example of which is shown in Figure 2.9. To give an indication of the pervasiveness of the phenomenon, two-component lineshapes have been reported in thin-metallic films of Nb[81,107,115–122], Ho and Gd[123], Ti[124], Pb[125], V[126], Fe[127], Y[127,128], Fe/Au multilayers[129], Cu/Co superlattices[130], Co[112], $TbFe_2$[131], Co/Pt superlattices[132], and Au[133], as well as semiconductor films of AlN[134,135], GaN[134,136–138], GaSb[139], ZnS[114], $Si_{0.7}Ge_{0.3}$[140] and ErAs[141], along with many oxides thin-films such as $YBa_2Cu_3O_x$[110,142–145], CeO_2[146–149], ZnO[150–152], $SrRuO_3$[153], $SrTiO_3$[154], Y_2O_3[155,156] as well as films of porous silicon[157], SiO_2[158,159] and C_{60}[160,161].

Often, only the breadth of the narrow component is quoted, and this can give the impression of anomalously high crystalline quality. The origin of the intensity in the two components is disputed, and here we shall discuss the various explanations of the phenomenon given in the literature.

2.4.2.6 "Perfect-layer" model

A simple explanation for the appearance of two components in the rocking curves is that there exist two distinct phases in the films, one of almost-perfect crystalline form, and the other a relaxed, defective layer[112,114,122,137,142,149,154,160]. This "perfect-layer model" follows a similar argument to that for the Matthews-Blakeslee criterion, with the perfect phase is often assumed to be closest to the substrate, having grown strained and "pseudomorphically", i.e. with the same in-plane lattice parameters as the substrate. As material is deposited above a critical thickness the formation of defects is energetically favourable and the 'relaxed' phase comprises the rest of the sample deposited on top. It is usually seen that thinner films have a greater proportion of intensity in the narrow component

relative to thicker films, evidence which supports the above argument. (If not explicitly stated otherwise, 'intensity' in this thesis refers to the *integrated intensity*, that is, the area under the curve of the particular scan.) Several predictions result from this hypothesis:

1. As seen above, the broadening of the peaks in the longitudinal scan direction is related to the extent of the crystal in the out-of-plane direction. The spatial extent of the two phases may be determined by executing longitudinal scans at different positions in q_x, or with a fixed offset, δ in ω, such that $\omega = \theta - \delta$. In a thick film from which the majority of the intensity is in the broad component, a longitudinal scan conducted with $q_x = \delta = 0$ would be broader than a scan conducted at a value of q_x greater than the extent of the narrow component if the two components correspond to a relatively thin "pseudomorphic" phase and a relatively thick disordered phase. For the studies referenced in this section, where such a comparison has been made the two longitudinal scans have the same breadth[84,107,116], which implies that diffraction in both components comes from the entire film thickness.

2. If the "pseudomorphic" portion were perfect in three-dimensions, a narrow component would be visible in rocking curves at all reciprocal lattice positions, including those with non-zero components of the momentum transfer in-the-plane of the film. No narrow components have been seen in studies that have searched for them[116], and Heying[162] reports a large disparity in the breadths of symmetric and asymmetric peaks.

An objection to the perfect-layer model might also be raised when the possibility of dislocation glide is taken into account. Since epitaxial strain originates at the interface between a strained epi-layer and the substrate, the energy of the system may be lowered if the core of a dislocation at some position in the layer is moved closer to the interface, since a greater volume of film will be relieved of stress[64,163]. There is therefore a force acting on the dislocation core, and the dislocation may move closer to the interface. In addition, a *self-force* causes dislocations to move away from a free surface[64]. Although there may

exist a "stand-off" of misfit dislocations, such that they come to rest a few Ångströms from the interface, as seen in Nb/sapphire[73], it is expected that dislocations in most materials will glide to a position close to the interface[164].

Bearing these objections in mind, some studies provide evidence that a perfect pseudomorphic layer might exist in some samples. TEM investigations by Brecht and coworkers[142,143] on $YBa_2Cu_3O_{7-x}$ films deposited on (111)-oriented $SrTiO_3$ by sputtering show that a strained pseudomorphic layer exists close to the substrate, with the continuation of the atomic rows of the substrate clearly visible up to a certain layer thickness, beyond which a disordered phase is seen. Films of thickness below around 10 nm show only the narrow component in the rocking curves, and no disordered regions in the TEM micrographs.

2.4.2.7 Flat planes

A number of researchers have taken the narrow component seen in transverse scans across symmetrical Bragg peaks as an indication of extreme flatness on average of the atomic planes parallel to the surface of the film[81,116,118,123]. Using the breadth of the peak to estimate a lower bound for the length scales over which the planes are flat has given figures ranging up to several tens of thousands of Ångströms. XRR and atomic-force microscopy (AFM)[107,115,165], show that since the surfaces of epitaxial layers are not flat on length scales of more than tens of ångströms this description, although not incorrect, is misleading.

2.4.2.8 Long-range orientational order

A better description might be one of long-range orientational order (LROO) given by Wölfing et al.[107]. Due to the presence of a large, almost atomically-flat substrate the positions, in the out-of-plane direction, of the atoms that compose atomic planes parallel

to the surface of the substrate are correlated over very large distances relative to the X-ray probe, and it is this correlation that gives rise to the narrow component. This description does not preclude disorder in this direction on smaller length-scales of, say, tens to hundreds of ångströms, nor of disorder along directions that lie in the plane of the film. Metzger et al.[134] show the presence of a narrow component to the scattering in AlN films that show a high degree of disorder in TEM micrographs.

2.4.2.9 Attenuation of the narrow component with increasing Q

The narrow component is attenuated by random disorder in the atomic positions, so-called *non-cumulative disorder*[102,166], and this attenuation is dependent on the length of the scattering vector, $Q = \frac{4\pi}{\lambda}\sin\theta$, with θ the scattering angle. This attenuation is of a similar form to that due to thermal fluctuations in position, and has the following dependence on Q:

$$I = I_0 \mathrm{e}^{-Q^2\sigma^2}, \tag{2.60}$$

where σ is known as the *static Debye-Waller factor*[167,168].

2.4.3 The analysis of peak broadening

The broadening of a diffraction peak may have several origins, which are not restricted to the size and "strain" broadening seen above. The contributions from different effects are convolved in the resulting intensity profile. Separation of the different effects is possible using a number of methods, of which we shall introduce a selection below, and allows a detailed description of the sample microstructure.

2.4.3.1 Single-line methods: Expected functional forms

In many cases it is possible to describe a given microstructural feature analytically, and deduce the functional form of the scattering profile due to this feature. Laue in 1928 was the first to use the standard Lorentzian and Gaussian functions to model line profiles[169], and these have become associated with different effects. Warren[170] has shown that broadening due to strains is approximately Gaussian, and broadening due to particle size is Lorentzian. In addition, by using a displacement-difference correlation function of the form

$$C(r) = \frac{< h(0)h(\mathbf{r}) >}{< h(0)h(0) >} = (1 + \kappa r)\exp(-\kappa r). \tag{2.61}$$

to describe the displacements of the lattice due to the presence of misfit dislocations, Gibaud et al.[117] showed that the lineshape resulting from such displacements is Lorentzian-squared, thereby explaining the form of the scattering seen in transverse scans from Nb films grown (110) on sapphire $(11\bar{2}0)$[63,81,117,118,171]. The different contributions are extracted by fitting a convolution of the line-profiles and the proportions of each component evaluated[108 , pp. 129–130]. More approximately a linear superposition of the expected functional forms may be fitted to the peak, resulting in a more straightforward extraction of their relative contributions.

2.4.3.2 Gaussian, Lorentzian and Lorentzian-squared functions

In this thesis the Gaussian function is defined as

$$f_{\text{Gaussian}}(x, A, c, w) = A\exp\left(-0.5\frac{(x-c)^2}{w^2}\right), \tag{2.62}$$

where A, c and w are the amplitude, centre and width of the peak, respectively. For this definition of the Gaussian peak, the full-width at half-maximum, $\text{FWHM}_{\text{Gaussian}} = 2\sqrt{2\ln 2}w$, and the integral breadth, $\beta_{\text{Gaussian}} = \sqrt{2\pi}w$. We also define the the Lorentzian,

or Cauchy function as:

$$f_{\text{Lorentzian}}(x, A, c, w) = \frac{A}{1 + \frac{(x-c)^2}{w^2}}, \text{ where} \tag{2.63}$$

$$\beta_{\text{Lorentzian}} = \pi w, \text{ and} \tag{2.64}$$

$$\text{FWHM}_{\text{Lorentzian}} = w, \tag{2.65}$$

and also the Lorentzian-squared function as:

$$f_{\text{Lorentzian-squared}}(x, A, c, w) = \frac{A}{\left(1 + \frac{(x-c)^2}{w^2}\right)^2}, \text{ where} \tag{2.66}$$

$$\beta_{\text{Lorentzian-squared}} = \frac{\pi}{2} w, \text{ and} \tag{2.67}$$

$$\text{FWHM}_{\text{Lorentzian-squared}} = 2\sqrt{\sqrt{2} - 1} w. \tag{2.68}$$

2.4.3.3 Analysis of the Q-dependence of broadening: the method of Williamson and Hall

As we saw in Section 2.4.2.2 the broadening due to finite crystal size is independent of the scattering angle, and hence of the length of the scattering vector, Q, whilst the broadening due to strain-effects is not.

By plotting a measure of the broadening from a number of peaks at different positions in Q against a measure of the length of the scattering vector, the broadening due to size (β_{S}) and strain effects or lattice distortions (β_{D}) may be separated. This method is known as the Williamson-Hall method, although the exact process is subject to variation. The original analysis[172] found the broadening due to strain effects by differentiating the Bragg equation, as above. The ratio of $\frac{\delta d}{d_0}$ is considered as the product of the root-mean-square strain $\epsilon_{\text{rms}} = \left\langle \epsilon^2 \right\rangle^{\frac{1}{2}}$ and a scaling factor, K_{D}, taking into account the nature of the distortions of the lattice. It was assumed that the strain and size broadened peaks are both described by Lorentzian functions, which isn't experimentally supported, but this

allows the total broadening to be expressed as

$$\beta = \beta_{\mathrm{S}} + \beta_{\mathrm{D}} \tag{2.69}$$

$$\beta_{2\theta} = \frac{K_{\mathrm{S}}\lambda}{\langle D\rangle_V \cos\theta} + 2K_{\mathrm{D}}\epsilon_{\mathrm{rms}}\tan\theta$$

$$\implies \beta_{2\theta}\frac{\cos\theta}{\lambda} = \frac{K_{\mathrm{S}}}{\langle D\rangle_V} + K_{\mathrm{D}}\epsilon_{\mathrm{rms}}\frac{2\sin\theta}{\lambda}, \tag{2.70}$$

where $\langle D\rangle_V$ is the volume-averaged crystallite size. $\langle D\rangle_V$ and $K_{\mathrm{D}}\epsilon_{\mathrm{rms}}$ are then found from a plot of $\beta\cos\theta$ against $\frac{2\sin\theta}{\lambda}$ for several peaks, which should give a straight line. This graphical method is referred to as a *Williamson-Hall plot*.

In order to account for the broadening from the strain-fields around dislocations, which is dependent on the orientation of the dislocation relative to the scattering vector, Ungár and Borbély [173] developed the *modified Williamson-Hall equation*. The equation takes into account the modulation of the peak broadening for different reflections, hkl, by the introduction of the *average dislocation contrast factor*, $\bar{C}_{hkl}$, which may be calculated for the reflections used in the analysis and the expected slip systems. The modified equation reads

$$\beta_{2\theta}\frac{\cos\theta}{\lambda} = \frac{K_{\mathrm{S}}}{\langle D\rangle_V} + \epsilon\sqrt{\bar{C}_{hkl}}\frac{2\sin\theta}{\lambda}. \tag{2.71}$$

Here the average microstrain, ϵ, is defined as $\epsilon = b\sqrt{\pi A\rho_{\mathrm{d}}/2}$, and results from the Burgers vector, b, the dislocation density ρ_{d} and a constant, A, determined from the elastic constants of the material.

A method based on analysis of the integral breadths of transverse scans over symmetric Bragg-peaks is developed by Durand et al. [150], and regards the broadening as due to mosaicity tilt, ΔM, giving a mosaicity broadening $\Delta\omega_M$, and a finite correlation length in the plane of the film ξ_x. Using the components of the scattering vector in and normal

to the film plane, here given as:

$$Q_x = \frac{2}{\lambda}\sin\theta\sin(\omega-\theta) \tag{2.72}$$

$$Q_z = \frac{2\sin\theta}{\lambda} \tag{2.73}$$

we find the integral breadths in reciprocal space in terms of those in angular space as follows:

$$\beta_x(Q) = \beta(\omega)\frac{2\sin\theta}{\lambda} \tag{2.74}$$

$$\beta_z(Q) = \beta(2\theta)\frac{\cos\theta}{\lambda}. \tag{2.75}$$

The broadening due to the finite correlation length is given in a version of the Scherrer formula, with shape constant, K as

$$\beta_{\xi_x}(Q) = \frac{K}{\xi_x}, \tag{2.76}$$

and is independent of Q, whereas the mosaic broadening is linearly dependent on Q:

$$\beta_M(Q) = \Delta M.Q_z. \tag{2.77}$$

With the assumption that the broadening from mosaicity has a Gaussian form (from the Central Limit Theorem, which states that a large number of random samples from any distribution will be normally distributed), and that from the correlation length has Lorentzian form, we can use an approximation to the integral-breadth of a convolution of the two profiles (a Voigt function[174]), $\beta(s)$, which is assumed to the the profile of the measured peak:

$$\beta^2(s) = \beta_{\text{Cauchy}}(Q).\beta(s) + \beta^2_{\text{Gauss}}(Q). \tag{2.78}$$

We can now write a linear relationship between the two effects:

$$\left(\frac{\beta(s)}{Q_z}\right)^2 = \Delta M^2 + \frac{1}{\xi_x}\frac{\beta(s)}{Q_z^2}. \tag{2.79}$$

The effects are separated by using what the authors describe as a Williamson-Hall-like plot of $\left(\frac{\beta(s)}{Q_z^2}\right)^2$ as a function of $\frac{\beta(s)}{Q_z^2}$.

The (110) and (220) peaks have identical dislocation contrast factors.

2.4.3.4 Scattering from dislocations

Kaganer et al.[121] has considered the influence of misfit dislocations on the shape of the rocking curves, and discusses the resulting data in each of two limits, one for low disorder, and one for high disorder. For the limit of low disorder, where the product of the dislocation density and the layer thickness, $\rho d \lesssim 1$, and the sharp component of scattering is seen and the static Debye-Waller factor may be estimated as $w \sim \rho d$. In this limit the sharp peak is seen as the mean spacing between dislocations exceeds the film thickness. In the limit of large disorder $\rho d \gg 1$ and there is no coherent diffraction as the correlation between the displacements of atoms separated by large distances vanishes. In this case the mean distortion due to the presence of dislocations determines the peak position perpendicular to the diffracting planes, and the mean-square distortion provides the peak widths. Their analysis is based on the derivation of the correlation function by Krivoglaz[175].

The authors also simulate the effect of different dislocation types on the shape of the diffraction peaks in the q_x, q_z-plane of reciprocal-space. They assert that 60° glide dislocations are the most comment type in heteroepitaxial systems, and are evidenced by a decrease in the aspect ratio of the peak in the q_x, q_z-plane to decrease below one. Lomer-type edge (90°) dislocations are also formed, at large dislocation densities, and cause no change in the peak aspect ratio from one.

2.4.3.5 Fourier methods

For completeness we shall mention the use of techniques that employ Fourier transformation of the diffraction data, based on the methods of Warren and Averbach[176]. From the convolution theorem[177], in the Fourier transform of the rocking curve the different broadening effects that are convolved in the diffraction pattern are simply multiplied together to give the Fourier coefficients, and are thus more straightforwardly separated. Discussion of the details of the analysis is given in the books of Birkholz[108] and Mittemeijer and Scardi[169].

2.4.4 Observation of the CDW in thin uranium films

X-ray scattering and neutron scattering are ideal probes of the CDW, as they are of any subtle deviation from perfect cystallinity. Both techniques probe the periodic lattice distortion (PLD) that accompanies the formation of the charge-density wave[20,178]. In Chapter 5 we report the results of X-ray experiments on uranium thin-films. Some necessary introductory theory, and an effort to place this work in a wider context comprises the remainder of this chapter.

We may denote the position of the kth atom in the jth unit-cell of the crystal, as

$$\mathbf{r}_{jk} = \mathbf{R}_j + \mathbf{r}_k + \mathbf{u}_{jk}, \tag{2.80}$$

with the displacements due to the CDW of wavevector $\mathbf{q}$ given by the term

$$\begin{aligned} \mathbf{u}_{jk} = \epsilon_x \mathbf{a} \cos\left[2\pi\mathbf{q}\cdot(\mathbf{R}_j + \mathbf{r}_k) \pm \phi_x\right] \\ + \epsilon_y \mathbf{b} \cos\left[2\pi\mathbf{q}\cdot(\mathbf{R}_j + \mathbf{r}_k) \pm \phi_y\right] \\ + \epsilon_z \mathbf{c} \cos\left[2\pi\mathbf{q}\cdot(\mathbf{R}_j + \mathbf{r}_k) \pm \phi_z\right], \end{aligned} \tag{2.81}$$

with the $\pm$ signs indicating the distortion of atomic positions related across an inversion

centre. This leads to the structure factor for the distorted atoms

$$F(\mathbf{G}+m\mathbf{q}) = \sum_{[m]} 2\cos(2\pi\mathbf{G}\cdot\mathbf{r} - m_x\phi_x - m_y\phi_y - m_z\phi_z) \times J_{mx}(\epsilon_x\mathbf{a}\cdot\mathbf{Q})J_{my}(\epsilon_y\mathbf{b}\cdot\mathbf{Q})J_{mz}(\epsilon_z\mathbf{c}\cdot\mathbf{Q}), \quad (2.82)$$

which shows that there is scattering from satellite peaks of increasing order, m, separated from the Bragg peaks at $\mathbf{G}$ in the reciprocal lattice by the vector $\mathbf{q}$ for the lattice distortion, and multiples thereof. J_m is the Bessel function of the first kind of order m, which for small displacements, ϵ, we can approximate to $J_m \approx \frac{(\epsilon/2)^m}{m!}$, and we see that the intensity of the satellites decreases with increasing order. In this derivation, which follows the derivation used in Marmeggi, 1982[179], we have assumed that the wavevector, q, has components in all three reciprocal-lattice directions. A derivation of the lattice distortion from a mean-field treatment of the electron-phonon interaction in a 1D electron gas is given in Grüner, 1994[19] and the cross-section for neutron scattering from the distortion developed in Eagen, 1975[180]. An X-ray diffuse scattering formalism is developed in Conwell, 1988[181], and Ravy, 2006[89] following Krivoglaz[175,182].

From these treatments we find that an extensive characterisation of the CDW is possible through analysis of the scattering at the satellite positions. Clear from the above is that the positions of the satellites in reciprocal space gives a direct measure of the wavevector of the CDW. This arises from the nesting portions of the Fermi surface, and its length along the reciprocal lattice vectors is slightly greater than twice the Fermi wavevector along those directions[178]. A theoretical study of uranium[30] finds nesting vectors, linking nearly parallel portions of the Fermi-surface, of length $\frac{\pi}{a}$ along the $\mathbf{a}^*$ reciprocal lattice direction, as shown in Figure 2.10, and $\sim \frac{\pi}{6b}$ along the $\mathbf{b}^*$ direction, with a and b crystal lattice parameters.

Experimental evidence shows that the wavevector of the distortion in uranium is strongly dependent on temperature, as shown in Figure 2.11. We see that on the appearance of

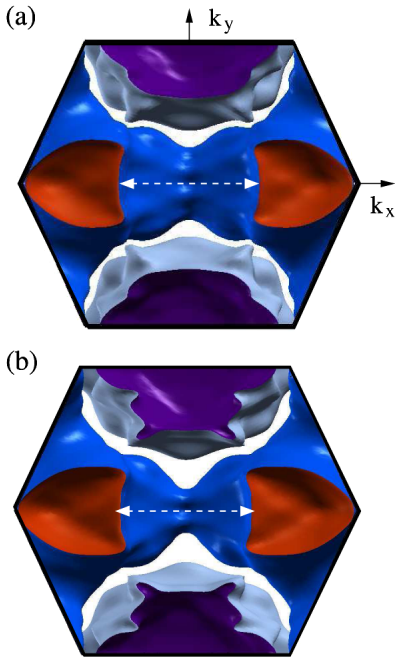

Figure 2.10: The Fermi-surface topology for the α-U structure calculated at (a) ambient pressure and (b) at 20 GPa. In each case, the diagram shows the [100] ($\mathbf{k}_x$) and [010] ($\mathbf{k}_y$) axes at a fixed position $z = 1/2$ along [001]. The different colors correspond to the different sheets of the Fermi surface. The arrow indicating the nesting vector $\{\approx 1/2(2\pi/a)$ along [100]$\}$ has been drawn the same length in both (a) and (b). Taken from Raymond et al. [183]

the CDW satellites at 47 K all three components, q_x, q_y and q_z, take positions unrelated to the reciprocal lattice vectors. The distortion is described as *incommensurate*. As the temperature is decreased, the component along $\mathbf{a}^*$, q_x, becomes *commensurate*, and the periodicity of the distortion in real space becomes an integer number (2) of unit cells in the [100] crystal direction. This *lock-in* to a commensurate CDW wavevector component coincides with the thermodynamic transition at 37 K mentioned above. At the 22 K transition, the q_y and q_z components lock-in to values of $\frac{1}{6}\mathbf{b}^*$ and $\frac{2}{11}\mathbf{c}^*$, respectively. (These values given are as seen by X-ray scattering; a slightly different value of $\frac{5}{27}\mathbf{c}^*$ is seen in neutron scattering experiments, as discussed in Grübel, 1991 [88]). We see, then, that the ground state of the CDW/PLD is to have wavevector components that correspond to the Fermi-surface nesting vectors along $\mathbf{a}^*$ and $\mathbf{b}^*$. In Figure 2.12 we have reproduced illustrations of the displacements below 22 K. The top panel shows the uranium unit-cell

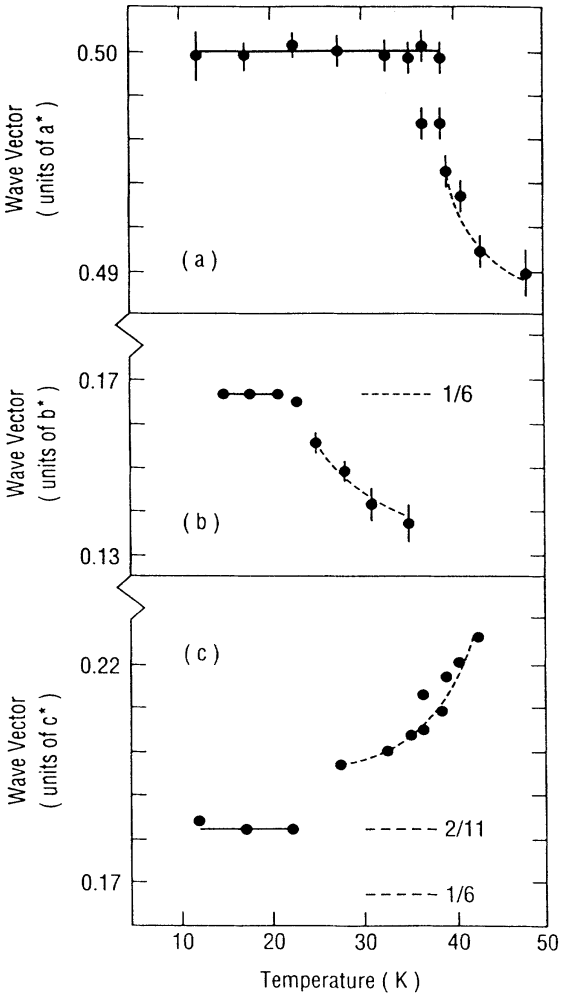

Figure 2.11: The temperature dependence of the components of the CDW wavevector from the X-ray and neutron scattering experiments of Grübel *et al*[88]. CDW phase transitions are visible at 22 K and 37 K.

displacements in real space, and we see in the bottom panel that these are greatest along the [100]-direction, and correspond to the displacements due to the condensed Σ_4 phonon described above.

The deviations from the commensurate values of $\frac{1}{2}$ and $\frac{1}{6}$ seen may be explained by the inclusion of phase slips or *discommensurations*, into the structure[88,185]. Similar to the phase slips in the magnetic structure of Ho[186], if every n unit cells along the [010]-direction, the phase change between unit cells is twice the expected $\frac{2\pi}{6}$, the average wave-vector of

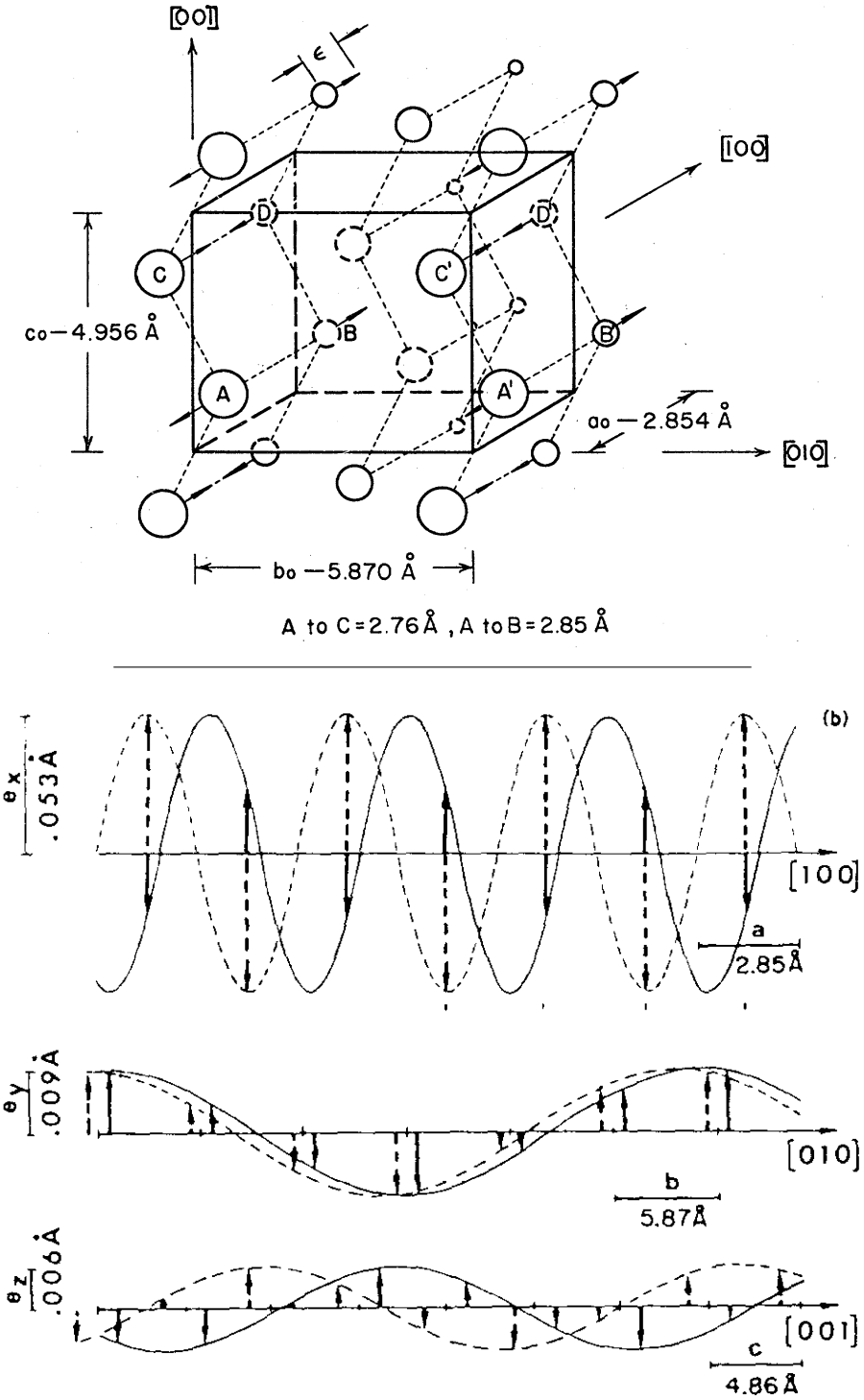

Figure 2.12: (top panel) The α-uranium unit cell with the displacements of the periodic lattice distortion in the [100]-direction indicated by arrows. Taken from Smith, 1984[184]. (bottom panel) The displacements along each of the lattice directions, with the atomic positions marked by arrows. The solid and dashed lines show the displacements of atoms across the inversion centre. Taken from Marmeggi, 1982[179]

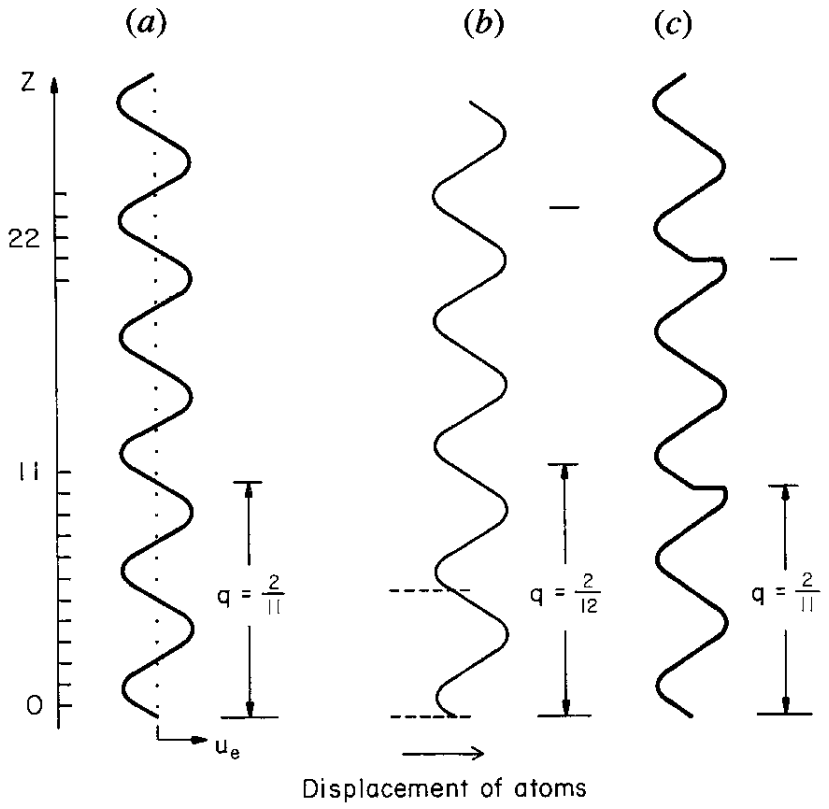

Figure 2.13: An illustration of CDW phase slips along q_z, as discussed in the text. Taken from Lander, 1994[1] and originally from G. Grübel (1991, unpublished)

the CDW is

$$\langle q_z(n) \rangle = \frac{1}{6} \left[1 + \frac{1}{n} \right] b^*. \tag{2.83}$$

Diffraction peaks would then be observed at wave-vectors given by

$$q_z(n, I) = \langle q_z(n) \rangle + \left(\frac{I}{n} \right) c^* = \frac{1}{6} \left(1 + \frac{6I + 1}{n} \right) c^*, \tag{2.84}$$

where I is the order of the satellite. It is believed that the q_z wavevector of the CDW in U is in fact $\frac{1}{6}$, but a stable discommensuration structure remains even at the lowest temperatures[88], as illustrated in Figure 2.13. Discommensurations, much like dislocations in the crystal lattice, will repel one another, but there will be a distribution of lengths between dislocations, which will contribute to a broadening of the CDW satellites.

Commensurability results from a minimisation of the energy resulting from the interaction between the CDW and the periodic lattice potential, and there will be an influence on the CDW if the periodicity of the lattice is modified in any way. Some lattice defects that involve local variations in the charge-density, such as dislocations, will couple directly to the phase of the CDW. This will lead to a loss in long range order, with the CDW phase *pinned* to specific sites in the material[187,188].

Fukuyama, Lee and Rice treated the CDW as an elastic medium, and showed that only modifications to the phase of the CDW are important[189–191]. In the limit of weak pinning, the phase is modified by each defect such that it changes by one cycle over a length-scale much larger than the distance between defects. This leads to a finite phase-phase correlation length, which leads to a broadening of the CDW satellite peaks[192], in a similar manner to the Scherrer size-broadening of Bragg peaks.

Finally, the integrated intensity of the satellite peaks is proportional to the square of the order parameter, Δ, which, in the weak-coupling limit where size of the energy gap is much less than the Fermi energy, may be described within the framework of the BCS theory for superconductors. This then allows for the evaluation of the temperature dependence of the order parameter. In Cr[22] the scaling of the order parameter with temperature corresponds to the mean-field theory and this is expected for U. The temperature dependence of the order parameter in the BCS theory in the vicinity of the CDW transition temperature is

$$\frac{|\Delta(T)|}{|\Delta(0)|} = 1.74\left(1 - \frac{T}{T_{\mathrm{CDW}}^{\mathrm{MF}}}\right)^{\frac{1}{2}}, \tag{2.85}$$

where $T_{\mathrm{CDW}}^{\mathrm{MF}}$ is the mean-field CDW transition-temperature.

The next chapter begins the report of our experimental results, beginning with a description of the process of sample-growth and their initial characterisation.

Chapter 3

Growth of single-crystal thin-films of uranium

The samples in this study were grown by the process of magnetron sputtering. Magnetron sputtering is a simple and widely-used technique for the growth of quality thin-films. As described earlier, it may be possible to grow higher-quality thin-films using a method such as MBE that allows slower growth rates, but for the purposes of this study the quality of the films obtained using magnetron sputtering is sufficient.

3.1 Growth method by magnetron sputtering

The following process was followed for the growth of all samples: After cleaning, the substrates are affixed to Mo blanks with a recess in which the sample sits. The samples are held tightly in place with screwed-in Mo clips. The blanks are placed on the rack in the loading chamber, with care taken to avoid contamination. The loading chamber is pumped down to base pressure and the valve separating the loading chamber from the main chamber opened. The manipulator arm allows transfer between the chambers, and

94

the blank holding the desired substrate is placed on the cradle in the main chamber. The manipulator arm is withdrawn and the height of the cradle adjusted to achieve a sputtering distance of 10 cm. The loading valve is closed and the main chamber pumped down to base pressure.

For the growth of the niobium buffer layer, a current of 4.5 A and 200 V was supplied to the heating wire, which lead to a stable temperature at the substrate of 970 K. For the growth of the uranium layers the current was lowered to 3.5 A, which gave a stable temperature of 720 K. The substrates were allowed to cool to below 350 K before deposition of the Nb capping layers.

A power of 50 W was supplied to the magnetrons for all samples. Pneumatic shutters located above each gun allowed control of the deposition time from each layer by computer using labView. During sputtering the thicker uranium layers, with deposition times of thousands of seconds, the power to the Nb targets was switched off. Similarly the U target was only given power after the Nb buffer layer was deposited.

3.1.1 In-situ characterisation—indication of layer quality using RHEED

After the growth of the buffer and uranium layers their quality was ascertained through the use of an in-situ reflection high-energy electron diffraction (RHEED) system. An image typical of that seen during growth is shown in Figure 3.1. Well-resolved patterns of streaks and spots were seen for all samples, which indicates good crystallinity of the layers.

Further growth studies may include a systematic measurement of the RHEED patterns, as any change in the growth mode from layer-by-layer to island growth as thickness is increased would be seen.

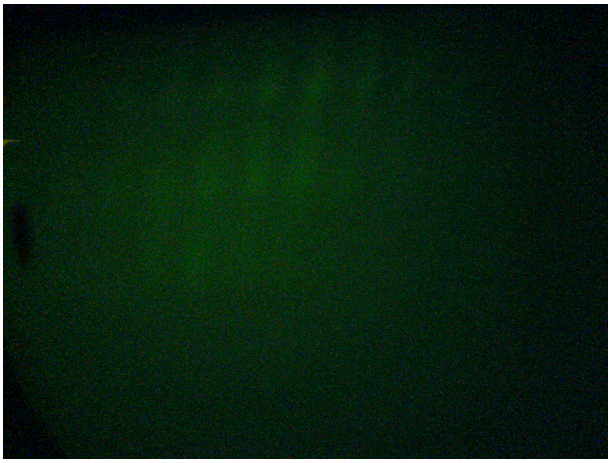

Figure 3.1: An image of the phosphor screen showing the RHEED diffraction pattern during growth of a uranium layer. The appearance of spots indicates the high quality of the epitaxial layer.

3.2 A list of the samples, and their nominal thicknesses, grown in this study

A list of the samples grown for this thesis is given in Table 3.1.

3.3 Ex-situ characterisation

3.3.1 Thickness-determination using X-ray reflectometry

3.3.1.1 Varying Nb-layer thickness

The reflectivities of the samples listed in Table 4.1 are shown in Figure 3.2. We have made fits to the data using the freely available software GenX, which is described in Björck and Andersson [193]. The software models the reflectivity using the Parrot formalism, with the Névot-Croce modification including a Gaussian distribution of roughnesses as described in Section 2.3.1. Its particular merit for an investigation of this type is that a very large region of parameter space may be sampled very quickly using the differential evolution

Sample number	Nb buffer[Å]	U layer[Å]	Nb cap[Å]
SN241	350	500	100
SN242	350	1000	100
SN243	350	50	100
SN258	350	300	100
SN259	350	200	100
SN260	350	100	100
SN282	350	75	100
SN317	350	500	150
SN320	350	750	150
SN321	350	2000	150
SN322	350	150	150
SN323	350	350	150
SN324	50	150	150
SN325	500	150	150
SN330	150	150	150
SN373	1000	150	150
SN374	2000	150	150

Table 3.1: The sample numbers and nominal layer thicknesses of the epitaxial uranium films grown for the present study, in chronological order.

algorithm, and robust fits to the data are found even from substantially differing starting positions. This is important for the present samples, as there are no Bragg-peaks resulting from a periodic structure, such as in the reflectivity spectrum from a multilayer sample, and it is difficult to deduce which layer is contributing to which portion of the data. Similar programs for the analysis of XRR data exist, such as StochFit[194], which uses a stochastic approaches and xPolly[195], which employs steepest-descent and simulated annealing approaches to data-fitting. These alternative programs were found to be less efficient at fitting the data from the current samples.

The form of the reflectivity curves for $0.05 < Q < 0.1$ are difficult to reproduce in the model. This region describes the upper layers of the samples. These layers are the most disordered, forming away from the epitaxial regions close to the substrate, as well as being deposited at low temperature, and also include oxidised layers that may be of unpredictable density and stoichiometry. Also, close to the critical angle, the kinematical approximation inherent in the model breaks down, so this may also be an issue. The parameters used in

Sample	SN324	SN330	SN322	SN325	SN373	SN374
$t_{Nb_2O_3}$[Å]	15.6±2	53.6±5	38.6±2	31.2±2	22.6±3	28.0±3
$t_{\text{Nb cap}}$[Å]	85.2±4	45.7±3	71.8±4	127.5±4	89.3±3	78.9±4
t_U[Å]	186±5	161±5	155±6	156±1	128±2	109±2
$t_{\text{Nb buffer}}$[Å]	31.4±1.7	61.2±2	157±6	306±4	598±18	1274±20
$\sigma_{Nb_2O_3}$[Å]	7.6±2	15.9±3	14.6±2	18.5±3	12.5±2	16.5±2
$\sigma_{\text{Nb cap}}$[Å]	8.1±2	11.0±1	11.5±2	16.2±2	13.0±3	17.0±3
σ_U[Å]	5.71±0.9	21.1±1.3	18.3±1.5	30.0±2.1	41.1±2.4	44.4±3
$\sigma_{\text{Nb buffer}}$[Å]	2.9±0.8	4.5±1	4.0±1.2	13.0±2	8.1±1	10.6±2

Table 3.2: The layer thicknesses, t, and roughnesses, σ, used to fit the X-ray reflectometry curves seen in Figure 3.2, for samples of different Nb buffer-layer thickness.

the fits are included in Table 3.2.

3.3.1.2 Varying U-layer thickness

The reflectivities of the samples listed in Table 4.4 are shown in Figures 3.4 and 3.5. The fit to the periodicity in intensity around the mid-points of the scans, with $Q \approx 0.1$–0.25 is most important in determining the thicknesses of the U layer. In most samples the fit this region is good, although as t_U is pushed above ~ 500 Å the decreasing period of the oscillation and increasing roughnesses are difficult to model. However, robust fits to these thicker U-layer thicknesses are still found as the attenuation of the X-ray beam by the U-layer gives a characteristic shape to the reflectivity curve for regions of $Q < 0.1$ Å^{-1}.

The 'washing out' of the higher frequency oscillations in films of $t_U > 500$ Å indicate that the sharpness of the interfaces in these thicker samples is lost, compared to those of lower thickness.

In most cases the fits to the layer thicknesses are robust, meaning that the fitting algorithm reproduces the fits from very different strating points. As a check, the reflectivity for SN243 was measured at XMaS in order to take advantage of the increased incident X-ray intensity. The fit to this data gave the same parameters as a fit to the laboratory data.

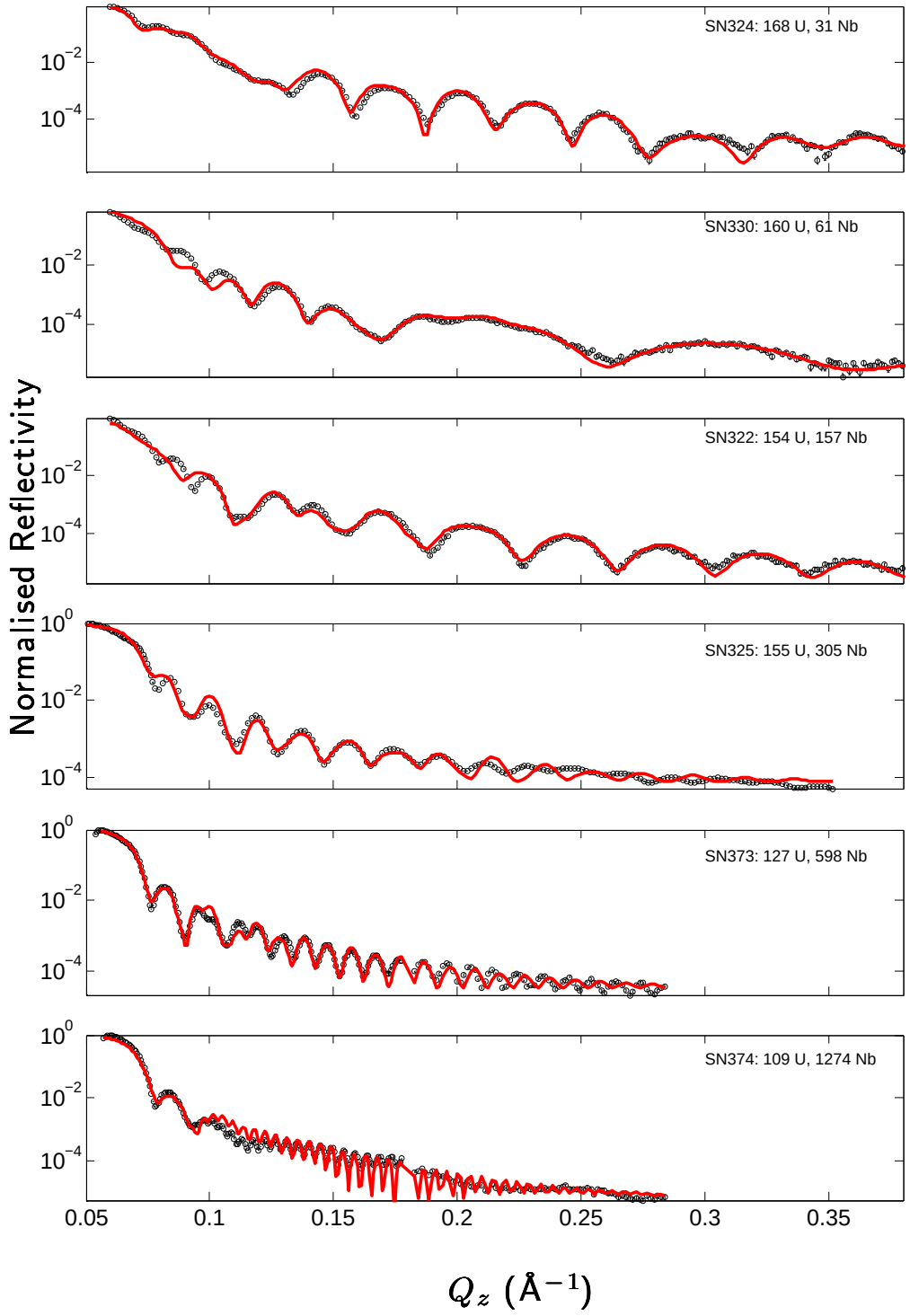

Figure 3.2: X-ray reflectivity for samples of different Nb-layer thickness listed in Table 3.2. The solid red lines show fits to the data using the GenX program[193]. A decrease in the period of the intensity oscillations is seen as the layer thicknesses increase frrom the top panel downwards. The fit to the model successfully reproduces the data, with an accuracy sufficient for the determination of the layer thicknesses.

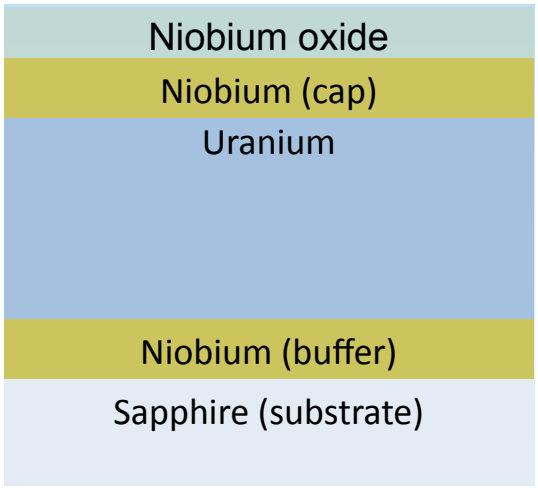

Figure 3.3: The model used for fitting the X-ray reflectivity data, including the sapphire substrate, the epitaxial Nb and U layers, the Nb cap, and a passivating layer of Nb_2O_3 that forms on exposure of the samples to air on removal from the growth chamber.

Other researchers[171] have improved the fit to reflectivity curves for Nb-on-sapphire films by including two extra layers between the sapphire and the Nb layer, but we have not found a significant improvement to the fits by introducing such a layer.

3.3.1.3 Summary

X-ray reflectometry is an excellent method of thickness-determination for periodic nanostructures such as multilayers, where the positions of the resultant Bragg peaks gives a reliable indication of the periodicity. For the current samples we have found it difficult to fit the reflectometry data without the presence of a periodic structure. In addition, a large degree of uncertainty is introduced by the presence of the Nb cap, which is oxidised to variable thicknesses and roughnesses. For these reasons, real-space measurements such as transmission electron microscopy (TEM) or atomic-force microscopy (AFM) might be more reliable methods of thickness determination.

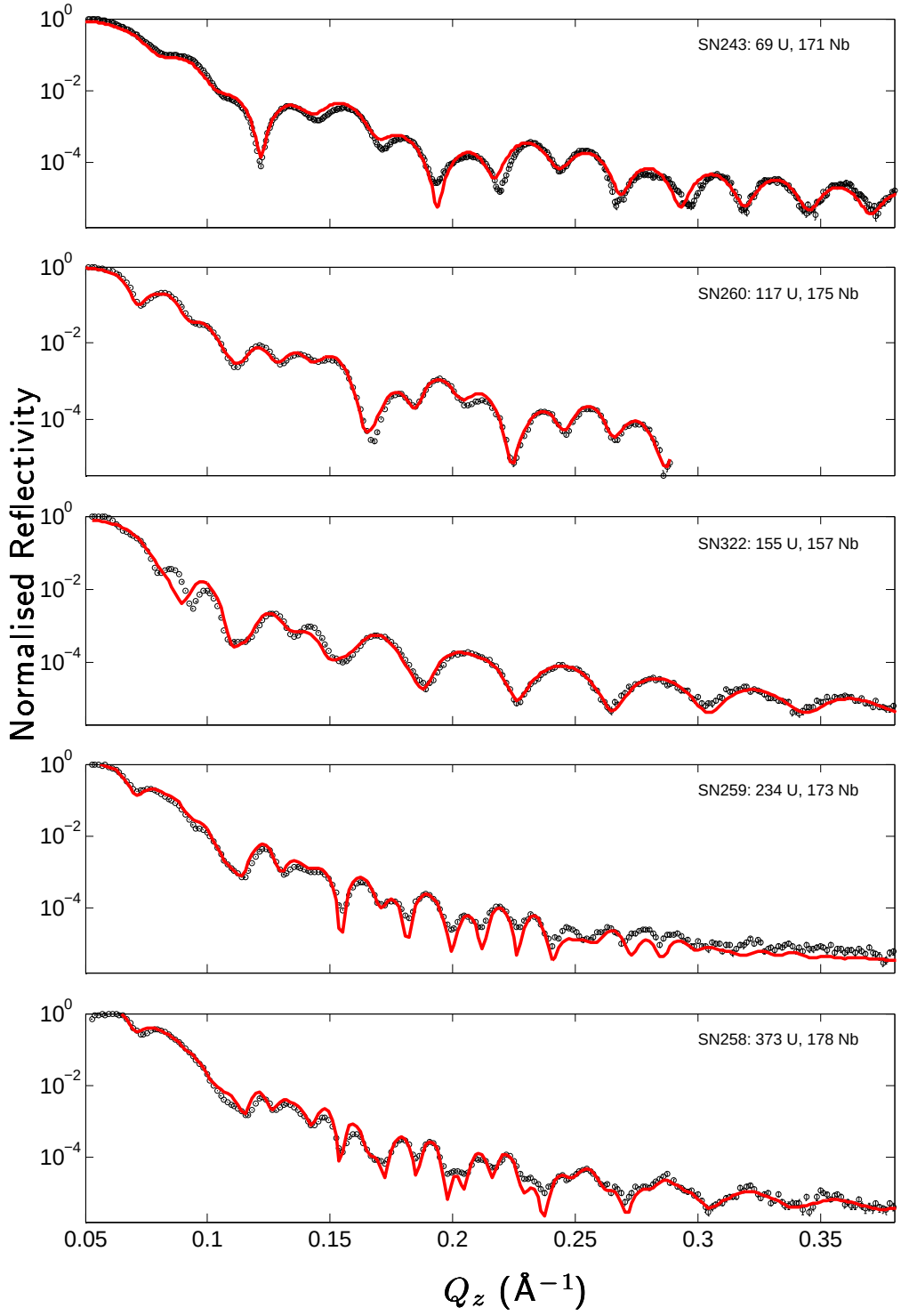

Figure 3.4: X-ray reflectivity for samplesof varying uranium-layer thickness listed in Table 4.4 . The solid red lines show fits to the data using the GenX program[193]. The increasing thickness of the layers is reflected in the decreasing period of the intensity oscillations. Oscillations of different periods arise from different layers of the sample.

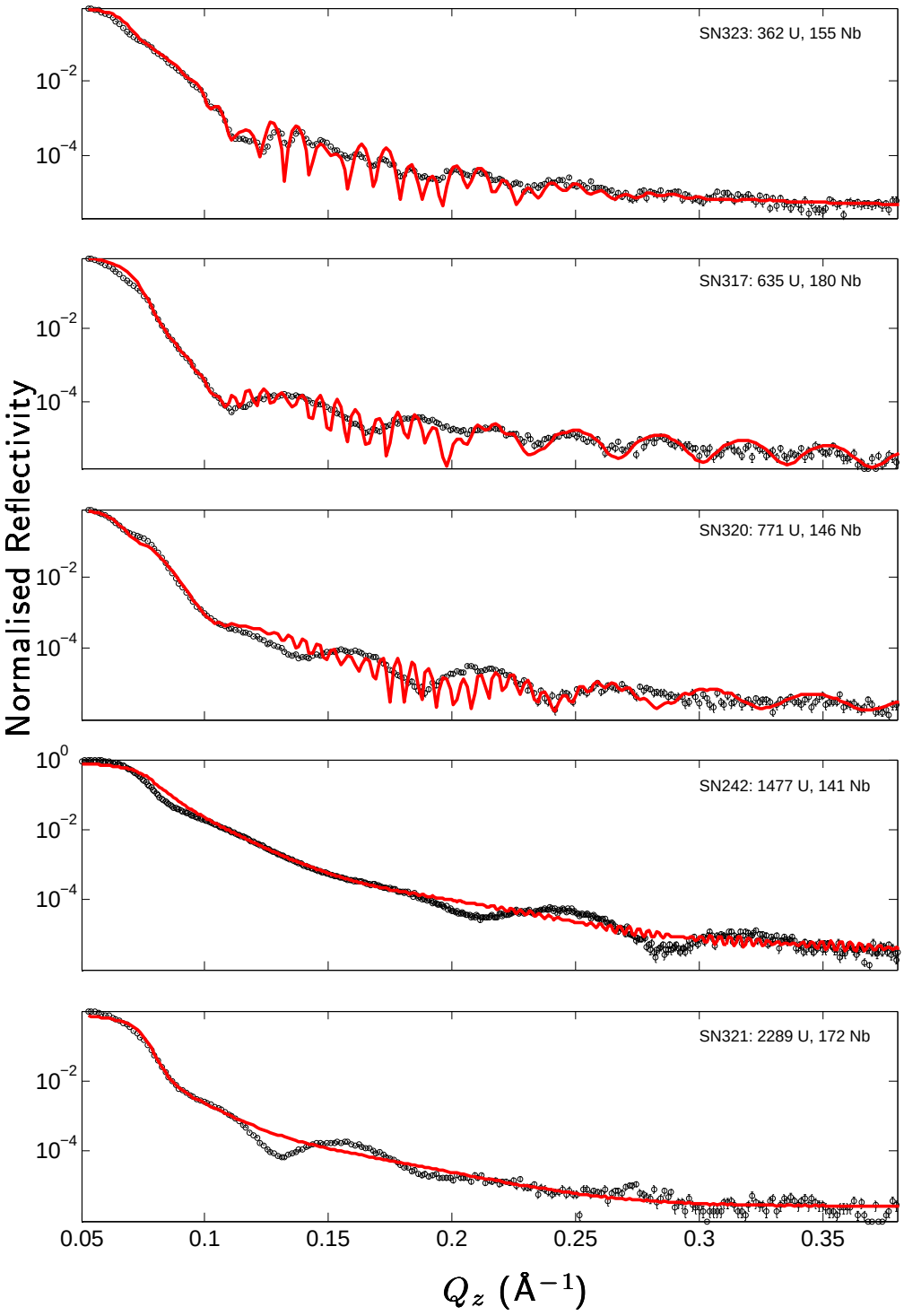

Figure 3.5: X-ray reflectivity for samples of varying uranium-layer thickness listed in Table 4.4. The solid red lines show fits to the data using the GenX program[193]. For the thicker U layers, the model does not reproduce the data above around 0.13 Å^{-1}. However, fits to these samples are strongly repeatable, and the thicknesses obtained are sensible based on the sputtering time.

Sample	SN243	SN282	SN260	SN322	SN259
$t_{Nb_2O_3}$[Å]	39±1.2	5±2.2	20.0±2.6	16.5±2.4	40±3.4
$t_{\text{Nb cap}}$[Å]	31.0±4	9.9±2	6.1±2	49±6	91.2±10
t_{U} [Å]	69.1±2	90.1±3	117±4	155±2	234±5
$t_{\text{Nb buffer}}$ [Å]	171±32	170±2	175±3	157±4	173±2
$\sigma_{Nb_2O_3}$[Å]	14.1±1.2	6.7±0.8	9.3±1.1	11.5±1.5	9.6±1.9
$\sigma_{\text{Nb cap}}$[Å]	6.6±0.4	1.9±2	47.9±0.2	14.2±0.5	50.1±2
σ_{U}[Å]	39.8±5.2	6.4±1.2	28.7±2.3	28.2±3.1	23.6±2
$\sigma_{\text{Nb buffer}}$[Å]	16.2±0.7	5±1.8	2.7±1	2.4±0.4	9.2±0.9

Sample	SN323	SN317	SN320	SN242	SN321
$t_{Nb_2O_3}$[Å]	18.4±2	2±0.6	11.9±2.3	5±1.4	31.5±3.2
$t_{\text{Nb cap}}$[Å]	95.4±4.2	101±5	61.7±2	97.1±3	52.1±4
t_{U} [Å]	363±5.6	635±6.8	771±6.3	1477±10	2289±12
$t_{\text{Nb buffer}}$ [Å]	155±2	180±4	146±2.6	142±5.4	172±2.1
$\sigma_{Nb_2O_3}$[Å]	13.5±1.2	12.2±3.2	11.8±2.4	6.3±1	11±2.4
$\sigma_{\text{Nb cap}}$[Å]	11.1±2	20.6±1.5	33±3.4	8.5±1.2	7.3±3.1
σ_{U}[Å]	10.2±2.1	8.3±2.5	19.7±4.3	3.4±1.1	3.6±0.8
$\sigma_{\text{Nb buffer}}$[Å]	6.6±2.3	7.7±1.8	4.7±1.3	10.2±1.1	7.9±2.8

Table 3.3: The layer thicknesses, t, and roughnesses, σ, used to fit the X-ray reflectometry curves seen in Figures 3.4 and 3.5

3.4 Characterisation of film crystallinity using high-angle X-ray diffraction

3.4.1 Varying Nb thickness

Figure 3.6 shows longitudinal X-ray scans from the samples listed in Table 3.2. The U(110) and Nb(110) peaks are clearly visible at or near $Q = 2.45$ and $Q = 2.70$ respectively, along with reflections from the $(11\bar{2}0)$ reflection from the sapphire substrate at $Q = 2.63$. We can see that the sapphire reflection has two components, which are due to the kα_1 and kα_2 components to the incident radiation, which differ slightly in wavelength.

The data is strongly thickness-dependent. For the thinnest samples, Pendellösung fringes are clearly visible around both the Nb and U peaks, but their amplitude of oscillation

decreases as thickness is increased until they are barely visible for the thickest samples. This is an indicator that the structural coherence of the crystal layers decreases as Nb thickness is increases.

As might be expected, the intensity of the Nb peak increases as thickness is increased, reflecting the increased scattering volume of the material. For the two thinnest samples, there is no distinct Nb peak visible above a broad background peak, which we attribute to the Nb capping layer, which is deposited at low temperature and therefore highly-disordered and poly-crystalline[119].

Along with the increase in intensity, there is also a narrowing of the peak and a movement of the peak centre towards higher Q_z values as thickness is increased. Peak broadening in this scan direction is most often associated with size and strain broadening, as discussed in section 2.4.1, and there is likely to be a reduction in the strain in Nb layer as the thickness is increased. This is because strain in the Nb layers at the interface between the Nb layer and the sapphire, due to the difference in the lattice parameters of the two layers, is released by the introduction of dislocations and other defects as the film thickness increases. More defects are formed at large thicknesses since the activation energy for dislocation formation is offset by an increase in the total strain energy, which is dependent on the film volume.

The variation in the peak position might also due to the strain in the film. The tensile strain in-the-plane of the film causes a contraction in the out-of-plane direction as described by the equations of elasticity[196]. This would lead to the movement of the peak to a larger Q_z-value in moving from from the thinnest, most highly-strained films to thicker layers. However, above 156 Å thickness, there is a movement of the peak away from the bulk value, which is likely to be due to increasing defect density[121] or strain. A quantitative discussion of these effects is given in Section 4.2.1.

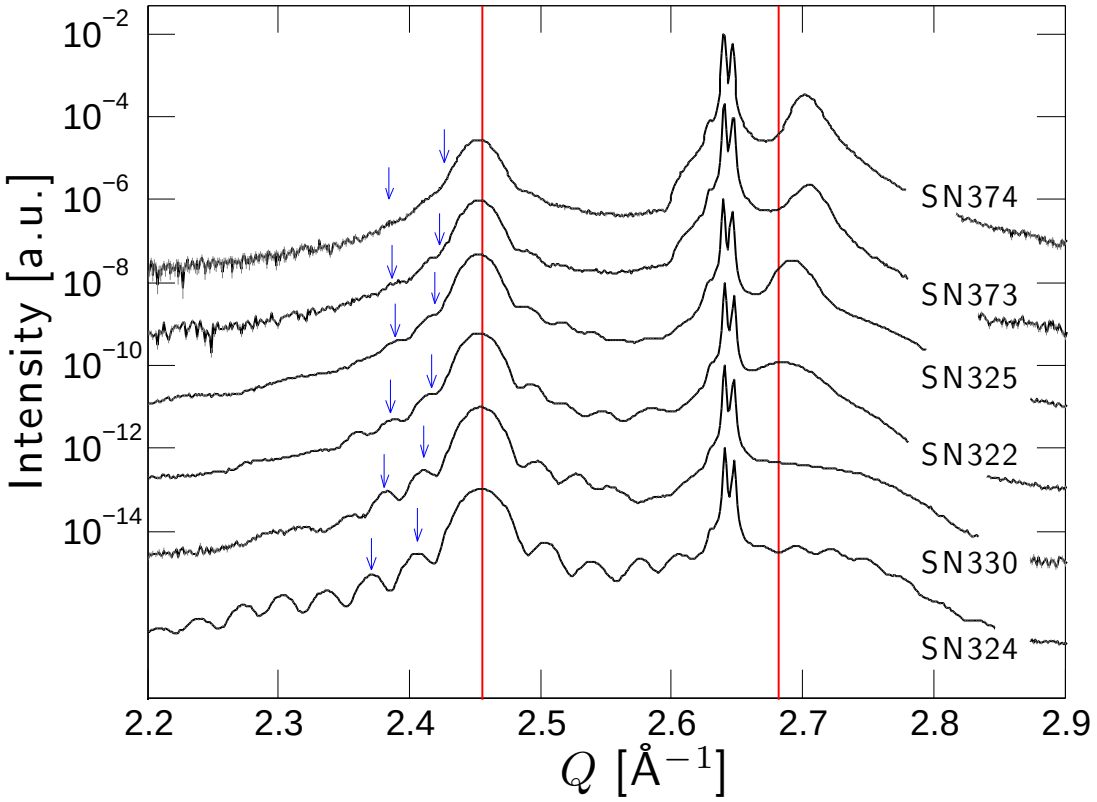

Figure 3.6: Longitudinal scans across the U(110) and Nb(110) Bragg peaks for the varying Nb-thickness sample series. The scans have been displaced in intensity for clarity. The blue arrows indicate the positions of Pendellösung fringes. The red lines at $Q_z = 2.456$ and 2.6817 Å^{-1} are guides to the eye, at the peak positions for bulk U and Nb respectively.

3.4.2 Determination of the coherent crystalline film thickness

3.4.2.1 Estimation from peak widths

Measurement of the full-width at half-maximum of the Bragg peaks in the above longitudinal scans gives an estimate of the coherence length in the out-of-plane direction. This is important in order to ascertain whether the film layers are a single crystal block throughout their thickness. The measurements for the Nb layers, along with the implied thicknesses are given in Table 3.4 for the varying Nb layer thickness series, and in Table 3.5 for the varying U layer thickness series.

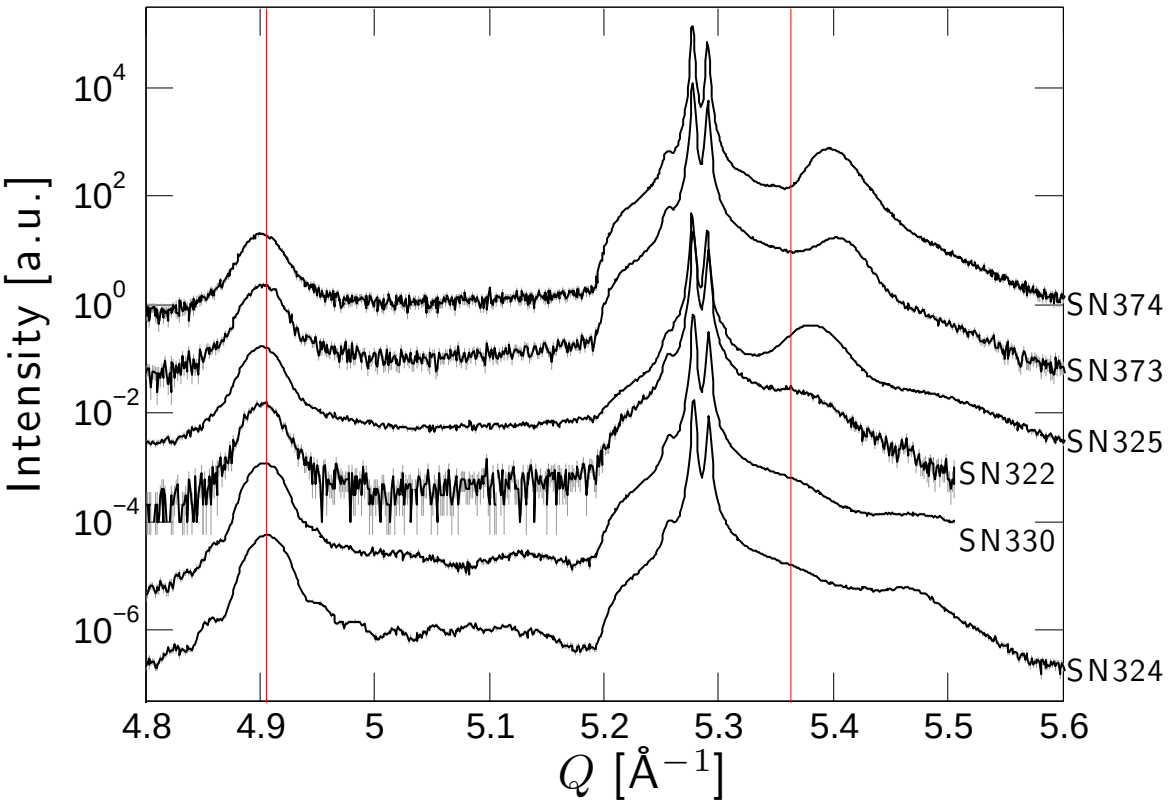

Figure 3.7: Longitudinal scans across the U(220) and Nb(220) Bragg peaks for the varying Nb-thickness sample series. The scans have been displaced in intensity for clarity. The red lines at $Q_z = 4.912\,\text{Å}^{-1}$and $5.364\,\text{Å}^{-1}$are guides to the eye, at the peak positions for bulk U and Nb respectively. The low intensity at the position of the sapphire reflection for sample SN325 is due to alignment of the sample in ω slightly off the narrow sapphire peak. Counting times per data point differ between samples, leading to increased background intensity relative to the peaks at short counting times, for sample SN330 in particular.

There is a large amount of uncertainty in the estimates for the Nb. This is due to a large contribution from background intensity; it is difficult to separate the intensity from the polycrystalline cap from that due to the crystalline portions of the buffer layer.

For the U layers we see that a significant portion of the nominal thickness is crystalline. Comparing these thicknesses to those found by reflectometry in Tables 3.2 and 3.3, which take into account both crystalline and amorphous regions of the layers, we see that between 50 and 75% of the layer thickness is scattering coherently at low U thicknesses. As the U

Nb Nominal thickness [Å]	2000	1000	500
Nb(110) FWHM [$Å^{-1}\times10^2$]	0.92 ± 0.006	1.07 ± 0.01	1.11 ± 0.02
Nb(220) FWHM [$Å^{-1}\times10^2$]	1.49 ± 0.01	1.67 ± 0.02	1.86 ± 0.9
Nb(110) Coherence length [Å]	109.14 ± 7.0	93.25 ± 9.5	89.94 ± 6.9
Nb(220) Coherence length [Å]	67.06 ± 18.3	59.91 ± 4.0	53.7 ± 13.1
U Nominal thickness [Å]	150	150	150
U(110) FWHM [$Å^{-1}\times10^2$]	1.13 ± 0.03	1.09 ± 0.019	1.07 ± 0.01
U(220) FWHM [$Å^{-1}\times10^2$]	1.26 ± 0.02	1.29 ± 0.02	1.19 ± 1.18
U(110) Coherence length [Å]	88.88 ± 2.5	91.84 ± 1.6	93.58 ± 0.93
U(220) Coherence length [Å]	79.40 ± 0.71	77.63 ± 0.69	83.71 ± 41.41
Nb Nominal thickness [Å]	350	150	30
Nb(110) FWHM [$Å^{-1}\times10^2$]	2.16 ± 0.08	4.71 ± 0.05	5.47 ± 0.07
Nb(220) FWHM [$Å^{-1}\times10^2$]	5.00 ± 0.91	4.50 ± 0.02	4.61 ± 0.03
Nb(110) Coherence length [Å]	46.33 ± 11.6	21.22 ± 2.2	18.28 ± 2.3
Nb(220) Coherence length [Å]	19.98 ± 21.8	22.24 ± 0.5	21.67 ± 8.0
U Nominal thickness [Å]	150	150	150
U(110) FWHM [$Å^{-1}\times10^2$]	1.16 ± 0.01	1.15 ± 0.01	1.29 ± 0.01
U(220) FWHM [$Å^{-1}\times10^2$]	1.29 ± 0.61	1.16 ± 0.004	1.21 ± 0.01
U(110) Coherence length [Å]	86.50 ± 0.87	86.92 ± 0.56	77.47 ± 0.82
U(220) Coherence length [Å]	77.73 ± 18.30	86.08 ± 0.16	82.62 ± 0.22

Table 3.4: The out-of-plane crystalline coherence lengths for the Nb and U layers estimated from the peak widths of the Nb and U peaks at the (110) and (220) positions.

thickness is increased, however, the coherent thickness appears to approach asymptotically a ceiling of around 370 Å.

Taking into account the fact that the relatively low resolution of the instrument means that these are lower bounds on the coherent film thickness, we conclude that the uranium layers, in particular, are of excellent crystalline quality.

3.4.2.2 Modelling the data

An alternative approach is to simulate the scattering from crystal blocks of the expected thickness and refine the model by comparison with the data until the simulation reproduces

Nb Nominal thickness [Å]	150	150	150	150
Nb(110) FWHM [$Å^{-1}\times10^2$]	0.89 ± 0.57	1.84 ± 0.27	1.53 ± 0.26	1.74 ± 0.07
Nb(110) Coherence length [Å]	112.0 ± 36	54.4 ± 4.0	65.4 ± 5.6	57.4 ± 1.1
U Nominal thickness [Å]	2000	1000	750	500
U(110) FWHM [$Å^{-1}\times10^2$]	0.27 ± 0.01	0.28 ± 0.01	0.32 ± 0.004	0.39 ± 0.003
U(110) Coherence length [Å]	369.3 ± 6.0	356.9 ± 3.2	312.9 ± 1.7	257.6 ± 0.9
Nb Nominal thickness [Å]	150	150	150	150
Nb(110) FWHM [$Å^{-1}\times10^2$]	1.86 ± 0.04	2.13 ± 0.05	1.50 ± 0.01	41.66 ± 0.02
Nb(110) Coherence length [Å]	53.8 ± 0.6	46.9 ± 0.6	66.7 ± 0.3	60.2 ± 0.4
U Nominal thickness [Å]	350	150	75	50
U(110) FWHM [$Å^{-1}\times10^2$]	0.46 ± 0.003	1.03 ± 0.01	1.74 ± 0.03	3.01 ± 0.03
U(110) Coherence length [Å]	217.9 ± 0.7	97.5 ± 0.6	57.4 ± 0.5	33.3 ± 0.15

Table 3.5: The out-of-plane crystalline coherence lengths for the Nb and U layers for the varying uranium layer thickness series, estimated from the peak widths of the Nb and U peaks at the (110) positions.

the data as much as possible to the required accuracy. A simple model using the Laue function has been applied to the current data, similar to the approaches of Gibaud *et al* [117] and Stierl *et al* [112]. We have also introduced a factor to account for the roughness of the interfaces by assuming a Gaussian distribution of the number of scattering planes with mean N_0 and variance σ, similar to that used by Sürgers *et al* [119], giving the intensity from a single layer with lattice spacing d:

$$I(Q) = \exp(-q^2\sigma^2) \sum_N (1/\sigma) \exp\left[-\frac{(N-N_o)^2}{\sigma^2}\right] \frac{\sin^2(QNd/2)}{\sin^2(Qd/2)}. \tag{3.1}$$

Fits to the data that show clear fringes are shown in Figure 3.8, with a separate Laue function being used for the U and Nb layers, and narrow Lorentzian-squared peaks used to model the kα_1 and α_2 scattering from the sapphire substrate.

The two parameters that are obtained most reliably are the lattice spacing for each layer, as this determines the position of the peak, and the number of lattice planes, as this determines the spacing of the fringes as well as the breadth of the primary peak. However,

in the absence of visible fringes the number of lattice planes is much more difficult to determine, leading to a several reasonable fits with quite different parameters.

There is evidently some broadening that is unaccounted for in the model, especially since the sharp minima between fringes in the model is not seen in the data. The damping of the oscillations is best modelled in the thinnest sample, but it was impossible to reproduce the intense fringes seen over the Nb peak position. The broadening at the Nb position is also impossible to model, but a large expected contribution from the polycrystalline capping layer is not included in the model. We also expect the Nb layer to be more highly strained at the substrate/niobium layer interface, and that this strain is decreasing with distance from the interface, leading to an asymmetric broadening of the peak that makes a deduction of the number of scattering planes difficult. It would be possible to account for this broadening by including a distribution of lattice spacings along the strain gradient in the model, but such a treatment remains beyond the scope of this thesis.

The layer thicknesses and roughnesses used in the model to fit the curves shown in Figure 3.8 are given in Table 3.6, along with the layer thicknesses for each layer implied by the values of N_0 and d.

The thicknesses for the Nb layer agree with the reflectometry data, but mostly the uncertainty is so large as to make the results of little use. There is a monotonic increase in the thickness of the U layer given by the model, which mirrors the trend found by analysing the period of the Pendellösung fringe spacings in the previous section.

Again, this simplified model gives only an estimate of the coherent crystalline thickness. As seen in the following section, the microstructure of the films varies considerably, and only a full simulation that takes into account the presence of defects and inhomogeneous strains in the samples will give reliable film parameters. Hence, we shall give more weight to the thicknesses found using the sophisticated modelling process in Section 3.3.1.1. Furthermore, these thicknesses may in general be more reliable since the reflectometry process at low Q is less sensitive to the presence of microstructural defects. However, we consider

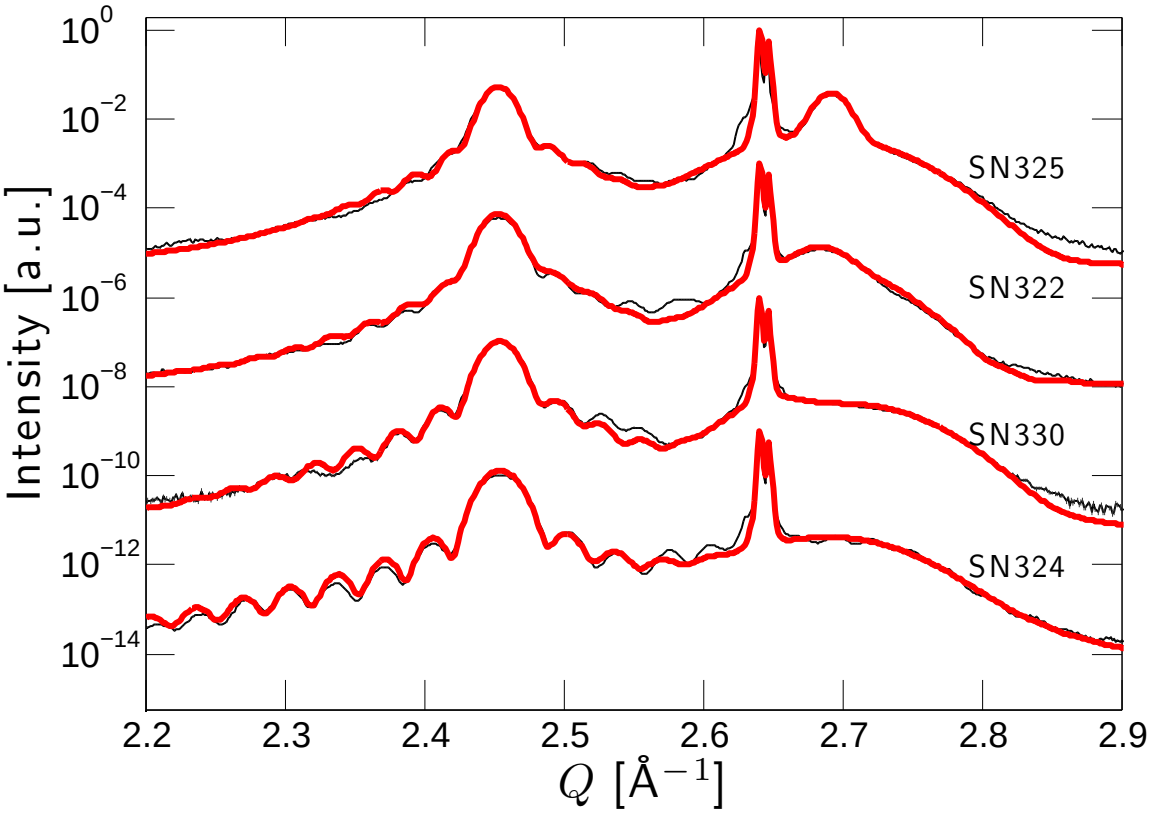

Figure 3.8: Longitudinal scans across the U(110) and Nb(110) Bragg peaks for the varying Nb-thickness sample series. The scans have been displaced in intensity for clarity. The red lines are fits to the data to a model as described in the text.

Sample	SN243	SN282	SN322	SN323
$d_{\mathrm{U}(110)}$[Å]	2.560±0.003	2.560±0.003	2.5605±0.001	2.561±0.001
$N_{\mathrm{U}(110)}$	72±3	85±2	92±3	96±3
$\sigma_{\mathrm{U}(110)}$[Å]	1.7 ±3	5±4	6±3	8±3
$\Rightarrow t_{\mathrm{U}}$[Å]	184±5.8	218±6.9	236±7.4	246±7.8
$d_{\mathrm{Nb}(110)}$[Å]	2.34±0.02	2.33±0.01	2.340±0.003	2.340±0.003
$N_{\mathrm{Nb}(110)}$	14 ± 4	28 ± 8	70±10	140±40
$\sigma_{\mathrm{Nb}(110)}$[Å]	8.1±3	11.0±4	11.5±4	16.2±5
$\Rightarrow t_{\mathrm{Nb}}$[Å]	32.8±8	65.2±17	163.8±42	327.6±85

Table 3.6: The parameters used for the fits to the data seen in Figure 3.8. Here, $d_{\mathrm{M}(hkl)}$, $N_{\mathrm{M}(hkl)}$ and $\sigma_{\mathrm{M}(hkl)}$ are the hkl lattice spacing, the number of lattice planes and the layer roughness of the metal, M, layer.

that the wealth of information available in the high-angle, high-resolution X-ray diffraction profiles to be a great strength of the the technique, and excellent progress is being made in modelling profiles from thin films that include significant defects, such as in Boulle et al.[167], and Shreeman and Matyi[197], where a combination of dynamical and kinematic approaches is taken.

3.4.3 Varying U thickness

Longitudinal scans from samples of varying U thickness but constant nominal Nb buffer-layer thickness are shown in Figure 3.9. The behaviour of the scattering around the U peak is strongly-dependent on thickness, and follows what is expected from the behaviour of the Laue-function as the number of scattering planes is increased, as will be seen below. The breadth of the peak decreases and its shape changes to become a sharper peak as thickness is increased. Pendellösung fringes are visible at nearly all thicknesses, and their periodicity decreases as thickness is increased. At the largest thicknesses the peak becomes very narrow and the two peaks resulting from scattering of Cu kα_1 and kα_2 radiation may be distinguished.

There is little movement of the peak as thickness is increased, although the peaks from the thinnest two samples are shifted in the positive Q direction from the bulk position, implying a contraction of the U(110) lattice planes and a tensile misfit strain. For these samples the thickness of the buffer layer is around twice that of the U layer, so is able to exert a net strain. For thicker samples the buffer layer is able to exert decreasing strain on the U layer, especially since uranium is stiffer than niobium.

There does not appear to be a monotonic dependence of the shape of the scattering around the Nb(110) position on the U thickness, although its intensity is diminished at large U thicknesses, probably due to the absorption of scattering from the buffer layer by the thick U layer.

Sample	SN243	SN282	SN322	SN323
$d_{\mathrm{U(110)}}$[Å]	2.55±0.01	2.557±0.002	2.560±0.002	2.560±0.002
$N_{\mathrm{U(110)}}$	28±3	48±1	90±4	180±10
$\sigma_{\mathrm{U(110)}}$[Å]	3±2	4±3	5±4	10±2
$\Rightarrow t_{\mathrm{U}}$[Å]	71.4±3.8	122.7±6.5	230±12	461±24
$d_{\mathrm{Nb(110)}}$[Å]	2.330±0.005	2.336±0.003	2.340±0.002	2.330±0.002
$N_{\mathrm{Nb(110)}}$	80 ± 10	75 ± 5	70±5	70±2
$\sigma_{\mathrm{Nb(110)}}$[Å]	1±0.5	6±4	2±1	0.5±0.4
$\Rightarrow t_{\mathrm{Nb}}$[Å]	186±14	175.2±13	163.8±12.5	163.1±12.4

Table 3.7: The layer-thicknesses and roughnesses found by simulation of the XRD, leading to the fits to the data in Figure 3.10.

Clear Pendellösung fringes are only seen around the Nb(110) position in the 117 Å and 69 Å U samples. This is evidence of high crystalline quality in these samples.

Fitting the model described in Section 3.4.2.2 has a certain degree of success at low U thicknesses, but again differs from the reflectivity data for all but the thinnest sample. It is of course an unsophisticated model, and does not take into account scattering from disorder, which leads to broadening of the peaks and decreases in the intensity of the fringes. The model might be modified to include a broad peak at each Bragg position to take this into account, and an analysis of the broadening due to disorder could follow, but it would be difficult to separate the effect of size broadening in these longitudinal scans. A simpler analysis is possible using transverse scans, and an investigation along these lines follows in Chapter 3.

3.5 Indication of strain-relief by film buckling using AFM

Figure 4.8 shows the film-surface relief using atomic-force microscopy. Distinct ripples are seen in the surface of the films. The peak-to-trough height is approximately 5 nm. This is likely to be a strain relief phenomenon, such as described in Jiang et al. [198]. Further discussion is given in Section 4.2.2.5.

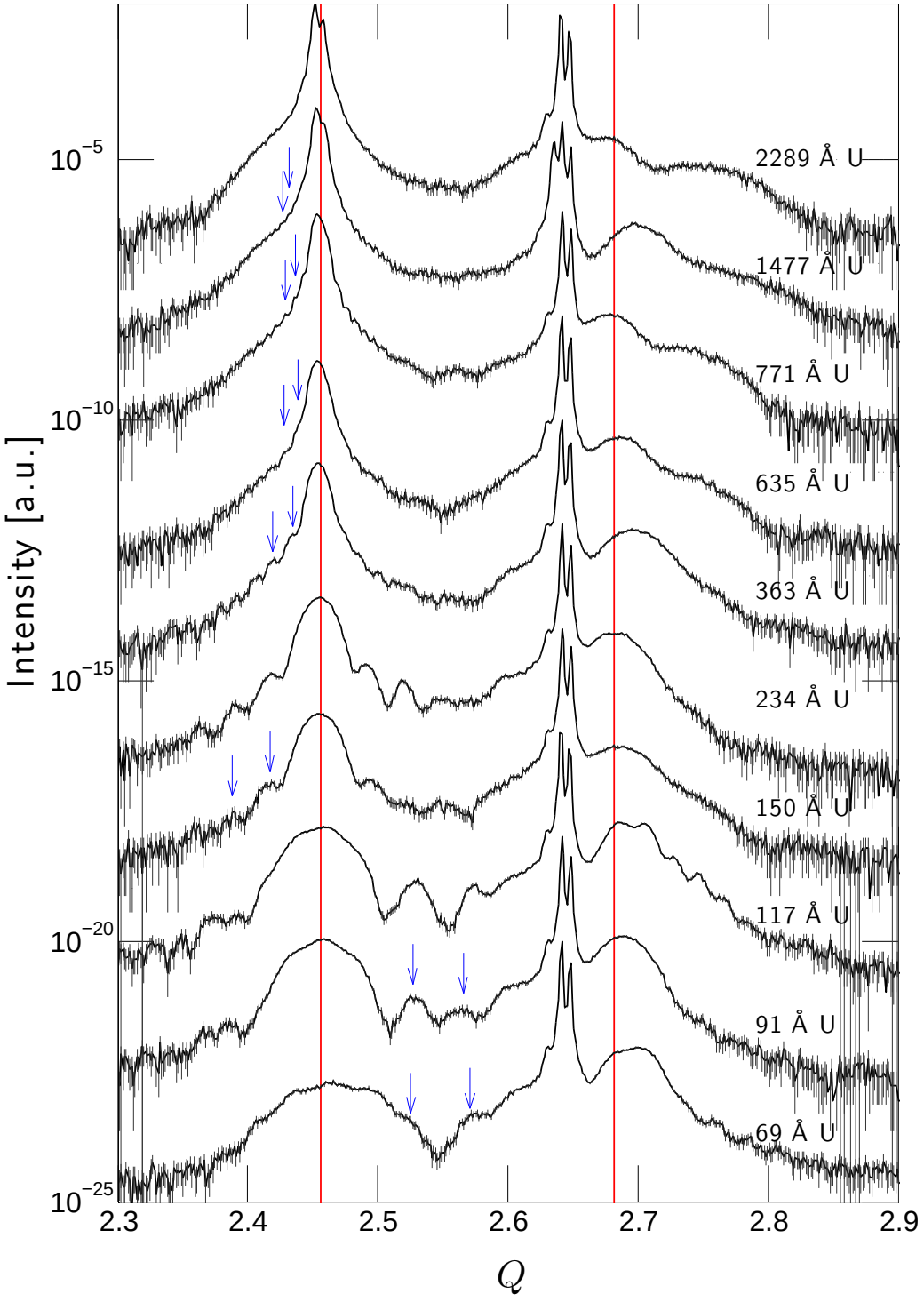

Figure 3.9: Longitudinal scans across the U(110) and Nb(110) Bragg peaks for the varying U-thickness sample series.The blue arrows indicate the positions of Pendellösung fringes. The red lines at $Q_z = 2.456$ and 2.6817 Å^{-1} are guides to the eye, at the peak positions for bulk U and Nb respectively.

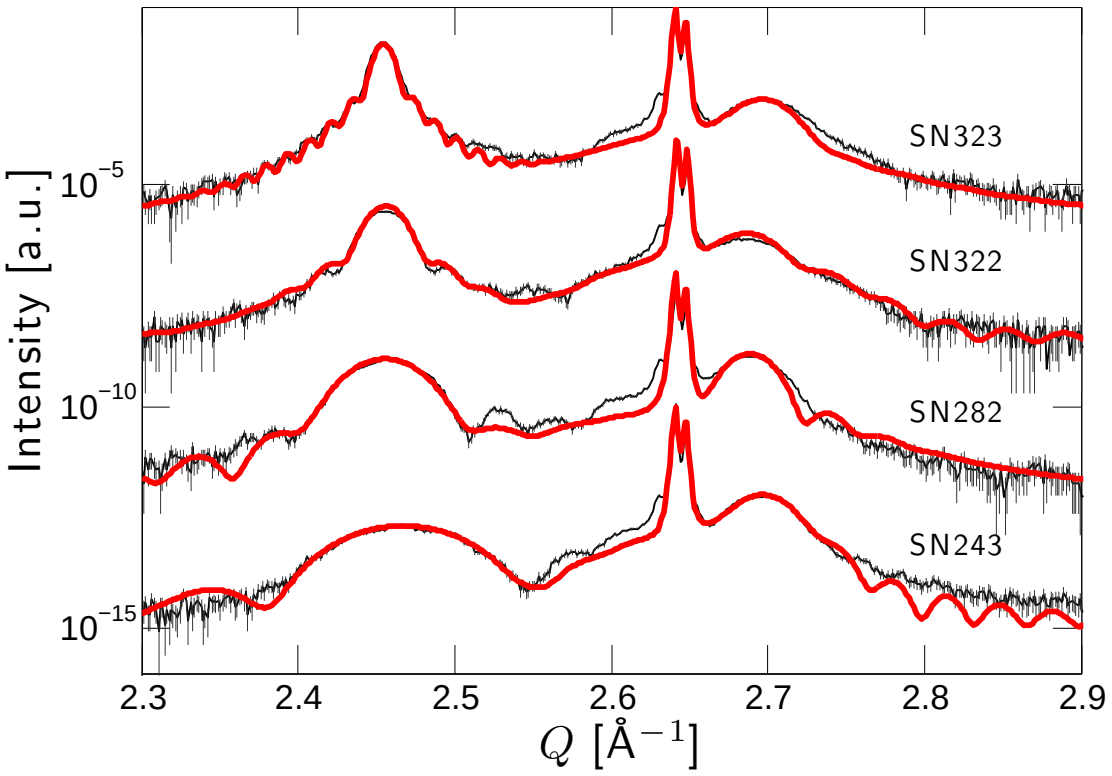

Figure 3.10: Longitudinal scans across the U(110) and Nb(110) Bragg peaks for the varying U-thickness sample series. The red lines are fits to the data as desctribed in the text.

3.6 Summary

We have grown very high quality uranium thin-films, which have a large crystalline thickness. We have determined the component layer thicknesses using X-ray reflectometry, which is straightforward experimentally, but the analysis of the results has been difficult. Real-space thickness-determination methods might be more appropriate for future samples. Initial measurements using AFM show that there is some buckling of the film surfaces, which may be due a stress-relaxation effect.

In the following chapter we shall follow more extensive analysis of high-angle XRD data in order to build up a picture of the microstructure of the films, and how it is affected by changing layer thickness.

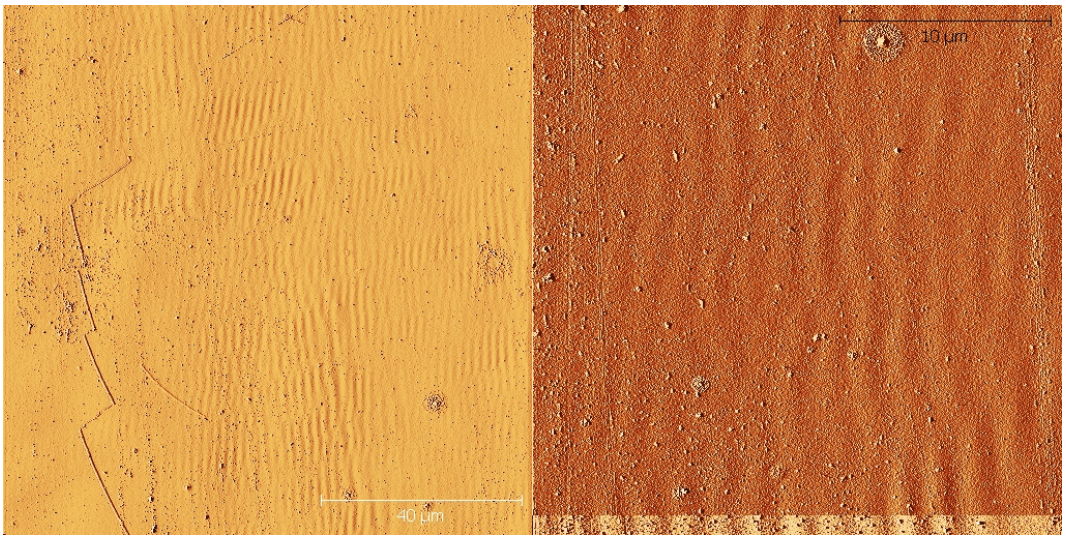

Figure 3.11: Atomic-force micrographs showing surface waves on the surface of sample SN322 of period approximately 1.6 μm. The field of view of the left panel is 100 μm, and 25 μm for the right panel. Images were taken at UCL using a Bruker Veeco Dimension 3100 in non-contact mode at 300 K, with the assistance of P. Cullen and D. Buckley.

Chapter 4

Microstructural characterisation of epitaxial uranium films

4.1 Experimental approach

4.1.1 Longitudinal scans

By comparing the positions of the niobium and uranium reflections on longitudinal scans to the bulk position, we may deduce the magnitude and sense of the misfit strain in the out-of-plane direction. By an assumption of maintenance of constant volume of the unit cell in each material this will allow us to deduce the sense and magnitude of the epitaxial strain in-the-plane of each layer.

The behaviour of the scattering in the longitudinal direction as q_x is varied will show the spatial extent of the layers that contribute to the broad and narrow components in these samples, allowing us to distinguish between the presence of a pseudomorphic component of the film and a condition of long-range orientational order.

4.1.2 Transverse scans

As mentioned above, the most common measure of film quality from rocking curves is the mosaicity, given as the full-width at half-maximum (FWHM), and is a gross measure of film quality. We shall examine the effect of the film thickness on the breadth of the rocking curve. An analysis of similar systems by Wildes *et al*[118] found a phenomenological power-law relationship between the breadth of the curves, κ, and the film thickness, d, such that $\kappa = Ad^x$, with $x = -0.68 \pm 0.08$. A quantitative analysis of the scattering from isolated dislocations using the Krivoglaz theory of diffraction from disordered crystals[175] by Barabash *et al*[120] predicted a $d^{-0.8}$ dependence on thickness.

We shall extend this analysis by considering the dependence of the peak broadening on Q. An analysis of the dependence of the intensity of the narrow component of the scattering on Q will allow us to determine the degree of uncorrelated disorder in the samples, whilst consideration of the Q-dependence of the broadening of the broad component will allow the separation of Q-dependent and Q-independent contributions through the use of the Williamson-Hall-like plot.

In addition, we shall fit a variety of functional forms to the broad components of the rocking curves such that we may further determine the broadening mechanisms and their microstructural origin, and how these depend on film thickness.

Finally, the computation of the aspect ratio of the peaks in 2D (i.e. the ratio of the radial breadth and the transverse breadth) will allow the evaluation of the proportions of the two dislocation systems present (90° or 60° dislocations)[121].

Sample	SN324	SN330	SN322	SN325	SN374	SN373
Nominal buffer thickness [Å]	50	150	350	500	1000	2000
Nominal U thickness [Å]	150	150	150	150	150	150
Nb buffer [Å]	31.4	61.1	157	306	598	1274
U layer [Å]	186	161	155	156	127	109

Table 4.1: The composition of samples of fixed nominal U-thickness grown in order to investigate the influence of Nb-layer thickness on the microstructure of U thin-films. All samples were deposited by UHV magnetron sputtering onto A-plane $(11\bar{2}0)$ sapphire substrates

4.2 The influence of the buffer-layer thickness on microstructure

It has been noted by previous researchers[118] that the rocking curves over Nb structure peaks obtained from Nb films grown on sapphire are strongly dependent on thickness, with changes both in the line shape and peak breadth as the layer-thickness is changed. The relative intensity of the broad feature is seen to increase with film thicknesses, from contributing a small proportion of the total intensity at low niobium thicknesses to overwhelming the narrow component in thick films (over 5000 Å) such that the narrow component is no longer seen. We aim to investigate further the effect of changing the thickness of the niobium buffer layer on the microstructure of the niobium and uranium layers. In addition we shall develop an in-depth description of the microstructure of the films for use in the following chapter.

4.2.1 Misfit strain

An analysis of the peak positions in the longitudinal scans shown in Section 3.4.1 gives the mean strain in the d_{110} lattice spacings for Nb and U for samples of differing Nb thickness as shown in Figure 4.1. Measurements are made at the (220) peak positions for increased resolution in reciprocal space, for a given angular resolution, that at the (110) position.

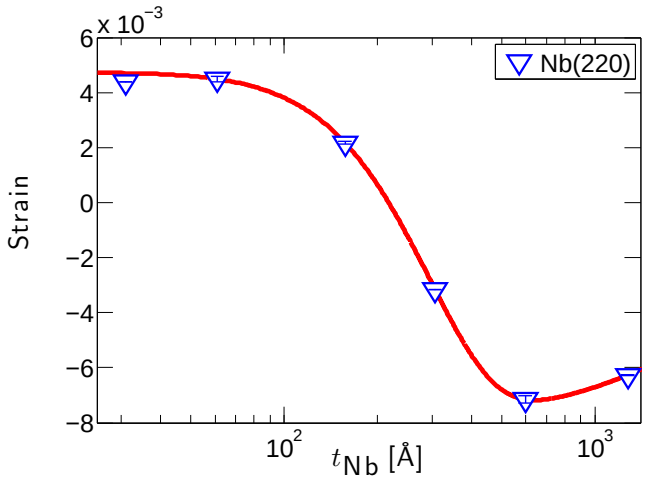

Figure 4.1: The mean strain in the d_{110} lattice spacings for the Nb layers, as deduced from the positions of the Nb(220) Bragg reflections. The red-line is a least-squares fit of the data to a Gaussian function, and is a guide to the eye.

For thin layers the Nb is under a tensile strain in the [110] direction, yet as the thickness increases the strain is released by around 200 Å thickness. As the Nb layer thickness is increased beyond this, however, the movement of the peak is such that the layer appears to be strained in the opposite direction.

The mean strains in the d_{110} lattice spacings for the U layer for samples of differing Nb thickness are shown in Figure 4.2.

At large thicknesses the strain in the uranium layers is tensile as expected from the epitaxy model shown in Figure 1.5. At smaller Nb thicknesses, however, the strain in the U layers decreases, with a strong dependence on the strain in the Nb layer.

Comparing Figures 4.1 and 4.2 we see that the change in the buffer-layer thickness affects the Nb and U layers in opposite directions.

It is expected that as the layer thickness increases the mean strain in the layer decreases, since a greater proportion of the film thickness is in a relaxed state. This effect is seen in the current films below thicknesses of around 200 Å. However, since the epitaxial strain in the plane of the film is tensile[73], the strain in the out-of-plane direction is expected to be

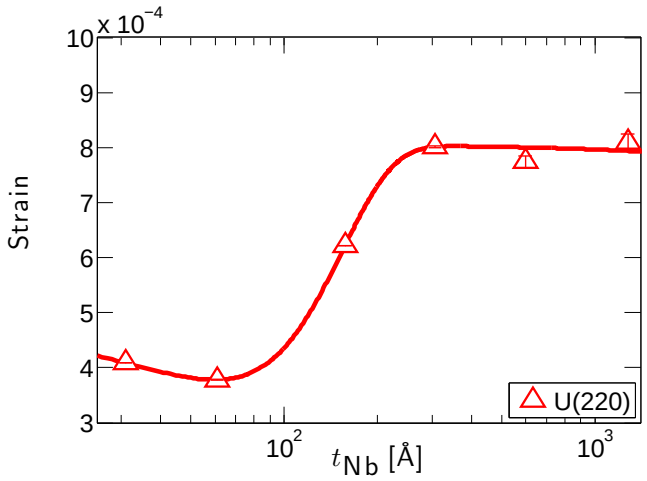

Figure 4.2: The strain in the d_{110} lattice spacings for the U layers, as deduced from the positions of the U(220) Bragg reflections

compressive, in order to conserve the volume of the unit cell, but this is only seen at larger thicknesses. It is noted that the thickness at which the change from tensile to compressive strain is close to the point at which the thicknesses of the two layers are equal, which suggests that the uranium layer is influencing the strain in the niobium layer. Uranium is stiffer than niobium and will exert a large influence on the niobium layer at these thicknesses. The expected strains might be estimated from a composite slab model [199].

Above this thickness the increase in the compressive strain as film thickness increases is also puzzling. There must be a movement towards the bulk state as thickness is increased, and perhaps the decrease in strain above 1000 Å is the beginning of this regime.

For thin Nb layers, the epitaxial strain of the Nb on the sapphire should improve the epitaxy of the uranium, as the compressive epitaxial strain on the uranium from thick Nb layers is reduced by the tensile effect of the sapphire on the niobium at small Nb thicknesses. This argument does not, however, agree with the the sense of the strain in the Nb at the thinnest thicknesses.

4.2.2 Transverse Scans

4.2.2.1 Nb(110)

ω-rocking curves performed at a fixed 2θ angle, corresponding to the Nb(110) Bragg-reflection, at UCL using Cu kα radiation, for six samples of fixed U-layer thickness but varying Nb-layer thickness, as described in Table 4.1 are shown in Figure 4.3. The shape of the curves is strongly dependent on the Nb thickness. For the thinnest samples, all three components are present: a central, narrow δ-like Bragg peak superimposed on a broad diffuse peak, and at intermediate intensity, symmetrically-spaced satellite peaks of finite breadth.

As the Nb thickness is increased the intensity of the broad component increases and the relative intensity of the narrow component decreases along with that of the satellite peaks. The character of the peak also changes as the Nb-layer thickness is increased. The line-shape becomes more Gaussian as the 'tails' at larger q_x values become less prominent, and the 'shoulders' at close to the peak intensity become more pronounced. These qualitative descriptions will be extended into a quantitative description below.

Significantly, the narrow component of the scattering is still present in the thickest Nb-layers. This is associated with a high-degree of order in the out-of-plane direction[118], along with a low density of defects, such as dislocations[121].

As the Nb thickness increases, the breadth of the broad component decreases. This indicates an increase in the correlation-length for the scattering that is responsible for the broadening of the peak.

Narrow satellite peaks symmetrically spaced around the central peak are also seen, such as for the sample shown in Figure 4.4. These peaks are present for a number of samples, and often comprise a significant proportion of the scattering intensity. There is only one strong order present, although some samples present oscillations in intensity that suggest

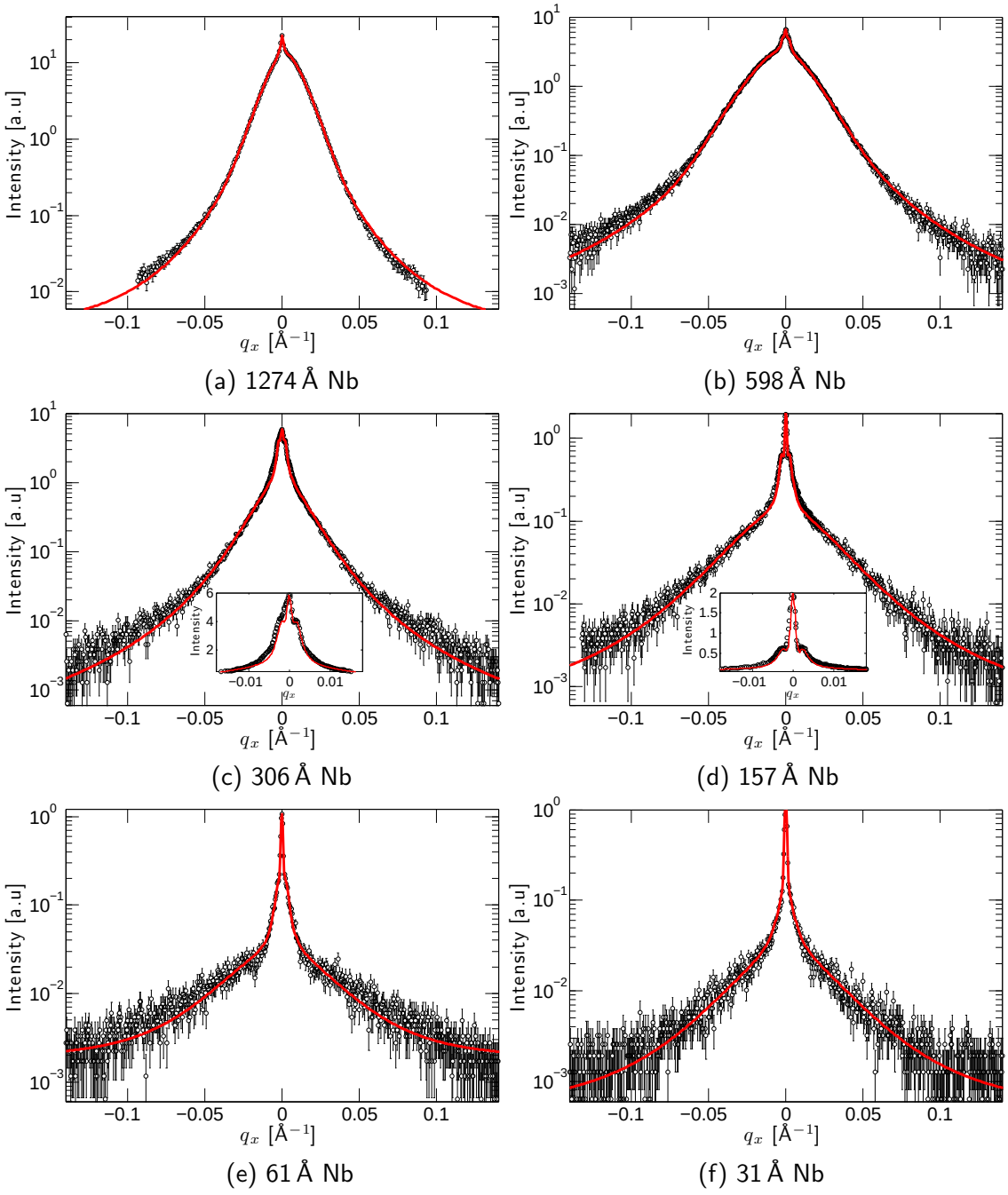

Figure 4.3: Transverse scans across the Nb(110) peak for the samples described in Table 4.1. Narrow and broad components are seen at all thicknesses, but the relative intensity of the broad component decreases with decreasing thickness. At low thicknesses symmetrically-spaced satellite peaks are seen. The intensities have been normalised by the peak value of the 31 Å sample to allow comparison of intensities. The red lines are least-squares fits to a model as described in the text.

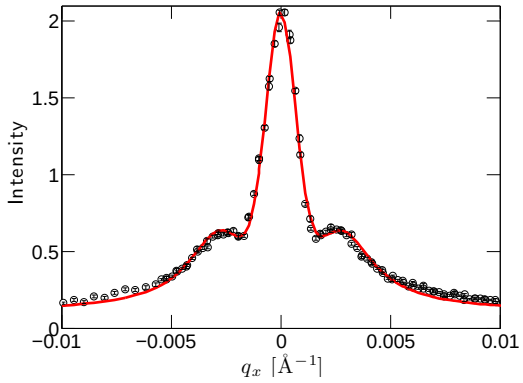

Figure 4.4: Narrow transverse scan across the Nb(110) peak for a 150 Å Nb, 350 Å U thin-film (SN322, in Table 4.1), showing satellite peaks at $q_x \approx \pm 0.0025$. The red line is a least-squares fit to a model consisting of a Gaussian central peak and symmetrically-spaced Lorentzian peaks either side.

the presence of higher satellite orders.

4.2.2.2 Nb(220)

The scattering around the Nb(220) Bragg-peak for the same set of samples is shown in Figure 4.5. In comparison with the rocking curves at the Nb(110)-position, the narrow components appear broader in q_x, but are of similar breadth in angular space, scaling approximately with the instrumental resolution. Intensity due to the satellite peaks is present but reduced in significance at these higher angle positions.

4.2.2.3 U(110)

Rocking curves from the transverse scans over the U(110) peaks are shown in Figure 4.6. In a similar manner to the Nb structure peaks, the curves are very well fitted by the two-component model described above, especially for the thinner samples. In contrast to the Nb structure-peaks, however, the narrow component in the rocking curve is not present in films of thicknesses above 500 Å, which suggests that any disorder in the Nb layers is magnified in the U layers. Above this thickness the fit of the remaining broad component is

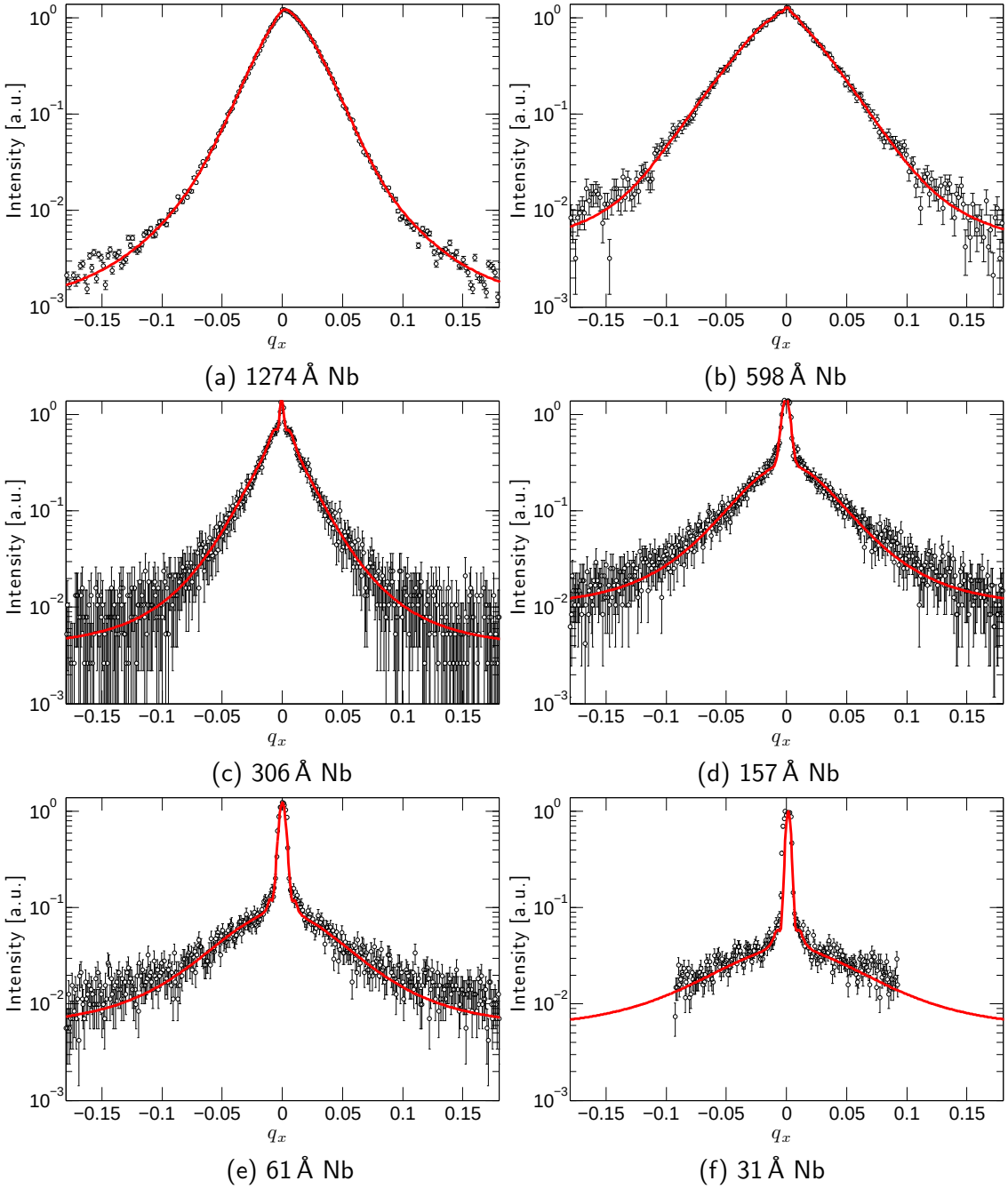

Figure 4.5: Transverse scans preformed at UCL across the Nb(220) peak for the samples described in Table 4.1. There is little sign of the narrow component for thicknesses greater than 306 Å. The intensities have been normalised by the peak value of the 31 Å sample to allow comparison of intensities.

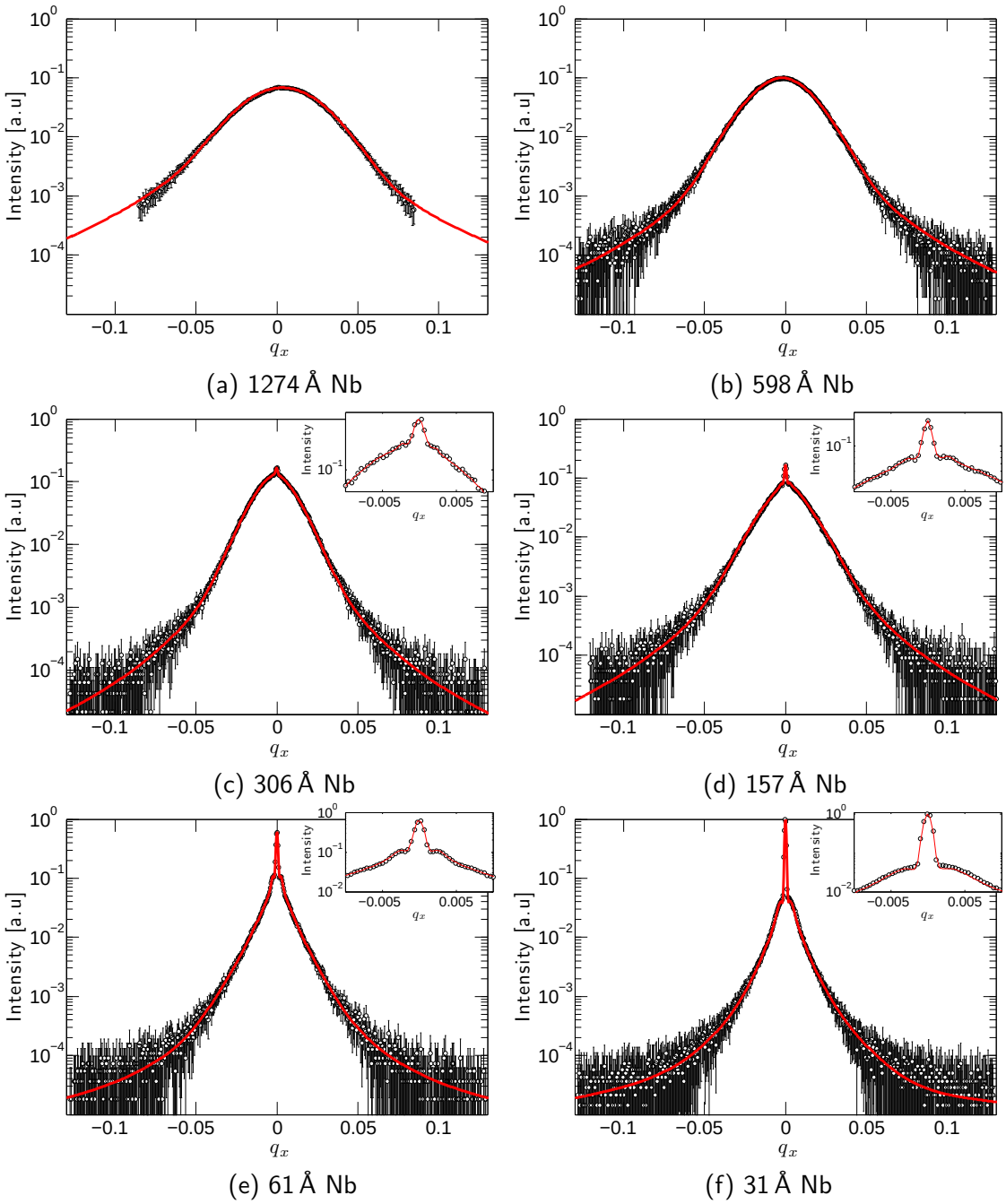

Figure 4.6: Transverse scans across the U(110) peak for the samples described in Table 4.1. Note the clear transition from a two-component lineshape at small thicknesses to a single component at large thickness. The intensities have been normalised by the peak value of the 31 Å sample to allow comparison of intensities.

less well-fitted by the Lorentzian-squared function, and its character becomes increasingly Gaussian as in[123]. The fits shown in Figure 4.6 give the correct FWHM and fit well smaller values of q_x, but the fit at larger values of q_x has been sacrificed to ensure accurate determination of the FWHM using this line-shape.

The satellites are prominent in the 61 Å Nb sample, and are seen at a displacement of 0.0025 $Å^{-1}$. There is little evidence of satellite peaks in the scans from the other samples.

4.2.2.4 U(220)

The narrow component is even less pronounced in the U(220) rocking curves, and not visible in films of greater than 350 Å. It is around twice as wide as for the the U(110) rocking curves; around 0.3 $Å^{-1}$.

4.2.2.5 The origin of the satellite peaks

Satellite peaks symmetrically spaced around the $q_x = 0$ position in reciprocal space have been seen in several studies[107,171]. The absence of higher satellite orders suggests that the satellites arise from a sinusoidal displacement of atoms along a particular direction in the plane of the film, analogous to a frozen optical phonon.

The presence of the satellites in the scattering from films of niobium grown on a-plane sapphire is discussed by Gibaud et al.[171]. The displacement arises from the miscut of the sapphire substrate, leading to vicinal terraces of regular depth. The sharp steps are 'washed-out' as material is deposited.

Satellites with a different origin have been observed by Wölfing et al.[107]. These satellites were at a larger value of $q_x \sim 0.43$, implying a periodicity of around 145 Å. This length was ascribed to the periodicity of the distortions arising from the semicoherent nature of the Nb/Al_2O_3 interface, with extra Nb lattice planes necessary at spacings of 20 Å in the

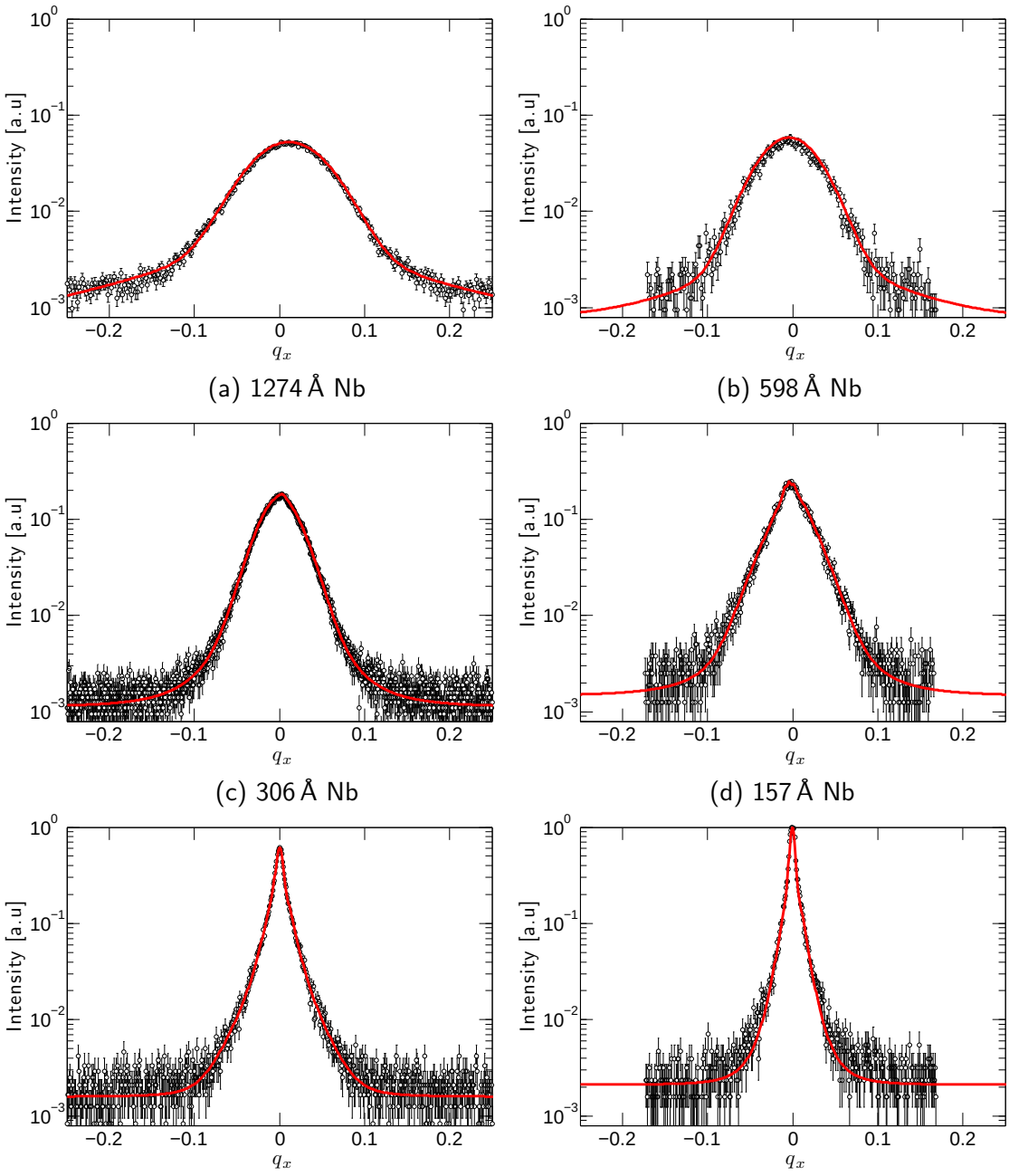

Figure 4.7: Transverse scans across the U(220) peak for the samples described in Table 4.1. The peaks from samples of low thickness have a two-component profile, but this is not as pronounced as at the (110) position. The intensities have been normalised by the peak value of the 31 Å sample.

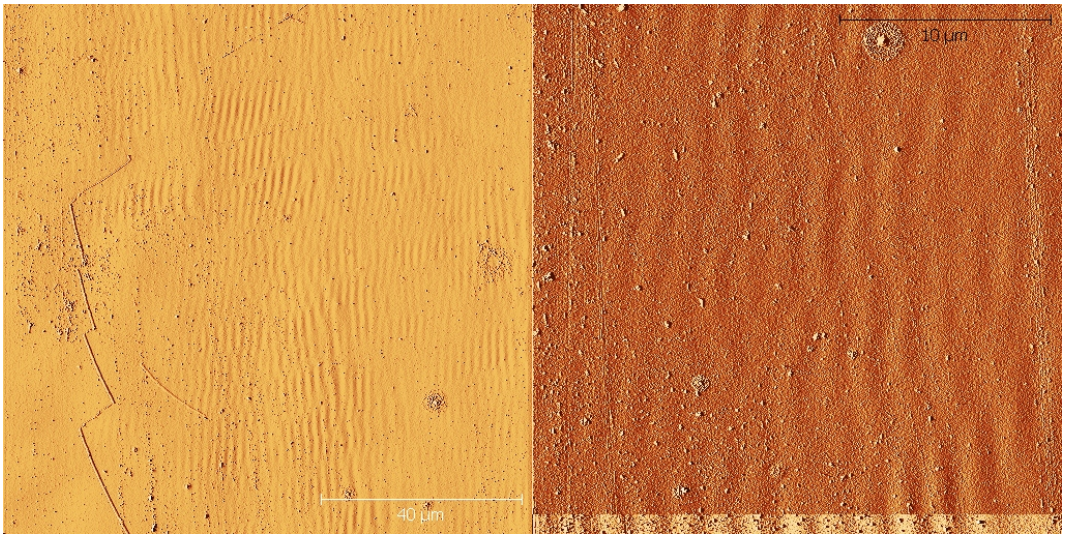

Figure 4.8: Atomic-force micrographs showing surface waves on the surface of sample SN322 of period approximately 1.6 μm. The field of view of the left panel is 100 μm, and 25 μm for the right panel. Images were taken at UCL using a Bruker Veeco Dimension 3100 in non-contact mode at 300 K, with the assistance of P. Cullen and D. Buckley.

[111]-direction and 160 Å in the [1$\bar{1}$1]-direction[115].

Satellite peaks or 'shoulders' on the line shapes at intermediate q_x are mentioned in Conchon[200, pp. 125] and Bentall et al.[123] and said to correspond to scattering from misfit dislocations randomly distributed and of low density.

In the current samples the satellites have a displacement in $q_x \approx \pm 0.0025$, which gives a real-space periodicity of 0.4 μm. Ripples on the surface of the film are visible in atomic-force micrographs, as seen in Figure 4.8.

Since the peak-to-trough height is approximately 5 nm, this feature is unlikely to arise from vicinal steps, which will be on the order of angstroms. This is likely to be a strain relief phenomenon, such as described in Jiang et al.[198].

The displacement of the satellites in q_x is the projection of the wave-vector of the distortion onto the component of the scattering vector in the plane, and is therefore dependent on the azimuthal angle, ϕ. This is verified by the changing position of the satellites in rocking

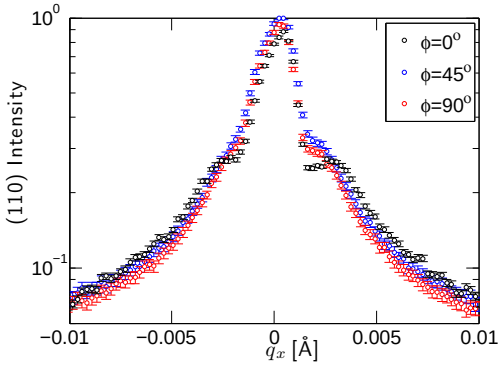

Figure 4.9: The satellite peaks' dependence on the azimuth angle, ϕ. $\phi = 0$ is along the $[0001]_{\text{sapphire}}$-direction. The sample is SN322, the same as Figure 4.4

curves taken at different azimuthal angles, as shown in Figure 4.9. Here, $\phi = 0$ is along the $[0001]_{\text{sapphire}}$-direction.

Further studies should ensure that rocking curves are performed at azimuthal positions where the intensity of the satellites is negligible. This will occur when the in-plane scattering vector is perpendicular to the wave-vector of the distortion that leads to the satellites' formation.

4.2.3 Analysis

4.2.3.1 Narrow component intensity — DWF

As the narrow component is resolution-limited we have used the peak heights in this analysis, so that it is not necessary to deconvolute the instrumental resolution function from the peak width in order to calculate the integrated intensities. As a check, the peak width at both the (110) and (220) positions was found to be similar to the nearby Bragg reflections from the highly-perfect sapphire substrate, which give a good measure of the instrumental width, disregarding any dynamical broadening effects due to the presence of the overlayer[197].

The values of static Debye-Waller factor, W, found for the various samples of varying Nb

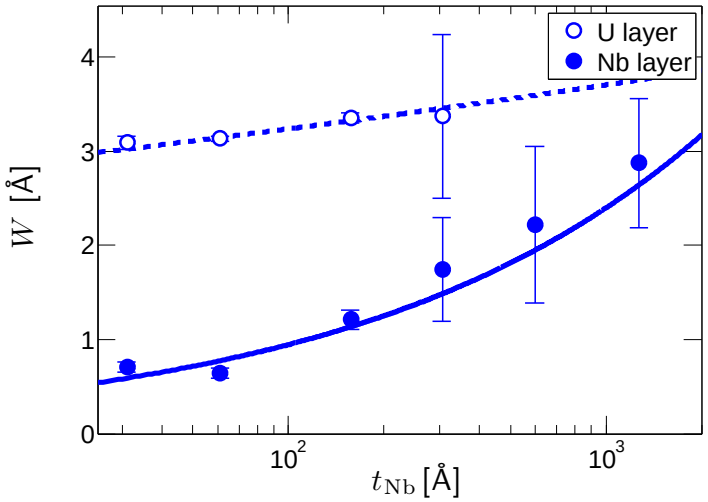

Figure 4.10: The Debye-Waller-like factor, W responsible for the attenuation of the narrow component of the U and Nb (110) and (220) peaks as a function of Q_z, as described in the text, for films of varying Nb thickness. The full and dashed lines are guides to the eye.

thickness are shown in Figure 4.10. We see a clear increase in the disorder represented by the static Debye-Waller factor as thickness is increased. The uncertainties in the data points at large thicknesses are due to the lack of intensity of the sharp component relative to the broad component at the (220) positions in these samples.

Further study should include a measurement of higher order Bragg-peaks which were unreachable using the current experimental set-up. Use of harder X-rays of shorter wavelength, for example those from a Mo kα source, would lead to Bragg scattering at lower angles.

For the U layer, wee see that the disorder in the atomic positions in the growth direction is consistently larger than for the Nb layer, but has less dependence on thickness.

4.2.3.2 The width of the broad component

As a starting point for our analysis, we shall follow that of Wildes *et al*[118]. The Wildes analysis modelled the broad component as a single function, a Lorentzian-squared. Our

Peak/Model	a [Å^{a-1}]	c
Nb(110)	0.46 ± 0.3	-0.43 ± 0.10
Nb(220)	0.48 ± 0.4	-0.33 ± 0.13
Wildes *et al*	0.23 ± 0.05	-0.51 ± 0.05
Barabash *et al*	Not given	-0.8 (predicted)

Table 4.2: The coefficients for the fits, FWHM$= a\, t_{\mathrm{Nb}}^{c}$, to the full-widths at half-maximum of the broad components of the Nb(110) and Nb(220) rocking curves as shown in Figure 4.11 and described in the text, along with the models given in Wildes *et al*[118] and Barabash *et al*[120].

analysis of the lineshape of the broad components has shown that many of them, particularly at large thicknesses have a Gaussian component. This complicates the analysis of the FWHM, needed to make a comparison between the Wildes and Barabash[120] studies and our own. In Figure 4.11 we have shown the FWHMs of the broad components to the peaks as fit using solely Lorentzian-squared functions. For the larger peaks this may underestimate the FWHM as some intensity is unaccounted for, and it is unfortunate that the Wildes group have not published the details of individual fits such that we may see if there is a similar issue at large thicknesses. However, the fit of a power law to our data as in[118] shows a phenomenological relationship

$$\mathrm{FWHM}_{\mathrm{Nb\ peaks}} = a\, t_{\mathrm{Nb}}^{c},$$

with the coefficients listed in Table 4.2. The experimentally-determined exponents are consistently less than those predicted by theory, possibly to due the neglect of contributions to the broadening other than that due to the strain fields of randomly-correlated dislocations, especially at large thicknesses.

It is often standard practice to obtain a correlation-length for the scattering from the reciprocal of the values of the peak widths in q_x, but as the peak width is dependent on Q, this analysis is non-trivial. An analysis to estimate the correlation length by separating the Q-dependent and -independent broadening follows this section.

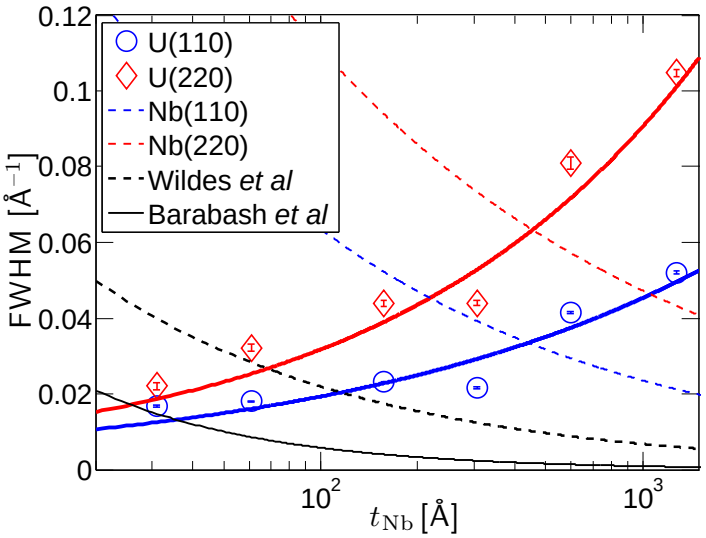

Figure 4.11: The full-width at half-maximum of the Lorentzian-squared peak fitted to the broad component of the scattering around the U(110) (circles) and U(220) (diamonds) reflections for samples of varying Nb thickness. The full lines show fits to the data as described in the text, and the dashed lines show the trends found in Section 4.2.3.2 and those published by Wildes *et al*[63] and Barabash *et al*[120].

The U(110) and U(220) peaks for the two thickest films in the series have been fitted with a single Gaussian peak, as the Lorentzian-squared lineshape is a poor fit for these peaks. A satisfactory fit was achieved with the Lorentzian-squared function for the other samples in the series.

As shown in Figure 4.11, the widths of the broad components of the rocking curves for the U layer have a dependence on Nb thickness that is in the opposite sense to the Nb peaks. This shows that the thickness of the buffer layer is an important factor for the growth of epitaxial films, and that the microstructure of the overlayer does not simply continue the evolution of that of the buffer. A similar study of the effects of buffer layer thickness on the structure of an overlayer cannot be found in the literature. We believe that there is insufficient consideration of the complexity of the microstructure of epilayers and the complex interactions of the microstructures of adjacent layers, and that the study of these effects merits considerable further effort. Further discussion will be made on this below.

Peak/Model	a [Å^{a-1}]	c
U(110)	0 ± 0.002	0.37 ± 0.095
U(220)	0 ± 0.002	0.46 ± 0.08
Nb(110)	0.46 ± 0.3	-0.43 ± 0.10
Nb(220)	0.48 ± 0.4	-0.33 ± 0.13
Wildes *et al*	0.23 ± 0.05	-0.51 ± 0.05
Barabash *et al*	Not given	-0.8 (predicted)

Table 4.3: The coefficients for the fits, FWHM$= a\, t_{\mathrm{Nb}}^{c}$, to the full-widths at half-maximum of the broad components of the U(110) and U(220) rocking curves as shown in Figure 4.11 and described in the text, along with the models given in Table 4.2, Wildes *et al*[118] and Barabash *et al*[120].

The coefficients of the fits to the data in Figure 4.11 are given in Table 4.11 are given in Table 4.3. The exponents are comparable in magnitude to the Nb layer, although the Q-dependence is also in the opposite sense, with the (220) full-widths having a larger dependence on thickness than the (110) full-widths in the U layers. This suggests a different mechanism of broadening in these layers.

4.2.3.3 Peak width as a function of Q; the Williamson-Hall like plot

As outlined above, by comparing the broadening of the diffuse component at different values of the out-of-plane momentum transfer, Q-dependent and -independent components may be separated. Following the analysis in Durand et al.[150] for the scattering around the Nb(110) and Nb(220) peaks, we have deduced the correlation length of the effects responsible for the broadening and also the mosaicity of the films, as shown in Figure 4.12.

The correlation-length for the scattering remains constant at around 20 Å below 120 Å thickness, and then increases exponentially to nearly 150 Å at 1200 Å thickness. The mosaicity found from the analysis decreases from 0.12±0.03° for the thinnest samples to around 0.05° for the thickest samples, with a minimum of 0.015° for the 306 Å Nb sample. It is difficult to say whether the relatively low mosaicity of the 306 Å sample represents a true minimum or if it is an outlier. Growth of more samples of thicknesses close to

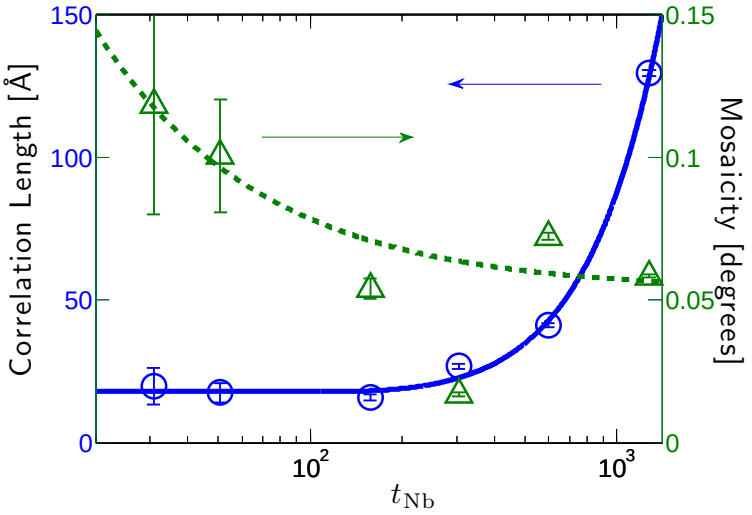

Figure 4.12: The in-plane defect-correlation-length, ξ_x, (triangles) and the mosaicity tilt, ΔM, (circles) for Nb layers as deduced from Williamson-Hall-like plots of the broadening of the Bragg-peaks around the Nb(110) and Nb(220) reciprocal-space-positions as described in the text. It is difficult to say whether the mosaicity of the 306 Å sample represents a true minimum or if it is an outlier. The full and dashed lines are guides to the eye.

300 Åwould allow firmer conclusions to be drawn.

In Figure 4.13 we see that in contrast to the data for the Nb layer in Figure 4.12 the mosaicity of the U layers is initially small and increases with thickness, although the dependence of the correlation length on thickness remains similar to that for the U films.

This analysis only works for thicknesses below 150 Å, beyond which the gradient of the $\left(\frac{\beta(Q)}{Q_z}\right)^2$ vs. $\frac{\beta(Q)}{Q_z^2}$ graph becomes negative.

4.2.3.4 Line-profile analysis to separate broadening from small displacements and lattice rotations

In Figure 4.14 we present the results of fitting a linear combination of Gaussian and Lorentzian-squared lineshapes to the broad components of the scattering from the Nb structure peaks, as a function of Nb thickness.

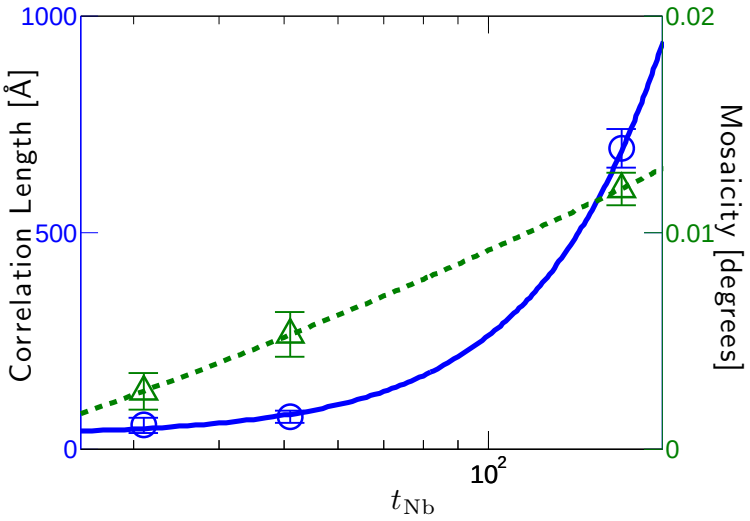

Figure 4.13: The in-plane defect-correlation-length, ξ_x, (triangles) and the mosaicity tilt, ΔM, (circles) for U layers as deduced from Williamson-Hall-like plots of the broadening of the Bragg-peaks around the U(110) and U(220) Bragg-positions as described in the text. The full and dashed lines are guides to the eye.

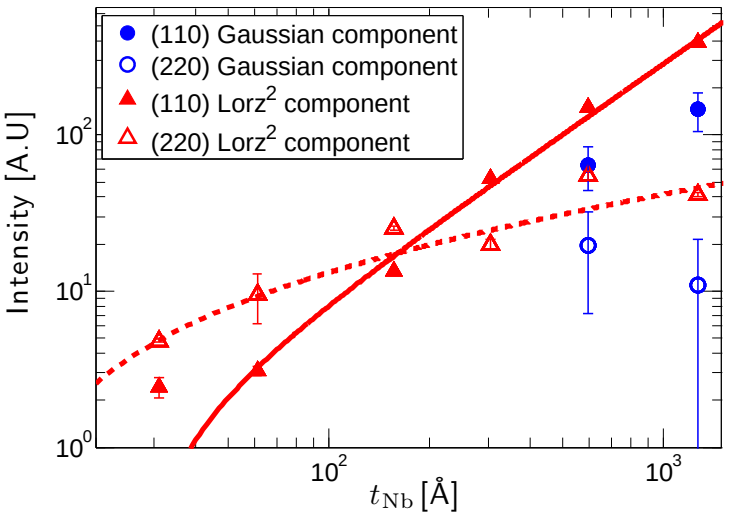

Figure 4.14: The intensities of the Gaussian (circles) and Lorentzian-squared (triangles) components used to fit the broad components of the Nb(110) and Nb(220) peaks, as a function of Nb-layer thickness. No Gaussian component was seen in samples of less than 598 Å. The full and dashed lines are guides to the eye.

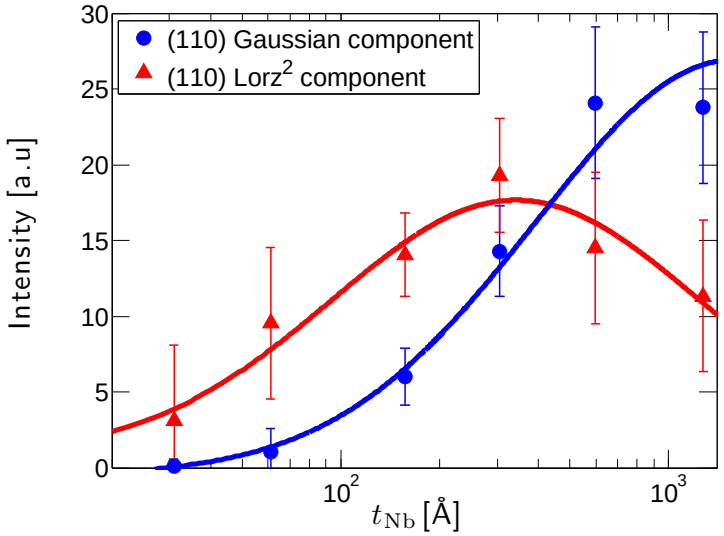

Figure 4.15: The intensities of the Gaussian (circles) and Lorentzian-squared (triangles) components used to fit the broad components of the U(110) peaks, as a function of Nb-layer thickness. The full lines are guides to the eye

For all Nb thicknesses the Lorentzian-squared component, which is due to small displacements of atoms from well-ordered lattice planes, dominates the scattering. For the two thickest samples a significant Gaussian component is present, which we associate with random rotations ('tilt') of the lattice planes.

We have found that other line-shapes, including Gaussian, Lorentzian and a linear-combination of the two (a pseudo-Voigt) do not give a satisfactory fit to the data at large thicknesses. No attempt has been made to fit the data using a Pearson VII function as in Bentall et al. [123], or Lévy-stable distributions as in Boulle et al. [167].

At low thicknesses there are large uncertainties in the form of the lineshape as the intensity in the broad component of the scattering is small. Both Gaussian and Lorentzian-squared peaks may be fitted within the experimental uncertainties, along with other functional forms, including a linear-combination of Gaussian and Lorentzian functions (a pseudo-voigt), but it is generally considered unreliable to draw conclusions from line-profile analyses when the number of counts in the peak is not above one thousand, and the peak is not visible above the background over more than two orders of magnitude.

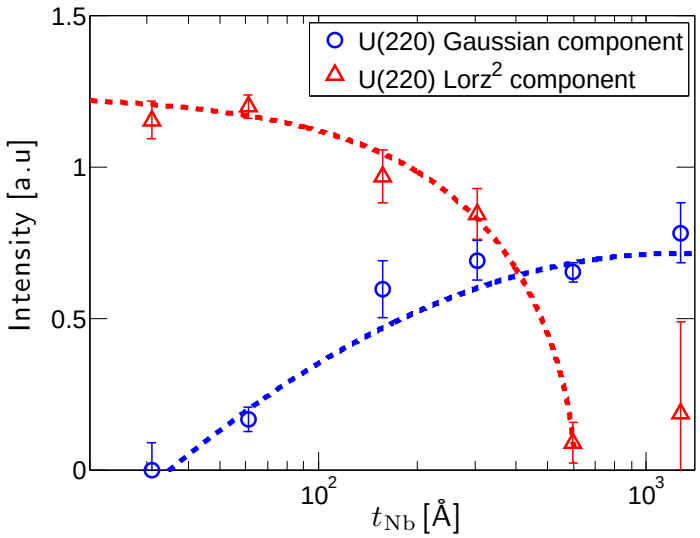

Figure 4.16: The intensities of the Gaussian (circles) and Lorentzian-squared (triangles) components used to fit the broad components of the U(220) peaks, as a function of Nb-layer thickness. The dashed lines are guides to the eye, assuming that the thickest and thinnest samples show pure Gaussian and pure Lorentzian-squared line-profiles, respectively.

Figures 4.15 and 4.16 show the contributions to the broad components of the scattering from Gaussian and Lorentzian-squared components from the U(110) and U(220) peaks respectively. There is a good deal of intensity in the broad components for the U(110) peaks at all thicknesses, and a clear distinction between the narrow and broad components, allowing a more reliable analysis than for the Nb peaks. The analysis of the U(220) lineshape is made difficult by the lack of distinction between the narrow and broad components for small Nb thicknesses, but since the narrow component remains similar across thicknesses it is straightforward to separate from the broad component, which changes markedly.

There is a clear change from a predominantly Lorentzian-squared lineshape to largely Gaussian at both positions. At large Nb thicknesses, the Gaussian component indicates mosaic-crystal structure. The Lorentzian-squared lineshape at lower thicknesses suggests that the defect density in these layers remains low.

4.2.3.5 Peak aspect ratio

Figure 4.17 shows the aspect ratios, defined as the ratio of the integral breadths in the q_x- and q_z-directions for the Nb and U (110) and (220) peaks as a function of Nb-layer thickness.

The longitudinal peaks have been fitted for simplicity by Gaussian peaks, which give very good fits over one or two decades of intensity, but do not take into account the Pendellösung fringes seen above.

There is a clear decrease in the aspect ratio of the peaks as thickness is increased, from around 0.75 at the (110) position for the thinnest samples to about 0.25 for the thickest samples. Referring to the arguments in Section 2.4.3.4 we consider that this represents a change from a majority edge-dislocation regime to a majority 60° dislocation regime. There is a Q-dependence to the aspect ratio, with the (220) peaks having consistently larger ratios than those at the (110) position. Large uncertainties are present in the measurements for the (220) peaks at low thicknesses due to the lack of intensity in the scattering for these peaks.

4.2.3.6 Aspect ratios of uranium-layer symmetrical Bragg-peaks

In contrast to the Nb peaks, the measurement of the aspect ratios is more straightforward as there is little change in the size broadening in the longitudinal direction due to the changing layer thickness. In addition, the U Bragg-reflections are well-separated from the sapphire substrate peak.

As for the Nb layers, there is a steady decrease in the aspect ratio for the U peaks. This suggests an increasing proportion of 60° dislocations as the Nb thickness is increased, and therefore an increase in the predominance of tilt boundaries.

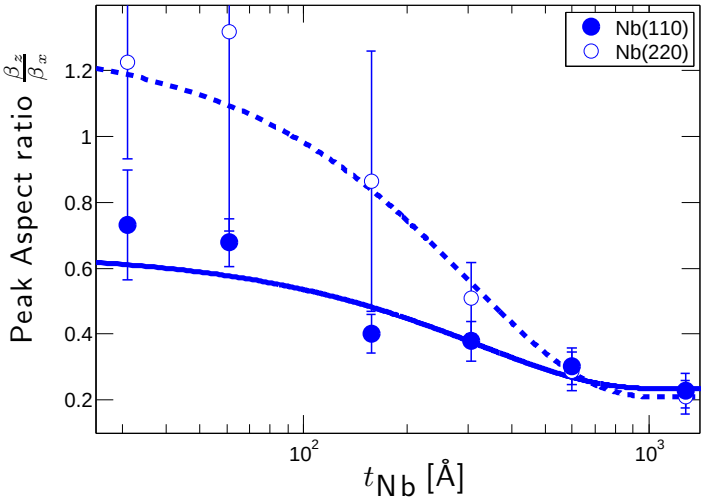

Figure 4.17: The ratios of the longitudinal and transverse integral breadths of the Nb(110) (closed circles) and Nb(220) (open circles) peaks as a function of Nb thickness. The full and dashed lines are guides to the eye.

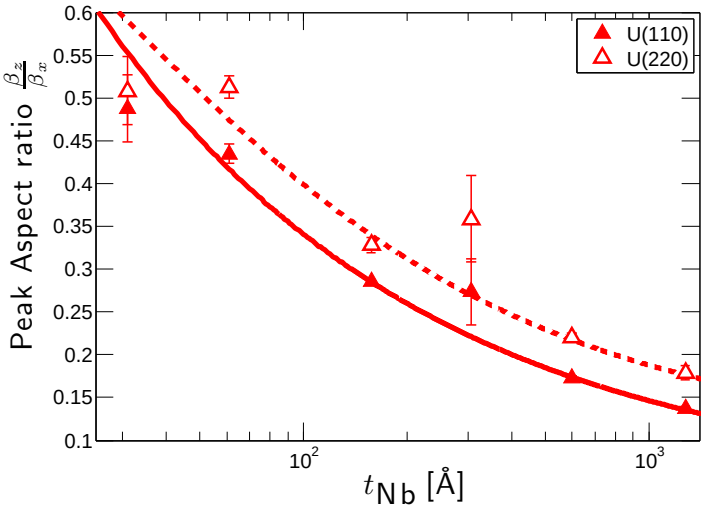

Figure 4.18: The ratios of the longitudinal and transverse integral breadths of the U(110) (closed triangles) and U(220) (open triangles) peaks as a function of Nb thickness. The full and dashed lines are guides to the eye.

4.2.4 Discussion

4.2.4.1 Peak-breadths

For small thicknesses below the critical thickness for dislocation formation a broadening is expected due to the large strain gradient through the thickness of the film, from the clamped to the free surface[64]. Above the critical thickness scattering from dislocations will lead to peak broadening and the contributions from each will be difficult to distinguish as they both have a Q-dependence. At large thicknesses most of the film is expected to be relaxed with a low dislocation-density and free of strain gradients.

The values of the correlation-length and mosaicity found using a Williamson-Hall-like approach point to a different explanation, in which the film growth occurs by domains or mosaic blocks misoriented in the plane of the film. As the film thickness is increased preferentially-oriented domains grow at the expense of others. This results in a large correlation length for the scattering, which increases with film thickness. Large numbers of randomly misoriented blocks leads to a large mosaicity, which decreases as the number of blocks decreases with increased film thickness. At large thicknesses random disorder is increased and faults in the crystal become more likely, increasing the mosaic, as well as reducing the intensity of the narrow component. An increase in the number of inclined (60°) dislocations is also expected as thickness increases[123], and this may explain the changes in the aspect ratio for the peaks.

The striking behaviour of the FWHM of the U peaks can be explained by the increasing influence of the Nb layer on the U layer as the Nb thickness is increased. At low thicknesses the U grows relatively unstrained, and the misfit dislocation density is low, resulting in low amounts of broadening. As the thickness of the Nb layer increases the misfit increases as the epitaxial relationship becomes more like U on bulk Nb, and the dislocation density is greater.

The discussion in Wölfing et al.[107] suggests that the domain size behaviour is also likely

to be different, with the flatness of the thin Nb layers allowing large U domains to form, but the increased roughness at large Nb thickness shown in the XRR fits in Section 3.3.1.1 precludes their formation. Despite the strikingly different dependence of the FWHM of the U layer peaks on Nb thickness to that of the Nb peaks, elsewhere in the above analysis there is little to distinguish the two layers. The greatest difference comes from the Williamson-Hall like plot which separates the q_z-dependent and -independent broadening. Clearly there is a great difference in the q_z-dependence of the broadening in each layer, which we have attributed either to strain or mosaic rotations. We discount the possibility of a difference in the mosaic rotations as the aspect ratios behave in a similar manner for each layer.

Therefore the difference between the two layers is primarily due to the amount of epitaxial strain present in each layer. Evidently, the ability of the Nb buffer to strain the U overlayer is small, a point that is significant for the following chapter.

4.2.4.2 Reciprocal-space maps

Figure 4.19 shows a two-dimensional representation of the scattering around the U(220) peaks measured using beamline BM28 at the ESRF. This show qualitatively the decrease in the aspect ratio of the peak as the Nb thickness is increased. Pendellösung fringes are visible in three of the four panels, as described above. The width does not change sharply as q_x is increased from zero, indicating that the narrow and broad components result from similar regions of the film.

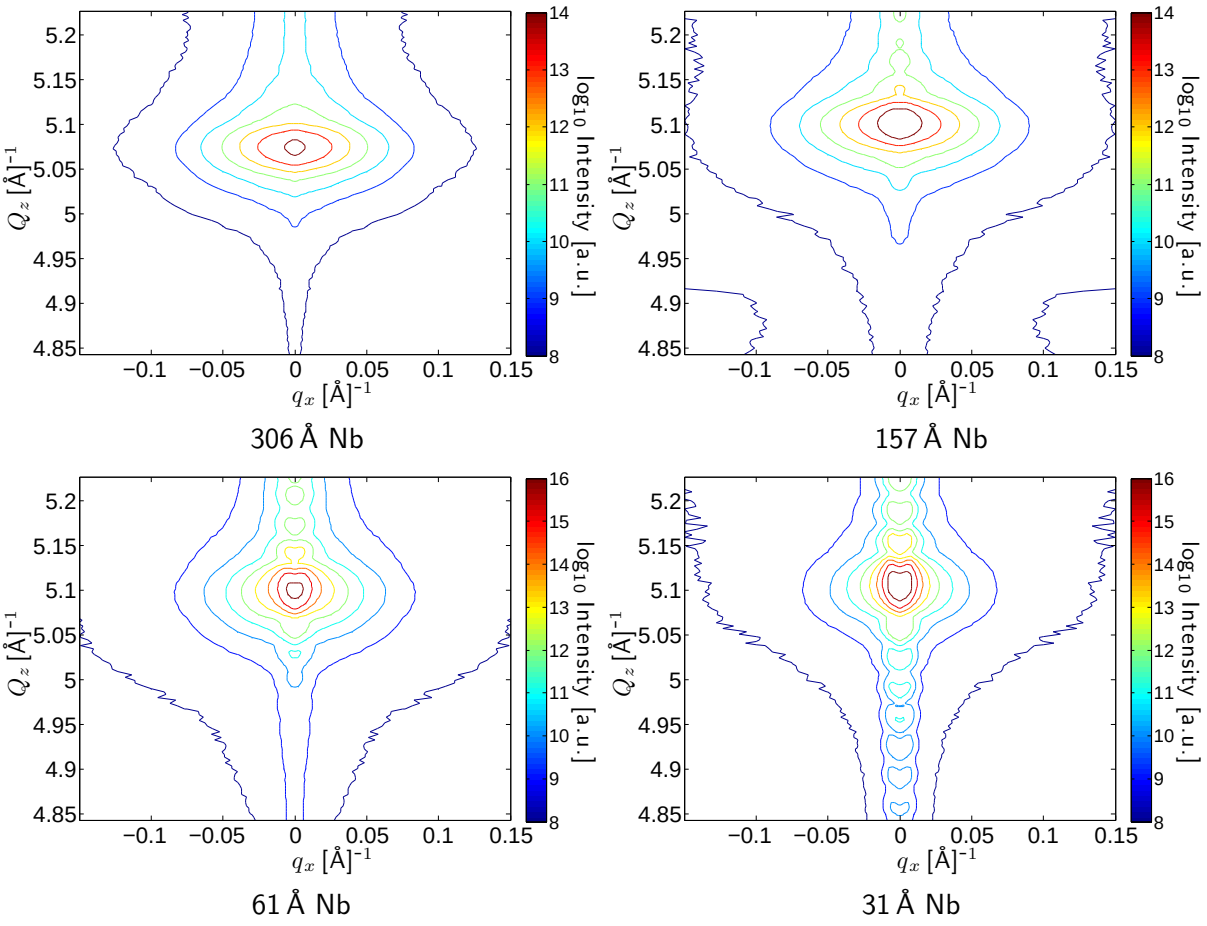

Figure 4.19: Intensity contour maps, plotted using data from XMaS, around the U(220) Bragg-peak at room temperature for the samples listed in Table 4.1.

4.3 The evolution of the microstructure of thin uranium layers with thickness

In this thesis the uranium layer is the primary object of study. The unique aspect of this study is that we have analysed the effect of the thickness of the buffer layer on the layer of interest. However, the structure of the uranium layer is itself strongly dependent on its thickness, and this following section will attempt to deduce the microstructure of the uranium layers from their diffuse X-ray scattering.

4.3.1 Transverse scans

4.3.1.1 U(110)

Two sets of data were obtained for the set of samples listed in Table 4.4.

Transverse scans were performed at the U(110) position using the diffractometer located at Oxford and using BM28. Most of the rocking curves obtained at Oxford at the U(110) position fit the two component Gaussian-plus-Lorentzian-squared model well over three decades of intensity. Some of the curves, such as those from the 2000, 750 and 50 Å U-thickness samples, show asymmetries which are likely to be due to secondary crystallites, but might also be due to dynamical diffraction effects. The narrow component is visible in samples with a U-thickness of 363 Å or less. This is almost an order of magnitude less than the Nb-thickness at which the Nb(110) rocking curves displayed a narrow component, above. The narrow peak at the U(110) position is still visible in the data from samples of greater total thickness, but in which the larger proportion of the total thickness is due to the Nb-layer (such as from the 150 Å U/500 Å Nb sample in Figures 4.20 and 4.21).

Sample	SN243	SN282	SN260	SN322	SN259
Nominal buffer thickness [Å]	350	350	350	350	350
Nominal U thickness [Å]	50	75	100	150	200
Nb buffer [Å]	171	170	175	157	173
U layer [Å]	69	90	117	150	234

Sample	SN323	SN317	SN320	SN242	SN321
Nominal buffer thickness [Å]	350	350	350	350	350
Nominal U thickness [Å]	350	500	750	1000	2000
Nb buffer [Å]	155	180	146	142	172
U layer [Å]	363	635	771	1477	2289

Table 4.4: The composition of the samples of fixed nominal Nb-thickness grown in order to investigate the influence of U-layer thickness on the microstructure of U thin-films, in order of increasing thickness. All samples were deposited by UHV magnetron sputtering onto A-plane $(11\bar{2}0)$ sapphire substrates

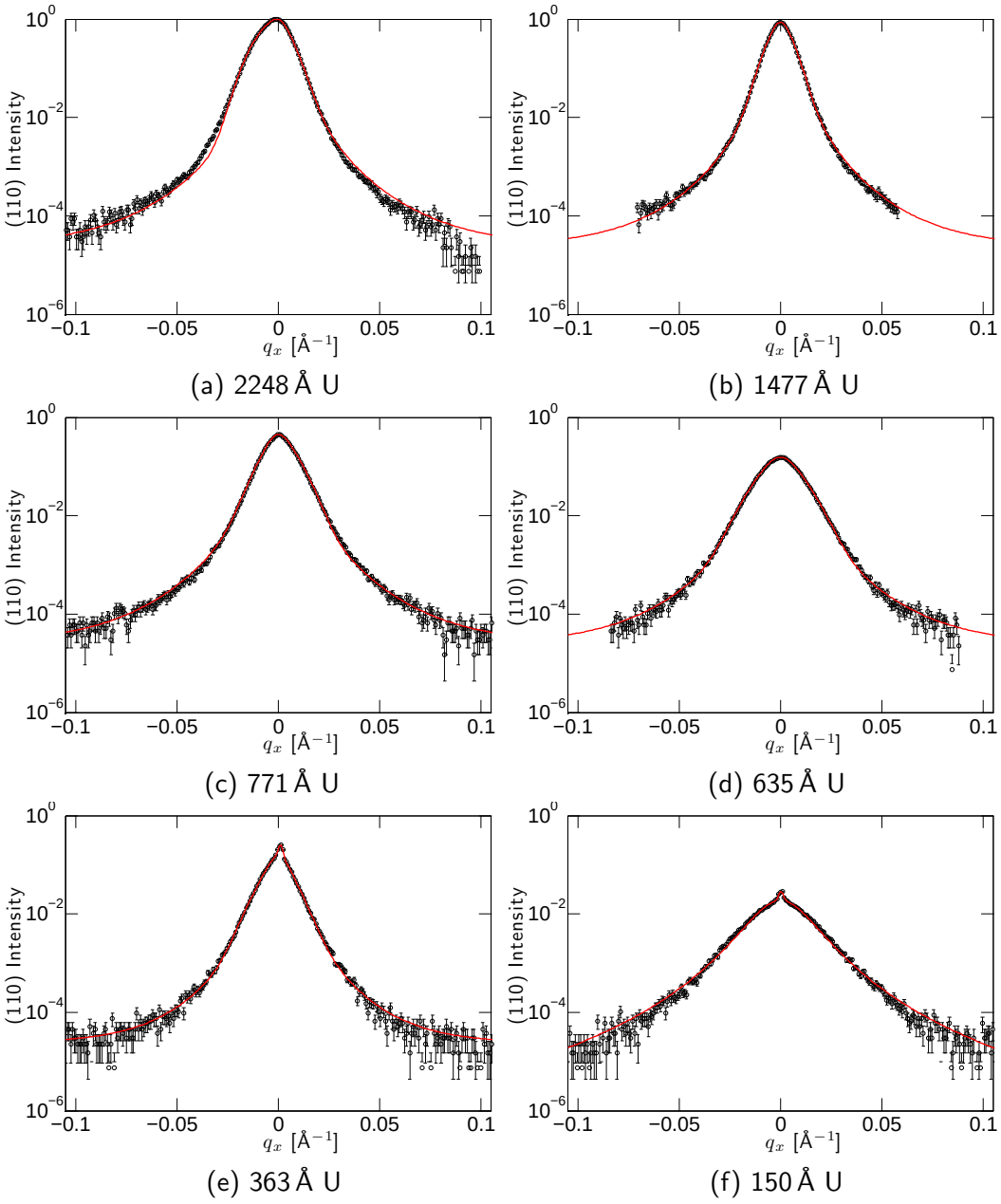

Figure 4.20: Transverse scans performed at Oxford across the U(110) peak for the samples described in Table 4.4. The intensities have been normalised to the peak value for the $t_U = 2248$ Å sample to enable comparison of intensity.

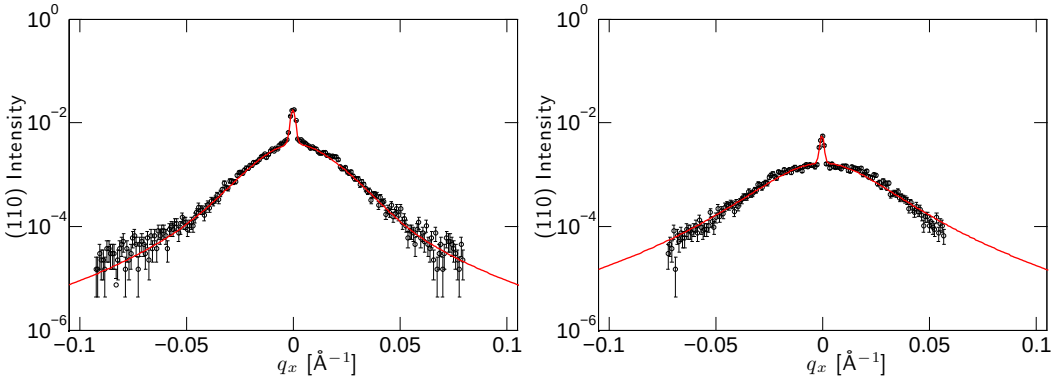

Figure 4.21: Transverse scans performed at Oxford across the U(110) peak for the samples described in Table 4.4. The intensities have been normalised to the peak value for the $t_U = 2248$ Å sample to enable comparison of intensity.

The short scan length of the 69 Å sample in Panel (h) means that the fit is likely to overestimate the peak width, due to the fact that an insufficient amount of background has been included in the scan.

The data from XMaS differ markedly from those taken from Oxford, and any differences are likely to be due to one or both of the following differences in the characteristics of the probe in each case:

1. The increased intensity, which means that features such as the tails of the peaks obscured by the background in the Oxford data become visible,

2. Decreased divergence and enhanced instrumental resolution, which mean that the shape of the peak is more representative of the scattering from the sample, as the contribution from the instrumental resolution function is smaller.

We have included both sets of data as that from the Oxford diffractometer is more straightforward to analyse qualitatively, yet the better counting statistics and resolution of the XMaS data make it more reliable for the quantitative analyses that follow. In addition, the data in the following chapter were taken using XMaS, and reference will be made to the scattering from the structural peaks presented here.

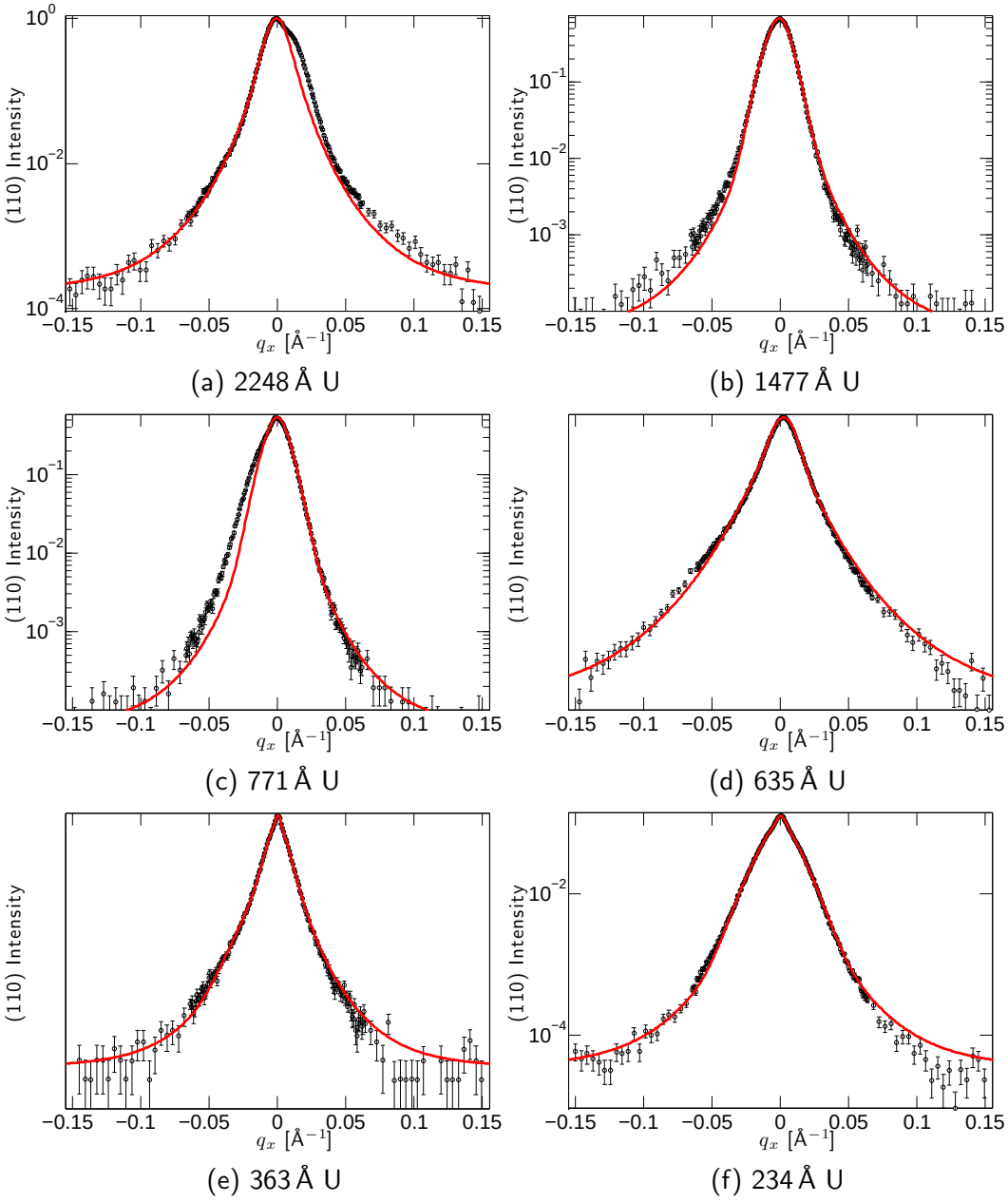

Figure 4.22: Transverse scans from XMaS across the U(110) peak for the samples described in Table 4.4. The intensities have been normalised to the peak value for the $t_{\mathrm{U}} = 2248\,$Å sample to enable comparisons of intensity.

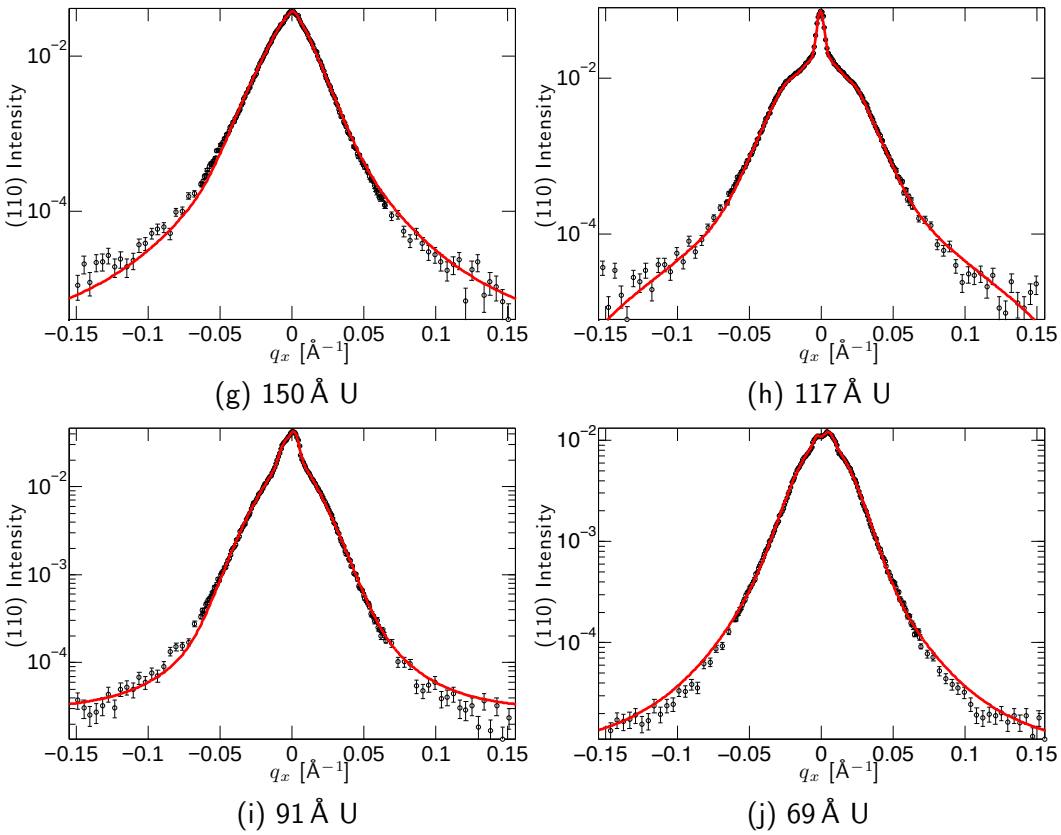

Figure 4.23: Transverse scans from XMaS across the U(110) peak for the samples described in Table 4.4. The intensities have been normalised to the peak value for the $t_U = 2248$ Å sample to enable comparisons of intensity.

Firstly, the asymmetries in the peak shapes at larger thicknesses are more pronounced. The fits shown in Figure 4.22, Panels (a) and (c), have taken into account this asymmetry by fitting a peak of similar shape to those shown to the asymmetry. The fact that the secondary peaks fitted to the asymmetry share a similar shape to the primary peak gives weight to the supposition that the asymmetry is due to the presence of a secondary crystallite.

Secondly, the narrow component at the lowest thicknesses has a degree of structure to it, with two components visible in scans from the 91 and 61 Å films, in Panels (i) and (j) respectively. A combination of two Gaussian peaks of similar width to the single narrow component seen in Panel (h) for the 117 Å sample has been fitted to these peaks. For both

samples the two peaks are a similar distance apart, about 0.0084 Å^{-1}.

Thirdly, the two-component model described above does not fit the broad component well for most thicknesses. A linear combination of Gaussian and Lorentzian-squared function gives very satisfactory fits at all thicknesses, and is preferable to a pseudo-voigt fit.

Finally, the broad component of the 117 Å sample has a distinctive shape, which resembles those in Boulle et al.[167] for a short transition region between correlated and uncorrelated disorder, and Bentall et al.[123], where the peak is compared to a model of the scattering from isolated 60° dislocations.

4.3.1.2 U(220)

No narrow component is seen in any of the rocking curves at the U(220) position, which are shown in Figure 4.25. Some structure is seen at the peaks of the thinnest samples, which in shape is similar to that at the U(110) positions. However, there is too little intensity to fit them in a similar way to the U(110) peaks. The curves fit well to a Lorentzian-squared lineshape, although the 2000 Å and 1000 Å samples show an asymmetry such that the Lorentzian-squared function only fits one side of the curve well. We have included a linear combination of Gaussian and Lorentzian-squared components in the fits as mentioned in Section 4.2.3. Radial scans at the central position of each peak show that the grains extend through the entire film thickness.

4.3.2 Analysis

4.3.2.1 The width of the broad component

Figure 4.26 shows the FWHM of the Lorentzian-squared fits to the peaks in Figures 4.20 and 4.21 (Oxford scans), along with the integral breadths, β, of peaks in Figures 4.24 and 4.25 (XMaS data), which have been fitted with a linear combination of a Gaussian and a

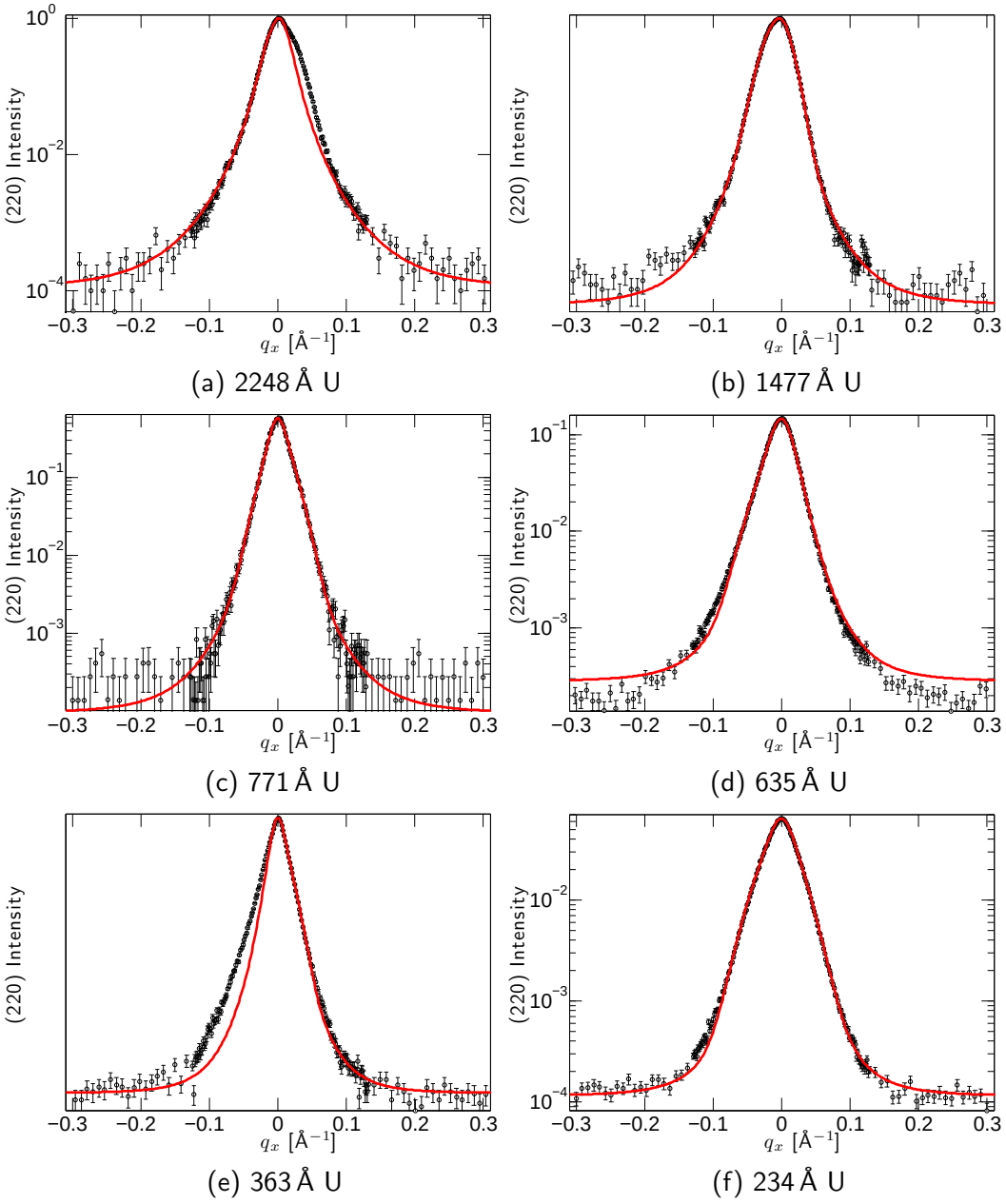

Figure 4.24: Transverse scans from XMaS across the U(220) peak for the samples described in Table 4.4. The intensities have been normalised to the peak value for the $t_U = 2248$ Å sample to allow comparisons of intensity.

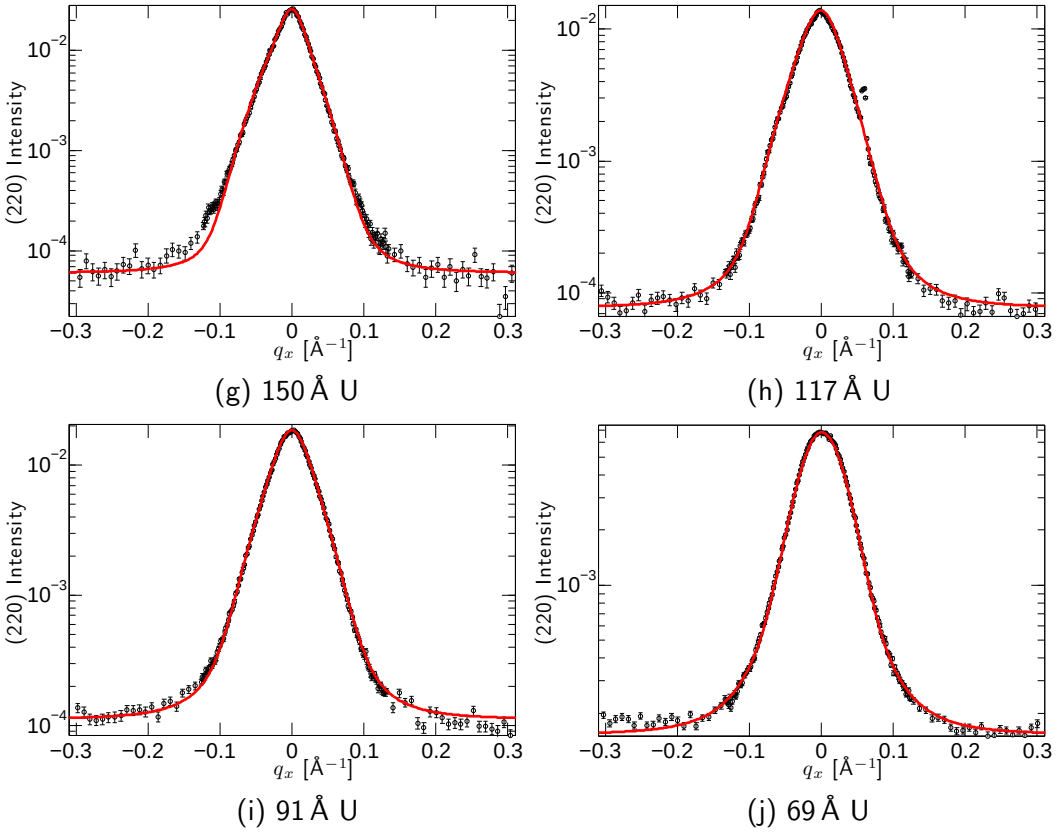

Figure 4.25: Transverse scans from XMaS across the U(220) peak for the samples described in Table 4.4. The intensities have been normalised to the peak value for the $t_U = 2248$ Å sample to enable comparisons of intensity.

Lorentzian-squared function. The integral breadth is analytically a more straightforward peak property to deal with than the FWHM[150], and in this case is a more reliable measure than an arbitrary combination of the peak widths from each function.

In a similar way to the dependence of the Nb structure-peaks on Nb thickness, the U structure peaks show a decrease in the FWHM of broad component with increasing U thickness, from around 0.04 Å^{-1}to close to 0.01 Å^{-1}at the (110) position. The integral breadths follow similar trends, but have values around 30% larger, changing from around 0.04 Å^{-1}to close to 0.02 Å^{-1}at the (110) position, and about 0.08 Å^{-1}to just under 0.04 Å^{-1}at the (220) position. The scattering from the 350 Å sample is anomalously narrow, suggesting an exceptional quality in this film. This data point was excluded from the analysis. The

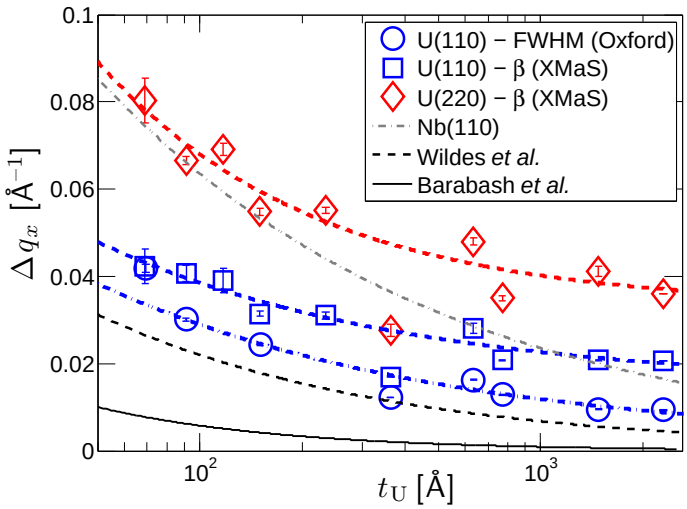

Figure 4.26: The FWHM and integral breadths, β, of the broad components to the scattering around the U(110) and U(220) peaks as a function of U-thickness. The full and dashed lines show fits to the data as described in the text, along with the trend found in Section 4.2.3, and those published by Wildes *et al* [63] and Barabash *et al* [120].

Peak/Model	a [Å^{c-1}]	c	b
U(110) FWHM (Oxford)	0.198 ± 0.006	-0.432 ± 0.005	0.002 ± 0.0004
U(110) β (XMaS)	0.219 ± 0.010	-0.483 ± 0.009	0.015 ± 0.0008
U(220) β (XMaS)	0.828 ± 0.053	-0.687 ± 0.013	0.033 ± 0.002
Nb(110) FWHM ($f(t_{Nb})$)	0.46 ± 0.3	-0.43 ± 0.10	0
Nb(220) FWHM ($f(t_{Nb})$)	0.48 ± 0.4	-0.33 ± 0.13	0
Wildes *et al*	0.23 ± 0.05	-0.51 ± 0.05	0
Barabash *et al*	Not given	-0.8 (predicted)	Not given

Table 4.5: The coefficients for the fits, (peak width)$= a\, t_U^c$, to the full-widths at half-maximum and integral breadths, β, of the broad components of the U(110) and U(220) rocking curves as shown in Figure 4.26 and described in the text, along with the models given in Table 4.2, and those published by Wildes *et al* [118] and Barabash *et al* [120].

coefficients of power law fits to the data are given in Table 4.5.

The data from Oxford and XMaS follow similar trends, despite qualitatively different lineshapes. In general there is a slighter dependence on thickness, which is understandable bearing in mind the observations from Section 4.2.4.1.

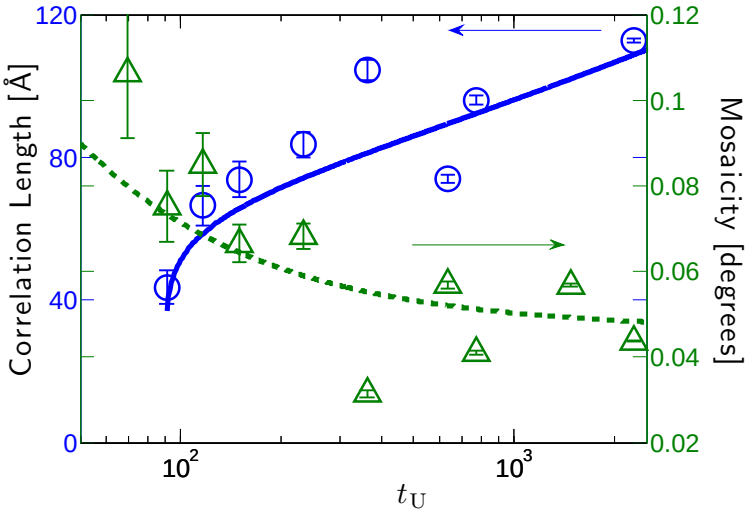

Figure 4.27: The in-plane defect-correlation-length, ξ_x, (triangles) and the mosaicity tilt, ΔM, (circles) for U layers as deduced from Williamson-Hall-like plots of the broadening of the Bragg-peaks around the U(110) and U(220) Bragg-positions as described in the text. The full and dashed lines are guides to the eye.

4.3.2.2 Peak width as a function of Q—Data from XMaS

An analysis of the of the broadening of the peaks at different positions in reciprocal-space allows a separation of the q_z-dependent and -independent components, which may be ascribed to different effects, as described above. In Figure 4.27 we show the results of using a Williamson-Hall like plot to deduce the correlation lengt to the scattering and the mosaicity of the films. We can compare this to the results shown in Figure 4.12 for the broadening of Nb structure peaks as the Nb thickness is changed. There is a similar trend in the mosaicity for both layers, although the mosaicity in the U layers is around 20% lower than in the Nb layers.

The trend in the correlation length, however, is markedly different for the two layers: in the uranium layers it appears to decrease to zero at a finite value of $t_U \sim 90\,\text{Å}$, whereas the correlation length for both the Nb and U layers tends to a finite value as $t_{Nb} \to 0$. The range of the correlation lengths is similar, however, for the U and Nb layers as their own thickness is varied, despite the different behaviour.

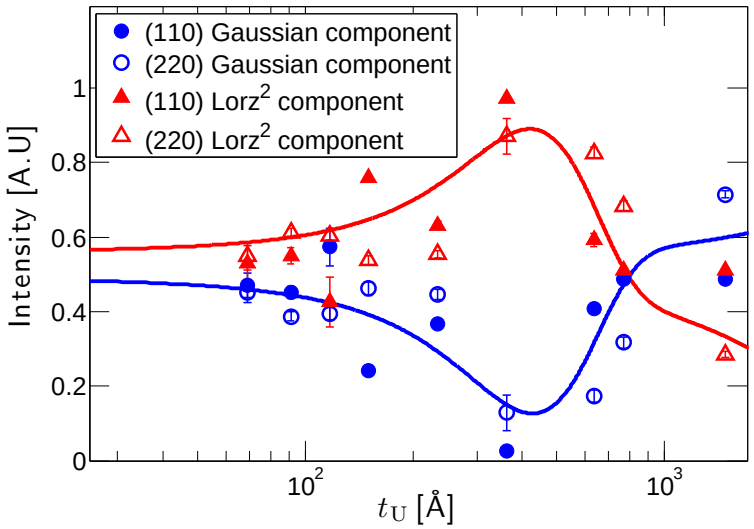

Figure 4.28: The intensities of the Gaussian (circles) and Lorentzian-squared (triangles) components used to fit the broad components of the U(110) (closed symbols) and U(220) (open symbols) peaks performed at XMaS, as a function of U-layer thickness. The lines are guides to the eye.

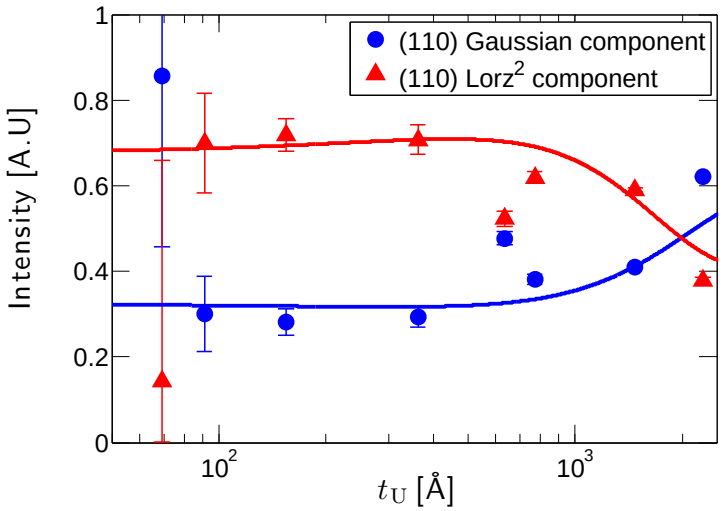

Figure 4.29: The intensities of the Gaussian (circles) and Lorentzian-squared (triangles) components used to fit the broad components of the U(110) peaks from scans performed at Oxford, as a function of U-layer thickness. The lines are guides to the eye.

4.3.2.3 Line profile analysis

In Figure 4.28 we show the results of fitting a two-component model to the broad component of the scattering around the U(110) and U(220) reflections for films of differing U thickness. Due to the wider range that the intensities cover compared with the Nb thickness series, we have shown the proportional intensity of each component function as opposed to the total intensity. We see that at intermediate thicknesses of $t_{\mathrm{U}} \sim 350\,\text{Å}$, the lineshape is nearly all Lorentzian-squared, but as thickness is increased or decreased from this intermediate thickness the Gaussian component becomes more significant. Towards low thicknesses there is a tendency for the components to be equal in intensity, yet towards large thicknesses it appears that the Gaussian component becomes dominant.

We have included the results of the analysis as applied to the Oxford data in Figure 4.29 for completeness. Due to the decreased resolution and count rate of this diffractometer, separation of the two components is less accurate. We see a qualitatively similar trend to that seen in the XMaS data, however.

4.3.2.4 Peak aspect ratio

The peak aspect ratios shown in Figure 4.30 follow a slighter overall trend with thickness to those in Section 4.2.3.5, with a decrease in the ratio as thickness is increased, from around 1 at low thicknesses to around 0.8 at large thicknesses. However there is a non-monotonic dependence on thickness, and what appears to be a lambda-type discontinuity between the 363 and 635 Å samples. In contrast with the Nb layers, the aspect ratios at the (220) positions is lesser than that at the (110) positions, although both sets of data follow very similar dependences on thickness.

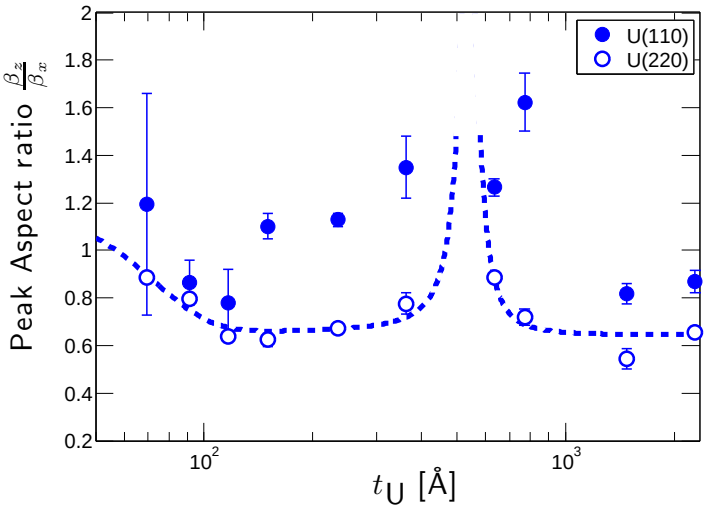

Figure 4.30: The ratios of the longitudinal and transverse integral breadths of the U(110) (closed circles) and U(220) (open circles) peaks as a function of Nb thickness. There is a decrease in the aspect ratio with thickness below 150 Å, but an apparent peak or discontinuity at around 500 Å. The dotted line is a guide to the eye.

4.4 Summary of film structure and uranium-layer thickness-dependence

The asymmetries of some of the peak profiles are "a universal peak property to be observed with a depth profile of the sample's metric." [108, pp.330]. It is likely that defect densities increase towards the film surface in thicker samples.

The strain in the U layer as a result of the mismatch with the Nb is less than that between the Nb and the sapphire substrate. Hence, there is less change as the film relaxes at larger thicknesses.

This is further evidence of the lower strain in the U layers than in the Nb layers. This might be evidence that initial U growth is highly disordered, as opposed to the layer-by-layer growth of Nb.

This analysis points to the following description of the film structure: At low thicknesses

the U is strained by the misfit between the leading to the Gaussian broadening, along with the introduction of misfit dislocations that cause small displacements out-of-the-plane and lead to the Lorentzian-squared broadening. As thickness increases, the dislocation concentration increases and strain is released, such that the predominant broadening is due to the small displacements.

Beyond thicknesses of around $t_{\mathrm{U}} \sim 350\,\text{Å}$ the proportion of 60°dislocations become significant, along with other defects. These dislocations lead to rotations of the lattice around in-plane axes, and Gaussian broadening, assuming finite variance of their distributions, according to the central limit theorem. In addition, the displacements due to the misfit dislocations at the interface propagate into the film as decaying surface waves, such that their magnitude decreases as thickness increases. Hence, therefore, the predominance of the Gaussian broadening at large thicknesses.

By this explanation we see that the high quality of the 363 Å sample might not be anomalous. This thickness appears to correspond to the optimum, where strain due to the epitaxial growth is largely relieved and the defect density is at its minimum. A previously grown sample, not included in this analysis, of 373 Å also had a characteristically narrow broad component.

As described in the previous section, this might correspond to a minimum in the dislocation-density, and corresponding high quality of the U layer.

4.5 The dependence of the line-shape of q_z-scans on q_x

Here, we present reciprocal space maps of the scattering intensity around the U(220) reflection for a selected sample of the varying U-thickness samples, and an analysis based on that of Wildes et al. [118]

In the Wildes analysis the widths were seen to be independent of q_x whilst $q_x d < 1$,

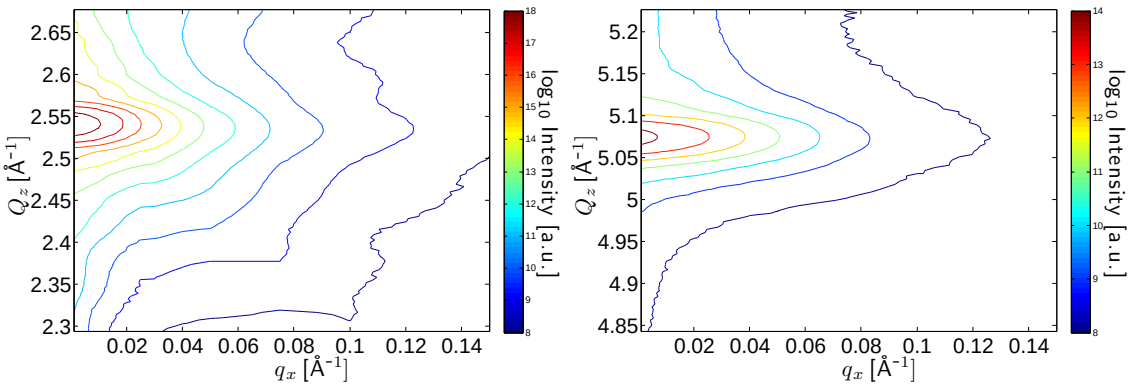

Figure 4.31: Intensity contour maps around the (Panel 1, left) U(110) and (Panel 2, right) U(220) Bragg-peaks, for sample SN325.

and approximately linearly dependent on q_x above this. This was taken to show that distortions with wavevectors greater than $q_x = 1/d$ do not propagate through the entire film thickness.

4.5.1 Reciprocal-space maps

To further characterise the scattering around the U(110) and U(220) peaks we have performed [hk0]-scans at different positions in q_x. In this way we can build up a picture of the diffuse scattering in the [110]-[001] plane of reciprocal-space.

Shown in Figure 4.31 are iso-intensity contour plots around the U(110) and U(220) Bragg-peaks for a 306 Å Nb/156 Å sample. We notice that proportionally the intensity drops off at a similar rate with q_x for each peak taking into account the differing colour scales for the two plots. However, the drop in intensity along q_z at $q_x = 0.001$ Å^{-1} is much sharper for the (220) position, reflecting the differing aspect ratios of the two peaks, as analysed in Section 4.2.3.6. At the (110) position, we see a line of intensity extending diagonally from the peak towards the low-q_z, high-q_x corner of the plot. This is due to the divergence of the incident beam, and is often referred to as a *monochromator* streak. Its intensity at the (220) position is too low be detected.

The following reciprocal-space maps were all performed around the (220)-position, as for most samples it was not possible to access the required positions in reciprocal space at the (110) position due to collisions of the diffractometer circles.

4.5.2 U series

In Figure 4.32 we have shown the line scans at positions of increasing q_x that we have used to plot the reciprocal-space maps shown in Figure 4.33. We see that the diffuse scattering extends further into q_x for the thickest samples, even in proportion to the main peak height. Note that the colour scales are different for each panel in Figure 4.33.

In Figure 4.32 it is clear that for some samples the peak position changes as q_x is increased. In Figure 4.36 we have plotted the peak positions as a function of q_x. Moving between the 150, 363 and 635 Å samples (cyan, green and yellow diamonds) there is a greater amount of movement the thicker the sample is, with each peak sample moving monotonically toward lower positions in q_z but the degree of movement over $0.08\,\text{Å}^{-1}$/ in q_x increasing from around 0.004 to $0.014\,\text{Å}^{-1}$. For the thickest samples of 1477 (orange triangles) and 2289 Å (red triangles) U there is a pronounced movement towards higher values of q_z below $0.02\,\text{Å}^{-1} q_x$ of about $0.0025\,\text{Å}^{-1}$, before a movement in the opposite direction at larger values of q_x, and a second change in direction beyond $0.01\,\text{Å}^{-1}$.

Due to the increased strain in the thinnest sample (blue squares) its position in q_z is shifted towards the sapphire and Nb reflections. In a similar way to the other thinnest samples, there is a monotonic shift towards low q_z positions.

We might explain these phenomena by surmising that distortions propagating through the sample lead to different changes in the lattice spacing depending on their wavevector along q_x. This is important firstly as simple transverse scans as described in Section 2.4.2.4 do not take into account this change in intensity due to a movement of the peak position with q_x, and secondly because an analysis of this peak movement may be a method of

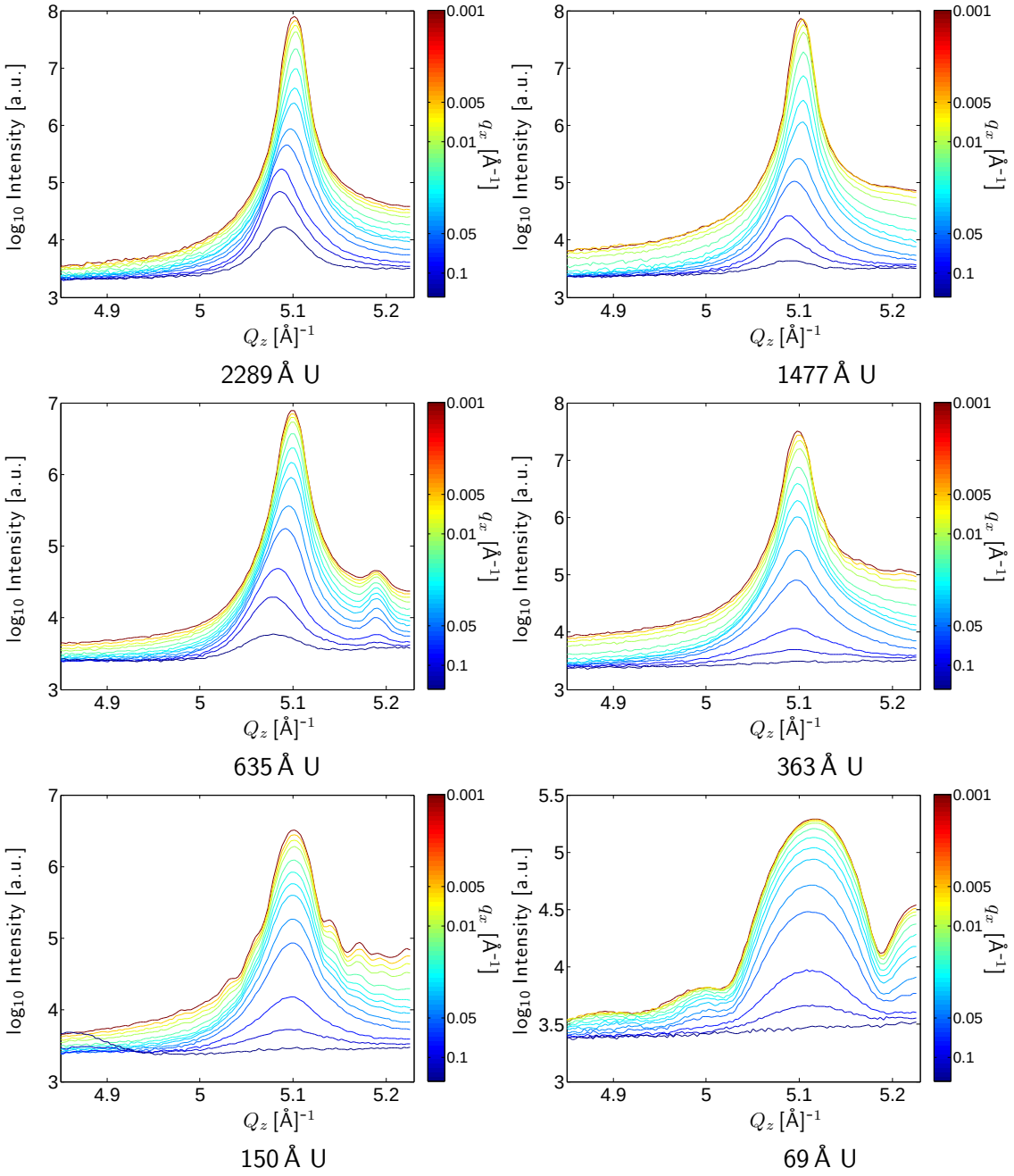

Figure 4.32: Line scans around the U(220) Bragg-peak for the samples listed in Table 4.4

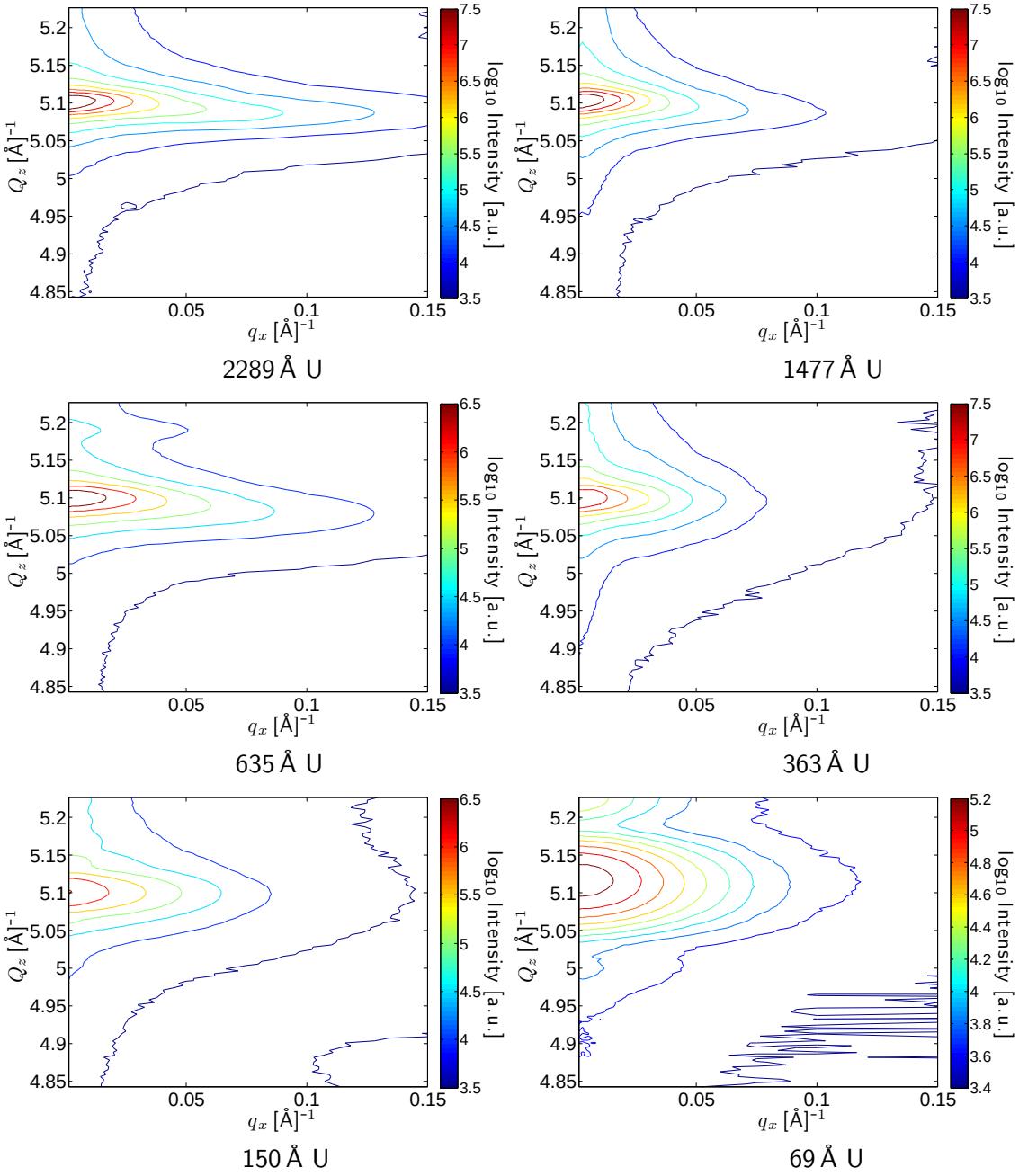

Figure 4.33: Intensity contour maps around the U(220) Bragg-peak for the samples listed in Table 4.4

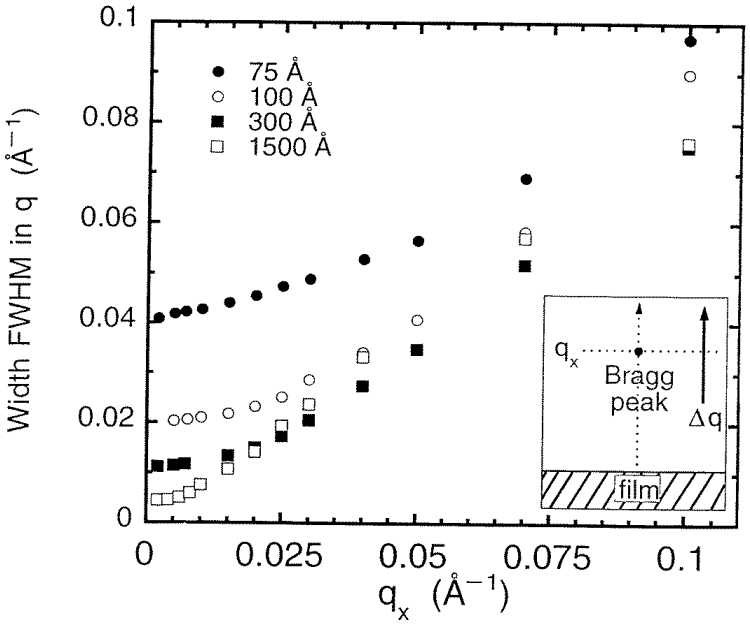

Figure 4.34: The width of the scattering in wavevector q_z when the wavevector transfer is scanned along (q_x , 0, $q + \tau$) for wavevectors q_x displaced from the (110) Bragg reflection of Nb. The insert indicates the scan direction in reciprocal space. From Wildes et al.[118].

studying the dynamics of distortions and dislocations within the lattice, a subject of some significance[201].

We present Figure 4.35 as a comparison with a Figure 4.34 from Wildes et al.[118]. The behaviour of the widths of the peaks is similar to that in the Wildes study, although we dispute the explanation given in that paper. There the increase in the width at large values of q_x is taken to be evidence that the distortions with large wavevector in q_x do not propagate as far into the lattice. We find it difficult to reconcile this interpretation with the observation that the spacing between Pendellösung fringes does not increase in a similar manner. This effect is more clear for the samples with fixed U thickness, below.

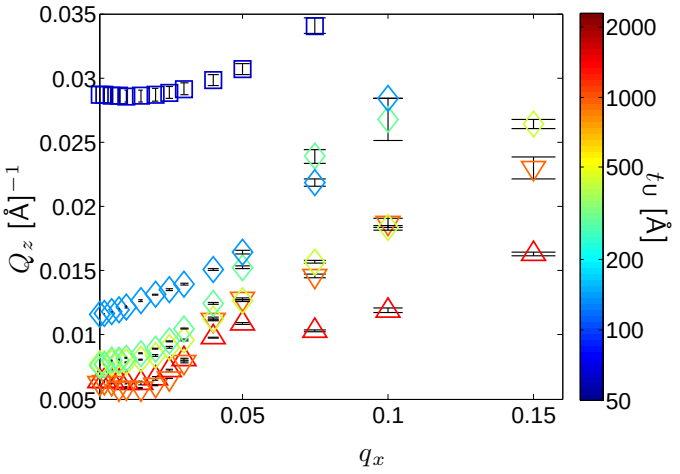

Figure 4.35: The full-widths at half-maximum of the Gaussian functions fitted to the peaks from the radial scans shown in Figure 4.32 at different positions in q_x.

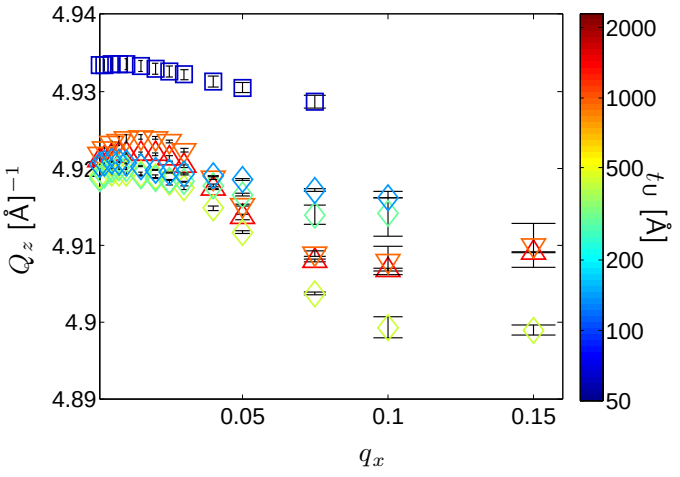

Figure 4.36: The peak positions from the radial scans shown in Figure 4.32 at different positions in q_x.

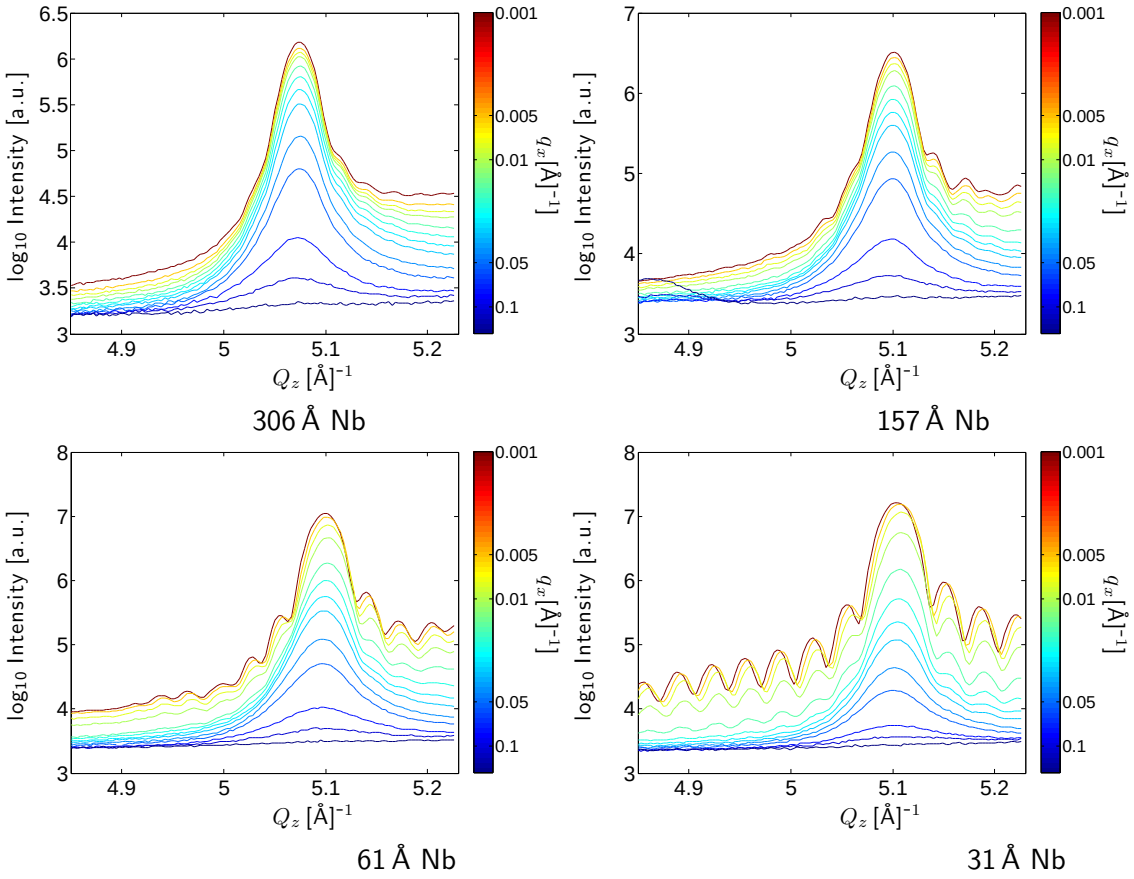

Figure 4.37: Line scans around the U(220) Bragg-peak for the samples listed in Table 4.1

4.5.3 Nb series

Figures 4.37 and 4.38 show line scans and intensity contour maps of the scattering around the U(220) position for samples of fixed U thickness, but varying Nb thickness. The clear Pendellösung fringes remain at approximately the same spacing as q_x is varied, although they do move with the position of the central peak. We have fitted the data for the thinnest sample in this series with the model used in Section 3.4.2.2 at all the positions in q_x , and seen that the thickness corresponding to the fringe spacing remains the same. We believe that the broadening of the peak is due primarily to the decrease in intensity at large q_x, such that broadening mechanisms leading to low scattering intensities yet decay

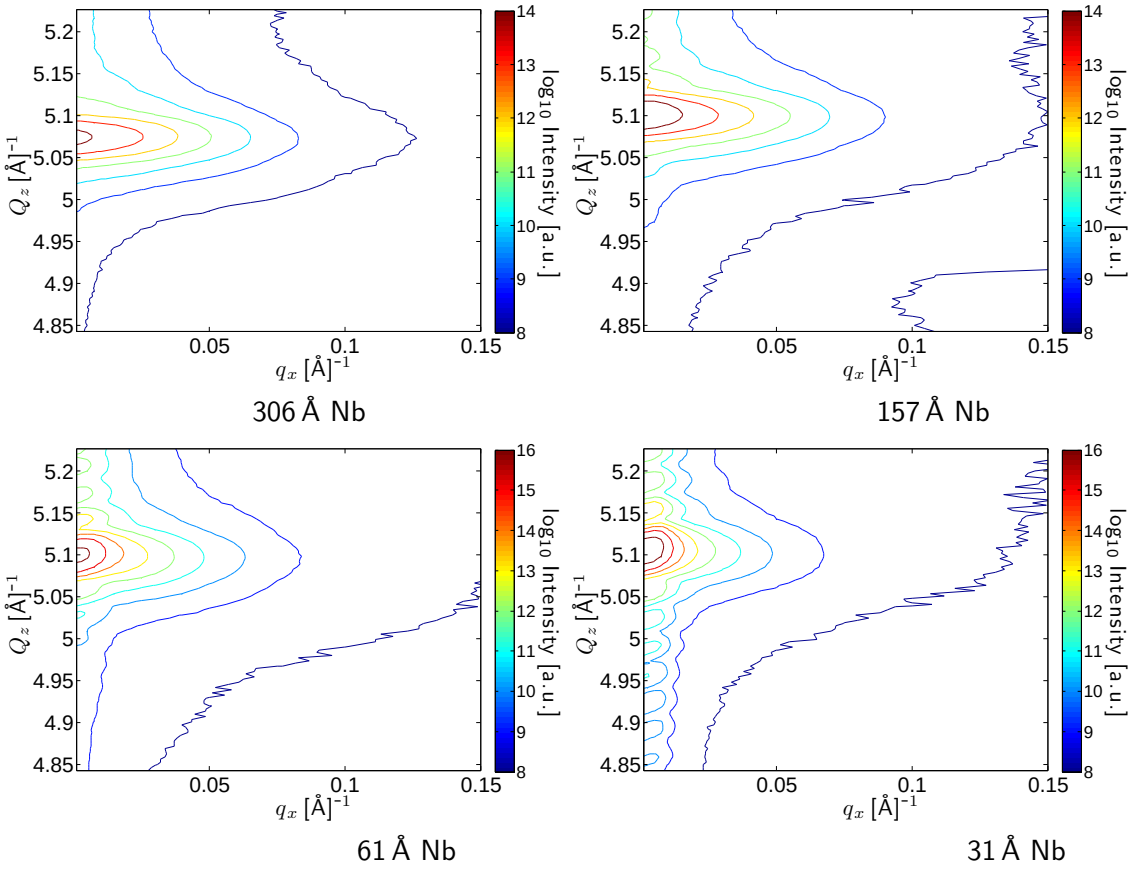

Figure 4.38: Intensity contour maps around the U(220) Bragg-peak for the samples listed in Table 4.1

more slowly with q_x are 'unmasked'.

In Figure 4.39 we see that in contrast to the changing U thickness series, the greatest movement of the peaks occurs for samples with the least thickness of Nb. This is a similar inversion in behaviour to that seen in Section 4.2.3.2 considering the behaviour of the transverse widths of the U structure peaks with regard to the buffer or overlayer thicknesses. It appears that similar behaviour is exhibited by each sample, but the thinner samples exhibit peak movement at lower values of q_x. Often it is the product $q_x d$ that is mentioned to determine film behaviour [118], but here we show that the buffer layer thickness has an equally important effect.

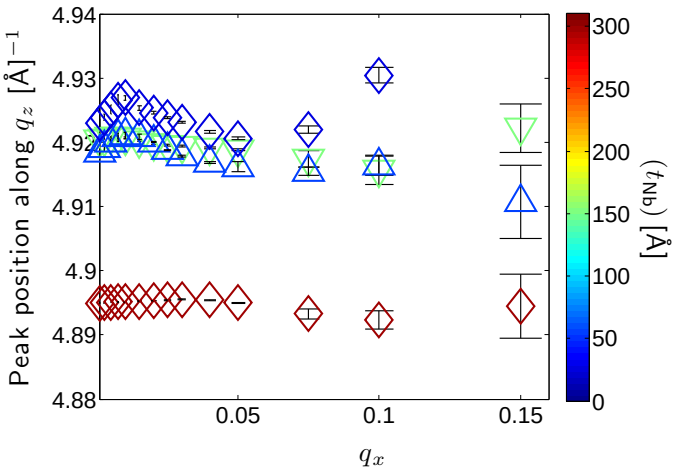

Figure 4.39: The peak positions from the radial scans shown in Figure 4.37 at different positions in q_x.

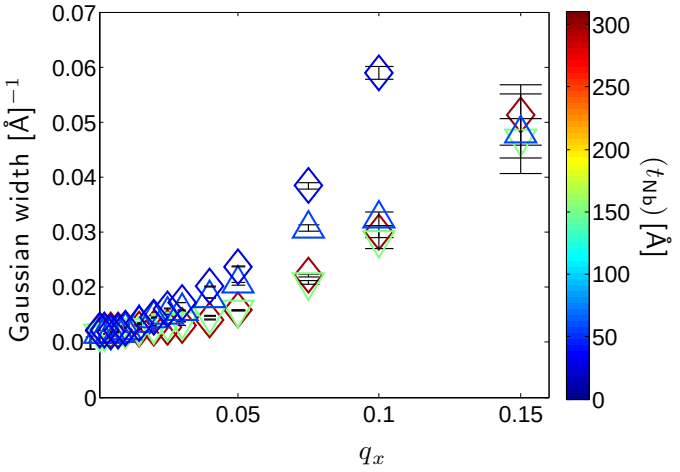

Figure 4.40: The full-widths at half-maximum of the Gaussian functions fitted to the peaks from the radial scans shown in Figure 4.37 at different positions in q_x.

In contrast to that in Figure 4.35 we see that the dependence of the widths of the peaks on q_x shown in Figure 4.40 is greatest for the thinnest samples. The gradient of the width curve increases at smaller values of q_x for thinner samples. This corresponds to samples with greatest misfit strain, as shown in Figure 4.1.

4.5.4 Summary

There is a wealth of interesting behaviour resulting from a study of the diffuse scattering, and we have shown that this behaviour is strongly dependent on the thicknesses of both the functional overlayer and the buffer layer, as well as the strains that are present in each layer. Given the importance of the microstructure of thin-films for many applications, further investigation of these effects is certainly warranted.

4.6 Summary of film microstructure

In this chapter we have used high-angle X-ray diffraction techniques to gain insight into the microstructure of thin-films, and seen how changing the thickness of the buffer layer, as well as the uranium layer itself, has a large influence on the film microstructure.

We have shown that the buffer layer thickness has an important effect on the microstructure of the uranium layer, and it is likely that this is an under-investigated feature of other systems. Unexpectedly, varying the buffer-layer thickness has the opposite effect on the microstructure of the uranium-layer as on the buffer-layer itself.

Secondly, we have found that an optimal microstructure exists over a narrow range of uranium and buffer-layer thicknesses. We believe that in similar systems with epitaxial misfit strains, varying the buffer layer thickness as well as the over layer thickness may allow further optimisation of the microstructure than varying the over layer thickness alone.

In addition, we have endeavoured to show that quoting the "mosaic spread" of a thin film is an insufficient measure of film quality. The pervasiveness of the two-component line shape means that the description is at best incomplete. This must be considered along with the fact that since many broadening mechanisms are Q-dependent, comparison of different films based on their peak width is difficult, even if the position in Q is given.

For the current samples, there are non-monotonic changes in the microstructure with thickness. The first consideration was the strain in each layer, deduced from the position of the Bragg peaks in the longitudinal direction. As the buffer-layer thickness was increased from 31 to 1274 Å, the sense of the strain in the Nb d_{110} lattice spacings change from a tensile to a compressive strain, decreasing from about +0.5% to around -0.6%. A conservation of volume argument leads us to conclude that the net strain in the plane of the film is compressive at small buffer-layer thicknesses and tensile at large thicknesses. A minimum in the magnitude of the strain in these layers falls at around 200 Å. The magnitude of the strain in the uranium layers is about an order of magnitude less than in the Nb layers, and the dependence on thickness has the opposite sense, increasing with increasing Nb thickness from around 4×10^{-4} to 9×10^{-4}.

The width of the diffraction peaks in the transverse direction was used as a coarse indicator of disorder in the plane of the film. A two-component line shape typical of many thin-film systems was seen for many samples, particularly at low thicknesses, and additional satellite peaks due to a periodic distortion of the film plane were seen in some samples. The dependence of the peak widths on buffer-layer thickness was found to follow a power-law dependence, and for the Nb layers the exponent was -0.43 for the (110) peaks, and -0.33 for the (220) peaks. The sense of the dependence was opposite for the uranium layer, with an exponent of around +0.4 for (110) and (220) peaks. We have not found a similar study in the literature, but we expect this surprising result to be a feature of other epitaxial systems. As a function of increasing uranium layer thickness, the dependence of the width of the the uranium layers was in the same sense as the dependence of the width of the niobium layers on increasing niobium layer thickness, with an exponent of -0.43.

The narrow component of the scattering is attenuated as the magnitude of the scattering vector increases in the presence of uncorrelated disorder. We have investigated the dependence of a measure of this disorder, the static Debye-Waller factor, on thickness, and found that the mean displacements of the Nb atoms perpendicular to the (110) lattice-planes increases from around 0.5 Å at small Nb to about 3 Å at large Nb thicknesses. In

the uranium layers disorder is greater, but the increase is smaller, from 3 to 4 Å.

An analysis of the dependence of the peak broadening on the length of the scattering vector allows us to separate Q-dependent and Q-independent broadening. This analysis shows that for Nb layers, the mosaicity decreases from around 0.15° to around 0.05° as Nb thickness is increased from 31 to 1274 Å , but for U layers the mosaicity increases, from around 0.002° to around 0.15°. The correlation-length for both layers increases as Nb thickness is increased, from tens of ångströmsto several hundred ångströmsfor the Nb layer, and to over 1000 Å for the U layer. As U layer-thickness is increased from 69 to 2289 Å, the mosaicity of the U layers decreased from 0.1°to 0.04°, and the correlation-length increased from 40-120 Å.

In general, the functional form of the Bragg peaks changes from a Lorentzian-squared form at low Nb thicknesses to a more Gaussian form at larger thicknesses, indicating the change from a small-displacements model of the structure to one of more general disorder. As U thickness is increased, there is a non-monotonic change, and the Lorentzian-squared component is dominant at intermediate thicknesses, of around 370 Å.

As Nb thickness is increased, the aspect ratio of the peaks in the q_z, q_x-plane tends to decrease from 0.6 to 0.15 for U (110) and (220) peaks, from 0.6 to 0.2 for Nb (110) peaks and from 1.2 to 0.2 for Nb (220) peaks. As U thickness is increased there is a maximum in the aspect ratio for U (110) and (220) peaks at around 400 Å.

Our initial model of the films was the perfect layer model described by many researchers. Reciprocal-space maps around the Bragg-reflections have shown that the dependence of the width of the peaks in the longitudinal direction on q_x does not support this model.

Samples of intermediate thickness show anomalous peak aspect ratios, minimum mosaicity and peak width, as well as showing different behaviour in the peak-width as q_x is increased. Scattering from these samples corresponds most closely with a small-displacements model, in which the main cause of distortion in the lattice arises from the strain fields around

edge misfit dislocations of low density. We believe that this thickness corresponds to the optimum microstructure. In summary we have seen that as the thickness of a layer increases, the structural correlation length within that layer increases, but uncorrelated disorder over large distances also increases.

The thickness of each of the epitaxial layers in the samples has an important effect on the microstructure of those layers, as well as those grown epitaxially on top. In the literature we note that there is generally insufficient discussion of the buffer-layer thickness for similar systems. Furthermore, we have demonstrated the wide variety of techniques that can be used to analyse the form of transverse X-ray scans, and the instructive conclusions that may be drawn.

In the following chapter we shall investigate the effect of thickness on the charge-density wave ground state existing in uranium at low temperature.

Chapter 5

The thickness-dependence of the chage-density wave state in uranium thin-fims

5.1 Experimental approach

In this study we aim to characterise the α-U CDW in thin-film samples as temperature and thickness are varied. By analysis of the scattering from the CDW satellites, primarily around the U(221)-reflection, we shall characterise the CDW in terms of its periodicity, correlation-length and order parameter. We shall also see how the anomalous temperature-dependence of the lattice at low-temperature, which is a result of the CDW formation, changes with film thickness.

Here we present the results of scattering experiments performed at the XMaS beamline at ESRF on epitaxial uranium films. We have used the results from a total of four experiments, for each of which a different set of samples was examined. After a preliminary experiment on a 5000 Å film mentioned above, the initial motivation was to determine

Experiment	Sample reference	t_U (Nominal) [Å]	t_U determined by XRR [Å]
SI-01699	SN242	1000	1477
	SN241	500	715
	SN243	50	69
SI-01841	SN258	300	373
	SN259	200	234
	SN260	100	117
	SN282	75	91
SI-01862	SN321	2000	2289
	SN242	1000	1477
	SN320	750	771
	SN317	500	635
	SN323	350	363
	SN259	200	234
	SN322	150	154
	SN260	100	117
	SN282	75	91
	SN243	50	69
SI-01879	SN260	100	117

Table 5.1: The samples of varying uranium-layer thickness studied during each of the four experimental runs at XMaS

whether a minimum film-thickness existed for formation of the CDW. A series of samples of 69–1477 Å-thickness was prepared for experiment SI-01699. No CDW satellites were found for thicknesses below 715 Å, so a further set of samples of 91–373 Å-thickness was prepared for the second experiment, SI-01841, to determine the minimum thickness more finely, but the CDW-satellites were seen in all samples. Experiment SI-0162 allowed a survey of a wide range of uranium and niobium-buffer-layer thicknesses, from 69–2289 Å, and a 117 Å sample was examined during experiment SI-01879. We have kept the results from each experiment separate for the temperature-dependence studies, as some differences calibration of the thermo-regulation occurred between experiments.

The samples studied during each experiment are listed in Tables 5.1 and 5.2.

Experiment	Sample reference	t_{Nb} (Nominal) [Å]	t_{Nb} determined by XRR [Å]
SI-01862	SN325	500	306
	SN322	350	157
	SN330	150	61
	SN324	50	31

Table 5.2: The samples of varying niobium-buffer-layer thickness studied at XMaS

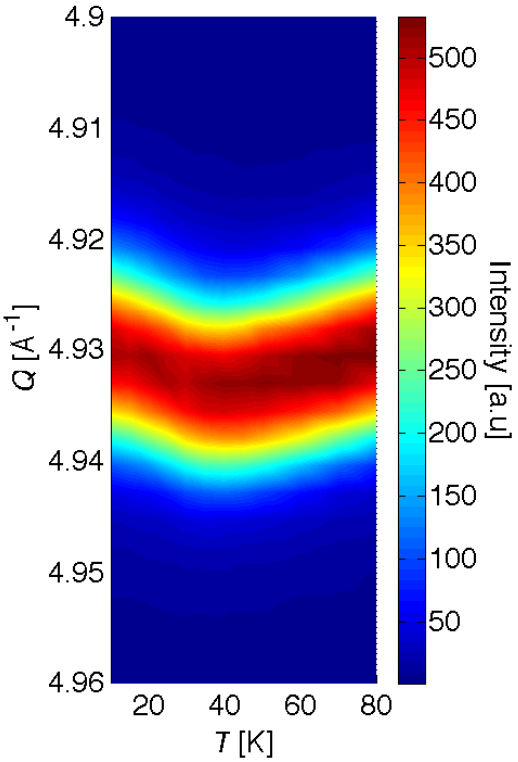

Figure 5.1: The temperature-dependence of the scattered intensity around the U(220) position for a 1477 Å sample

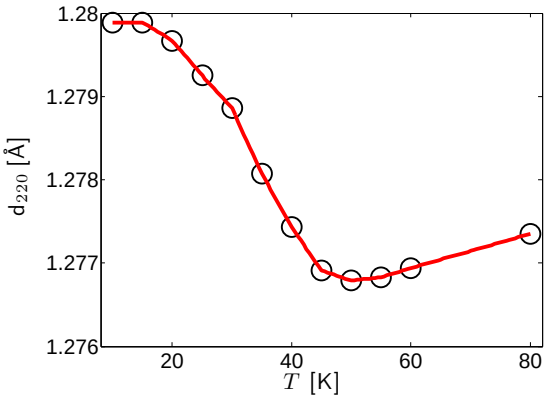

Figure 5.2: The temperature-dependence of the d_{220} lattice-spacing in the bulk. Calculated for α-U using the data in Figure 1.3. The solid line is a guide for the eye.

5.2 Temperature-dependence of the lattice

Figure 5.1 shows the intensity of scattering around the U(220) Bragg-reflection along the [220] direction, normal to the plane of the film for the 1477 Å sample examined in experiment SI-01699. The decrease in the length of the scattering vector, Q, at the peak below around 40 K, shows that there are minima in the a and b lattice-parameters, and points to the presence of the CDW. The peaks for each sample in this experiment were parametrised by a least-squares fit to a Gaussian lineshape at each temperature, and the behaviour of the d_{220} lattice-spacing deduced from the peak-positions is shown in Figure 5.3 as a function of temperature.

There is a minimum seen in the lattice parameter for all samples, and therefore we expect to observe the CDW satellites in each of these samples, including the sample of 69 Å. This is significant, since it indicates that there is no suppression of the CDW due to thickness in a sample of as little as 69 Å thickness.

The depth of the minimum in the lattice parameter shows a clear thickness-dependence, with the greatest relative change occurring in the smallest sample, and the relative change decreasing as thickness is increased. The position of the minimum also changes with thickness, but the change is not monotonic. The 715 Å sample shows a minimum in the

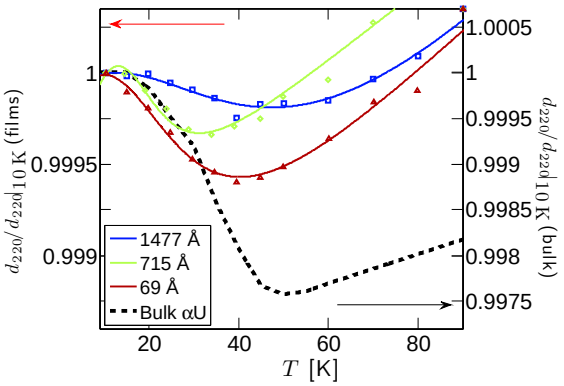

Figure 5.3: The temperature dependence of the d_{220} lattice-spacing, deduced by analysis of the U(220) lattice peak from Experiment SI-01699. The full lines are guides to the eye, and the dashed line indicates the bulk behaviour.

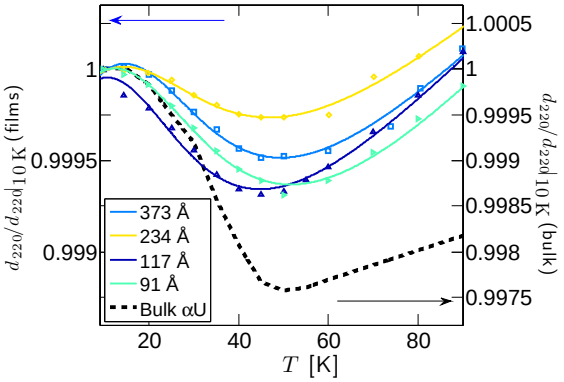

Figure 5.4: The temperature dependence of the d_{220} lattice-spacing, deduced by analysis of the U(220) lattice peak from Experiment SI-01841.The full lines are guides to the eye, and the dashed line indicates the bulk behaviour.

lattice parameter at the lowest temperature.

A similar analysis was performed for the scattering from samples included in Experiment SI-01841, with thicknesses between 91 and 373 Å. The d_{220} lattice-spacing at base temperature of 10.4 K is similar across the series, which indicates that the epitaxial strain within the samples is approximately similar. There is no clear trend in either the temperature at which the minimum in the lattice parameter occurs or the depth of the minimum as thickness is increased.

For the samples in Experiment SI-01862 there is a symmetrical dependence of the d_{220}

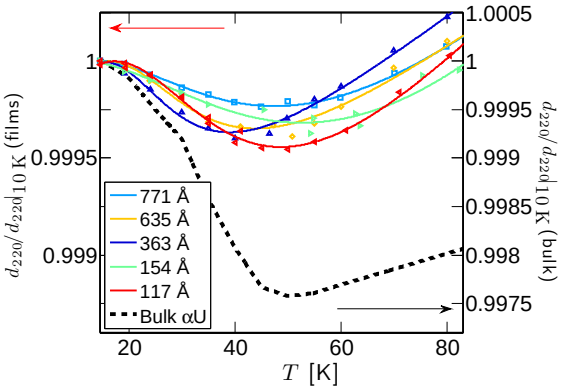

Figure 5.5: The temperature dependence of the d_{220} lattice-spacing, deduced by analysis of the U(220) lattice peak from Experiment SI-01862. The full lines are guides to the eye, and the dashed line indicates the bulk behaviour.

lattice-spacing at base temperature on thickness about the 363 Å sample. The lattice-spacing is largest for this sample, and this also corresponds to the sample for which the minimum of the lattice parameter is reached at the lowest temperature. The trend in $d_{220}|_{14.5\,\mathrm{K}}$ with layer thickness also mirrors the trend in the temperature and the depth of the minimum, if we exclude the 154 Å sample. This suggests that the epitaxial strain in the samples is affecting the transition to the CDW state.

5.2.1 Summary

Figure 5.6 shows the variation in the temperature at which the minimum in the d_{220} lattice-spacing occurs with layer thickness, corresponding to the onset of the transition to the CDW state. Below film-thicknesses of around 200 Å there is a decrease in the temperature of the transition with decreasing thickness, but above 200 Å there is a non-monotonic variation.

The discussion above has lead us to believe that there is a relationship between the lattice spacing at base temperature and the temperature of the minimum in the lattice spacing. The left panel of Figure 5.7 shows the variation in the lattice spacing at base temperature with the film thickness. The non-systematic variation in the lattice spacings with thick-

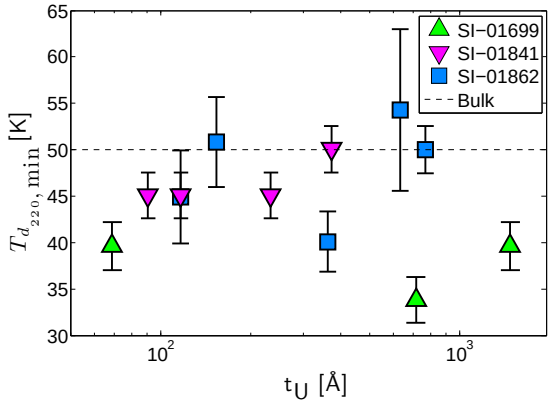

Figure 5.6: The temperature at which there is a minimum in the d_{220} lattice-spacing, indicating the onset of the CDW transition, as a function of U-layer thickness. The dashed line indicates the temperature at which the minimum occurs in the bulk[7]

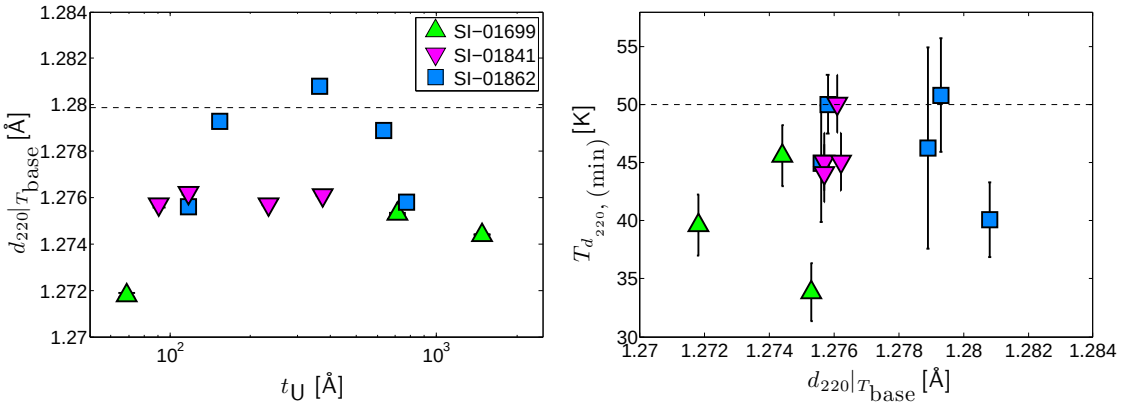

Figure 5.7: (left panel) The d_{220} lattice-spacing at 10 K for samples of different uranium-layer-thickness. For this plot the error-bars lie within the markers. (right panel) The temperature at which there is a minimum in the d_{220} lattice-spacing, indicating the onset of the CDW transition, as a function of the d_{220} lattice-spacing at 10 K. The dashed line indicates the temperature at which the minimum occurs in the bulk[7]

ness suggests varying strain states in the samples due to unaccounted for changes in the deposition conditions such as base chamber pressure, and degradation or replacement of the targets between runs. It is for this reason that we have kept the data from each experiment separate since the samples for each experiment were grown together in batches, but at different times.

A more clear trend is seen if the film thickness is removed as a variable, however, and

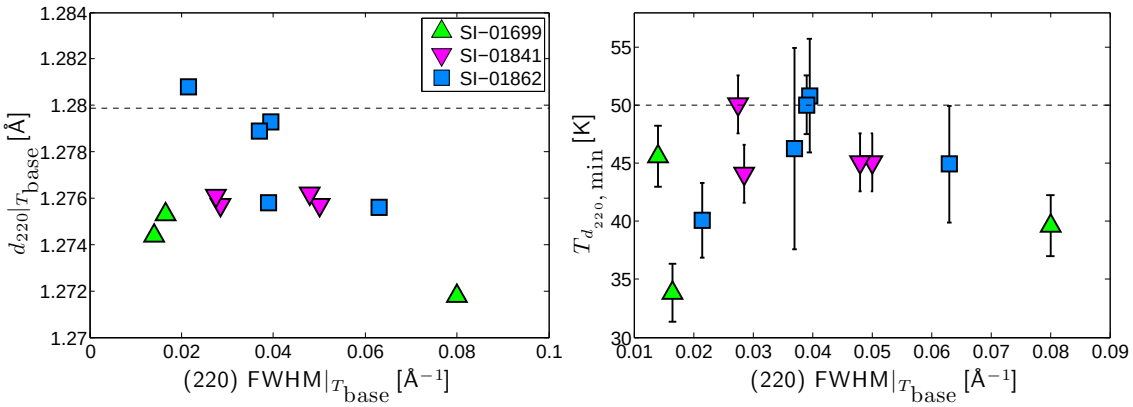

Figure 5.8: (left panel) The dependence of the d_{220} lattice spacing at base temperature on the FWHM of the (220) lattice reflection at base temperature. (right panel) The temperature at which there is a minimum in the d_{220} lattice-spacing, indicating the onset of the CDW transition, as a function of the full-width at half-maximum of the U(220) reflection. The dashed line indicates the temperature at which the minimum occurs in the bulk[7]

the temperature of the minimum plotted as a function of the lattice spacing at base temperature, which is indicative of the strain in the film. The CDW persists to higher temperatures for samples with intermediate levels of strain, with $d_{220} \approx 1.279\,\text{Å}$. The data from Experiment SI-01699 show a dependence on d_{220} that does not fit with those of the other experiments.

There is a link, explored in the previous chapters of this thesis, between the strain in the films and the density of defects such as misfit dislocations. This defect density may be coarsely characterised by the measurement of the FWHM of the lattice peaks. It might be that the CDW is affected less by the strain in the film and more by the density of defects. Figure 5.7 shows the variation in the temperature of the minimum of the d_{220} lattice-spacing with the FWHM of the (220) lattice peak at base temperature. There is clearly an optimum density of defects for the persistence of the CDW to higher temperatures. It could be that the CDW lattice is pinned by defects, so for low defect densities there is a small energy barrier for the transformation to the normal state.

Some caveats are mentioned here. There is likely to be a systematic difference in the temperature measured at the sample position between experiments. This is due to the

fact that the thermocouples in different cryostats may be calibrated differently, and even replaced between runs. For this reason the experimental uncertainty associated with each temperature data point may be another 5 K in magnitude when making comparisons between experimental runs. It is significant that for such large variations in thickness and microstructure as seen in this series of samples, the temperature of the CDW transition does not change a significant amount, and might even be unaffected to within the uncertainties of our measurements.

5.3 Observation of the CDW satellites

5.3.1 Reciprocal-space maps

Reciprocal-space mapping is a useful tool in the representation of the satellite peaks in reciprocal-space, allowing quick qualitative comparisons to be made between samples. We have mapped the intensity in the (2.504 K L) plane, around around the (2.504 2 1) position in reciprocal-space for the samples examined during experiments SI-01699 and SI-01841. The findings are presented below. It is noted that over such large areas of reciprocal-space, alignment of the diffractometer may not be perfect, so absolute positions are approximate.

5.3.1.1 1477 Å sample

An intensity-surface depicting the intensity of scattering in the (2.5 K L)-plane for a 1477 Å samples is shown in Figure 5.9. The satellite peaks are clearly visible at ($H = 2.5045$, $K \approx 2 \pm .2$, $L \approx 1 \pm .2$). As in the 5000 Å film there is a clear IA between the $2^+2^+1^\pm$ and $2^+2^-1^\pm$ satellites, with the peak intensity ratios in this case found to be $\frac{2^+2^+1^+}{2^+2^-1^+} \approx 8.7$ and $\frac{2^+2^+1^-}{2^+2^-1^-} \approx 11$.

It is also clear that the $2^+2^+1^\pm$ satellites may be resolved into two separate peaks. These are identified as 1st and 5th order satellites. The fifth-order satellites can be denoted

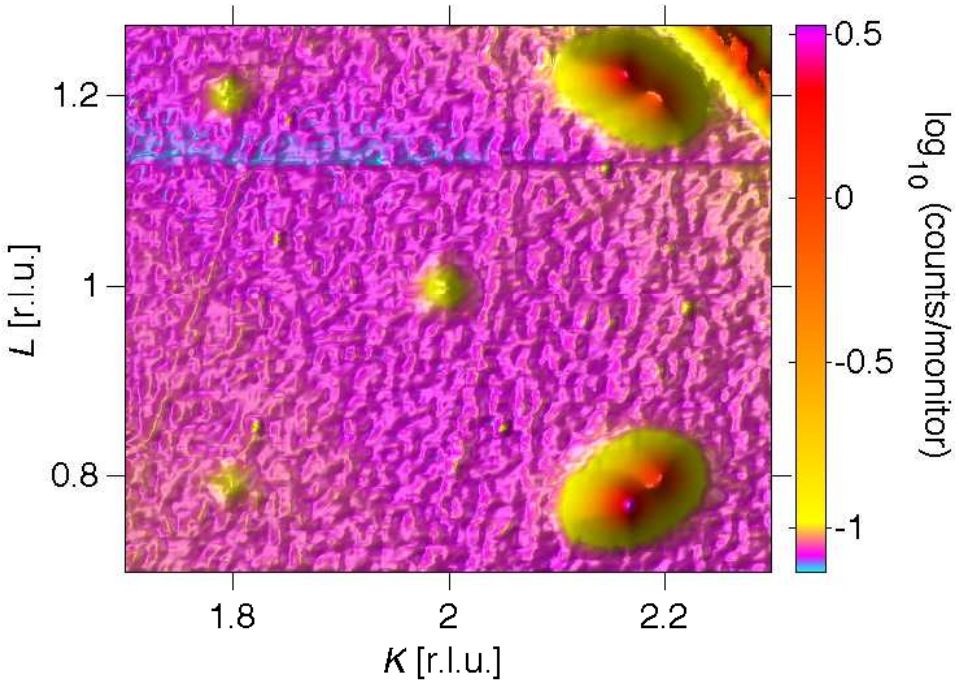

Figure 5.9: An intensity-surface depicting the scattering in the (2.5045 K L) plane of reciprocal space for a 1477 Å sample at 10 K. CDW satellites are seen at ($H = 2.5045$ $K \approx 2 \pm .2$ $L \approx 1 \pm .2$). The strong peaks at the ($H = 2.5045$ $K \approx 2.2$ $L \approx 1 \pm .2$) are composed of first (most-intense) and fifth-order satellites. In addition the 'Smith-satellite' is visible at $\mathbf{Q} = (2.5045\ 2\ 1)$. There is a step change in the background intensity along $L \approx 1.12$, which is an artefact from the synchrotron refill. An arc of intensity in the top right-hand corner is due to scattering from the polycrystalline Be dome of the cryostat, which encloses the sample.

$2^{+}3^{5-}0^{5+}$ and $2^{+}3^{5-}2^{5-}$, and their presence indicates that the periodic lattice-distortion is not a pure sine-wave but has higher harmonics. This is discussed in Marmeggi et al. [202].

In contrast to the data reported in Springell et al. [85], the 'Smith-satellite' seen in Figure 5.9 does not appear to be spurious. The temperature-dependence of the intensity at the position of the peak is shown in Figure 5.10. The intensity is below the background level at temperatures above 25 K, which is far below the CDW ordering temperature. In the bulk [10], intensity at this position persists above 40 K. The position and movement of the peak is different to that of the bulk. In the bulk, a peak is seen at (2.491 K L) at 10 K and there is a movement to lower H as the temperature is increased. The peak in Figure 5.10

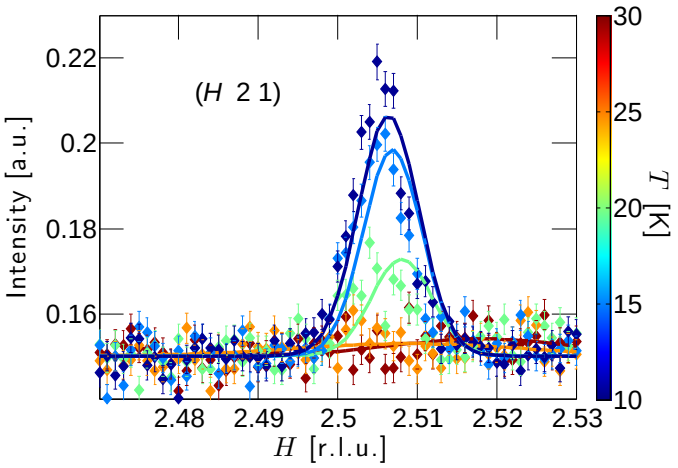

Figure 5.10: The temperature-dependence of the peak at (H 2 1) in Figure 5.9. The full lines are the results of a least-squares fit of a Gaussian function to the data points at each temperature and serve as guides to the eye.

is located slightly above (2.506 2 1) and moves in the positive-H direction upon heating.

5.3.1.2 635 Å sample

Figure 5.11 shows reciprocal-space maps of intensity around the expected positions of the satellite peaks seen in Figure 5.10 for a 635 Å sample. The $2^{+}2^{+}1^{\pm}$ are clearly visible, but there is little difference in intensity from the background intensity at the positions of the $2^{+}2^{-}1^{\pm}$ satellites or the Smith-satellite. The fifth-order satellites are still visible, however, and are approximately one-third of the peak intensity of the first-order satellites.

5.3.1.3 Summary

As thickness is decreased the ability to resolve the peaks above the background becomes more difficult, and reciprocal-space mapping becomes impractical. A composite figure depicting the intensity of scattering around the $2^{+}2^{+}1^{\pm}$ satellite positions for samples varying U thickness at 10 K is shown in Figure 5.12. For samples of thickness less than 234 Å the peak is difficult to distinguish. The satellites in the 373 Å sample appear slightly

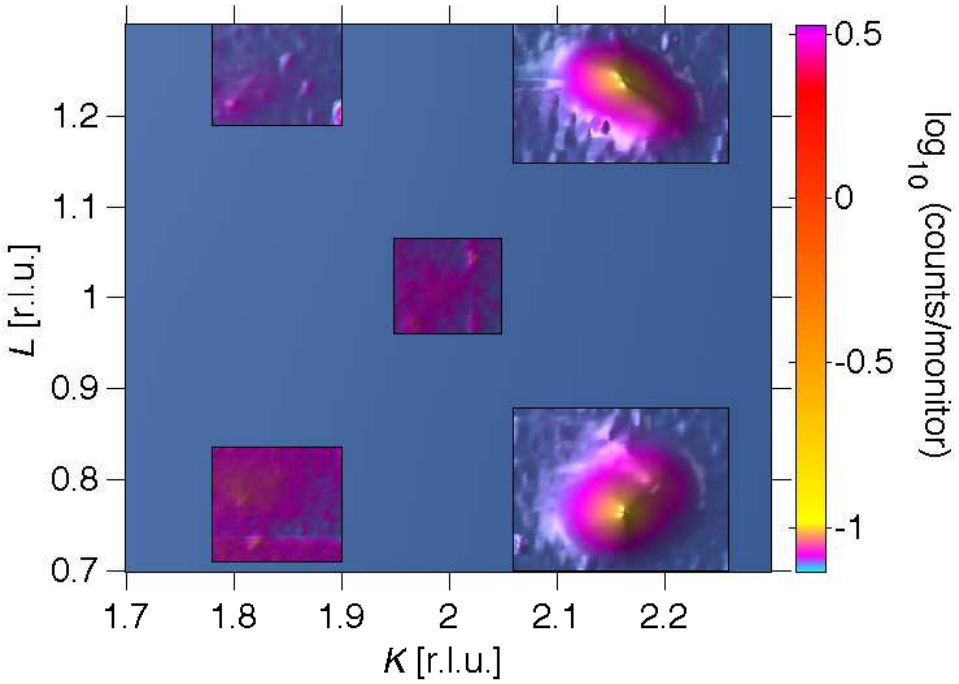

Figure 5.11: A composite figure depicting the scattering in the (2.5 K L) plane of reciprocal space for a 635 Å sample at 10 K. Reciprocal space maps around the expected positions of the CDW satellites and the Smith-satellite are plotted against a computer-generated background for clarity

shifted towards lower K values, and there is a decrease in the breadth of the peaks with decreased thickness.

5.3.2 69 Å sample

The CDW satellites in the thinnest sample measured are weakly visible, and presented here in Figure 5.13. This measurement gives an upper limit to the value of the minimum thickness needed to support the CDW. Long counting times were needed to resolve the peaks above the background. Consequently the number of counts taken at each point was large, and the statistical uncertainty at each point is relatively small, leading to small errors bars on each point. However, since a large proportion of the counts are from the random scattering effects leading to the background intensity, the data does not appear smooth.

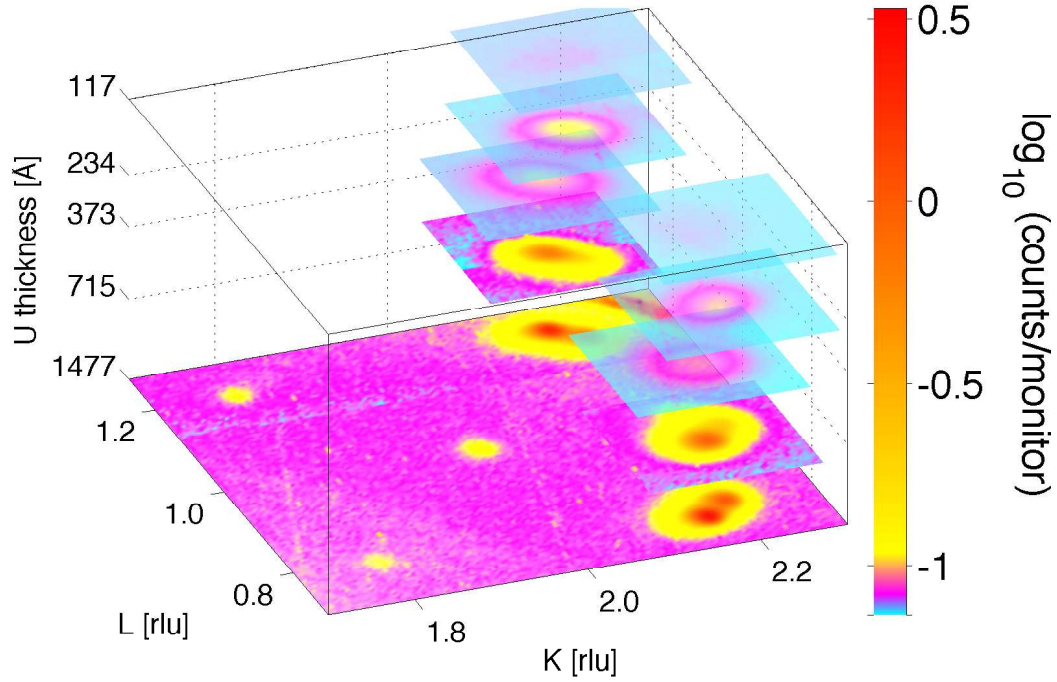

Figure 5.12: A composite figure depicting the intensity of scattering in the (2.5 K L) plane of reciprocal space for a samples of varying U thickness at 10 K

5.3.3 Varying U thickness

5.3.3.1 L-scans—Characterisation of the CDW state

Here we present the results of X-ray scattering from the CDW satellite positions in samples of a range of U-thicknesses, performed during experiment SI-01869. We have performed scans across the $2^+2^+1^+$ and $2^+2^+1^-$ satellites in samples of varying uranium layer thickness, from 69 Å to 2289 Å, as listed in Table 5.1. The peaks were parametrised by a least-squares fit to a Gaussian function. The integrated intensity and FWHM of the peaks are shown in Figure 5.14 as a function of U layer thickness, along with the length of the component of the CDW wavevector along L, q_z, which lies in the plane of the film.

There is a strong similarity between the thickness-dependence of the breadth of the CDW peak and that of the FWHM of the structure peaks in Section 4.3.2. This is suggestive

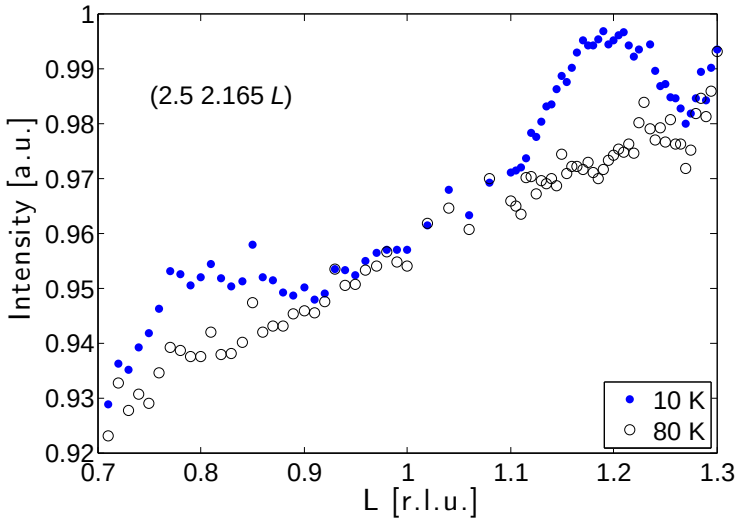

Figure 5.13: Scans in L across the $2^+2^+1^+$ and $2^+2^+1^-$ satellite positions at 10 K and 80 K for a 69 Å U sample. Long counting times were needed to resolve the peaks above the background. Consequently the number of counts taken at each point was large, and the statistical uncertainty at each point is relatively small, leading to small errors bars on each point. However, since a large proportion of the counts are from the random scattering effects leading to the background intensity, the data does not appear smooth.

Peak	a [Å^{c-1}]	c	b [Å^{-1}]
$2^+2^+1^+$	8.52 ± 1.7	-1.438 ± 0.038	0.017 ± 0.0005
$2^+2^+1^-$	74.3 ± 36.3	-1.864 ± 0.10	0.014 ± 0.0005
U(221)	1.245 ± 0.070	-0.643 ± 0.012	0.058 ± 0.002
U(110)	0.219 ± 0.010	-0.483 ± 0.009	0.015 ± 0.0008
U(220)	0.828 ± 0.053	-0.687 ± 0.013	0.033 ± 0.002

Table 5.3: The coefficients for the fits, (peak width)$= a\,t_{\mathrm{U}}^c + b$, to the integral breadths, β, of the $2^+2^+1^+$ and $2^+2^+1^-$ CDW-satellite peaks shown in Figure 5.14, along with the coefficients of similar fits to the U Bragg-reflections listed in Table 4.5.

that disorder in the crystal promotes disorder in the CDW lattice. Least-squares fits to a power law of the form $a(t_{\mathrm{U}})^c + b$ have been made to the integral breadths of the Gaussian functions fitted to the CDW-satellite peaks, and the coefficients are listed in Table 5.3, along with the coefficients from similar fits to the U structure peaks. The larger value of the exponent suggests that the sensitivity of the CDW to changes in the microstructure that accompany decreasing thickness is greater than that of scattering from the lattice.

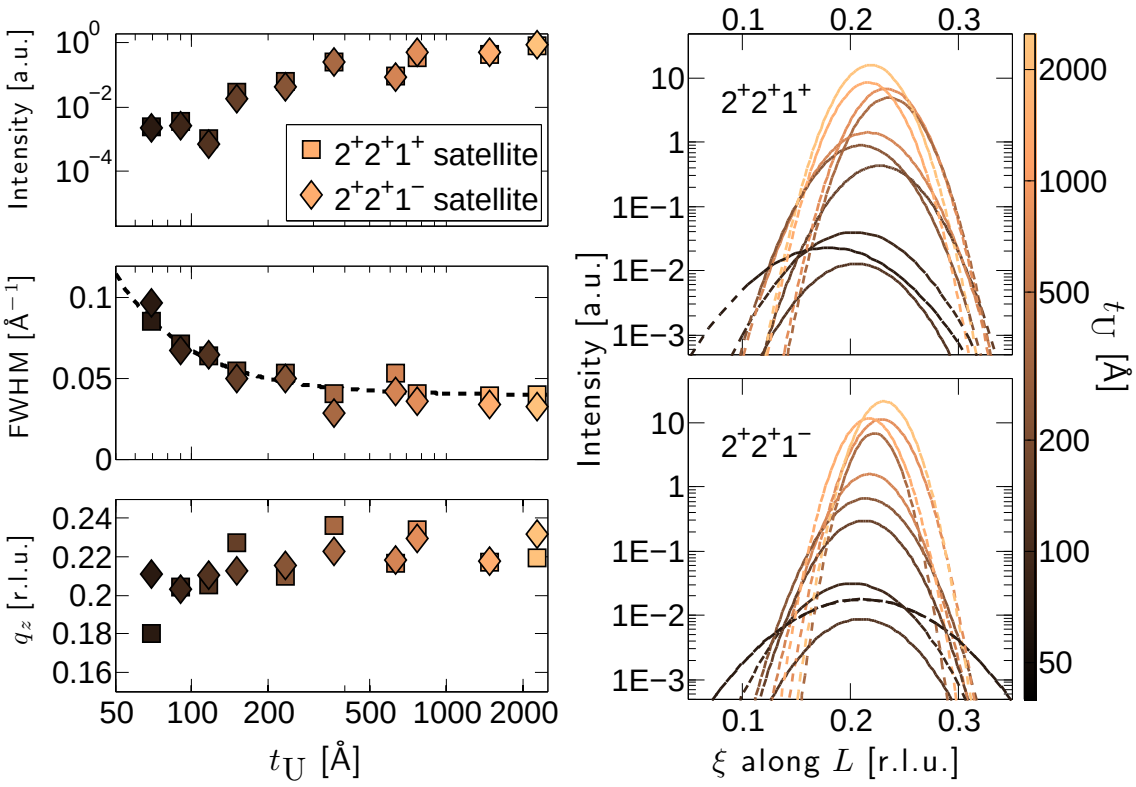

Figure 5.14: (left panel) The intensity and FWHM of the $2^+2^+1^+$ and $2^+2^+1^-$ satellites of the charge-density wave, with least-squares fits of Gaussian functions to the peaks shown in the right panel. The left panel also shows the length of the q_z component of the CDW wavevector, as deduced from the position of the satellite peaks along L, as a function of uranium-layer thickness at 10 K. The dotted line in the central panel is a least-squares fit of the data to a power law dependence on thicknesses as described in the text.

Comparing the value of of $q_z|_{10\,\mathrm{K}}$ in the films to that in the bulk shown in Figure 2.11, however, the tendency is towards the bulk value in the thinnest films, not the thickest as might be expected. There is a strong correlation between the behaviour of the FWHM of the CDW and q_z. It is possible that the large number of discommensurations in thin-films allows the CDW to adopt a bulk-like behaviour over short-distances. One important observation is that the positions of the $2^+2^+1^+$ and $2^+2^+1^-$ satellites are not symmetrical about $L = 1$.

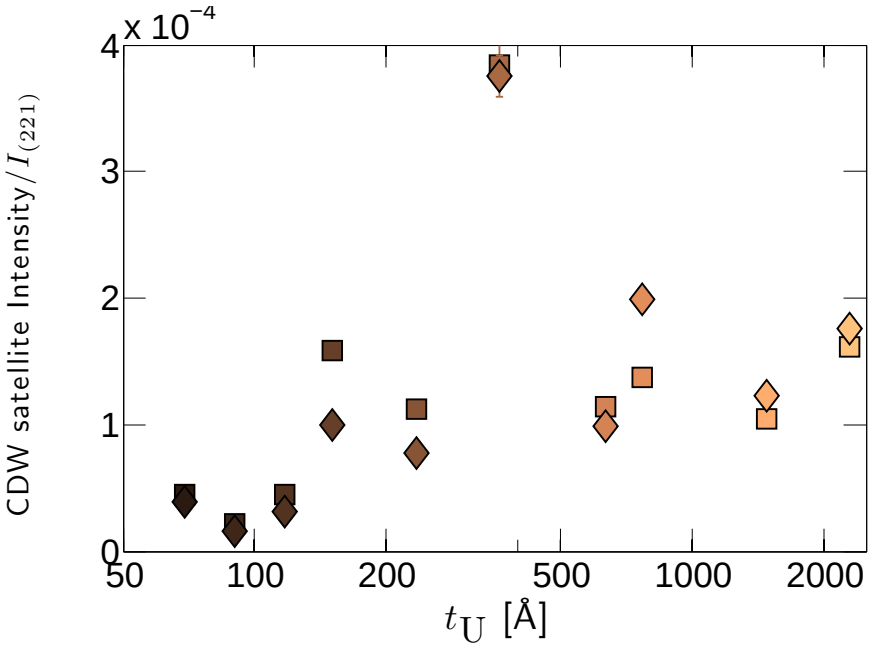

Figure 5.15: The intensity of the CDW satellites normalised to that of the (221) structure reflection, as a function of U layer-thickness. Intensities are the peak heights×integral-breadths of Gaussian functions fitted to L-scans across the satellite-peaks and U(221) reflections.

5.3.3.2 L-scans—The intensity of the CDW satellites

For a measure of the 'strength' of the CDW transition in the films, we have compared the intensity of scattering in the CDW satellites to the intensity of the 'parent' Bragg-reflection, which in this case is the U(221). Figure 5.15 shows the normalised intensities of the CDW satellites for films of varying t_U. There is a general increase in the intensity with the thickness, which is suggestive of greater CDW ordering in the thicker samples.

The 363 Å sample is clearly an outlier in the statistical sense, and should be excluded from further analysis. However, the large relative strength of the CDW in this sample corresponds with its exceptional microstructure, as seen in the previous chapter.

5.4 Temperature-dependence of the CDW satellites

In this section we shall investigate how the characteristics of the CDW change on heating from around 10 K. In bulk uranium there exist three well-defined transitions to different CDW phases, α_1, α_2 and α_3, in which none, one or all of the CDW wavevector components is commensurate with the lattice, as seen in Figure 2.11. The transitions occur at the following temperatures: $T_{\alpha\to\alpha_1} = 43\,\mathrm{K}$, $T_{\alpha_1\to\alpha_2} = 37\,\mathrm{K}$ and $T_{\alpha_2\to\alpha_3} = 22\,\mathrm{K}$. In a 5000 Å U film[85] no obvious lock-in transitions were seen, but at base temperature of 10 K the q_X and q_y components are approximately at the bulk values in the α_3 phase.

5.4.1 Scans along H

Figure 5.16 shows scans across the $2^+2^+1^+$ and $2^+2^+1^-$ CDW satellites performed at temperatures from 10–50 K. The scans on the 715 and 1477 Å samples were performed during Experiment SI-01699 and the remainder performed during Experiment SI-01841. A spurious peak is seen in the scan across the $2^+2^+1^+$ satellite for the 1477 Å sample; as its intensity persists above the CDW transition it is considered unrelated to the phenomena of interest, and is possibly due to Bragg reflection from the sapphire substrate, its movement with temperature indicating that it is from a cooled part of the system.

All peaks show a movement towards $H = 2$ as temperature is increased, and this is similar to the behaviour in the 5000 Å film shown in Figure 1.8. However, in the 5000 Å film q_x is approximately $\frac{\pi}{a}$ at 10 K, corresponding to the bulk value, whereas in the current samples the value of q_x is systematically larger, reaching the value of $\frac{\pi}{a}$ only at 45–50 K. In order to ensure that this was not due a systematic misalignment of the diffractometer, we searched for the $2^-2^+1^+$ CDW satellite in a 154 Å sample during Experiment SI-01862. The $2^+2^+1^+$ and $2^-2^+1^+$ satellites were located at positions of $(2.508, 2.1605, 1.222)$ and $(1.509, 2.1615, 1.222)$ respectively at 10 K. If we take the length of q_x to be half the separation of the two peaks in H we obtain the expected value of $q_z = \frac{\pi}{a}$. We mention here that

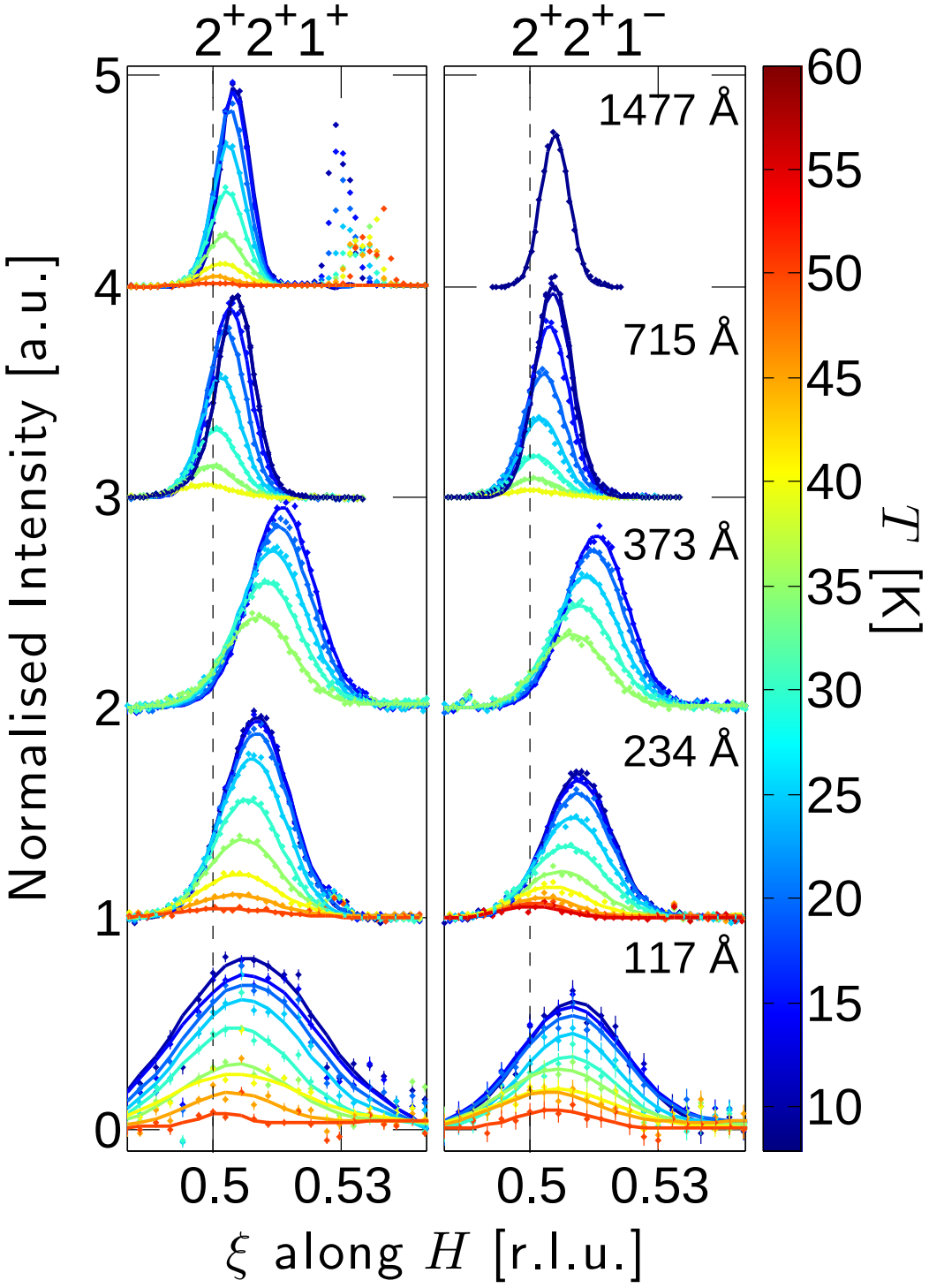

Figure 5.16: Scans in H across the $2^+2^+1^+$ and $2^+2^+1^-$ CDW satellites performed at temperatures from 10–50 K, for samples of 117–1477 Å thickness. Data from experiments SI-01699 and SI-01841. Solid lines show least-squares fits to Gaussian functions. $\xi = |2 - H|$. The dotted lines indicate the position of the peak centre in the bulk α_3-phase.

this misalignment is despite alignment of the sample at the same temperature such that the two reflections used to calculate the transformation between diffractometer-space and reciprocal space, the (220) and (221) reflections, were located at (2.004 2.0176 -0.010172) and (2.0068 2.0067 0.99977) respectively. The difficulty in calculating accurate positions in reciprocal space is likely to be due to the changes in the symmetry of the uranium unit cell due to the presence of the CDW, which were not taken into account in the diffractometer software.

These considerations prompt a brief discussion of the limitations in the accuracy of the present data. The samples were aligned at base temperature$\approx$10 K, but changes in the U lattice parameters as the sample is heated lead to inaccuracies in the calculation of reciprocal-space positions. A more accurate experiment would require realignment of diffractometer- and reciprocal-spaces at each temperature, which involves finding the positions of the (220) and (221) Bragg-peaks, and was deemed prohibitively time-consuming for the current work. Another consideration is that the current scans were performed along the same reciprocal-space vectors at each temperature, but the movement of the satellite peaks is not along the same vector, as shown below. This has two consequences: First, the peak in intensity will not fall on the scan vector, so the measured intensity will not correspond to the peak intensity. Second, the projection of the position of peak intensity along the scan vector will only correspond to the true position if the peak is spherical, which is not necessarily true.

There appears to be less movement of the peaks, so less change in the CDW vector, with temperature as the film thickness is reduced. An analysis of the peak parameters follows this section.

5.4.2 Scans along K

Scans along K across the satellites are shown in Figure 5.17. Similar behaviour is seen to the scans along H, which is to be expected as both H and K point out of the plane of the

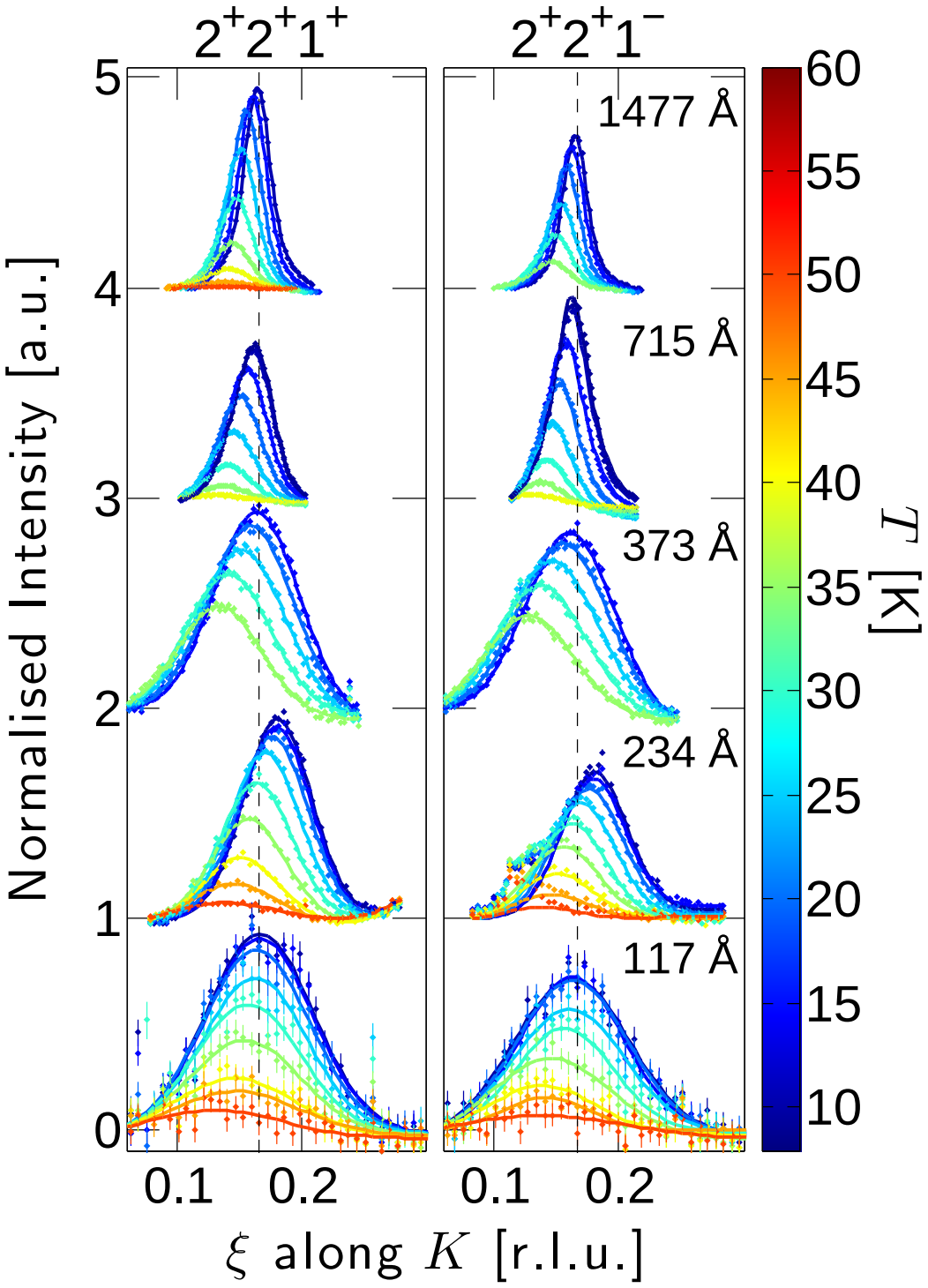

Figure 5.17: Scans in K across the $2^+2^+1^+$ and $2^+2^+1^-$ CDW satellites performed at temperatures from 10–50 K, for samples of 117–1477 Å thickness. Data from experiments SI-01699 and SI-01841. Solid lines show least-squares fits to Gaussian functions. $\xi = |2 - K|$. The dotted lines indicate the position of the peak centre in the bulk α_3-phase.

film. Clear from this figure is the increase in the breadths of the peaks compared to those in H. This is due to the poorer resolution of the diffractometer in this direction.

5.4.3 Scans along L

For scans along both H and K there is little difference between the behaviour of the $2^+2^+1^+$ and $2^+2^+1^-$ satellites. For the scans in L shown in Figure 5.18, however, clear differences in the direction of movement of the satellites are seen. The greatest difference appears in the scans for the 373 Å sample, which also shows anomalous breadth in this direction.

5.4.4 CDW satellite Intensity

Figure 5.19 shows how the integrated intensities of the CDW satellites decreases on heating from base temperature. Two features of the data are striking. First, there is no suppression of the maximum temperature at which intensity from the CDW satellites is visible as thickness is increased. Second, there is no sharp drop off in intensity as the transition temperature is reached, as would be expected if the CDW were governed by a BCS-type order parameter. Instead there is a point of inflection in the curves at around 30 K, and a subsequent slow decrease in intensity up to around 50 K.

5.4.5 CDW wavevector components

Figure 5.20 shows the components of the CDW wavevector as a function of temperature, obtained from parametrisation of the peaks in Figures 5.16, 5.17 and 5.18, averaged across the $2^+2^+1^+$ and $2^+2^+1^-$ satellites. As seen in the 5000 Å film, there do not appear to be any lock-in transitions at the temperatures sampled. In general the behaviour in these thinner films echoes that in the 5000 Å film, but there is a variation across the samples. This variation is not, however, monotonic, and there are no obvious trends, except in q_z.

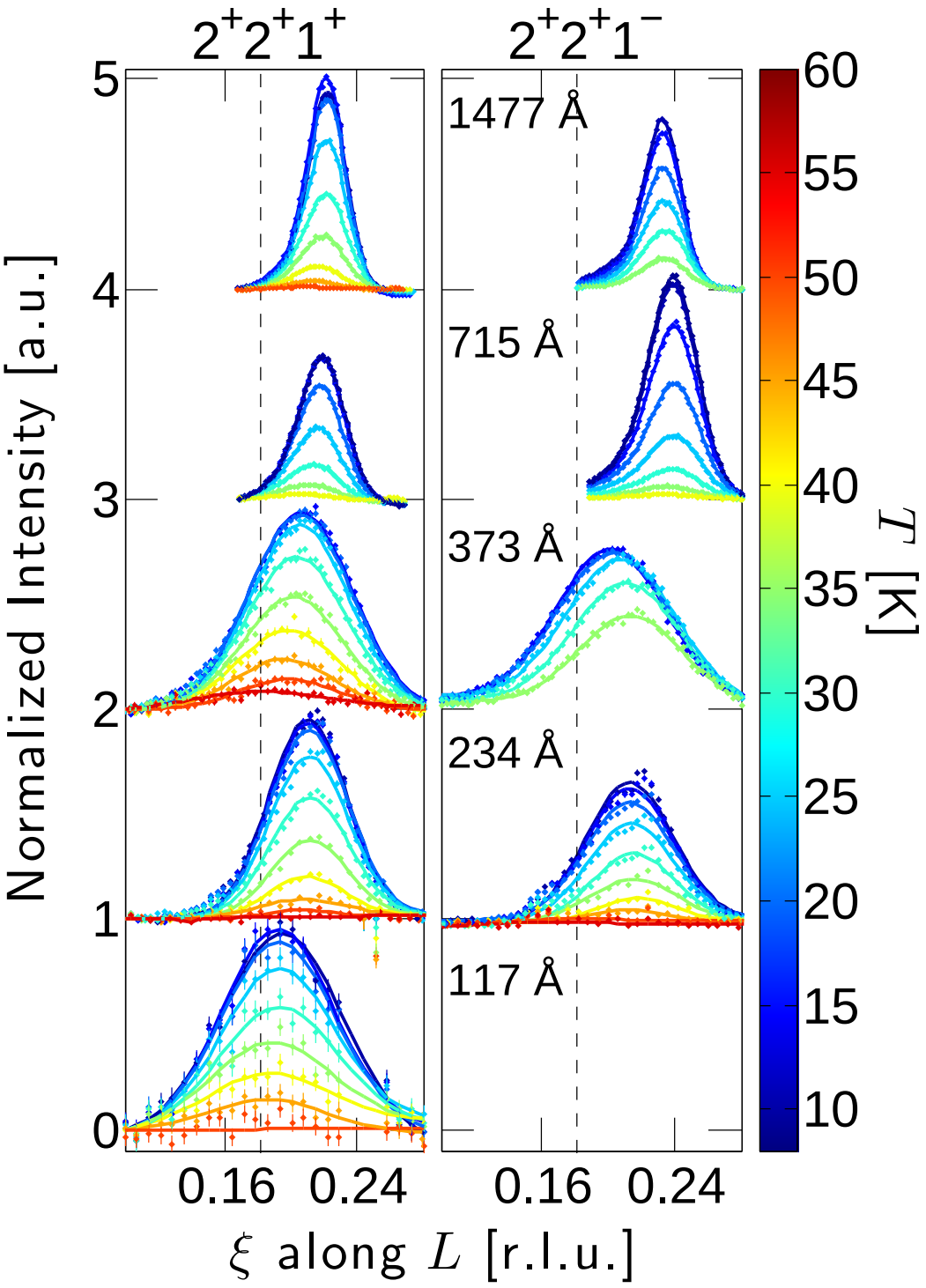

Figure 5.18: Scans in L across the $2^+2^+1^+$ and $2^+2^+1^-$ CDW satellites performed at temperatures from 10–50 K, for samples of 117–1477 Å thickness. Data from experiments SI-01699 and SI-01841. Solid lines show least-squares fits to Gaussian functions. $\xi = |1 - L|$. The dotted lines indicate the position of the peak centre in the bulk α_3-phase.

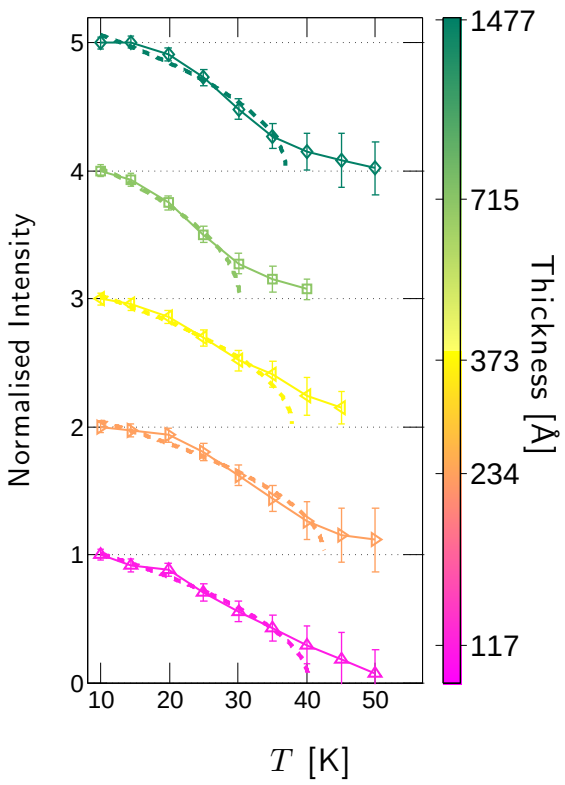

Figure 5.19: The mean value of the areas under the $2^+2^+1^+$ and $2^+2^+1^-$ CDW satellite peaks along H, K and L normalised to the lowest temperature measurement, as temperature is raised from 10–50 K. The data for each sample have been offset for clarity. The solid lines join the data points, and the dashed lines show the expected temperature-dependence of the intensities if the CDW behaviour were governed by a BCS-type order-parameter, as described in Equation 2.85[18].

Here, the length of the component of the CDW wavevector in the plane of the film tends to increase as thickness increases.

5.4.6 CDW satellite peak widths

The FWHM of the satellite peaks along L in each sample were averaged at each temperature point, and the results are shown in Figure 5.21. There is a clear increase in the FWHM as the thickness is decreased, reflecting the trend shown in Figure 5.14. In addition, there is a general trend for the temperature-dependence of the FWHM to change with thickness. For increasing temperature below 40 K the FWHM increases for the thick-

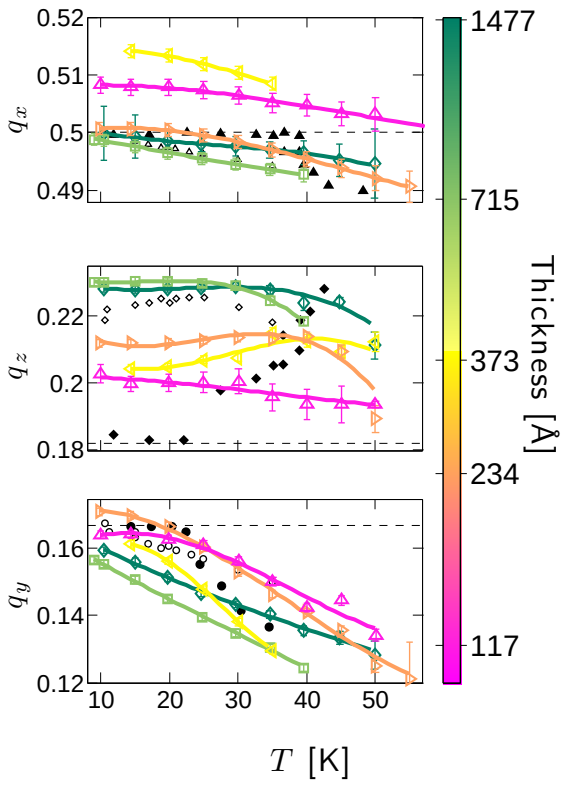

Figure 5.20: The means of the lengths of the CDW wavevector components along (down, from top panel) H, L and K for the $2^+2^+1^+$ and $2^+2^+1^-$ CDW satellites as temperature is raised from 10–50 K. The solid lines are least-squares fits of the data to quartic functions of no particular significance, and serve as guides to the eye. The dashed lines indicate the values of the CDW-components in the bulk α_3-phase, and the solid black points indicate the values of q_{CDW} in the bulk measured by Grübel et al.[88]. The open black points indicate measurements on a 5000 Å sample by Springell et al.[85]

est samples, yet decreases for the 234 and 373 Å samples. The large uncertainties in the mean FWHM for the thinnest sample means that the temperature dependence is unclear.

5.5 Summary

The above evidence shows clear differences in the behaviour of the CDW in thin films and the bulk. Three effects are summarised below.

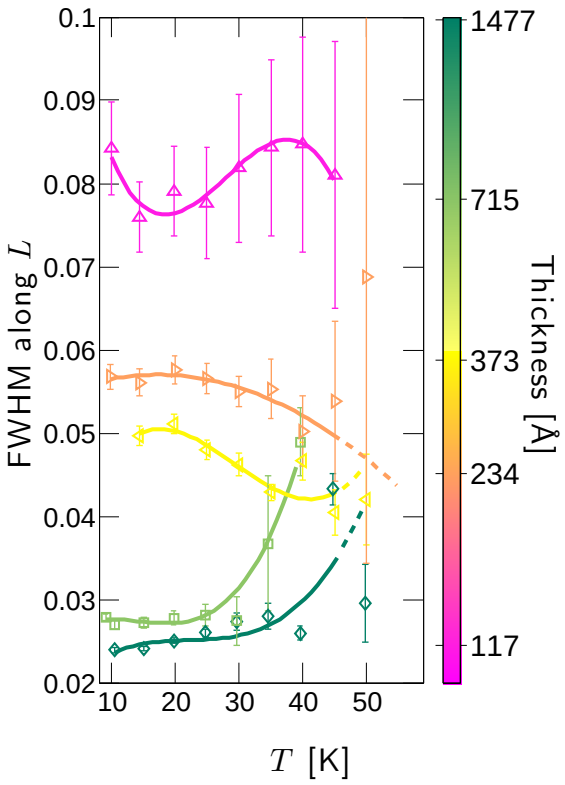

Figure 5.21: The mean FWHM of the $2^+2^+1^+$ and $2^+2^+1^-$ CDW satellite peaks along L as temperature is raised from 10–50 K. The width in L of the (221) Bragg reflection for each sample at 10 K has been subtracted in quadrature from the data. The solid and dashed lines are least-squares fits of the data to quartic functions of no particular significance, and serve as guides to the eye.

5.5.1 Differences in behaviour in between the thin-film state and the bulk

5.5.1.1 Temperature-dependence of the lattice

There is much less variation in the d_{220} lattice-parameter in the thin-film state than in the bulk. The minimum in the out-of-plane d_{220} lattice spacing is much shallower in thin-films. In addition, the data suggest that the temperature at which the minimum occurs is suppressed in thin films, although more accurate measurement is needed to reduce the uncertainty in the measured temperature before clear conclusions may be drawn.

5.5.1.2 Scattering from the CDW satellites

The strong intensity asymmetry in the satellite peaks at $\pm q_y$ seen in the 5000 Å film by Springell et al.[85], but is not present in the bulk, is present in the current films, such that no clear satellite peaks at the $2^+2^-1^\pm$ positions were seen in samples of thickness less that 1477 Å. There is also evidence of intensity asymmetry between the $2^+2^+1^+$ and $2^+2^+1^-$ CDW satellite peaks in some samples.

In contrast, however, to the 5000 Å film, the Smith satellite was seen in a 1000 Å sample, the peak disappearing above 35 K.

5.5.1.3 The temperature-dependence of the CDW

No lock-in transitions are seen in thin-films, despite them being a prominent feature of the bulk CDW. Out-of-the-plane of the film there is a similar increase in the length of the CDW-components as temperature is decreased, in both the thin-film and bulk samples. However, along L which lies in-the-plane, the length of the CDW-component tends to increase, whilst it decreases in the bulk.

The intensity of the CDW-satellite peaks does not show a similar temperature dependence to a BCS-type order parameter, and instead gradually decrease to zero.

5.5.2 Changes in the behaviour of the CDW as film thickness is decreased

5.5.2.1 Temperature-dependence of the lattice

There is a non-trivial dependence of the temperature at which the minimum in the lattice parameter occurs on the thickness of the film. In general the minimum lattice-spacing is lower for thinner samples, counterintuitively showing behaviour that is closer to that of

the bulk.

5.5.2.2 Scattering from the CDW satellites

There is a decrease in the intensity of the CDW satellites relative to the intensity of the nearest Bragg reflection as film thickness is decreased. However, the decrease is not monotonic, and there is wide variation in the relative intensity between samples of similar thickness. Below around 150 Å there is an apparent step change reduction in the relative intensity.

Satellite peaks have been observed in all samples of thicknesses between 2289 and 69 Å.

The length of the CDW-component that lies in the plane of the film shows a decrease as the film thickness is reduced.

5.5.2.3 The temperature-dependence of the CDW

The maximum temperature at which intensity is seen in the CDW shows little dependence on thickness. The sense of the dependence of the FWHM of the CDW satellites on temperature appears to change as the film thickness is decreased.

5.5.3 Correlations between behaviour of the CDW and the microstructure of the films

5.5.3.1 Temperature-dependence of the lattice

There is a convincing dependence of the temperature at which the minimum of the out-of-plane lattice-spacing occurs in thin films. For the narrowest and broadest peaks, the suppression of the temperature of the minimum tends to be largest, whilst films with FWHM of around $0.04\,\text{Å}^{-1}$ show the least suppression, and the minimum appears at

around the same temperature as in the bulk. Strain, mosaic block size and uncorrelated disorder are likely to affect the formation of the CDW. The samples with intermediate FWHM correspond to samples with sufficient thickness to be relatively unstrained and have large structural correlation lengths, yet do not suffer from the presence of large amounts of uncorrelated disorder present in thicker samples with small peak width.

5.5.3.2 Scattering from the CDW satellites

A major observation is that the correlation-length of the CDW in the plane of the film is limited by the thickness in the out-of-plane direction. A dependence of the satellite peak-widths on thickness similar to that seen for the Bragg-reflection widths in Chapter 3. This suggests that the film-microstructure is limiting the size of the CDW domains, and consequently that the CDW is more sensitive to film microstructure than it is to the film thickness.

There is a clear trend towards a decrease in the length of the component CDW wavevector that lies in the plane of the film as the film thickness is decreased. The decrease in the length of this component is strongly correlated with the decrease in the correlation-length of the CDW. This points to an increase in the density of discommensurations in the the CDW, with a corresponding decrease in the size of the CDW domains between discommensurations. This evidence also suggests that the reduction in the uncorrelated disorder as film thickness is decreased, seen in Chapter 3, does not affect the CDW to a greater degree than the size of the mosaic blocks of the crystal.

Chapter 6

Conclusion

This thesis has aimed to present the arguments that microstructural effects in thin films are important in the behaviour of "bulk" physical phenomena, and are also highly dependent on film thickness.

The exhibition of superconductivity and a charge-density wave (CDW) make uranium unique amongst the elements and a fascinating object of study for the condensed-matter physicist. The fabrication of single-crystals of the element is, however, very difficult due to reconstructive phase-transitions upon cooling from the melt. We saw in Chapter 1 how DC magnetron sputtering under UHV conditions allows the growth of single-crystal films of uranium. We have grown a series of high quality epitaxial films of uranium grown in the (110) orientation, on epitaxial niobium buffer-layers grown in the (110) orientation on A-plane sapphire substrates. This is the first in-depth study of a single-crystal actinide thin film, and represents a unique opportunity to study the charge-density wave in a pure elemental solid.

The motivating questions driving the thesis concern the effect of the thin-film state on the CDW. There are two major features of the films that will have an effect: The reduced dimensionality of the film due to its thickness, and the microstructure of the film due to

the epitaxial growth process. Is there a minimum thickness of material for the CDW to form, and what effect does the constraint of the film by the presence of a rigid substrate have on the ability of the CDW to form? In particular, these studies are motivated by the possibility that suppression of the CDW in the thin-film state may be possible, leading to an increase in the superconducting transition temperature.

In Chapter 3 we saw that there are large variations in the mesoscopic structure of thin films as thickness is changed, as both interface roughness and atomic disorder within layers is affected by changes in film thickness. Both X-ray reflectivity and high-angle X-ray diffraction allow determination of the film thickness, although for typical laboratory-based diffractometers simulation of the X-ray reflectivities gives the best measure of film thickness. Both XRR and HAXRD also give qualitative indications of the microstructural quality of the films, and the appearance of strong Pendellösung fringes in the diffraction spectra for many samples show that such films grown for this study are of very high quality.

Chapter 4 showed that the most important microstructural characteristics, strain and dislocation density, are both closely linked to, and depend in non-trivial ways on, the thickness not only of the layers of interest themselves, but the other layers of the film. One of the most important results from this chapter was the opposite senses of the dependences of the Bragg-peak widths of the uranium and niobium layers on the niobium buffer layer thickness. For the current samples, the width of a Bragg peak arising from a particular tends to decrease when the thickness of the layer is increased, but when the thickness of the layer upon which it is grown is increased the Bragg-peak-width increases. We are not aware of a similar study having being made in the literature.

We have shown that in many reports the two-component lineshape is mis-attributed to a "perfect-layer" model, in which the first few layers of an epitaxial film are "pseudomorphic", leading to a very narrow component in transverse scans across Bragg-peaks. In most cases the narrow peak is simply due to the long-range positional correlations in the out-of-plane direction due to the presence of a rigid, flat substrate. For the current sam-

ples we have disproved the presence of such a perfect layer by measuring the dependence of the width of Bragg-peaks in the out-of-plane direction as the in-plane component of the scattering vector is increased.

In addition, the presence of Q-dependent and Q-independent broadening mechanisms means that the peak-breadth, commonly quoted as the film mosaic, is an insufficient description of the film quality. However, analysis of the Q-dependence of broadening, allows a great deal of microstructural information to be deduced from data collected on reasonably unsophisticated laboratory-based X-ray diffractometers.

In Chapter 5 we have seen that the constraint of the thin-film state has wide-reaching effects on the formation of the charge-density wave phase-transition. The incom-mensurate–commensurate transition is suppressed to below the base temperature of 10 K, meaning that there are no lock-in temperatures seen in thin films; a major departure from the bulk behaviour. Furthermore, the correlation-length of the CDW itself is limited in the plane of the film and dependent on the film thickness, such that the CDW exists as a kind of sphere in reciprocal-space. We have shown that the CDW is still present in a film of thickness as small as 69 Å, but a large intensity asymmetry between the $2^{+}2^{+}1^{\pm}$ and $2^{+}2^{-}1^{\pm}$ CDW satellites persists in all films studied, such that the $2^{+}2^{-}1^{\pm}$ satellites were not observed in films of thickness below 1477 Å.

Films of intermediate thickness show the strongest CDW, and also the greatest deviation in the q_x component. The 363 Å sample exhibits a CDW much stronger than in the other samples. This sample also appears to have the optimal microstructure, yet samples only a hundred angstroms thicker or thinner are not nearly as good. Further work will aim to confirm that this remarkably narrow composition range repeatedly leads to the best films.

6.1 Planned work

As described in Chapter 1, experiments are ongoing to characterise uranium films grown in the (001) orientation on W buffer layers on sapphire, and intriguing results have been obtained using beam lines ID20 and ID31 at the ESRF.

In addition, the U/RE multilayers project continues, and time for polarised neutron reflectometry experiments on polREF at ISIS has been allocated.

6.2 Planned publications from the present work

J. Chivall, R. Springell, P.S. Normile, S. Langridge, R.C.C. Ward, S.W. Zochowski, and G.H. Lander. Thickness-dependence of the charge-density wave state in thin-film alpha-uranium. *In Preparation*

J. Chivall, R. Springell, A. Wildes, R.C.C. Ward, S.W. Zochowski, and G.H. Lander. The structure of heteroepitaxial metal films grown on sapphire. *In Preparation*

Bibliography

1. G H Lander, E. S. Fisher, and S. D. Bader. The solid-state properties of uranium — A historical perspective and review. *Advances in physics*, **43** 1, (1994).

2. A. M. Gabovich, A. I. Voitenko, T. Ekino, Mai Suan Li, and H. Szymczak. Competition of superconductivity and charge density waves in cuprates: Recent evidence and interpretation. *Advances in Condensed Matter Physics*, **2010** 681070, (2010).

3. H. L. Laquer. Atomic energy commission report AECD 3706. (unpublished), 1952.

4. Ted G. Berlincourt. Hall effect, resistivity, and magnetoresistivity of Th, U, Zr, Ti, and Nb. *Physical Review*, **114** 969, (1959).

5. H. M. Rosenberg. The thermal conductivity of metals at low temperatures. *Philosophical Transactions of the Royal Society of London. Series A, Mathematical and Physical Sciences*, **247** 441–497, (1955).

6. E. S. Fisher and H. J. McSkimin. Low-temperature phase transition in alpha uranium. *Physical Review*, **124** 67, (1961).

7. C S Barrett, M H Mueller, and R L Hitterman. Crystal structure variations in alpha uranium at low temperatures. *Physical review*, **129** 625, (1963).

8. J Crangle and J Temporal. Heat capacity and transformations in α uranium at low temperature. *Journal of Physics F: Metal Physics*, **3** 1097, (1973).

9. J. C. Lashley, B. E. Lang, J. Boerio-Goates, B. F. Woodfield, G. M. Schmiedeshoff, E. C. Gay, C. C. McPheeters, D. J. Thoma, W. L. Hults, J. C. Cooley, Jr. Hanrahan, R. J., and J. L. Smith. Low-temperature specific heat and critical magnetic field of α-uranium single crystals. *Physical Review B*, **63** 224510, (2001).

10. H. G. Smith, N. Wakabayashi, W. P. Crummett, R. M. Nicklow, G. H. Lander, and E. S. Fisher. Observation of a charge-density wave in α-U at low temperature. *Phys. Rev. Lett.*, **44** 1612–1615, (1980).

11. R E Peierls. Quantum theory of solids. *Physics today*, **9** 29, (1956).

12. J. A. Wilson, F. J. Di Salvo, and S. Mahajan. Charge-density waves in metallic, layered, transition-metal dichalcogenides. *Physical Review Letters*, **32** 882, (1974).

13. J. A. Wilson, F. J. Di Salvo, and S. Mahajan. Charge-density waves and superlattices in the metallic layered transition metal dichalcogenides. *Advances in Physics*, **24** 117–201, (1975).

14. Joseph M. Carpinelli, Hanno H. Weitering, E. Ward Plummer, and Roland Stumpf. Direct observation of a surface charge density wave. *Nature*, **381** 398–400, (1996).

15. I Eremin and M Eremin. CDW as a possible reason for the pseudogap in the normal state of high-t_C cuprates. *Journal of superconductivity*, **10** 459, (1997).

16. Yogesh Singh, R. Nirmala, S. Ramakrishnan, and S. K. Malik. Competition between superconductivity and charge-density-wave ordering in the $Lu_5Ir_4(Si_{1-x}Ge_x)_{10}$ alloy system. *Physical Review B*, **72** 045106, (2005).

17. R. H. Liu, D. Tan, Y. A. Song, Q. J. Li, Y. J. Yan, J. J. Ying, Y. L. Xie, X. F. Wang, and X. H. Chen. Physical properties of the layered pnictide oxides $Na_2Ti_2P_2O$ (P=As,Sb). *Physical Review B*, **80** 144516, (2009).

18. G. Grüner. The dynamics of charge-density waves. *Reviews of Modern Physics*, **60** 1129, (1988).

19. G Grüner. *Density waves in solids.* Addison-Wesley, 1994. ISBN 0-201-62654-3.

20. R H Friend. Periodic lattice distortions and charge density waves in one-and two-dimensional metals. *Journal of physics. C. Solid state physics*, **12** 1441, (1979).

21. S. M. Dubiel and J. Cieślak. Influence of crystalline boundaries on spin- and charge-density waves in chromium. *Physical Review B*, **51** 9341, (1995).

22. J. P. Hill, G. Helgesen, and Doon Gibbs. X-ray-scattering study of charge- and spin-density waves in chromium. *Physical Review B*, **51** 10336, (1995).

23. V. L. R. Jacques, D. Le Bolloc'h, and S. Ravy. Density wave defects in chromium probed by coherent x-rays. *Physica B: Condensed Matter*, **404** 573–575, (2009).

24. J. L. Fry, N. E. Brener, J. L. Thompson, and P. H. Dickinson. Hartree band structure, fermi surface, and nesting wave vector for paramagnetic chromium. *Physical Review B*, **21** 384, (1980).

25. D. G. Laurent, J. Callaway, J. L. Fry, and N. E. Brener. Band structure, fermi surface, compton profile, and optical conductivity of paramagnetic chromium. *Physical Review B*, **23** 4977, (1981).

26. Eric Fawcett. Spin-density-wave antiferromagnetism in chromium. *Reviews of Modern Physics*, **60** 209, (1988).

27. F. J. Lamelas and S. A. Werner. Searches for charge-density waves in the alkali metals: Recent neutron-scattering results for sodium. *Physical Review B*, **54** 16585, (1996).

28. A. W. Overhauser. Exchange and correlation instabilities of simple metals. *Physical Review*, **167** 691, (1968).

29. G. F. Giuliani and A. W. Overhauser. Charge-density-wave satellite intensity in potassium. *Physical Review B*, **22** 3639, (1980).

30. Lars Fast, Olle Eriksson, Börje Johansson, J. M. Wills, G. Straub, H. Roeder, and Lars Nordström. Theoretical aspects of the charge density wave in uranium. *Physical Review Letters*, **81** 2978, (1998).

31. K. T. Moore, M. A. Wall, and R. G. Haire. No evidence of a bulk charge density wave in α-Np or α-Pu at 10 K through electron diffraction. *Physical Review B*, **78** 033112, (2008).

32. http://www.epsrc.ac.uk/ourportfolio/researchareas/Pages/supercond.aspx. Superconductivity, 2011.

33. Mark Buchanan. Mind the pseudogap. *Nature*, **409** 8–11, (2001).

34. O Degtyareva, M. V. Magnitskaya, J. Kohanoff, G. Profeta, S. Scandolo, M. Hanfland, M. I. McMahon, and E. Gregoryanz. Competition of charge-density waves and superconductivity in sulfur. *Physical review letters*, **99** 155505, (2007).

35. H Fu, N. Oeschler, R.A. Fisher, N.E. Phillips, J.E. Gordon, D.-H. Lee, M.-L. Foo, and R.J. Cava. Competition between superconductivity and charge-density wave order in $Na_{0.3}CoO_2{\cdot}1.3H_2O$. *Journal of superconductivity and novel magnetism*, **22** 295, (2009).

36. M Vojta. Lattice symmetry breaking in cuprate superconductors: stripes, nematics, and superconductivity. *Advances in Physics*, **58** 699–820, (2009).

37. E. Morosan, H. W. Zandbergen, B. S. Dennis, J. W. G. Bos, Y. Onose, T. Klimczuk, A. P. Ramirez, N. P. Ong, and R. J. Cava. Superconductivity in Cu_xTiSe_2. *Nat Phys*, **2** 544–550, (2006).

38. K. E. Wagner, E. Morosan, Y. S. Hor, J. Tao, Y. Zhu, T. Sanders, T. M. McQueen, H. W. Zandbergen, A. J. Williams, D. V. West, and R. J. Cava. Tuning the charge density wave and superconductivity in Cu_xTaS_2. *Physical Review B*, **78** 104520, (2008).

39. A. Bussmann-Holder and A. R. Bishop. Suppression of charge-density formation in $TiSe_2$ by Cu doping. *Physical Review B*, **79** 024302, (2009).

40. A. F. Kusmartseva, B. Sipos, H. Berger, L. Forró, and E. Tutiscaron. Pressure induced superconductivity in pristine 1T-$TiSe_2$. *Physical Review Letters*, **103** 236401, (2009).

41. A. Sacchetti, C. L. Condron, S. N. Gvasaliya, F. Pfuner, M. Lavagnini, M. Baldini, M. F. Toney, M. Merlini, M. Hanfland, J. Mesot, J.H. Chu, I. R. Fisher, P. Postorino, , and L. Degiorgi. Pressure-induced quenching of the charge-density-wave state in rare-earth tritellurides observed by x-ray diffraction. *Physical review. B, Condensed matter and materials physics*, **79** 201101, (2009).

42. B. Sipos, A. F. Kusmartseva, A. Akrap, H. Berger, L. Forro, and E. Tutis. From Mott state to superconductivity in 1T-TaS_2. *Nature Materials*, **7** 960–965, (2008).

43. Xiangde Zhu, Hechang Lei, and C. Petrovic. Coexistence of bulk superconductivity and charge density wave in Cu_xZrTe_3. *Physical Review Letters*, **106** 246404, (2011).

44. G. M. Schmiedeshoff, D. Dulguerova, J. Quan, S. Touton, C. H. Mielke, A. D. Christianson, A. H. Lacerda, E. Palm, S. T. Hannahs, T. Murphy, E. C. Gay, C. C. McPheeters, D. J. Thoma, W. L. Hults, J. C. Cooley, A. M. Kelly, R. J. Hanrahan, and J. L. Smith. Magnetotransport and superconductivity of -uranium. *Philosophical Magazine*, **84** 2001–2022, (2004).

45. J. L. O'Brien, A. R. Hamilton, R. G. Clark, C. H. Mielke, J. L. Smith, J. C. Cooley, D. G. Rickel, R. P. Starrett, D. J. Reilly, N. E. Lumpkin, Jr. R. J. Hanrahan, and W. L. Hults. Magnetic susceptibility of the normal-superconducting transition in high-purity single-crystal α-uranium. *Physical review. B, Condensed matter*, **66** 064523, (2002).

46. D. Graf, R. Stillwell, T. P. Murphy, J.H. Park M. Kano, E. C. Palm, P. Schlottmann, J. Bourg, K. N. Collar, J. C. Cooley, J. C. Lashley, J. Willit, and S. W. Tozer. Fermi

surface of α-uranium at ambient pressure. *Physical review. B, Condensed matter and materials physics*, **80** 241101, (2009).

47. M. B. Maple and D. Wohlleben. Superconducting transition temperature and magnetic susceptibility of polycrystalline α-uranium under pressure. *Physics Letters A*, **38** 351–352, (1972).

48. T F Smith and E. S. Fisher. Superconductivity and phase transitions in single-crystal and polycrystal α-u at high pressure. *Journal of low temperature physics*, **12** 631, (1973).

49. C. Palmy and E. S. Fisher. Superconductivity of an α-uranium single crystal under pressure. *Solid State Communications*, **8** 655–657, (1970).

50. A. H. Castro Neto. Charge density wave, superconductivity, and anomalous metallic behavior in 2d transition metal dichalcogenides. *Physical Review Letters*, **86** 4382, (2001).

51. R. C. Morris. Connection between charge-density waves and superconductivity in $NbSe_2$. *Physical Review Letters*, **34** 1164, (1975).

52. P. Sonntag, P. Bödeker, T. Thurston, and H. Zabel. Charge-density waves and strain waves in thin epitaxial Cr(001) films on Nb. *Physical Review B*, **52** 7363, (1995).

53. M Mori and Y Tsunoda. Searching for charge density waves in chromium. *Journal of Physics: Condensed Matter*, **5** L77, (1993).

54. P. Abbamonte. Charge modulations versus strain waves in resonant x-ray scattering. *Phys. Rev. B*, **74** 195113, (2006).

55. W. M. Lomer. Defects in pure metals. *Progress in Metal Physics*, **8** 255–320, (1959).

56. R.L. Snyder, J. Fiala, and H.J. Bunge. *Defect and microstructure analysis by diffraction*. International Union of Crystallography monographs on crystallography. Oxford University Press, 1999. ISBN 9780198501893.

57. S Strite and H Morkoc. GaN, AlN, and InN: a review. *Journal of vacuum science & technology*, **10** 1237, (1992).

58. S J Pearton, J C Zolper, R J Shul, and F Ren. GaN: processing, defects, and devices. *Journal of applied physics*, **86** 1–78, (1999).

59. M A Moram and M E Vickers. X-ray diffraction of III-nitrides. *Reports on Progress in Physics*, **72** 036502, (2009).

60. A Zhylik, A Benediktovich, A Ulyanenkov, H Guerault, and M Myronov. High-resolution x-ray diffraction investigation of relaxation and dislocations in SiGe layers grown on (001), (011), and (111) Si substrates. *Journal of applied physics*, **109** 123714, (2011).

61. J L MacManus-Driscoll, P Zerrer, H Wang, H Yang, J Yoon, A Fouchet, R Yu, M. G. Blamire, and Quanxi Jia. Strain control and spontaneous phase ordering in vertical nanocomposite heteroepitaxial thin films. *Nature Materials*, **7** 314, (2008).

62. S. R. Foltyn, L. Civale, J. L. MacManus-Driscoll, Q. X. Jia, B. Maiorov, H. Wang, and M. Maley. Materials science challenges for high-temperature superconducting wire. *Nat Mater*, **6** 631–642, (2007).

63. A. R. Wildes, J. Mayer, and K. Theis-Brühl. The growth and structure of epitaxial niobium on sapphire. *Thin Solid Films*, **401** 7–34, (2001).

64. L B Freund. *Thin Film Materials : Stress, Defect Formation and Surface Evolution*. Cambridge University Press, 2003. ISBN 0-521-82281-5.

65. E. J. Grier, M. L. Jenkins, A. K. Petford-Long, R. C. C. Ward, and M. R. Wells. Misfit dislocations of epitaxial (110) niobium ‖ (1120) sapphire interfaces grown by molecular beam epitaxy. *Thin Solid Films*, **358** 94–98, (2000).

66. R. Springell, B. Detlefs, G. H. Lander, R. C. C. Ward, R. A. Cowley, N. Ling, W. Goetze, R. Ahuja, W. Luo, and B. Johansson. Elemental engineering: Epitaxial

uranium thin films. *Physical review. B, Condensed matter and materials physics*, **78** 193403, (2008).

67. V Oderno, C Dufour, K Dumesnil, A Mougin, P Mangin, and G Marchal. Hexagonal surface structure during the first stages of niobium growth on sapphire ($11\bar{2}0$). *Philosophical magazine letters*, **78** 419–426, (1998).

68. G. Song, A. Remhof, K. Theis-Bröhl, and H. Zabel. Extraordinary adhesion of niobium on sapphire substrates. *Physical Review Letters*, **79** 5062, (1997).

69. A. H Cottrell. Theory of dislocations. *Progress in Metal Physics*, **1** 77–126, (1949).

70. C N Reid, A. Gilbert, and G. T. Hahn. Twinning, slip and catastrophic flow in niobium. *Acta metallurgica*, **14** 975, (1966).

71. R W Cahn. Plastic deformation of alpha-uranium; twinning and slip. *Acta metallurgica*, **1** 49, (1953).

72. J. W. Matthews and A. E. Blakeslee. Defects in epitaxial multilayers: I. misfit dislocations. *Journal of Crystal Growth*, **27** 118–125, (1974).

73. D M Tricker and W. M. Stobbs. Interface structure and overgrowth orientation for niobium and molybdenum films on sapphire substrates I. A-plane substrates. *Philosophical magazine. A, Physics of condensed matter, defects and mechanical properties*, **71** 1037, (1995).

74. G. Gutekunst, J. Mayer, and M. Rhle. The niobium/sapphire interface: Structural studies by hrem. *Scripta Metallurgica et Materialia*, **31** 1097–1102, (1994).

75. G Gutekunst, T. Mayer, V Vitek, and M. Rohle. Atomic structure of epitaxial Nb-Al_2O_3 interfaces. II. Misfit dislocations. *Philosophical magazine. A, Physics of condensed matter, defects and mechanical properties*, **75** 1357–1382 1357, (1997).

76. G Gutekunst, S J T. Mayer, and M. Ruhl. Atomic structure of epitaxial Nb-Al_2O_3

interfaces. I. Coherent regions. *Philosophical magazine. A, Physics of condensed matter, defects and mechanical properties*, **75** 1329–1355 1329, (1997).

77. R C C Ward and E. J. GRIER. MBE growth of (1 1 0) refractory metals on a-plane sapphire. *Journal of materials science. Materials in electronics*, **14** 533, (2003).

78. R C C Ward, R A Cowley, N Ling, W Goetze, G H Lander, and W G Stirling. The structure of epitaxial layers of uranium. *Journal of physics. Condensed matter*, **20** 135003, (2008).

79. C P Flynn. Constraints on the growth of metallic superlattices. *Journal of Physics F: Metal Physics*, **18** L195, (1988).

80. W Braun. *Applied Rheed: Reflection High-Energy Electron Diffraction During Crystal Growth*, chapter 3. Springer, 1999. ISBN 3-540-65199-3.

81. D. F. McMorrow, R. A. Cowley, A. Gibaud, R. C. C. Ward, and M. R. Wells. Structure of niobium thin films on sapphire. *Applied Physics Letters*, **63** 2195–2197, (1993).

82. A. H. Cottrell. Theory of dislocations. *Progress in Metal Physics*, **4** 205–264, (1953).

83. P. B. Hirsch. Mosaic structure. *Progress in Metal Physics*, **6** 236–339, (1956).

84. P. F. Miceli and C. J. Palmstrom. X-ray scattering from rotational disorder in epitaxial films: An unconventional mosaic crystal. *Physical Review B*, **51** 5506, (1995).

85. R Springell, B. Detlefs, G. H. Lander, R. C. C. Ward, R. A. Cowley, N. Ling, W. Goetze, R. Ahuja, W. Luo, and B. Johansson. Elemental engineering: Epitaxial uranium thin films. *Physical review. B, Condensed matter and materials physics*, **78** 193403, (2008).

86. P.M. Martin. *Handbook of Deposition Technologies for Films and Coatings: Science, Applications and Technology*. Elsevier, 2009. ISBN 9780815520313.

87. D.M. Mattox. *Handbook of Physical Vapor Deposition (PVD) Processing*. William Andrew, 2010. ISBN 9780815520375.

88. G. Grübel, J. D. Axe, Doon Gibbs, G. H. Lander, J. C. Marmeggi, and T. Brückel. Incommensurate charge-density-wave state in alpha -uranium: A high-resolution x-ray and neutron-scattering study. *Physical Review B*, **43** 8803, (1991).

89. S. Ravy, S. Rouzière, J. P. Pouget, S. Brazovskii, J. Marcus, J. F. Bérar, and E. Elkaim. Disorder effects on the charge-density waves structure in V- and W-doped blue bronzes: Friedel oscillations and charge-density wave pinning. *Physical Review B*, **74** 174102, (2006).

90. Y. Yamada. Theoretical study of anomalous incommensurability in α-phase uranium. *Physical Review B*, **47** 5614, (1993).

91. A. M. N. Niklasson, Börje Johansson, and Lars Nordström. Spin density waves in thin chromium films. *Physical Review Letters*, **82** 4544, (1999).

92. Ravi K. Kummamuru and Yeong-Ah Soh. Electrical effects of spin density wave quantization and magnetic domain walls in chromium. *Nature*, **452** 859–863, (2008).

93. G. Helgesen, J. P. Hill, T. R. Thurston, Doon Gibbs, J. Kwo, and M. Hong. Temperature dependence of resonant x-ray magnetic scattering in holmium. *Physical Review B*, **50** 2990, (1994).

94. D. A. Jehan, D. F. McMorrow, R. A. Cowley, R. C. C. Ward, M. R. Wells, N. Hagmann, and K. N. Clausen. Magnetic structure of holmium-yttrium superlattices. *Physical Review B*, **48** 5594, (1993).

95. M Sajieddine, Ph. Bauer, A. Bruson, and G. Marchal. Perpendicular magnetic anisotropy in an annealed Fe/Tb multilayer: A ^{57}Fe Mössbauer study. *Solid State Communications*, **99** 965, (1996).

96. K Mibu. Magnetic anisotropy in Fe/rare-earth multilayers. *Hyperfine interactions*, **113** 287, (1998).

97. D A Jehan. Magnetic structure of holmium-yttrium superlattices. *Physical review. B, Condensed matter and materials physics*, **48** 5594, (1993).

98. J. A. Bearden. X-ray wavelengths. *Reviews of Modern Physics*, **39** 78–124, (1967).

99. Jose Baruchel, J.L. Hodeau, M.S. Lehmann, J.R. Regnard, and C Schlenker, editors. *Neutron and synchrotron radiation for condensed matter studies*, 1, Theory Instruments and Methods. Springer-Verlag, Berlin and New York and Ulis, France, 1994.

100. J. Als Nielsen and D. F. McMorrow. *Elements of modern X-ray physics*. John Wiley & Sons, 2001. ISBN 0-471-49857-2.

101. S D Brown, L Bouchenoire, D Bowyer, J Kervin, D Laundy, M J Longfield, D Mannix, D F Paul, A Stunault, P Thompson, M J Cooper, C A Lucas, and W G Stirling. The xmas beamline at esrf: instrumental developments and high-resolution diffraction studies. *J. Synchrotron Rad.*, **8** 1172, (2001).

102. B E Warren. *X-ray Diffraction*. Dover Publications, Inc., New York, 1990. ISBN 0-486-66317-5.

103. L. G. Parratt. Surface studies of solids by total reflection of x-rays. *Physical Review*, **95** 359, (1954).

104. P Croce and L Névot. Étude des couches minces et des surfaces par réflexion rasante, spéculaire ou diffuse, de rayons x. *Revue de physique appliquée*, **11** 113, (1976).

105. I. K. Robinson. Crystal truncation rods and surface roughness. *Physical Review B*, **33** 3830, (1986).

106. P. Scherrer. Bestimmung der Größe und der inneren Struktur von Kolloidteilchen mittels Röntgenstrahlen. *Nachrichten von der Gesellschaft der Wissenschaften zu Göttingen*, **2** 98–100, (1918).

107. Bernd Wölfing, Katharina Theis-Bröhl, Christoph Sutter, and Hartmut Zabel. AFM and x-ray studies on the growth and quality of Nb(110) on Al_2O_3 . *Journal of Physics: Condensed Matter*, **11** 2669, (1999).

108. M Birkholz. *Thin Film Analysis by X-Ray Scattering*. Wiley-VCH, Weinheim, 2006. ISBN 3-527-31052-5.

109. J. Kwo, M. Hong, and S. Nakahara. Growth of rare-earth single crystals by molecular beam epitaxy: The epitaxial relationship between hcp rare earth and bcc niobium. *Applied Physics Letters*, **49** 319–321, (1986).

110. Wen-Jih Lin, Peter D. Hatton, F. Baudenbacher, and J. Santiso. Observation of ultrahigh-quality crystalline $YBa_2Cu_3O_x$ in submicron thick films. *Applied Physics Letters*, **73** 2995–2997, (1998).

111. A Del Moral and et al. Magnetic phase diagram of holmium/dysprosium superlattices. *Journal of magnetism and magnetic materials*, **226** 1700, (2001).

112. A. Stierle, A. Abromeit, N. Metoki, and H. Zabel. High resolution x-ray characterization of co films on al[sub 2]o[sub 3]. *Journal of Applied Physics*, **73** 4808–4814, (1993).

113. M. Iizumi, J. D. Axe, G. Shirane, and K. Shimaoka. Structural phase transformation in K_2SeO_4. *Physical Review B*, **15** 4392, (1977).

114. J. W. McCamy, Douglas H. Lowndes, J. D. Budai, R. A. Zuhr, and Xiao Zhang. Epitaxial ZnS films grown on GaAs (001) and (111) by pulsed-laser ablation. *Journal of Applied Physics*, **73** 7818–7822, (1993).

115. G. L. Zhou and C. P. Flynn. Fingered morphology of niobium (110) grown by molecular-beam epitaxy. *Physical Review B*, **59** 7860, (1999).

116. P. M. Reimer, H. Zabel, C. P. Flynn, and J. A. Dura. Extraordinary alignment of Nb films with sapphire and the effects of added hydrogen films with sapphire and the effects of added hydrogen. *Phys. Rev. B*, **45** 11426–11429, (1992).

117. A. Gibaud, R. A. Cowley, D. F. McMorrow, R. C. C. Ward, and M. R. Wells. High-resolution x-ray-scattering study of the structure of niobium thin films on sapphire. *Phys. Rev. B*, **48** 14463–14471, (1993).

118. A R Wildes, R A Cowley, R C C Ward, M R Wells, C Jansen, L Wireen, and J P Hill. The structure of epitaxially grown thin films: a study of niobium on sapphire. *Journal of Physics: Condensed Matter*, **10** L631, (1998).

119. C. Sürgers, C. Strunk, and H. v. Löhneysen. Effect of substrate temperature on the microstructure of thin niobium films. *Thin Solid Films*, **239** 51–56, (1994).

120. R. I. Barabash, W. Donner, and H. Dosch. X-ray scattering from misfit dislocations in heteroepitaxial films: The case of Nb(110) on Al_2O_3 . *Applied Physics Letters*, **78** 443–445, (2001).

121. V. M. Kaganer, R. Köhler, M. Schmidbauer, R. Opitz, and B. Jenichen. X-ray diffraction peaks due to misfit dislocations in heteroepitaxial structures. *Physical Review B*, **55** 1793, (1997).

122. M M C Allain and Brent J. Heuser. Lattice strain measurements of deuteride (hydride) formation in epitaxial Nb: Additional results and further insights into past measurements. *Physical review. B, Condensed matter and materials physics*, **72** 054102, (2005).

123. M J Bentall, R A Cowley, R C C Ward, M R Wells, and A Stunault. The structure of rare earth thin films: holmium and gadolinium on yttrium. *Journal of Physics: Condensed Matter*, **15** 7155, (2003).

124. M. Huth and C. P. Flynn. Titanium thin film growth on small and large misfit substrates. *Applied Physics Letters*, **71** 2466–2468, (1997).

125. L. Lazar, K. Westerholt, H. Zabel, Yu. V. Goryunov, and I. A. Garifullin. Growth and structural characterization of Pb/Fe layered system. *Thin Solid Films*, **354** 93–99, (1999).

126. Y. Huttel, E. Navarro, and A. Cebollada. Epitaxy and lattice distortion of V in MgO/V/MgO(001) heterostructures. *Journal of Crystal Growth*, **273** 474–480, (2005).

127. J. L. Menèndez, G. Armelles, C. Quintana, and A. Cebollada. Lattice distortion and magnetic properties of nanometer size Fe(110) islands. *Surface Science*, **482-485** 1135–1140, (2001).

128. A. R. Wildes. The structural properties of Nb / Al2O3 and Y / Nb / Al2O3: high resolution X-ray scattering from epitaxial thin films. (unpublished data), 1998.

129. B D Fulthorpe, P A Ryan, T P A Hase, B K Tanner, and B J Hickey. High-resolution x-ray diffraction studies of roughness and mosaic defects in epitaxial Fe/Au multilayers. *Journal of Physics D: Applied Physics*, **34** A203, (2001).

130. P. Bödeker, A. Abromeit, K. Bröhl, P. Sonntag, N. Metoki, and H. Zabel. Growth and x-ray characterization of Co/Cu (111) superlattices. *Physical Review B*, **47** 2353, (1993).

131. M. Huth and C. P. Flynn. Magnetism and microstructure in epitaxial TbFe_{2} (111) thin films. *Physical Review B*, **58** 11526, (1998).

132. P. Haibach, J. Kble, M. Huth, and H. Adrian. MgO surface microstructure and crystalline coherence of Co/Pt superlattices. *Thin Solid Films*, **336** 168–171, (1998).

133. G. Kästle, H. G. Boyen, B. Koslowski, A. Plettl, F. Weigl, and P. Ziemann. Growth of thin, flat, epitaxial (1 1 1) oriented gold films on c-cut sapphire. *Surface Science*, **498** 168–174, (2002).

134. T. Metzger, R. Höpler, E. Born, S. Christiansen, M. Albrecht, H. P. Strunk, O. Ambacher, M. Stutzmann, R. Stömmer, M. Schuster, and H. Göbel. Coherent x-ray scattering phenomenon in highly disordered epitaxial AlN films. *Physica Status Solidi (a)*, **162** 529–535, (1997).

135. H C Kang, S.H. Seo, and D.Y. Noh. X-ray scattering study on the structural evolution of AlN/sapphire (0001) films during radiofrequency sputter growth. *Journal of materials research*, **16** 1814, (2001).

136. M. S. Yi, H. H. Lee, D. J. Kim, S. J. Park, D. Y. Noh, C. C. Kim, and J. H. Je. Effects of growth temperature on GaN nucleation layers. *Applied Physics Letters*, **75** 2187–2189, (1999).

137. M C. Moram, S. Ghedia, D. V. S. Rao, J. S. Barnard, Y. Zhang, M. J. Kappers, and C. J. Humphreys. On the origin of threading dislocations in GaN films. *Journal of applied physics*, **106** 73513–73513, (2009).

138. H Heinke et al. X-ray scattering from GaN epitaxial layers - an example of highly anisotropic coherence. *Journal of Physics D: Applied Physics*, **34** A25, (2001).

139. A Yu Babkevich, R A Cowley, N J Mason, S Sandiford, and A Stunault. X-ray scattering from epitaxial GaSb/InAs thin films below and above the critical thickness. *Journal of Physics: Condensed Matter*, **14** 7101, (2002).

140. J. H. Li, C. S. Peng, Z. H. Mai, J. M. Zhou, Q. Huang, and D. Y. Dai. Evolution of mosaic structure in $Si_{0.7}Ge_{0.3}$ epilayers grown on Si(001) substrates. *Journal of Applied Physics*, **86** 1292–1297, (1999).

141. P. F. Miceli, C. J. Palmstrom, and K. W. Moyers. X-ray scattering study of lattice relaxation in ErAs epitaxial layers on GaAs. *Applied Physics Letters*, **58** 1602–1604, (1991).

142. E. Brecht, R. Fromknecht, J. Geerk, O. Meyer, J. Reiner, M. Rodewald, R. Schneider, and G. Linker. The [1 1 3] growth direction of $YBa_2Cu_3O_{7-\delta}$ thin films. *Solid State Communications*, **102** 849–853, (1997).

143. E. Brecht, J. Reiner, M. Rodewald, and G. Linker. Epitaxial growth of $YBa_2Cu_3O_{7-x}$ thin films on (111) $SrTiO_3$ substrates. *Thin Solid Films*, **319** 202–206, (1998).

144. Guus Rijnders, Seve Curras, Mark Huijben, Dave H. A. Blank, and Horst Rogalla. Influence of substrate-film interface engineering on the superconducting properties of $YBa_2Cu_3O_{7-\delta}$. *Applied Physics Letters*, **84** 1150–1152, (2004).

145. W. J. Lin, P. D. Hatton, F. Baudenbacher, and J. Santiso. Observation of small interfacial strains in $YBa_2Cu_3O_x$ sub-micron-thick films grown on $SrTiO_3$ substrates. *Applied Physics Letters*, **72** 2966–2968, (1998).

146. M. Becht, F. Wang, J. G. Wen, and T. Morishita. Evolution of the microstructure of oxide thin films. *Journal of Crystal Growth*, **170** 799–802, (1997).

147. Fröhlich, K., Machajdík, D., Hellemans, L., and Snauwaert, J. Growth of high crystalline quality thin epitaxial CeO_2 films on (1102) sapphire. *J. Phys. IV France*, **09** 341–347, (1999).

148. G. Linker, R. Smithey, J. Geerk, F. Ratzel, R. Schneider, and A. Zaitsev. The growth of ultra-thin epitaxial CeO_2 films on r-plane sapphire. *Thin Solid Films*, **471** 320–327, (2005).

149. S E Webster, R Kumaran, S Penson, and T Tiedje. Structural analysis of thin epitaxial Y_2O_3 films on sapphire. *Journal of vacuum science & technology. B, Microelectronics and nanometer structures processing, measurement and phenomena*, **28** C3A20, (2010).

150. O. Durand, A. Letoublon, D. J. Rogers, and F. Hosseini Teherani. Interpretation of the two-components observed in high resolution x-ray diffraction [ω] scan peaks for mosaic ZnO thin films grown on c-sapphire substrates using pulsed laser deposition. *Thin Solid Films*, **519** 6369–6373, (2011).

151. Sang Il Park, Tae Sik Cho, Seok Joo Doh, Jong Lam Lee, and Jung Ho Je. Structural evolution of ZnO/sapphire(001) heteroepitaxy studied by real time synchrotron x-ray scattering. *Applied Physics Letters*, **77** 349–351, (2000).

152. In-Woo Kim and Kyu-Mann Lee. Temperature dependence of microstructure and strain evolution in strained ZnO films on Al_2O_3 (0001). *Nanotechnology*, **19** 355709, (2008).

153. Sang Sub Kim, Tae Yeon Seong, Hyun Seung Kim, and Jung Ho Je. Heteroepitaxial growth behavior of $SrRuO_3/SrTiO_3$(001) by pulsed laser deposition. *Journal of Applied Physics*, **92** 4820–4824, (2002).

154. Maitri P. Warusawithana, Cheng Cen, Charles R. Sleasman, Joseph C. Woicik, Yulan Li, Lena Fitting Kourkoutis, Jeffrey A. Klug, Hao Li, Philip Ryan, Li-Peng Wang, Michael Bedzyk, David A. Muller, Long-Qing Chen, Jeremy Levy, and Darrell G. Schlom. A ferroelectric oxide made directly on silicon. *Science*, **324** 367–370, (2009).

155. Y J Lee. High-quality nanothick single-crystal Y_2O_3 films epitaxially grown on Si (111): Growth and structural characteristics. *Journal of vacuum science & technology. B, Microelectronics and nanometer structures processing, measurement and phenomena*, **26** 1124, (2008).

156. C W Nieh. Nanometer thick single crystal Y_2O_3 films epitaxially grown onSi (111) with structures approaching perfection. *Applied physics letters*, **92** 061914, (2008).

157. A. A. Lomov, D. Bellet, and Dolino G. X-ray diffraction study of thin porous silicon layers. *Physica Status Solidi (b)*, **190** 219, (1995).

158. A. Munkholm, S. Brennan, F. Comin, and L. Ortega. Munkholm et al. reply:. *Physical Review Letters*, **79** 4933, (1997).

159. A. Munkholm, S. Brennan, F. Comin, and L. Ortega. Observation of a distributed epitaxial oxide in thermally grown SiO_2 on Si(001). *Physical Review Letters*, **75** 4254, (1995).

160. D. Stifter and H. Sitter. Hot wall epitaxy of C_{60} thin films on mica. *Applied Physics Letters*, **66** 679–681, (1995).

161. H. Sitter, D. Stifter, and T. Nguyen Manh. Preparation of pristine and Ba-doped C_{60} films by hot-wall epitaxy. *Journal of Crystal Growth*, **174** 828–836, (1997).

162. B Heying. Role of threading dislocation structure on the xray diffraction peak widths in epitaxial GaN films. *Applied physics letters*, **68** 643, (1996).

163. G. Dhanaraj, K. Byrappa, V. Prasad, and M. Dudley. *Springer Handbook of Crystal Growth*. Springer, 2009. ISBN 9783540741824.

164. Peter J Goodhew. Strain relaxation in thin films: the effect of dislocation blocking. *MRS Proceedings*, **594** 93, (1999).

165. R. Moons, S. Blsser, J. Dekoster, A. Vantomme, J. De Wachter, and G. Langouche. Structural characterization of thin epitaxial fe films. *Thin Solid Films*, **324** 129–133, (1998).

166. Jonathan Rivnay, Rodrigo Noriega, R. Joseph Kline, Alberto Salleo, and Michael F. Toney. Quantitative analysis of lattice disorder and crystallite size in organic semiconductor thin films. *Physical Review B*, **84** 045203, (2011).

167. A Boulle, R Guinebretière, and A Dauger. Phenomenological analysis of heterogeneous strain fields in epitaxial thin films using x-ray scattering. *Journal of Physics D: Applied Physics*, **38** 3907, (2005).

168. P. F. Miceli, J. Weatherwax, T. Krentsel, and C. J. Palmstrom. Specular and diffuse reflectivity from thin films containing misfit dislocations. *Physica B: Condensed Matter*, **221** 230–234, (1996).

169. E.J. Mittemeijer and P. Scardi. *Diffraction analysis of the microstructure of materials*. Springer series in materials science. Springer, 2004. ISBN 9783540405191.

170. B. E. Warren. X-ray studies of deformed metals. *Progress in Metal Physics*, **8** 147–202, (1959).

171. A Gibaud, D F McMorrow, and P P Swaddling. Determination of the x-ray scattering lineshape from a Nb thin film using synchrotron radiation. *Journal of Physics: Condensed Matter*, **7** 2645, (1995).

172. G K Williamson and W H Hall. X-ray line broadening from filed aluminium and wolfram. *Acta metallurgica*, **1** 22, (1953).

173. T Ungár and A. Borbély. The effect of dislocation contrast on xray line broadening: A new approach to line profile analysis. *Applied physics letters*, **69** 3173, (1996).

174. Th H de Keijser, J I Langford, E J Mittemeijer, and A B P Vogels. Use of the voigt function in a single-line method for the analysis of x-ray diffraction line broadening. *Journal of applied crystallography*, **15** 308, (1982).

175. M A Krivoglaz. *Diffuse Scattering of X-rays and Neutrons by Fluctuations*. Springer, 1996. ISBN 3-540-57627-4.

176. B E Warren and B L Averbach. The separation of cold-work distortion and particle size broadening in x-ray patterns. *Journal of applied physics*, **23** 497, (1952).

177. K.F. Riley, M.P. Hobson, and S.J. Bence. *Mathematical methods for physics and engineering*. Cambridge University Press, 2006. ISBN 9780521861533.

178. A. W. Overhauser. Observability of charge-density waves by neutron diffraction. *Physical Review B*, **3** 3173, (1971).

179. J. C. Marmeggi, A. Delapalme, G. H. Lander, C. Vettier, and N. Lehner. Atomic displacements in the incommensurable charge-density wave in alpha-uranium. *Solid State Communications*, **43** 577–581, (1982).

180. C. F. Eagen, S. A. Werner, and R. B. Saillant. Amplitude and nature of the charge-density-wave displacements in $K_2Pt(CN)_4Br_{0.3} \cdot 3.2D_2O$ (KCP) at low temperatures. *Physical Review B*, **12** 2036, (1975).

181. E M Conwell. *Semiconductors and semimetals*. Academic Press, Boston, Mass. & London, 1988. ISBN 0-12-752127-5.

182. M A Krivoglaz. *Theory of X-ray and Thermal-Neutron Scattering by Real Crystals*. Plenum, New York, 1969.

183. S. Raymond, J. Bouchet, G. H. Lander, M. Le Tacon, G. Garbarino, M. Hoesch, J. P. Rueff, M. Krisch, J. C. Lashley, R. K. Schulze, and R. C. Albers. Understanding the complex phase diagram of uranium: The role of electron-phonon coupling. *Physical Review Letters*, **107** 136401, (2011).

184. H. G. Smith and G. H. Lander. Neutron scattering investigations of -uranium in the charge-density-wave state. *Physical Review B*, **30** 5407, (1984).

185. R. A. Cowley. Structural phase transitions i. landau theory. *Advances in Physics*, **29** 1–110, (1980).

186. R A Cowley and S Bates. The magnetic structure of holmium. i. *Journal of Physics C: Solid State Physics*, **21** 4113, (1988).

187. K B Efetov and A I Larkin. Charge-density wave in a random potential. *Journal of experimental and theoretical physics*, **45** 1236, (1977).

188. B. Mihaila, C. P. Opeil, F. R. Drymiotis, J. L. Smith, J. C. Cooley, M. E. Manley, A. Migliori, C. Mielke, T. Lookman, A. Saxena, A. R. Bishop, K. B. Blagoev, D. J. Thoma, J. C. Lashley, B. E. Lang, J. Boerio-Goates, B. F. Woodfield, and G. M. Schmiedeshoff. Pinning frequencies of the collective modes in α-Uranium. *Physical Review Letters*, **96** 076401, (2006).

189. H. Fukuyama and P. A. Lee. Dynamics of the charge-density wave. i. impurity pinning in a single chain. *Physical Review B*, **17** 535, (1978).

190. P. A. Lee and T. M. Rice. Electric field depinning of charge density waves. *Physical Review B*, **19** 3970, (1979).

191. T. M. Rice, S. Whitehouse, and P. Littlewood. Impurity pinning of discommensurations in charge-density waves. *Physical Review B*, **24** 2751, (1981).

192. S. Girault, A. H. Moudden, J. P. Pouget, and J. M. Godard. X-ray study of vanadium-doped blue bronze. *Physical Review B*, **38** 7980, (1988).

193. Matts Björck and Gabriella Andersson. *GenX*: an extensible X-ray reflectivity refinement program utilizing differential evolution. *Journal of Applied Crystallography*, **40** 1174–1178, (2007).

194. Stephen M. Danauskas, Dongxu Li, Mati Meron, Binhua Lin, and Ka Yee C. Lee. Stochastic fitting of specular X-ray reflectivity data using *StochFit*. *Journal of Applied Crystallography*, **41** 1187–1193, (2008).

195. ISIS Sean Langridge, Large Scale Structures. http://www.isis.stfc.ac.uk/instruments/crisp/softwar 2001.

196. LD Landau and EM Lifshitz. *Elasticity Theory*. Pergamon Press, Oxford, 1975.

197. P K Shreeman and R. J. Matyi. Implementation of statistical dynamic diffraction theory for defective semiconductor heterostructure modelling. *Journal of applied crystallography*, **43** 550, (2010).

198. Hanqing Jiang, Dahl-Young Khang, Jizhou Song, Yugang Sun, Yonggang Huang, and John A. Rogers. Finite deformation mechanics in buckled thin films on compliant supports. *Proceedings of the National Academy of Sciences*, **104** 15607–15612, (2007).

199. D. Hull and T.W. Clyne. *An introduction to composite materials*. Cambridge solid state science series. Cambridge University Press, 1996. ISBN 9780521388559.

200. F. Conchon. *Défauts et déformations au sein de couches d'oxydes épitaxiées: étude par diffraction des rayons X en haute-résolution*. PhD thesis, Université de Limoges, http://epublications.unilim.fr/theses/2008/conchon-florine/conchon-florine.pdf, 2008.

201. L. B. Hovakimian and Shun-Ichiro Tanaka. Collective modes of misfit dislocations in lattice - mismatched thin films. *MRS Proceedings*, **472** 143, (1997).

202. J C Marmeggi, G H Lander, S van Smaalen, T. Brückel, and C. M. E. Zeyen. Neutron-diffraction study of the charge-density wave in α-uranium. *Physical review. B, Condensed matter and materials physics*, **42** 9365, (1990).